

THE UNIVERSITY OF CHICAGO

METAL-ORGANIC FRAMEWORKS FOR BIOMEDICAL APPLICATIONS

A DISSERTATION SUBMITTED TO
THE FACULTY OF THE DIVISION OF THE PHYSICAL SCIENCES
IN CANDIDACY FOR THE DEGREE OF
DOCTOR OF PHILOSOPHY

DEPARTMENT OF CHEMISTRY

BY

KUANGDA LU

CHICAGO, ILLINOIS

AUGUST 2016

© 2016

KUANGDA LU

ALL RIGHTS RESERVED

Table of Contents

List of Schemes.....	vi
List of Tables	vii
List of Figures	viii
List of Abbreviations	xii
Abstract	xvi
Acknowledgements.....	xix
Chapter 1. Introduction	1
1.1 Metal-organic frameworks	1
1.2 Nanoscale metal-organic frameworks for drug delivery.....	4
1.3 Cancer.....	6
1.3.1 Head and neck cancer	7
1.3.2 Colorectal cancer	8
1.3.3 Ovarian cancer	9
1.4 Photodynamic therapy.....	10
1.5 Checkpoint blockade immunotherapy.....	14
1.6 RNA interference and small interfering RNA.....	15
1.7 References	16
Chapter 2. A Porphyrin-Based Nanoscale Metal-Organic Framework for Photodynamic therapy	29
2.1 Rationale of the nMOF design	29
2.2 Results and Discussion.....	30
2.2.1 Synthesis and characterization of the H ₂ DBP ligand	30
2.2.2 Synthesis and characterization of DBP-Hf.....	35
2.2.3 Photophysics and photochemistry of H ₂ DBP and DBP-Hf.....	40
2.2.4 <i>In vitro</i> and <i>in vivo</i> efficacy.....	46
2.3 Conclusion.....	52
2.4 Methods.....	52

2.5 References	55
Chapter 3. A Chlorin-Based Nanoscale Metal-Organic Framework for Photodynamic therapy .	57
3.1 Rationale of the nMOF design	57
3.2 Results and Discussion.....	59
3.2.1 Synthesis and characterization of the H ₂ DBC ligand.....	59
3.2.2 Synthesis and characterization of DBC-Hf	66
3.2.3 Photophysics and photochemistry of H ₂ DBC and DBC-Hf.....	70
3.2.4 <i>In vitro</i> and <i>in vivo</i> studies.....	75
3.3 Conclusion.....	83
3.4 Methods.....	84
3.5 References	89
Chapter 4. A Chlorin-based Nanoscale Metal-Organic Framework Systemically Rejects Colorectal Cancers via Synergistic Photodynamic Therapy and Checkpoint Blockade Immunotherapy	91
4.1 Rationale of the nMOF design	91
4.2 Results	93
4.2.1 Synthesis and characterization of H ₄ TBC ligand and TBC-Hf nMOF	93
4.2.2 Singlet oxygen generation	107
4.2.3 <i>In vitro</i> PDT efficacy and mechanistic study	107
4.2.4 The abscopal effect of IDOi@TBC-Hf	114
4.2.5 Antitumor Immunity.....	117
4.3 Discussion	123
4.4 Conclusion.....	125
4.5 Methods.....	126
4.6 References	132
Chapter 5. A Nanoscale Metal-Organic Framework for the Co-delivery of Chemotherapeutic Agents and Nucleic Acid Drugs	134
5.1 Rationale of the nMOF design	134
5.2 Results and Discussion.....	135
5.2.1 Synthesis and characterization of the 2'-amino-p-terphenyl-4,4''-dicarboxylate ligand	135

5.2.2 Synthesis of the cisplatin prodrug	138
5.2.3 Synthesis and characterization of nMOF-1	142
5.2.4 Cisplatin prodrug and siRNA loading	144
5.2.5 <i>In vitro</i> gene silencing study.....	150
5.2.6 <i>In vitro</i> anticancer efficacy on resistant tumor models.....	155
5.3 Conclusion.....	160
5.4 Methods.....	161
5.5 References	168
Chapter 6. Nanoscale Metal-organic Frameworks for Real-Time Intracellular pH Sensing in Live Cells	169
6.1 Rationale of the nMOF design	169
6.2 Results and Discussion.....	171
6.2.1 Preparation and Characterization of F-nMOF	171
6.2.2 Response curve calibration.....	180
6.2.3 Live cell pH sensing	186
6.3 Conclusion.....	196
6.4 Methods.....	196
6.5 References	202
Description of Supplemental Files.....	204

List of Schemes

Scheme 2-1 Synthesis of the 5,15-di(p-benzoato)porphyrin ligand.....	30
Scheme 2-2 Synthesis of DBP-Hf and the schematic description of singlet oxygen generation process	36
Scheme 3-1 Schematic description of the singlet oxygen generation by DBC-Hf photosensitization with LED light	58
Scheme 3-2 Synthesis of the 5,15-di(p-benzoato)chlorin (H ₂ DBC)	59
Scheme 4-1 Synthesis of 5,10,15,20-tetra(p-benzoato) chlorin (H ₄ TBC)	93
Scheme 5-1 MOF synthesis and drug loading.....	134
Scheme 5-2 Synthesis of 2'-amino-p-terphenyl-4,4''-dicarboxylic acid (H ₂ L)	135
Scheme 5-3 Synthesis of the cisplatin prodrug	138

List of Tables

Table 2-1 Chemical structure of Zn-DPDBP and crystal structure information of Zn-DPDBP-Zr	37
Table 2-2 Lifetimes of H ₂ DBP and DBP-Hf fluorescence in different medium, fitted by software.....	43
Table 2-3 Fitting parameters of singlet oxygen generation rate.....	46
Table 3-1 Fluorescence lifetimes of H ₂ DBC, DBC-Hf and HfCl ₄ +H ₂ DBC control, fitted by software.....	72
Table 3-2 Fitting parameters for ¹ O ₂ generation curves.....	73
Table 3-3 Statistical analysis of tumor weights by t-test shown with P values.....	83
Table 4-1 Lifetimes of H ₄ TBP, H ₄ TBC, TBP-Hf and TBC-Hf fluorescence in different media, fitted by software.....	106
Table 4-2 Statistical analysis of the tumor sizes at the end of treatment on CT26 tumor bearing mice.....	115
Table 4-3 Statistical analysis of the tumor sizes at the end of treatment on MC38 tumor bearing mice.....	115
Table 5-1 IC ₅₀ (μM) values in A2780 and A2780/CDDP cells.....	158

List of Figures

Figure 1-1 Lattice structures (middle), corresponding SBUs (left), and organic linkers (right) of a variety of MOFs	2
Figure 1-2 Structure models of SBUs and MOFs	4
Figure 1-3 Different strategies for loading cargo into nMOFs	6
Figure 1-4 Ten Leading Cancer Types for the Estimated New Cancer Cases and Deaths by Sex, United States, 2016	7
Figure 1-5 The mechanism of photodynamic therapy	11
Figure 1-6 The UV-vis absorption spectrum of porphyrin in correspondence to the illustration of Gouterman four-orbital theory	12
Figure 1-7 (a) The UV-vis absorption spectra of protoporphyrin IX (PpIX) and chlorin e6 (Ce6). (b) The effective penetration depth of UV-visible light in human tissue	13
Figure 1-8 T cell proliferation induced by PDT	14
Figure 2-1 ¹ H NMR spectrum of dipyrromethane in chloroform-D	31
Figure 2-2 ¹ H NMR spectrum of 5,15-di(p-methylbenzoato)porphyrin in chloroform-D	32
Figure 2-3 ¹³ C NMR spectrum of 5,15-di(p-benzoato)porphyrin in DMSO-D ₆	33
Figure 2-4 ¹ H NMR spectrum of 5,15-di(p-benzoato)porphyrin in DMSO-D ₆	34
Figure 2-5 Mass spectrum of 5,15-di(p-benzoato)porphyrin.....	35
Figure 2-6 Structural confirmation of DBP-Hf.....	37
Figure 2-7 TEM images of DBP-Hf	38
Figure 2-8 (a) Nitrogen adsorption isotherm of DBP-Hf at 77K and (b) Thermogravimetric analysis of DBP-Hf.....	39
Figure 2-9 DLS plot showing the particle size of DBP-Hf.....	40
Figure 2-10 UV-visible spectra of H ₂ DBP and DBP-Hf	41
Figure 2-11 Fluorescence of H ₂ DBP and DBP-Hf in PBS	42
Figure 2-12 Time-resolved fluorescence decay traces of H ₂ DBP (left) and DBP-Hf (right) in different media	42
Figure 2-13 Singlet oxygen generation by DBP-Hf, H ₂ DBP, and H ₂ DBP+HfCl ₄	46
Figure 2-14 Cellular uptake of DBP-Hf after 4 or 12 hour incubation.....	47
Figure 2-15 In vitro PDT cytotoxicity of H ₂ DBP, DBP-Hf, and PpIX at different PS concentrations and irradiation doses	49
Figure 2-16 In vivo efficacy of PDT on SQ20B tumor bearing mice.....	50
Figure 2-17 Histology of tumor slices of mice after PDT treatment	51
Figure 3-1 ESI-MS of 5,15-di(p-methylbenzoato)chlorin	60
Figure 3-2 ¹ H NMR spectra of 5,15-di(p-methylbenzoato)chlorin in chloroform-D	61
Figure 3-3 ¹ H NMR spectrum of 5,15-di(p-benzoato)chlorin in DMSO-D ₆	63

Figure 3-4 ESI-MS of 5,15-di(p-benzoato)chlorin	65
Figure 3-5 Structural characterization of DBC-Hf	67
Figure 3-6 DLS plot showing the particle size of DBC-Hf	69
Figure 3-7 TEM images of DBC-Hf	69
Figure 3-8 Photophysical and photochemical properties of H ₂ DBC and DBC-Hf.....	71
Figure 3-9 Photostability of DBC-Hf, H ₂ DBC, DBP-Hf, and Me ₂ DBB	74
Figure 3-10 Cellular uptake evaluation of H ₂ DBC and DBC-Hf in HT29 (a) or CT26 (b) cells	76
Figure 3-11 In vitro PDT efficacies on different cell lines	77
Figure 3-12 Annexin V/PI analysis of CT26 cells incubated with DBC-Hf, H ₂ DBC or PBS with or without irradiation (90 J/cm ²).....	78
Figure 3-13 Immunogenic cell death detection.....	79
Figure 3-14 In vivo PDT efficacy on CT26 mouse tumor model.....	81
Figure 3-15 In vivo PDT efficacy on HT29 subcutaneous xenograft mouse model	82
Figure 3-16 Histology of frozen tumor tissue slices after H-E staining	83
Figure 4-1 Schematic presentation of combined PDT and immunotherapy by IDOi@TBC-Hf.	92
Figure 4-2 ¹ H NMR of 5,10,15,20-tetra(p-methylbenzoato)porphyrin	94
Figure 4-3 ¹ H NMR of 5,10,15,20-tetra(p-methylbenzoato)chlorin	95
Figure 4-4 ESI-MS of 5,10,15,20-tetra(p-methylbenzoato)chlorin	96
Figure 4-5 ¹ H NMR of 5,10,15,20-tetra(p-benzoato)chlorin	97
Figure 4-6 ESI-MS of 5,10,15,20-tetra(p-benzoato)chlorin	98
Figure 4-7 Structures of TBC-Hf and TBP-Hf	100
Figure 4-8 Nitrogen adsorption isotherms of TBC-Hf (a) and TBP-Hf (b) at 77K.....	101
Figure 4-9 TEM images showing the morphology of TBP-Hf and TBC-Hf.....	102
Figure 4-10 DLS plots showing the particle sizes of TBP-Hf (top) and TBC-Hf (bottom)	103
Figure 4-11 (a) TGA of TBC-Hf before and after IDOi loading. (b) The chemical structure of the IDOi, 4-amino-N-(3-chloro-4-fluoro-phenyl)-N'-hydroxy-1,2,5-oxadiazole-3-carboximidamide.....	104
Figure 4-12 Photophysics and photochemistry of the ligands and nMOFs	105
Figure 4-13 Cellular uptake of TBP-Hf and TBC-Hf in CT26 cells	108
Figure 4-14 In vitro PDT efficacy on CT26 (a,c), MC38 (b,d) and B16F10 (e) cells.....	109
Figure 4-15 Annexin V/PI analysis of CT26 (a) and MC38 (b) cells incubated with PBS, TBC-Hf, TBP-Hf, H ₄ TBC, and H ₄ TBP with or without irradiation (90 J/cm ²)	111
Figure 4-16 CRT exposure on the cell surface	112
Figure 4-17 Immunofluorescence microscopy of CRT expression on the cell surface.....	113
Figure 4-18 In vivo anticancer efficacy showing abscopal effect	116
Figure 4-19 Photos of excised tumors of each group after PDT treatment in the CT26 (a) and MC38 (b) models	117

Figure 4-20 Antigen-specific IFN- γ spot forming cells (SFC) at 14 days after IDOi@TBC-Hf PDT treatment.....	118
Figure 4-21 Population of leukocytes in the tumor 12 h after IDOi@TBC-Hf PDT treatment	119
Figure 4-22 The MHC-II expression level in the tumor 12 h after IDOi@TBC-Hf PDT treatment	120
Figure 4-23 Tumor-infiltrating leukocyte profiles in the tumors 12 days after IDOi@TBC-Hf PDT treatment.....	122
Figure 4-24 In vivo T cell blocking experiments.....	123
Figure 5-1 ^1H NMR spectrum of Me ₂ L in chloroform-D.....	136
Figure 5-2 ^1H NMR spectrum of H ₂ L in DMSO-d ₆	137
Figure 5-3 ^{13}C NMR spectrum of H ₂ L in DMSO-d ₆	137
Figure 5-4 ^1H NMR spectrum of Pt(NH ₃) ₂ Cl ₂ (OH)(OEt) in DMSO-d ₆	138
Figure 5-5 ^1H NMR spectra of cis,cis,trans-[Pt(NH ₃) ₂ Cl ₂ (OEt)(OCOCH ₂ CH ₂ CO ₂ H)] in DMSO-d ₆	139
Figure 5-6 ^{13}C NMR spectrum of cis,cis,trans-[Pt(NH ₃) ₂ Cl ₂ (OEt)-(OCOCH ₂ CH ₂ CO ₂ H)] in DMSO-d ₆	141
Figure 5-7 ^{195}Pt NMR spectrum of cis,cis,trans-[Pt(NH ₃) ₂ Cl ₂ (OEt)(OCOCH ₂ CH ₂ CO ₂ H)] in DMSO-d ₆	141
Figure 5-8 Structural characterization of the nMOFs before and after drug loading	143
Figure 5-9 Structure models of nMOF-1	143
Figure 5-10 ^1H NMR spectrum of Cis@nMOF-1 after digestion.....	145
Figure 5-11 Release profiles of cisplatin prodrug from Cis@nMOF-1 in 5 mM PBS by dialysis method.....	145
Figure 5-12 ^{195}Pt NMR of the released drug.....	146
Figure 5-13 Structure model of the interaction between the siRNA and nMOF surface.....	148
Figure 5-14 DLS plot showing the particle size of nMOF-1 (a), Cis@nMOF-1 (b) and siRNA/Cis@nMOF-1 (c).....	149
Figure 5-15 Stabilization effect after loading siRNA to the nMOF	150
Figure 5-16 Cellular uptake and endosomal escape of siRNA/Cis@nMOF-1 in SKOV-3 cells	152
Figure 5-17 CLSM images showing the time-dependent endosomal escape of siRNA in SKOV-3 cells	153
Figure 5-18 Percent co-localization of siRNA and endosome/lysosome quantified by Image J based on the CLSM images	154
Figure 5-19 siRNA/Cis@nMOF-1 mediated gene silencing in SKOV-3 cells	154
Figure 5-20 In vitro cytotoxicity in different cells.....	157
Figure 5-21 Annexin V/PI analysis of SKOV-3 cells after the incubation for 24 h.....	158
Figure 5-22 DNA ladder analysis	159

Figure 5-23 CLSM images showing cell apoptosis and siRNA internalization in SKOV-3 cells	159
Figure 5-24 Immunogenic response of nMOF-1 and pooled siRNAs/Cis@ nMOF-1 in SKOV-3 (a) and Raw 264.7 (b) cells	160
Figure 6-1 Schematic presentation of FITC loading.....	170
Figure 6-2 Structures and morphologies of nMOF-1 and F-nMOF	171
Figure 6-3 DLS measurements of nMOF-1 (a) and F-nMOF (b)	172
Figure 6-4 ¹ H NMR spectra to confirm covalent attachment	173
Figure 6-5 Mass spectrum of F-nMOF digest.....	175
Figure 6-6 Studies of FITC leaching upon HBSS incubation.....	176
Figure 6-7 TEM images of F-nMOF after incubation in HBSS for different time.....	177
Figure 6-8 FITC loading quantification	178
Figure 6-9 Correlation between FITC feed wt.% and FITC loading wt.%	179
Figure 6-10 Absorption spectra of F-nMOFs at a series of FITC loading amounts	179
Figure 6-11 Fluorescence efficiency of F-nMOFs with different FITC loadings	180
Figure 6-12 Calibration curves of r-pH responses.....	181
Figure 6-13 Images of F-nMOF dispersed in HBSS with a series of pH acquired by CLSM..	182
Figure 6-14 CLSM images of live cells clamped at various pH.....	187
Figure 6-15 pH calibration in live cells by clamping the cells at various pH values.....	189
Figure 6-16 Cellular uptake and intracellular distribution of F-nMOF in H460 cells.....	190
Figure 6-17 Time relapse pH changes in individual endosomes	192
Figure 6-18 Orthogonal views of cells incubated with F-nMOF showing that the particle of interest was stuck on the cell membrane over time	194
Figure 6-19 CLSM images and histograms showing the numbers of endosomes of different pH values	195

List of Abbreviations

Ce6	chlorin e6
CLSM	confocal laser scanning microscopy
CRT	calreticulin
CTLA-4	cytotoxic T-lymphocyte-associated protein 4
DAPI	4',6-diamidino-2-phenylindole
DC	dendritic cell
DCM	dichloromethane
DDQ	2,3-dichloro-5,6-dicyano-1,4-benzoquinone
DEF	N,N-diethylformamide
DLS	dynamic light scattering
DMEM	Dulbecco's Modified Eagle's Medium
DMF	N,N-dimethylformamide
DMSO	dimethyl sulfoxide
DPDBP	5,15-di(p-benzoato)-10,20-diphenyl-porphyrin
ELISPOT	Enzyme-Linked ImmunoSpot
EPR	enhanced permeability and retention
FFT	fast Fourier transform
FITC	fluorescein isothiocyanate
FOLFIRI	folinic acid, fluorouracil and irinotecan

FOLFOX	Folinic acid, Fluorouracil and Oxaliplatin
HBSS	Hank's Balanced Saline Solution
H ₂ DBC	5,15-di(p-benzoato)chlorin
H ₂ DBP	5,15-di(p-benzoato)porphyrin
HOMO	highest occupied molecular orbital
H ₄ TBC	5,10,15,20-tetra(p-benzoato)chlorin
H ₄ TBP	5,10,15,20-tetra(p-benzoato)porphyrin
IACUC	Institutional Animal Care and Use Committee
ICD	immunogenic cell death
ICP-MS	inductively coupled plasma-mass spectrometry
IDO	indoleamine 2,3-dioxygenase
IDOi	indoleamine 2,3-dioxygenase inhibitor
IgG	Immunoglobulin G
IRF	Instrument Response Function
Kyn	kynurenine
LE	loading efficiency
LED	light-emitting diode
LUMO	lowest unoccupied molecular orbital
MDR	multidrug resistance
Me ₂ DBB	5,15-di(p-methyl-benzoato)bacteriochlorin
Me ₂ DBC	5,15-di(p-methyl-benzoato)chlorin

Me ₂ DBP	5,15-di(p-methyl-benzoato)porphyrin
MHC-II	major histocompatibility complex class II
MOF	metal-organic framework
mRNA	messenger RNA
Me ₄ TBC	5,10,15,20-tetra(p-methyl-benzoato)chlorin
Me ₄ TBP	5,10,15,20-tetra(p-methyl-benzoato)porphyrin
MTS	(3-(4,5-dimethylthiazol-2-yl)-5-(3-carboxymethoxyphenyl)-2-(4-sulfophenyl)-2H-tetrazolium)
NEt ₃	triethylamine
nMOF	nanoscale metal-organic framework
OCT	optimal cutting temperature
PBS	phosphate buffered saline
PCP	porous coordination polymer
PD-1	programmed cell death protein 1
PDI	polydispersity index
PD-L1	programmed death-ligand 1
PDT	photodynamic therapy
P-gp	P-glycoprotein
pH _i	intracellular pH
PI	propidium iodide
PpIX	protoporphyrin IX

PS	photosensitizer
PXRD	powder X-ray diffraction
RNA	ribonucleic acid
RNAi	RNA interference
ROI	region of interest
ROS	reactive oxygen species
r.t.	room temperature
SBU	secondary building unit
SCCHN	squamous cell carcinomas of the head and neck
SDS	sodium dodecyl sulfate
SFC	spot forming cells
siRNA	small interfering RNA
SOSG	single oxygen sensor green
TCSPC	Time-Correlated Single Photon Counting
TEM	transmission electron microscopy
TFA	trifluoroacetic acid
THF	tetrahydrofuran
Trp	tryptophan
UiO	University of Oslo (Universitetet i Oslo)
UV-vis	ultraviolet-visible spectroscopy

Abstract

Kuangda Lu: Metal-Organic Frameworks for Biomedical Applications

Under Direction of Professor Wenbin Lin

Metal-organic frameworks (MOFs) have emerged as a new class of hybrid molecular materials with potential for a broad range of applications. When scaled down to the nanosize, nanoscale metal-organic frameworks (nMOFs) have been explored for applications in diagnosis, imaging, and biomedicine by virtue of their structural and functional tunability. In this dissertation, we have further demonstrated the use of nMOFs in cancer therapies and pH sensing in live cells.

Chapter 1 briefly introduces the basic concepts of nMOFs and their potential applications. I also provide brief overviews on cancer, photodynamic therapy (PDT), checkpoint blockade immunotherapy, and RNA interference.

Chapter 2 describes the rational design of the first porphyrin-based nMOF, DBP-Hf, for PDT of resistant head and neck cancer. In the nMOF design, porphyrin ligands are incorporated as the strut to maximize the loading of photosensitizers; the porosity and plate morphology of the nMOF facilitate the diffusion of the reactive oxygen species; the coordination of the ligands to Hf centers improve the performance of the photosensitizers. Thus, the nMOF displays greatly enhanced PDT efficacy both *in vitro* and *in vivo*, representing a new class of promising PDT agents for resistant cancer treatment.

Chapter 3 reports the design of first chlorin-based nMOF, DBC-Hf, with even more enhanced PDT efficacy. Chlorin is the reduced form of porphyrin and exhibits much improved photophysical properties for PDT application. While inheriting the crystallinity, stability, porosity, and nanoplate morphology of DBP-Hf, the reduction of the DBP ligand to chlorin red-shifts the absorption by 13 nm and increases the extinction coefficient by 11 fold. DBC-Hf thus outperforms DBP-Hf in PDT of two colon cancer mouse models.

Chapter 4 details the design of another chlorin-based nMOF with large 1-D channels for combination of PDT and checkpoint blockade immunotherapy. A small molecular inhibitor of indoleamine 2,3-dioxygenase (IDO) is encapsulated into the MOF channels to alter the tumor microenvironment, which synergizes with the nMOF-mediated PDT to elicit systemic antitumor immune response. The synergistic combination therapy achieves effective local and distant tumor rejection in colorectal cancer models. We also elucidated the underlying immunological mechanisms and revealed compensatory roles of neutrophils and B cells in presenting tumor-associated antigens to T cells in this combination therapy.

Chapter 5 describes the first use of an nMOF as a co-delivery system of chemotherapeutics and small interfering RNAs (siRNAs). A cisplatin prodrug was encapsulated into the pores of the nMOF and pooled siRNAs were loaded onto the nanocrystal surface by coordination to the metal sites. nMOFs protect siRNAs from nuclease degradation, enhance siRNA cellular uptake, and promote siRNA escape from endosomes to silence MDR genes in cisplatin-resistant ovarian cancer cells. Co-delivery of cisplatin and siRNAs with nMOFs led to an order of magnitude enhancement in chemotherapeutic efficacy *in vitro*.

Chapter 6 illustrates the first use of an nMOFs for intracellular pH sensing in live cells. Fluorescein isothiocyanate (FITC) was covalently conjugated to an nMOF, with exceptionally high FITC loadings, efficient fluorescence, and excellent ratiometric pH-sensing properties. Live cell imaging studies revealed endo and exocytosis of the nMOF and endosome acidification in real time (videos available as supplementary files). Fluorescently labeled nMOFs thus represent a new class of nanosensors for intracellular pH sensing and provide an excellent tool for studying nMOF-cell interactions.

Acknowledgements

It has been a long way of learning before I can write this dissertation. At this moment to finish my graduate study, I would like to acknowledge many people who made this thesis possible.

At the top of the list is my advisor, Professor Wenbin Lin. It is not just for the opportunity he provided for me to study here and work on these challenging but significant projects. I have learned a lot from his passionate but rigorous manner of research. He is always fearless to the unknowns, adventurous on the virgin of knowledge, and restless in discovery. It would be impossible for me to grow from a fledgling to an independent researcher without his guidance.

It is my great luck to meet Dr. Chunbai He, my closest colleague on all the work in this dissertation. She is always reliable as a collaborator and nice as a friend. She deliberated me from the complex biological experiments so that I can focus on the work of my interest. I also gained much experience on management of projects from her.

Special thanks to Dr. Cheng (Wave) Wang, who is profound in knowledge and inspiring in research. He has been and will still be my idol in my career path. I would also thank Dr. Teng Zhang, my old roommate and lab mate, for the inspiring discussion on work and assistance in life.

There are too many people to be acknowledged in the lab: in no particular order — Dr. Demin Liu, Christina Chan, Kaiyuan Ni, Guangxu Lan, Dr. Nathan Thacker, Dr. Nining Guo, Youfu Wang, Ruoyu Xu, Zekai Lin, Pengfei Ji, Christopher Poon, Dr. Carter Abney, Dr. Xiaopin Duan, Dr. Takahiro Sawano, Marek Piechowicz, Dan Micheroni, Wenbo Han, Dr. Zhiming Zhang, Dr. Xiangjian Kong, Dr. Xin Zhou, Dr. Kuntal Manna, Irene Hsiao, Dr. Yu Peng, Dr.

Micha ě Carboni, Seth Barrett, Dr. Rachel Huxford, Dr. Marcela Wanderly, Dr. Shuang Yao, Dr. Yan Liu, Dr. Stephanie Kramer, Alexei Owen, and anyone I forgot to mention in this list. Thank you all for the experimental help and the discussion and advices on my projects.

I would like to thank my committee members, Prof. Chuan He and Prof. Michael Hopkins, for the advices on my defense and dissertation. I also thank all the faculty and staff members in University of Chicago and University of North Carolina at Chapel Hill for the teaching and help on experiments.

Finally, I would like to thank my family. It is hard to stay away from them for so long time and I am grateful for their supports and love in my whole life.

Chapter 1. Introduction

1.1 Metal-organic frameworks

Metal-organic frameworks (MOFs), also known as porous coordination polymers (PCPs), are a class of crystalline, porous hybrid materials constructed from metal-containing nodes, also known as secondary building units (SBUs), bridged by organic linkers. The archetypal MOF is Prussian blue,¹ a dark blue pigment with a cubic crystal structure constructed from Fe(II)-CN-Fe(III) coordination units. MOFs have been an object of intense study since the 1990s because of their tunability and versatility. Their application to issues as diverse as gas storage/separation,²⁻⁶ nonlinear optics,^{7,8} ferroelectricity,^{9,10} conductivity/semiconductivity,¹¹⁻¹⁵ magnetism,¹⁶ luminescence and chemical sensing,¹⁷⁻²³ catalysis,²⁴⁻²⁹ energy conversion,³⁰⁻³² biomedical imaging,³³⁻³⁶ and drug delivery^{35,37-43} have been intensively explored.

The ability to control coordination bond formation between the SBUs and the linkers allows for orthogonal design of the MOF structures (Figure 1-1).⁴⁴ By selecting metals with the desired coordination chemistry and ligands with the desired geometry, MOF structures can be designed with significant precision.⁴⁵⁻⁴⁸ Functionalities can thus be intentionally incorporated into MOFs by focusing on its components: the ligand,^{46,49,50} the SBU sites,^{26,44,49-52} the channels,⁵³⁻⁵⁶ and the surface of the material.⁵⁷

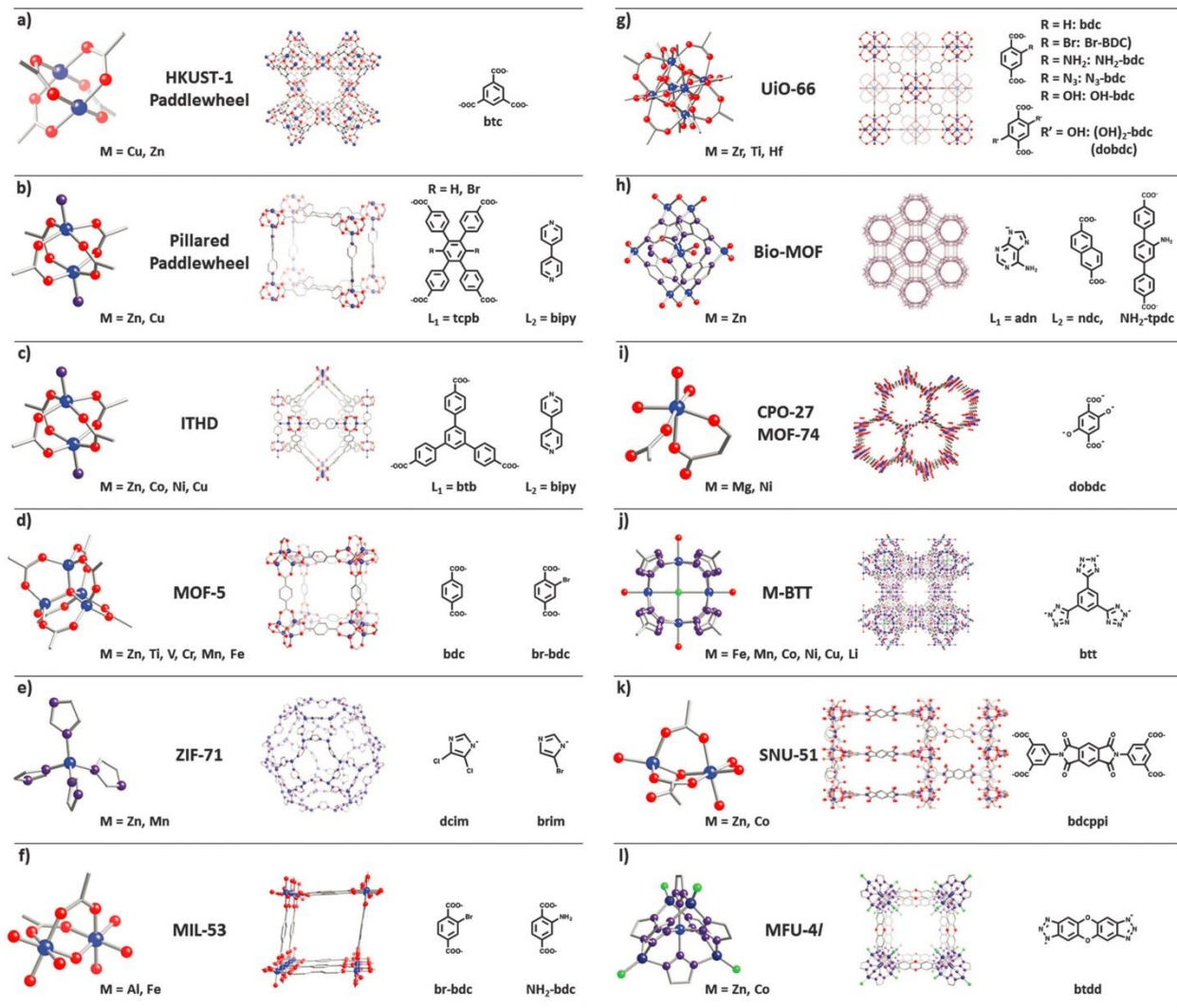


Figure 1-1 Lattice structures (middle), corresponding SBUs (left), and organic linkers (right) of a variety of MOFs. Atoms are as follows: blue - metal; red - oxygen; purple - nitrogen; grey - carbon; green - chlorine. Adapted with permission from *Chem. Soc. Rev.*, **2014**, *43*, 5896-5912. Copyright 2014 The Royal Society of Chemistry.

Due to lanthanide contraction, hafnium and zirconium are approximately the same size and thus similar in their coordination chemistry. Zr^{4+} and Hf^{4+} are hard acid metal ions that exhibit high affinity to oxygen. As a result, Zr and Hf can form strong bonds with carboxylates to build exceptionally water-stable MOFs. Zr- and Hf-based MOFs are also biocompatible because Zr/Hf

oxides and phosphates are not very soluble in water so they are not bioavailable to interrupt protein and nucleic acid functions *in vivo*. For example, zirconium phosphate has extremely low solubility ($K_{sp}=10^{-134}$), which demonstrates the high affinity of Zr(IV) to phosphate ions. We thus anticipated an accelerated decomposition rate of Zr/Hf-MOFs inside cells, where the phosphate concentration is significantly higher than the extracellular environment.^{58,59} For these reasons, we believe that Zr/Hf based MOFs should be suitable for biomedical applications.

Several types of Zr-oxo clusters have been previously reported.^{48,60-64} Of these, $Zr_6(\mu_3-O)_4(\mu_3-OH)_4$ is the most common option for highly stable MOFs.⁶⁵⁻⁶⁹ UiO⁶⁵ and MOF-545⁶⁶ are two typical examples. In UiO MOFs, all 12 edges of the Zr_6 octahedron are bridged by carboxylates, and the 8 faces are each capped by μ_3 -oxo or μ_3 -hydroxyl. The resultant $Zr_6(\mu_3-O)_4(\mu_3-OH)_4(CO_2)_{12}$ SBUs are linked by linear dicarboxylate ligands to build a face-centered cubic structure ($Fm\bar{3}m$, Figure 1-2a,d), with a formula of $Zr_6(\mu_3-O)_4(\mu_3-OH)_4L_6$ (L refers to the ligand, similarly hereafter). In the MOF-545 structure, only 8 edges of the Zr_6 octahedron are bridged by carboxylates, and the remaining coordination sites on an equatorial plane are occupied by water or hydroxyl groups (Figure 1-2b). The $Zr_6(\mu_3-O)_4(\mu_3-OH)_4(OH)_4(H_2O)_4(CO_2)_8$ SBUs are bridged by tetracarboxylate ligands to construct a hexagonal ($P6/mmm$) structure with a formula of $Zr_6(\mu_3-O)_4(\mu_3-OH)_4(OH)_4(H_2O)_4L_2$ (Figure 1-2 e,f). This structure features a large 1-D channel along the [001] direction with a channel diameter of 3.3 nm. We also discovered a new structure (**nMOF-1**) constructed from linear dicarboxylate ligands and a novel Zr_{12} SBU, $[Zr_6(\mu_3-O)_4(\mu_3-OH)_4(CO_2)_9]_2(\mu_2-OH)_6$, which can be viewed as two Zr_6 clusters bridged by six μ_2 -OH (Figure 1-2c). Each Zr_6 cluster coordinates to 6 carboxylates from the linear dicarboxylate ligands on the equatorial plane to form a 2-D layer, and the other ligands link

above and below to connect between layers (Figure 1-2 g,h). The Zr_{12} clusters thereby adopt an ABAB packing style along the c axis to form a trigonal structure ($P\bar{3}1c$).

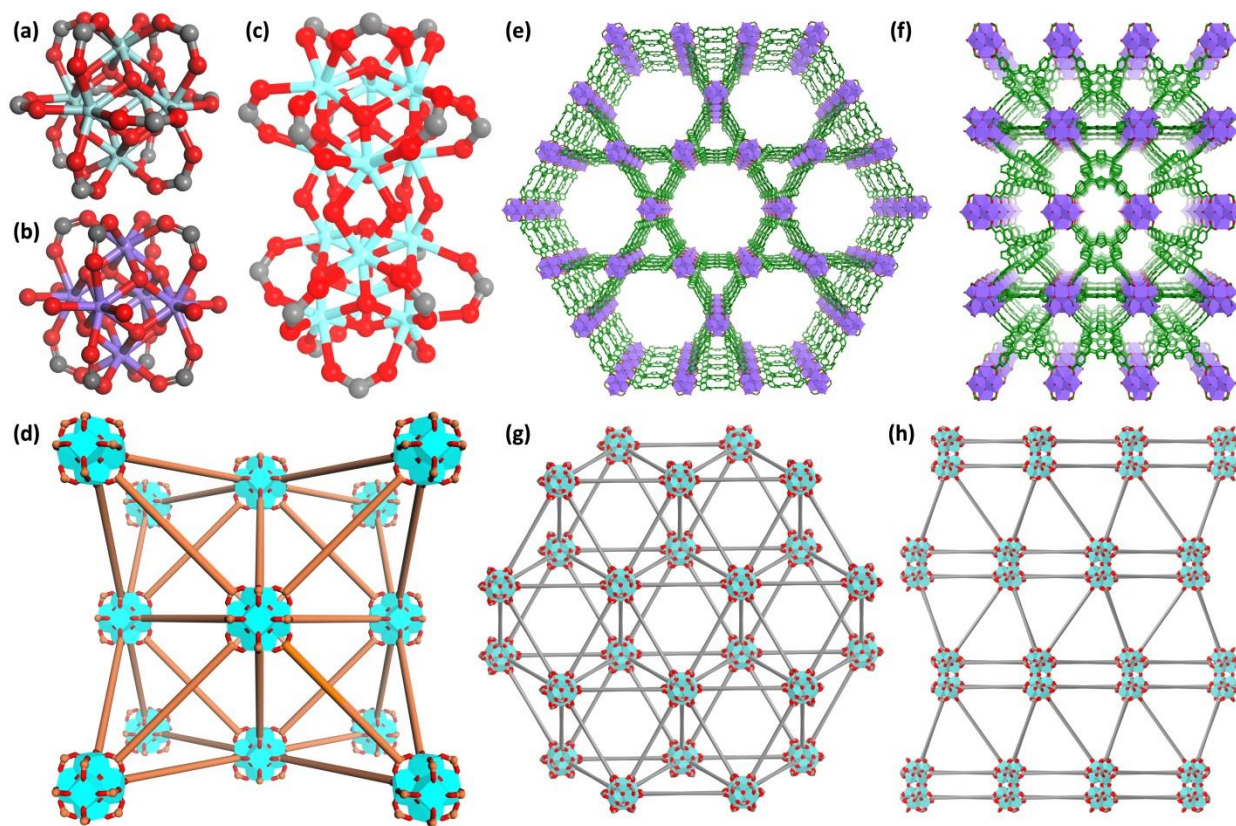


Figure 1-2 Structure models of SBUs and MOFs. The SBUs of UiO ($[Zr_6(\mu_3-O)_4(\mu_3-OH)_4(CO_2)_{12}]$, a), MOF-545 ($[Zr_6(\mu_3-O)_4(\mu_3-OH)_4(OH)_4(H_2O)_4(CO_2)_8]$, b) and **nMOF-1** ($[Zr_6(\mu_3-O)_4(\mu_3-OH)_4(CO_2)_9]_2(\mu_2-OH)_6$, c). Cyan and purple, Zr/Hf; red, O; gray, C. (d) The structure model of UiO MOF: cyan, Zr/Hf; red, O; orange, ligand. The structure models of MOF-545 along [001] (e) and [100] (f) directions: purple, Zr/Hf; red, O; green, ligand. The structure models of **nMOF-1** along [001] (g) and [100] (h) directions: cyan, Zr/Hf; red, O; gray, ligand.

1.2 Nanoscale metal-organic frameworks for drug delivery

The past two decades have witnessed the rapid development of nanotechnology for medical applications such as the detection, diagnosis, and treatment of cancer and other diseases.^{39,70-75}

Because of their size, which allows them to penetrate the leaky vasculatures of tumors,

nanocarriers are able to accumulate through passive tumor targeting, also known as the enhanced permeability and retention (EPR) effect.^{76,77} More advanced delivery platforms have also been designed that incorporate target moieties for tumor-specific delivery.^{72,78-80}

In contrast to purely inorganic⁸¹⁻⁸⁴ or organic nanomaterials,⁸⁵⁻⁸⁸ nanoscale MOFs (nMOFs) are hybrid materials with characteristics that make them excellent candidates for drug delivery^{35,39,40}: (1) structural and compositional tunability for precise material design; (2) high porosity permitting a high cargo payload; and (3) relatively labile coordination bond connections, which make nMOFs intrinsically biodegradable in a biological environment. nMOFs have been successfully applied to the delivery of chemotherapeutic agents,^{37,41,42,89} imaging contrast agents,^{33,34,42,90} photosensitizers,⁹¹⁻⁹⁴ proteins^{95,96} and gene therapy drugs.^{89,97,98}

There are multiple strategies for loading cargo into nMOFs (Figure 1-3): encapsulation into the channels,^{37,89,96} attachment to the ligands^{90,97} or SBUs,⁸⁹ or using them directly as struts^{91,92,99} or nodes.^{33,95} The encapsulation method is the simplest and most frequently used, but premature cargo release can be a concern. Attachment to the linkers or nodes is a better option for postsynthetic functionalization if the attachment strength, feasibility of loading, and the release of cargo can be well balanced. nMOFs directly built from active agents have unique challenges because they require specific alignment of coordination sites, and the functionality of the cargo may be affected after constructing the framework. However, successful cases usually achieve ultra-high payloads, and we have shown that our nMOFs can perform significantly better than the free cargo.

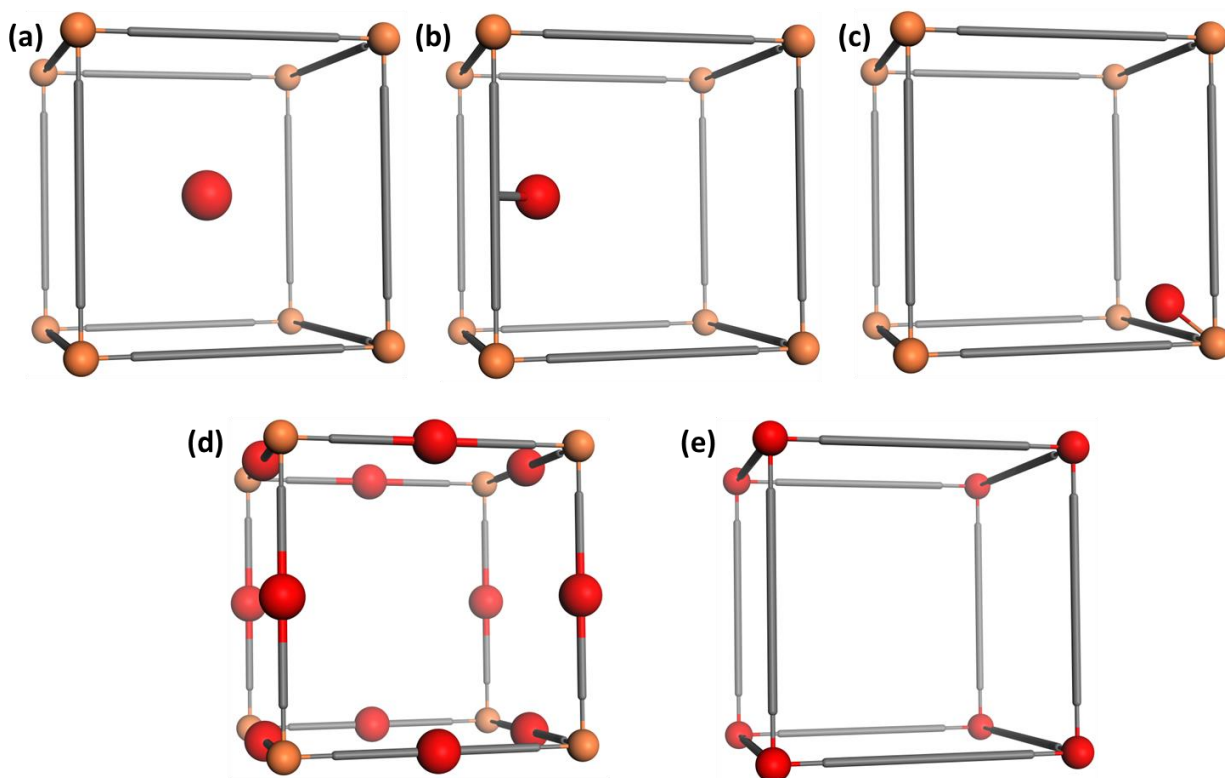




Figure 1-3 Different strategies for loading cargo into nMOFs, (a) Encapsulation in the channels; (b) attachment to the linkers; (c) coordination to the SBUs; (d) used as struts; (e) serving as connection nodes. The red balls represent the cargo.

1.3 Cancer

Cancer is a major public health concern worldwide. It is currently the second leading cause of death in the United States, with ~1.7 million new cases estimated in 2016.¹⁰⁰ However, owing to rapid development of cancer treatment technology, the death rate is decreasing despite the increase in number of new cases every year. Figure 1-4 summarizes the incidence and death rate by sex in the United States. Lung, prostate, colorectal, pancreatic, and liver cancer are the most lethal cancer types for men, and lung, breast, colorectal, pancreatic, and ovarian cancer most fatal for women. Here we will introduce a few types of cancer related to our work.

Estimated New Cases

		Males		Females			
Prostate	180,890	21%			Breast	246,660	29%
Lung & bronchus	117,920	14%			Lung & bronchus	106,470	13%
Colon & rectum	70,820	8%			Colon & rectum	63,670	8%
Urinary bladder	58,950	7%			Uterine corpus	60,050	7%
Melanoma of the skin	46,870	6%			Thyroid	49,350	6%
Non-Hodgkin lymphoma	40,170	5%			Non-Hodgkin lymphoma	32,410	4%
Kidney & renal pelvis	39,650	5%			Melanoma of the skin	29,510	3%
Oral cavity & pharynx	34,780	4%			Leukemia	26,050	3%
Leukemia	34,090	4%			Pancreas	25,400	3%
Liver & intrahepatic bile duct	28,410	3%			Kidney & renal pelvis	23,050	3%
All Sites	841,390	100%	All Sites	843,820	100%		

Estimated Deaths



		Males		Females			
Lung & bronchus	85,920	27%			Lung & bronchus	72,160	26%
Prostate	26,120	8%			Breast	40,450	14%
Colon & rectum	26,020	8%			Colon & rectum	23,170	8%
Pancreas	21,450	7%			Pancreas	20,330	7%
Liver & intrahepatic bile duct	18,280	6%			Ovary	14,240	5%
Leukemia	14,130	4%			Uterine corpus	10,470	4%
Esophagus	12,720	4%			Leukemia	10,270	4%
Urinary bladder	11,820	4%			Liver & intrahepatic bile duct	8,890	3%
Non-Hodgkin lymphoma	11,520	4%			Non-Hodgkin lymphoma	8,630	3%
Brain & other nervous system	9,440	3%			Brain & other nervous system	6,610	2%
All Sites	314,290	100%	All Sites	281,400	100%		

Figure 1-4 Ten Leading Cancer Types for the Estimated New Cancer Cases and Deaths by Sex, United States, 2016. Reprinted with permission from *CA: CANCER J CLIN*, 2016, 66, 7–30. Copyright 2016 John Wiley & Sons, Inc.

1.3.1 Head and neck cancer

Head and neck cancer is a group of biologically similar epithelial malignancies that arise in the head or neck region (including the nasal cavity, sinuses, lips, mouth, salivary glands, throat, and larynx). Primary treatment of head and neck cancers include surgery and radiation therapy, with chemotherapy and chemoradiotherapy serving as a secondary treatment.¹⁰¹ Almost all of

these epithelial malignancies are squamous cell carcinomas of the head and neck (SCCHN), and of those affected, about two-thirds will develop advanced stage disease, commonly involving regional lymph nodes.¹⁰² At least 50% of patients with locally advanced SCCHN relapse, usually within the first 2 years of treatment.¹⁰¹

Surgery remains the mainstay treatment of SCCHN but requires wide excision margins and usually causes functional deficits by damaging adjacent structures.¹⁰³ Radiotherapy gives good prognosis on early stage tumors but is problematic for recurrent disease due to cumulative toxicity.¹⁰⁴ Chemotherapy develops from a palliative care to a central component of treatment in SCCHN,¹⁰⁵ though systemic toxicity and drug resistance remain a concern. Targeted therapy, such as cetuximab for EGFR inhibition, has emerged as a novel treatment strategy for SCCHN.¹⁰⁶ Since SCCHN is usually superficial, photodynamic therapy (PDT) represents a potential alternative treatment modality. PDT is a localized therapy that can minimize peripheral tissue damage, and the lack of cumulative tissue toxicity enables repeated treatments without excluding the possibility of other treatments.¹⁰⁷ It is as effective as surgery or radiotherapy for small superficial tumors and also works as a last recourse for recurrent head and neck cancer in patients who have failed conventional therapy.¹⁰⁸

1.3.2 Colorectal cancer

Colorectal cancer is cancer that begins in the colon or rectum. Colorectal cancer ranks third in both incidence and death rate for both sexes.¹⁰⁰ Only 40% of patients with colorectal cancer are diagnosed at a local stage, for which the 5-year survival rate is 90.3%, while for regional and distant metastatic stages the survival drops to 70.4% and 12.5%, respectively.¹⁰⁹

Chemotherapy has been the mainstay treatment of colorectal cancer.¹¹⁰ Cocktails of a few chemotherapeutic drugs, such as FOLFOX (oxaliplatin, fluorouracil and leucovorin)¹¹¹ and FOLFIRI (fluorouracil, folinic acid and irinotecan),¹¹² have become gold standards in the first-line treatment of colorectal cancer. Moreover, better understanding of the biology of colorectal cancer promotes the combination of chemotherapy with targeted therapy drugs such as cetuximab, bevacizumab and panitumumab in the clinic.¹¹³⁻¹¹⁵

Despite developments in colorectal cancer treatment, the high probability of metastases remains an issue that cause over one third of death eventually.¹⁰⁹ The limitations of surgery and adjuvant chemo/radio/targeted therapies to treat metastatic colorectal cancer urge the development of novel approaches.¹¹⁶ Immunotherapy is the most welcome candidate, since antitumor immunity generated by stimulation of the host immune system is likely capable of controlling metastatic tumor growth. However, combination with other treatment modalities is necessary to maximize the benefits of immunotherapy and increase the durable response rate. Unlike most of the commonly used cancer therapies, which are immunosuppressive at treatment doses,^{117,118} PDT can stimulate the immune system to recognize and destroy distant metastases during treatment of the primary tumor, owing to a consequent acute inflammatory reaction.¹¹⁹ Nevertheless, the studies of PDT on colorectal cancer are still in a preclinical stage.

1.3.3 Ovarian cancer

Ovarian cancer is the deadliest gynecological cancer with a high mortality rate that has remained unchanged over the past four decades.^{120,121} Modern management helps a significant proportion of women attain complete remission in response to treatments, but most of those with

the advanced disease will develop recurrence within 18 months.¹²² Epithelial ovarian cancer is the most common type, with about 22,000 cases diagnosed each year in the United States.¹²³

Due to the nature of this disease, debulking surgery is only auxiliary to chemotherapy in advanced ovarian cancer. Platinum drugs (cisplatin or the less toxic carboplatin) in combination with paclitaxel or docetaxel have been the standard of care for past decades.¹²² Other strategies, such as targeted therapy and hormone therapy, have been explored, but little improvement in overall survival has been achieved.^{89,124} The dismal prognosis of ovarian cancer is in large part due to acquired resistance to chemotherapy.¹²⁵ Though initial epithelial ovarian cancer is responsive to platinum drug based chemotherapy,¹²⁶ relapses are often refractory to treatment and ultimately lead to mortality.¹²⁷ New strategies to overcome drug resistance are urgently needed in order to reduce the mortality rate of ovarian cancer.

Treatment of cancers with chemotherapy drugs often results in multidrug resistance (MDR). The suggested resistance mechanism includes membrane transportation alteration, genetic responses, DNA repair enhancement, target molecules alteration, metabolic effects, and growth factor influence.¹²⁸ Resistance pathways and mutations have been deeply explored both genetically and epigenetically,^{89,129-131} and a number of inhibitors targeting MDR genes or proteins have been developed in recent years.¹³¹⁻¹³³ However, none of the new agents have significantly influenced the diagnosis and treatment of ovarian cancer in the clinic.¹³⁴

1.4 Photodynamic therapy

Photodynamic therapy (PDT) is a phototherapy that combines three nontoxic components—a photosensitizer (PS), a light source, and oxygen in the tissue—to destroy tumors and other

malignancies.¹³⁵ PDT transfers energy from the light-excited PS to oxygen and other molecules in the tissue to generate reactive oxygen species (ROS), particularly, singlet oxygen ($^1\text{O}_2$), which induces cellular toxicity (Figure 1-5).^{135,136} PDT can lead to localized destruction of diseased tissues via selective uptake of the PS and/or local exposure to light, providing a minimally invasive cancer therapy.

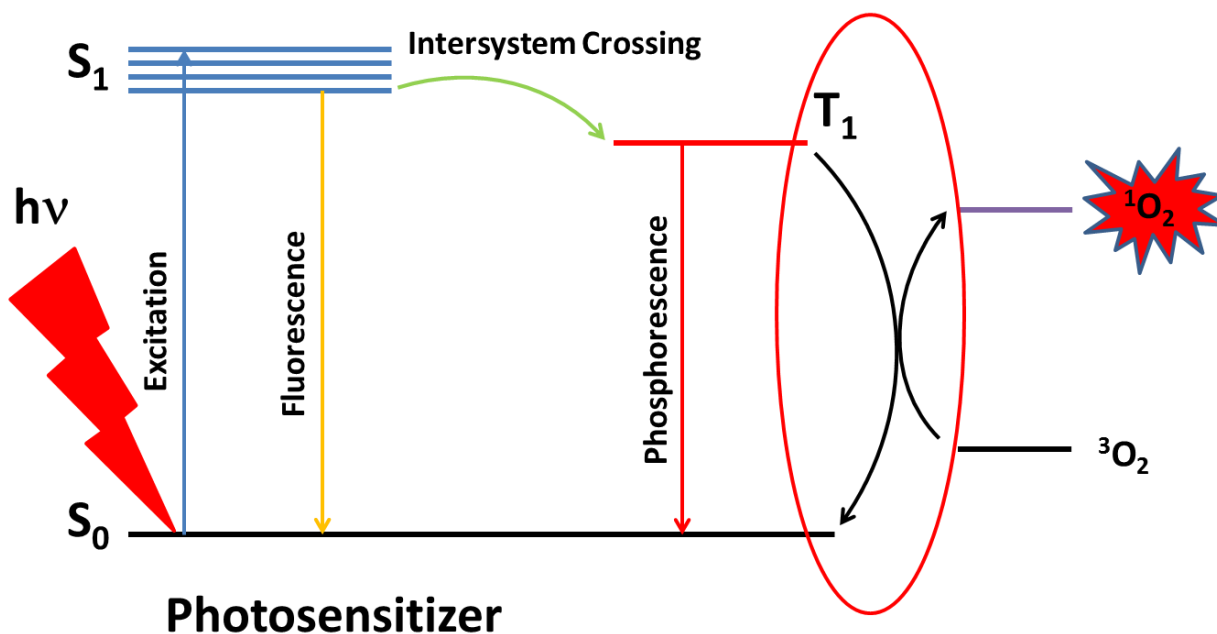


Figure 1-5 The mechanism of photodynamic therapy.

The application of PDT to cancer treatment dates back to the 1970s, when hematoporphyrin derivatives were studied for PDT efficacy *in vivo*.¹³⁵ The first PDT agent photofrin[®] was approved for clinical use in 1993. Most PSs on the market are from the porphyrin family, with a few other dyes emerging in researches in recent years.^{137,138}

For better performance in PDT, the PSs should generate high levels of singlet oxygen. In other words, PSs require strong absorption at the excitation wavelength, high intersystem

crossing efficiency, and low fluorescence and phosphorescence. Porphyrin and its derivatives feature high intersystem crossing quantum yield owing to their strong vibronic spin-orbit coupling.¹³⁹ UV-visible absorptions of porphyrins and their derivatives have been interpreted by Martin Gouterman with a four-orbital model,¹⁴⁰ in which the transition between two HOMOs and two LUMOs generates two pairs of absorption bands, B bands (Soret bands) and Q bands. For freebase porphyrins, the Q-bands further split to four peaks on the spectrum due to the lowering of molecular symmetry (Figure 1-6).

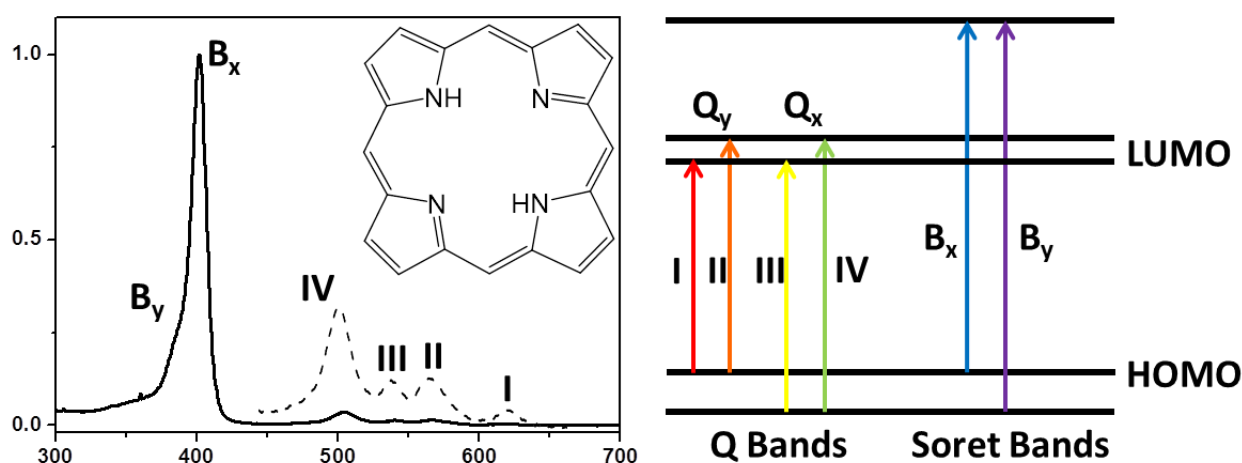


Figure 1-6 The UV-vis absorption spectrum of porphyrin in correspondence to the illustration of Gouterman four-orbital theory.

Chlorin is the reduced form of porphyrin in which one β - β double bond of the porphyrin is hydrogenated. The reduced molecular symmetry (from D_{4h} or D_{2h} to C_{2h}) and the destabilization of MOs causes red shift of Q_y bands, while the Q_y band intensity increases due to higher oscillator strength of these excited states (Figure 1-7a).¹⁴¹ Such changes in absorption vastly improve the performance of chlorins in PDT since near infrared light can penetrate deeper into the tissue (Figure 1-7b). Further reduction of another β - β double bond on the opposite side of

chlorin affords bacteriochlorin, whose Q_y absorption dramatically red shifts to ~ 740 nm. Unfortunately, because bacteriochlorins are usually unstable upon light irradiation, no bacteriochlorin PSs are developed for the clinic.¹⁴²

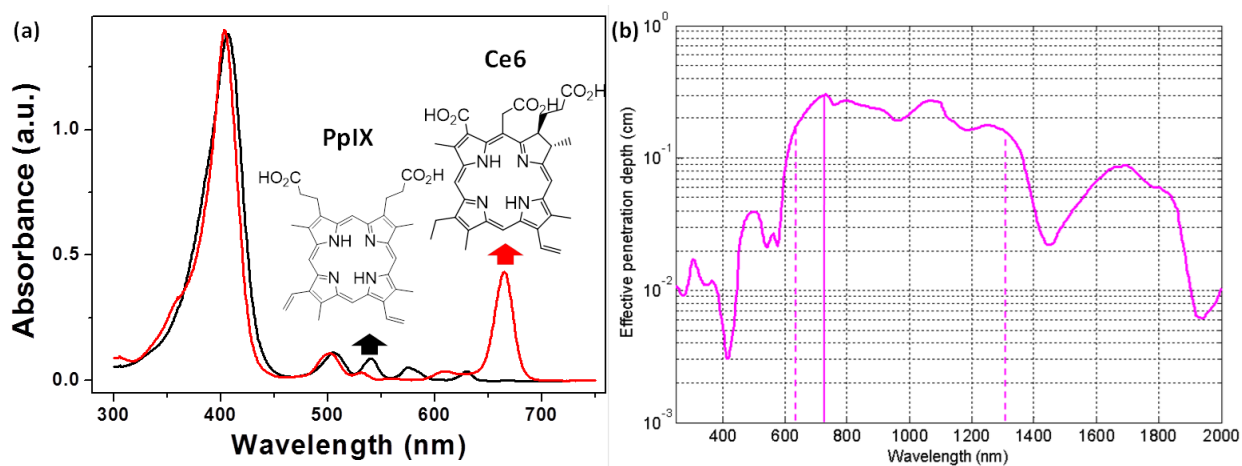


Figure 1-7 (a) The UV-vis absorption spectra of protoporphyrin IX (PpIX) and chlorin e6 (Ce6). (b) The effective penetration depth of UV-visible light in human tissue. Reprinted from Wikipedia: Near-infrared window in biological tissue, created by Zhun310 at English Wikipedia.

Though recognized as a local therapy, PDT is found to be highly immune-active. PDT can induce both apoptosis and necrosis, producing a strong inflammatory response that activates antigen presentation to the lymph nodes (Figure 1-8).¹¹⁹ The consequent T cell maturation and proliferation not only enhances local tumor destruction but also potentiates systemic antitumor vaccination. Nevertheless, PDT-induced antitumor immunity has not yet been applied in the clinic.

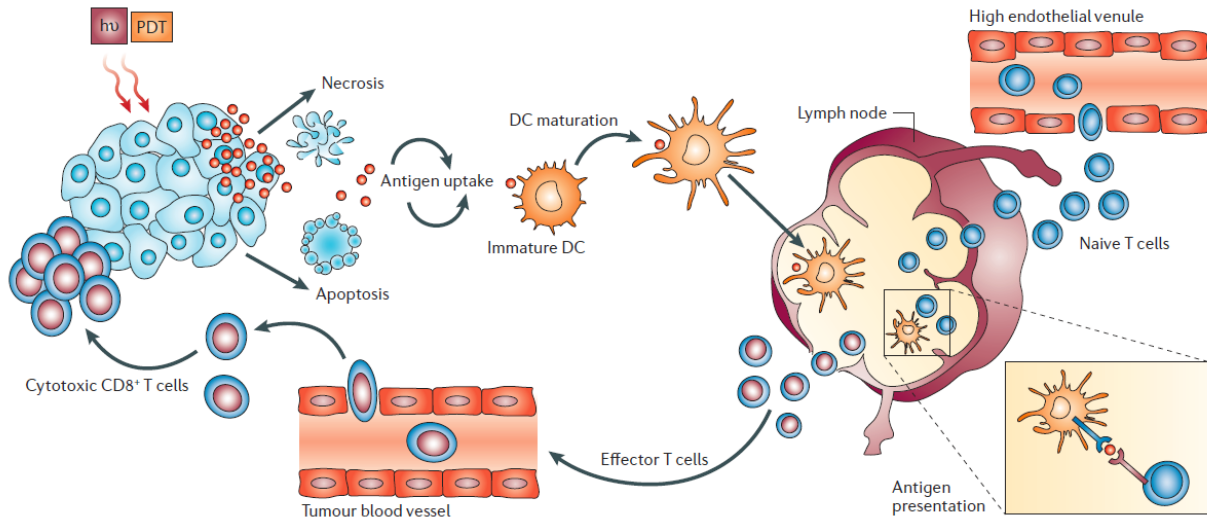


Figure 1-8 T cell proliferation induced by PDT. Reprinted with permission from *Nat. Rev. Cancer* **2006**, *6*, 535-545. Copyright 2006 Nature Publishing Group.

1.5 Checkpoint blockade immunotherapy

Immunotherapy that uses the patient's own immune system to help fight cancer has recently emerged as a highly effective cancer treatment strategy. It exhibits high overall response rates in multiple cancer types and durable tumor control enjoyed by a small subset of patients.^{143,144} Checkpoint blockade immunotherapy, which uses small molecules or antibodies to stimulate the immunosuppressive microenvironment of tumors by modulating protein expression and/or functions at dysregulated immune checkpoints, is currently a focal point of clinical interest.^{144,145} Multiple checkpoint blockade immunotherapy drugs have been approved by FDA for clinical use recently, including Ipilimumab, which targets CTLA-4, approved in 2011 for treatment of melanoma and Pembrolizumab and Nivolumab, two antibodies against PD-1, approved in 2014.¹⁴⁵

Indoleamine 2,3-dioxygenase (IDO) is an immunoregulatory enzyme highly expressed in tumors that catalyzes the oxidative catabolism of tryptophan (Trp) to kynurenine (Kyn).¹⁴⁶⁻¹⁴⁸ The results of this catalytic process leads to depletion of Trp and production of Kyn, thus preventing the clonal expansion of T cells and promoting T cell anergy and apoptosis.^{149,150} Small molecule IDO inhibitors such as 1-methyl-tryptophan,^{149,151} INCB24360,¹⁵² and NLG919,¹⁵³ can effectively block Trp catabolism but show modest effect as monotherapies, due in part to ineffective antigen presentation and insufficient antitumor immunity.

The combination of immunotherapy with conventional cancer therapies has been under investigation, since cell death caused by other therapies potentiates tumor antigen release that initiates T cell activation.¹⁴⁵ For example, there are multiple ongoing trials on the combination of radiation therapy with anti-CTLA-4 or anti-PD-1/PD-L1 antibodies,^{154,155} while studies of chemotherapy in combination with immunotherapeutics are also ongoing.¹⁵⁶

1.6 RNA interference and small interfering RNA

RNA interference (RNAi) is a biological process that inhibits gene expression by RNA, typically by causing mRNA destruction. The discovery of sequence-specific gene silencing by double-stranded RNA in the nematode worm *Caenorhabditis elegans* won its discoverers, Fire and Mello, the Nobel Prize in Physiology or Medicine in 2006.¹⁵⁷ Small interfering RNA (siRNA), first detected as a product of RNA degradation in plants as RNA pieces of ~25 nucleotides, induce mRNA degradation and cause post-transcriptional gene silencing.^{158,159} This discovery strongly influenced drug development, since RNA interference provides potential

solutions to dysfunctional gene/protein expression, in addition to expediting the elucidation of a variety of molecular biology mechanisms.^{160,161}

The major challenge of siRNA drug development is delivery. Rapid renal clearance in circulation limits the direct intravenous injection of naked siRNA, which is also complicated by clearance by serum RNase A-type nucleases.^{162,163} Preventing degradation of nucleic acid drugs is another significant challenge in extracellular and intracellular trafficking control.^{162,164} Multiple delivery platforms have been evaluated on siRNA delivery, including liposomes and lipid-like materials,¹⁶⁵⁻¹⁶⁷ cationic polymers and other polymer nanoparticles,¹⁶⁸⁻¹⁷¹ virus vectors,^{172,173} and inorganic nanoparticles,¹⁷⁴⁻¹⁷⁶ but real clinical success is far ahead. The dilemma lies in the balance between the stealth of the vehicle from reticuloendothelial system clearance and the effective cellular uptake and transfection. Liposomes and some neutral polymeric coating strategies can prolong the blood circulation and increase the tumor uptake of siRNA, but the incapability of endosomal escape leads to degradation of the cargo; the cationic vehicles and virus vectors enhance siRNA transfection, but also invite immune system clearance. In chapter 5, we will introduce the invention of a novel nMOF delivery platform for co-delivery of chemotherapeutics and siRNAs.⁸⁹

1.7 References

1. Itaya, K., Uchida, I. & Neff, V.D. Electrochemistry of polynuclear transition metal cyanides: Prussian blue and its analogues. *Accounts Chem Res* **19**, 162-168 (1986).
2. Eddaoudi, M., *et al.* Systematic design of pore size and functionality in isorecticular MOFs and their application in methane storage. *Science* **295**, 469-472 (2002).
3. He, Y., Zhou, W., Qian, G. & Chen, B. Methane storage in metal–organic frameworks. *Chem Soc Rev* **43**, 5657-5678 (2014).

4. Suh, M.P., Park, H.J., Prasad, T.K. & Lim, D.-W. Hydrogen storage in metal–organic frameworks. *Chem. Rev.* **112**, 782-835 (2011).
5. Li, J.-R., Sculley, J. & Zhou, H.-C. Metal–organic frameworks for separations. *Chem. Rev.* **112**, 869-932 (2011).
6. Sumida, K., *et al.* Carbon dioxide capture in metal–organic frameworks. *Chem. Rev.* **112**, 724-781 (2011).
7. Evans, O.R. & Lin, W. Crystal engineering of NLO materials based on metal-organic coordination networks. *Accounts Chem Res* **35**, 511-522 (2002).
8. Wang, C., Zhang, T. & Lin, W. Rational synthesis of noncentrosymmetric metal–organic frameworks for second-order nonlinear optics. *Chem. Rev.* **112**, 1084-1104 (2011).
9. Jain, P., *et al.* Multiferroic behavior associated with an order– disorder hydrogen bonding transition in metal– organic frameworks (MOFs) with the perovskite ABX₃ architecture. *J. Am. Chem. Soc.* **131**, 13625-13627 (2009).
10. Zhang, W. & Xiong, R.-G. Ferroelectric metal–organic frameworks. *Chem. Rev.* **112**, 1163-1195 (2011).
11. Ramaswamy, P., Wong, N.E. & Shimizu, G.K. MOFs as proton conductors–challenges and opportunities. *Chem Soc Rev* **43**, 5913-5932 (2014).
12. Kobayashi, Y., Jacobs, B., Allendorf, M.D. & Long, J.R. Conductivity, doping, and redox chemistry of a microporous dithiolene-based metal– organic framework. *Chem Mater* **22**, 4120-4122 (2010).
13. Silva, C.G., Corma, A. & García, H. Metal–organic frameworks as semiconductors. *Journal of Materials Chemistry* **20**, 3141-3156 (2010).
14. Narayan, T.C., Miyakai, T., Seki, S. & Dincă, M. High charge mobility in a tetrathiafulvalene-based microporous metal–organic framework. *J. Am. Chem. Soc.* **134**, 12932-12935 (2012).
15. Talin, A.A., *et al.* Tunable electrical conductivity in metal-organic framework thin-film devices. *Science* **343**, 66-69 (2014).
16. Kurmoo, M. Magnetic metal–organic frameworks. *Chem Soc Rev* **38**, 1353-1379 (2009).
17. Hu, Z., Deibert, B.J. & Li, J. Luminescent metal–organic frameworks for chemical sensing and explosive detection. *Chem Soc Rev* **43**, 5815-5840 (2014).
18. Ma, L., Evans, O.R., Foxman, B.M. & Lin, W. Luminescent lanthanide coordination polymers. *Inorg Chem* **38**, 5837-5840 (1999).

19. Cui, Y., Yue, Y., Qian, G. & Chen, B. Luminescent functional metal–organic frameworks. *Chem. Rev.* **112**, 1126-1162 (2011).
20. Allendorf, M., Bauer, C., Bhakta, R. & Houk, R. Luminescent metal–organic frameworks. *Chem Soc Rev* **38**, 1330-1352 (2009).
21. Allendorf, M.D., *et al.* Stress-induced chemical detection using flexible metal–organic frameworks. *J. Am. Chem. Soc.* **130**, 14404-14405 (2008).
22. Xie, Z., Ma, L., deKrafft, K.E., Jin, A. & Lin, W. Porous phosphorescent coordination polymers for oxygen sensing. *J. Am. Chem. Soc.* **132**, 922-923 (2009).
23. Kreno, L.E., *et al.* Metal–organic framework materials as chemical sensors. *Chem. Rev.* **112**, 1105-1125 (2011).
24. Liu, J., *et al.* Applications of metal–organic frameworks in heterogeneous supramolecular catalysis. *Chem Soc Rev* **43**, 6011-6061 (2014).
25. Seo, J.S., *et al.* A homochiral metal–organic porous material for enantioselective separation and catalysis. *Nature* **404**, 982-986 (2000).
26. Lee, J., *et al.* Metal–organic framework materials as catalysts. *Chem Soc Rev* **38**, 1450-1459 (2009).
27. Ma, L., Falkowski, J.M., Abney, C. & Lin, W. A series of isorecticular chiral metal–organic frameworks as a tunable platform for asymmetric catalysis. *Nature chemistry* **2**, 838-846 (2010).
28. Zhao, M., Ou, S. & Wu, C.-D. Porous metal–organic frameworks for heterogeneous biomimetic catalysis. *Accounts Chem Res* **47**, 1199-1207 (2014).
29. Corma, A., García, H. & Llabrés i Xamena, F. Engineering metal organic frameworks for heterogeneous catalysis. *Chem. Rev.* **110**, 4606-4655 (2010).
30. Zhang, T. & Lin, W. Metal–organic frameworks for artificial photosynthesis and photocatalysis. *Chem Soc Rev* **43**, 5982-5993 (2014).
31. Kent, C.A., *et al.* Energy transfer dynamics in metal–organic frameworks. *J. Am. Chem. Soc.* **132**, 12767-12769 (2010).
32. Wang, J.-L., Wang, C. & Lin, W. Metal–organic frameworks for light harvesting and photocatalysis. *ACS Catalysis* **2**, 2630-2640 (2012).
33. Rieter, W.J., Taylor, K.M., An, H., Lin, W. & Lin, W. Nanoscale metal-organic frameworks as potential multimodal contrast enhancing agents. *J. Am. Chem. Soc.* **128**, 9024-9025 (2006).

34. Taylor, K.M., Rieter, W.J. & Lin, W. Manganese-based nanoscale metal–organic frameworks for magnetic resonance imaging. *J. Am. Chem. Soc.* **130**, 14358-14359 (2008).
35. Della Rocca, J., Liu, D. & Lin, W. Nanoscale Metal–Organic Frameworks for Biomedical Imaging and Drug Delivery. *Accounts Chem Res* **44**, 957-968 (2011).
36. Liu, D., Lu, K., Poon, C. & Lin, W. Metal–organic frameworks as sensory materials and imaging agents. *Inorg Chem* **53**, 1916-1924 (2013).
37. Horcajada, P., *et al.* Porous metal-organic-framework nanoscale carriers as a potential platform for drug delivery and imaging. *Nat Mater* **9**, 172-178 (2010).
38. Huxford, R.C., Della Rocca, J. & Lin, W. Metal–organic frameworks as potential drug carriers. *Curr. Opin. Chem. Biol.* **14**, 262-268 (2010).
39. He, C., Liu, D. & Lin, W. Nanomedicine Applications of Hybrid Nanomaterials Built from Metal–Ligand Coordination Bonds: Nanoscale Metal–Organic Frameworks and Nanoscale Coordination Polymers. *Chem. Rev.* **115**, 11079-11108 (2015).
40. Horcajada, P., *et al.* Metal–organic frameworks in biomedicine. *Chem. Rev.* **112**, 1232-1268 (2011).
41. Horcajada, P., *et al.* Metal–organic frameworks as efficient materials for drug delivery. *Angewandte chemie* **118**, 6120-6124 (2006).
42. Taylor-Pashow, K.M.L., Della Rocca, J., Xie, Z., Tran, S. & Lin, W. Postsynthetic Modifications of Iron-Carboxylate Nanoscale Metal-Organic Frameworks for Imaging and Drug Delivery. *J. Am. Chem. Soc.* **131**, 14261-14263 (2009).
43. McKinlay, A.C., *et al.* BioMOFs: metal–organic frameworks for biological and medical applications. *Angewandte Chemie International Edition* **49**, 6260-6266 (2010).
44. Deria, P., *et al.* Beyond post-synthesis modification: evolution of metal–organic frameworks via building block replacement. *Chem Soc Rev* **43**, 5896-5912 (2014).
45. Stock, N. & Biswas, S. Synthesis of metal-organic frameworks (MOFs): routes to various MOF topologies, morphologies, and composites. *Chem. Rev.* **112**, 933-969 (2011).
46. Lu, W., *et al.* Tuning the structure and function of metal–organic frameworks via linker design. *Chem Soc Rev* **43**, 5561-5593 (2014).
47. Eddaoudi, M., *et al.* Modular chemistry: secondary building units as a basis for the design of highly porous and robust metal-organic carboxylate frameworks. *Accounts Chem Res* **34**, 319-330 (2001).

48. Tranchemontagne, D.J., Mendoza-Cortes, J.L., O'Keeffe, M. & Yaghi, O.M. Secondary building units, nets and bonding in the chemistry of metal-organic frameworks. *Chem Soc Rev* **38**, 1257-1283 (2009).
49. Ma, L., Abney, C. & Lin, W. Enantioselective catalysis with homochiral metal-organic frameworks. *Chem Soc Rev* **38**, 1248-1256 (2009).
50. Cohen, S.M. Postsynthetic methods for the functionalization of metal-organic frameworks. *Chem. Rev.* **112**, 970-1000 (2011).
51. Brozek, C. & Dincă, M. Cation exchange at the secondary building units of metal-organic frameworks. *Chem Soc Rev* **43**, 5456-5467 (2014).
52. Chen, B., Wang, L., Zapata, F., Qian, G. & Lobkovsky, E.B. A luminescent microporous metal-organic framework for the recognition and sensing of anions. *J. Am. Chem. Soc.* **130**, 6718-6719 (2008).
53. Wang, C., deKrafft, K.E. & Lin, W. Pt nanoparticles@ photoactive metal-organic frameworks: efficient hydrogen evolution via synergistic photoexcitation and electron injection. *J. Am. Chem. Soc.* **134**, 7211-7214 (2012).
54. Lu, G., *et al.* Imparting functionality to a metal-organic framework material by controlled nanoparticle encapsulation. *Nature chemistry* **4**, 310-316 (2012).
55. Zhu, Q.-L. & Xu, Q. Metal-organic framework composites. *Chem Soc Rev* **43**, 5468-5512 (2014).
56. Yaghi, O.M., Li, G. & Li, H. Selective binding and removal of guests in a microporous metal-organic framework. *Nature* **378**, 703-706 (1995).
57. Rieter, W.J., Taylor, K.M. & Lin, W. Surface modification and functionalization of nanoscale metal-organic frameworks for controlled release and luminescence sensing. *J. Am. Chem. Soc.* **129**, 9852-9853 (2007).
58. Alfrey, A.C. & Ibels, L.S. Role of phosphate and pyrophosphate in soft tissue calcification. in *Homeostasis of Phosphate and Other Minerals* 187-193 (Springer, 1978).
59. Tanokura, M. & Kazuhiro, Y. Changes in intracellular pH and inorganic phosphate concentration during and after muscle contraction as studied by time-resolved ³¹P-NMR. *FEBS Lett.* **171**, 165-168 (1984).
60. Kickelbick, G., Holzinger, D., Brick, C., Trimmel, G. & Moons, E. Hybrid inorganic-organic core-shell nanoparticles from surface-functionalized titanium, zirconium, and vanadium oxo clusters. *Chem Mater* **14**, 4382-4389 (2002).

61. Otero, A., *et al.* New Complexes of Zirconium (IV) and Hafnium (IV) with Heteroscorpionate Ligands and the Hydrolysis of Such Complexes To Give a Zirconium Cluster#. *Inorg Chem* **43**, 1350-1358 (2004).
62. Baumann, S.O., Puchberger, M. & Schubert, U. Oximate-substituted zirconium alkoxides. *Dalton Transactions* **40**, 1401-1406 (2011).
63. Gross, S. Oxocluster-reinforced organic–inorganic hybrid materials: effect of transition metal oxoclusters on structural and functional properties. *Journal of Materials Chemistry* **21**, 15853-15861 (2011).
64. Feng, D., *et al.* Metal–Organic Frameworks Based on Previously Unknown Zr₈/Hf₈ Cubic Clusters. *Inorg Chem* **52**, 12661-12667 (2013).
65. Cavka, J.H., *et al.* A new zirconium inorganic building brick forming metal organic frameworks with exceptional stability. *J. Am. Chem. Soc.* **130**, 13850-13851 (2008).
66. Morris, W., *et al.* Synthesis, structure, and metalation of two new highly porous zirconium metal–organic frameworks. *Inorg Chem* **51**, 6443-6445 (2012).
67. Feng, D., *et al.* Construction of ultrastable porphyrin Zr metal–organic frameworks through linker elimination. *J. Am. Chem. Soc.* **135**, 17105-17110 (2013).
68. Mondloch, J.E., *et al.* Vapor-phase metalation by atomic layer deposition in a metal–organic framework. *J. Am. Chem. Soc.* **135**, 10294-10297 (2013).
69. Furukawa, H., *et al.* Water adsorption in porous metal–organic frameworks and related materials. *J. Am. Chem. Soc.* **136**, 4369-4381 (2014).
70. Peer, D., *et al.* Nanocarriers as an emerging platform for cancer therapy. *Nat Nanotechnol* **2**, 751-760 (2007).
71. Kim, J., Piao, Y. & Hyeon, T. Multifunctional nanostructured materials for multimodal imaging, and simultaneous imaging and therapy. *Chem Soc Rev* **38**, 372-390 (2009).
72. Gu, F.X., *et al.* Targeted nanoparticles for cancer therapy. *Nano today* **2**, 14-21 (2007).
73. Mura, S., Nicolas, J. & Couvreur, P. Stimuli-responsive nanocarriers for drug delivery. *Nature materials* **12**, 991-1003 (2013).
74. Sapsford, K.E., *et al.* Functionalizing nanoparticles with biological molecules: developing chemistries that facilitate nanotechnology. *Chem. Rev.* **113**, 1904-2074 (2013).
75. Chou, L.Y., Ming, K. & Chan, W.C. Strategies for the intracellular delivery of nanoparticles. *Chem Soc Rev* **40**, 233-245 (2011).

76. Matsumura, Y. & Maeda, H. A new concept for macromolecular therapeutics in cancer chemotherapy: mechanism of tumoritropic accumulation of proteins and the antitumor agent smancs. *Cancer Res.* **46**, 6387-6392 (1986).
77. Iyer, A.K., Khaled, G., Fang, J. & Maeda, H. Exploiting the enhanced permeability and retention effect for tumor targeting. *Drug discovery today* **11**, 812-818 (2006).
78. Brannon-Peppas, L. & Blanchette, J.O. Nanoparticle and targeted systems for cancer therapy. *Advanced drug delivery reviews* **56**, 1649-1659 (2004).
79. Yu, M.K., Park, J. & Jon, S. Targeting strategies for multifunctional nanoparticles in cancer imaging and therapy. *Theranostics* **2**, 3 (2012).
80. Cheng, Z., Al Zaki, A., Hui, J.Z., Muzykantov, V.R. & Tsourkas, A. Multifunctional nanoparticles: cost versus benefit of adding targeting and imaging capabilities. *Science* **338**, 903-910 (2012).
81. Gao, X., Cui, Y., Levenson, R.M., Chung, L.W. & Nie, S. In vivo cancer targeting and imaging with semiconductor quantum dots. *Nat. Biotechnol.* **22**, 969-976 (2004).
82. Huang, X., El-Sayed, I.H., Qian, W. & El-Sayed, M.A. Cancer cell imaging and photothermal therapy in the near-infrared region by using gold nanorods. *J. Am. Chem. Soc.* **128**, 2115-2120 (2006).
83. Gupta, A.K. & Gupta, M. Synthesis and surface engineering of iron oxide nanoparticles for biomedical applications. *Biomaterials* **26**, 3995-4021 (2005).
84. Shen, J., Zhao, L. & Han, G. Lanthanide-doped upconverting luminescent nanoparticle platforms for optical imaging-guided drug delivery and therapy. *Advanced drug delivery reviews* **65**, 744-755 (2013).
85. Torchilin, V.P. Recent advances with liposomes as pharmaceutical carriers. *Nature reviews Drug discovery* **4**, 145-160 (2005).
86. Lee, C.C., MacKay, J.A., Fréchet, J.M. & Szoka, F.C. Designing dendrimers for biological applications. *Nat. Biotechnol.* **23**, 1517-1526 (2005).
87. Kataoka, K., Harada, A. & Nagasaki, Y. Block copolymer micelles for drug delivery: design, characterization and biological significance. *Advanced drug delivery reviews* **47**, 113-131 (2001).
88. Hamidi, M., Azadi, A. & Rafiei, P. Hydrogel nanoparticles in drug delivery. *Advanced drug delivery reviews* **60**, 1638-1649 (2008).

89. He, C., Lu, K., Liu, D. & Lin, W. Nanoscale Metal–Organic Frameworks for the Co-Delivery of Cisplatin and Pooled siRNAs to Enhance Therapeutic Efficacy in Drug-Resistant Ovarian Cancer Cells. *J. Am. Chem. Soc.* **136**, 5181-5184 (2014).
90. He, C., Lu, K. & Lin, W. Nanoscale Metal-Organic Frameworks for Real-Time Intracellular pH Sensing in Live Cells. *J. Am. Chem. Soc.* **136**, 12253-12256 (2014).
91. Lu, K., He, C. & Lin, W. Nanoscale Metal–Organic Framework for Highly Effective Photodynamic Therapy of Resistant Head and Neck Cancer. *J. Am. Chem. Soc.* **136**, 16712-16715 (2014).
92. Lu, K., He, C. & Lin, W. A Chlorin-Based Nanoscale Metal–Organic Framework for Photodynamic Therapy of Colon Cancers. *J. Am. Chem. Soc.* **137**, 7600-7603 (2015).
93. Liu, J., *et al.* Nanoscale metal– organic frameworks for combined photodynamic & radiation therapy in cancer treatment. *Biomaterials* **97**, 1-9 (2016).
94. Park, J., Jiang, Q., Feng, D., Mao, L. & Zhou, H.-C. Size-Controlled Synthesis of Porphyrinic Metal–Organic Framework and Functionalization for Targeted Photodynamic Therapy. *J. Am. Chem. Soc.* **138**, 3518-3525 (2016).
95. Sontz, P.A., Bailey, J.B., Ahn, S. & Tezcan, F.A. A Metal Organic Framework with Spherical Protein Nodes: Rational Chemical Design of 3D Protein Crystals. *J. Am. Chem. Soc.* **137**, 11598-11601 (2015).
96. Li, P., *et al.* Encapsulation of a Nerve Agent Detoxifying Enzyme by a Mesoporous Zirconium Metal–Organic Framework Engenders Thermal and Long-Term Stability. *J. Am. Chem. Soc.* (2016).
97. Morris, W., Briley, W.E., Auyeung, E., Cabezas, M.D. & Mirkin, C.A. Nucleic Acid–Metal Organic Framework (MOF) Nanoparticle Conjugates. *J. Am. Chem. Soc.* (2014).
98. Liang, K., *et al.* Biomimetic mineralization of metal-organic frameworks as protective coatings for biomacromolecules. *Nature communications* **6**(2015).
99. An, J., Geib, S.J. & Rosi, N.L. Cation-triggered drug release from a porous zinc–adeninate metal– organic framework. *J. Am. Chem. Soc.* **131**, 8376-8377 (2009).
100. Siegel, R.L., Miller, K.D. & Jemal, A. Cancer statistics, 2016. *CA Cancer J. Clin.* **66**, 7-30 (2016).
101. Argiris, A., Karamouzis, M.V., Raben, D. & Ferris, R.L. Head and neck cancer. *The Lancet* **371**, 1695-1709 (2008).
102. Argiris, A. & Eng, C. Epidemiology, staging, and screening of head and neck cancer. in *Head and neck cancer* 15-60 (Springer, 2004).

103. Suarez-Cunqueiro, M.-M., *et al.* Speech and swallowing impairment after treatment for oral and oropharyngeal cancer. *Archives of Otolaryngology–Head & Neck Surgery* **134**, 1299-1304 (2008).
104. De Crevoisier, R., *et al.* Full-dose reirradiation for unresectable head and neck carcinoma: experience at the Gustave-Roussy Institute in a series of 169 patients. *J. Clin. Oncol.* **16**, 3556-3562 (1998).
105. Cohen, E.E., Lingen, M.W. & Vokes, E.E. The expanding role of systemic therapy in head and neck cancer. *J. Clin. Oncol.* **22**, 1743-1752 (2004).
106. Karamouzis, M.V., Grandis, J.R. & Argiris, A. Therapies directed against epidermal growth factor receptor in aerodigestive carcinomas. *JAMA* **298**, 70-82 (2007).
107. Nyst, H.J., Tan, I.B., Stewart, F.A. & Balm, A.J. Is photodynamic therapy a good alternative to surgery and radiotherapy in the treatment of head and neck cancer? *Photodiagnosis Photodyn. Ther.* **6**, 3-11 (2009).
108. Triesscheijn, M., Baas, P., Schellens, J.H. & Stewart, F.A. Photodynamic therapy in oncology. *The oncologist* **11**, 1034-1044 (2006).
109. Siegel, R., DeSantis, C. & Jemal, A. Colorectal cancer statistics, 2014. *CA Cancer J. Clin.* **64**, 104-117 (2014).
110. Lee, J.J. & Chu, E. An update on treatment advances for the first-line therapy of metastatic colorectal cancer. *The Cancer Journal* **13**, 276-281 (2007).
111. Ruzzo, A., *et al.* Pharmacogenetic profiling in patients with advanced colorectal cancer treated with first-line FOLFOX-4 chemotherapy. *J. Clin. Oncol.* **25**, 1247-1254 (2007).
112. Tournigand, C., *et al.* FOLFIRI followed by FOLFOX6 or the reverse sequence in advanced colorectal cancer: a randomized GERCOR study. *J. Clin. Oncol.* **22**, 229-237 (2004).
113. Heinemann, V., *et al.* FOLFIRI plus cetuximab versus FOLFIRI plus bevacizumab as first-line treatment for patients with metastatic colorectal cancer (FIRE-3): a randomised, open-label, phase 3 trial. *The lancet oncology* **15**, 1065-1075 (2014).
114. Douillard, J.-Y., *et al.* Panitumumab–FOLFOX4 treatment and RAS mutations in colorectal cancer. *N. Engl. J. Med.* **369**, 1023-1034 (2013).
115. Tol, J., *et al.* Chemotherapy, bevacizumab, and cetuximab in metastatic colorectal cancer. *N. Engl. J. Med.* **360**, 563-572 (2009).
116. Xiang, B., Snook, A.E., Magee, M.S. & Waldman, S.A. Colorectal cancer immunotherapy. *Discov. Med.* **15**, 301 (2013).

117. Friedman, E.J. Immune modulation by ionizing radiation and its implications for cancer immunotherapy. *Curr. Pharm. Des.* **8**, 1765-1780 (2002).
118. Steele, T.A. Chemotherapy-induced immunosuppression and reconstitution of immune function. *Leuk. Res.* **26**, 411-414 (2002).
119. Castano, A.P., Mroz, P. & Hamblin, M.R. Photodynamic therapy and anti-tumour immunity. *Nature Reviews Cancer* **6**, 535-545 (2006).
120. Coleman, R.L., Monk, B.J., Sood, A.K. & Herzog, T.J. Latest research and treatment of advanced-stage epithelial ovarian cancer. *Nature Reviews Clinical Oncology* **10**, 211-224 (2013).
121. Vaughan, S., *et al.* Rethinking ovarian cancer: recommendations for improving outcomes. *Nature Reviews Cancer* **11**, 719-725 (2011).
122. Jayson, G.C., Kohn, E.C., Kitchener, H.C. & Ledermann, J.A. Ovarian cancer. *The Lancet* **384**, 1376-1388 (2014).
123. Morgan, R.J., *et al.* Epithelial ovarian cancer. *J. Natl. Compr. Canc. Netw.* **9**, 82-113 (2011).
124. Alvarez-Pez, J.M., Ballesteros, L., Talavera, E. & Yguerabide, J. Fluorescein excited-state proton exchange reactions: Nanosecond emission kinetics and correlation with steady-state fluorescence intensity. *Journal of Physical Chemistry A* **105**, 6320-6332 (2001).
125. Roberts, D., *et al.* Identification of genes associated with platinum drug sensitivity and resistance in human ovarian cancer cells. *Br. J. Cancer* **92**, 1149-1158 (2005).
126. Kelland, L. The resurgence of platinum-based cancer chemotherapy. *Nature Reviews Cancer* **7**, 573-584 (2007).
127. Lowery, W.J., *et al.* Cost-effectiveness of early palliative care intervention in recurrent platinum-resistant ovarian cancer. *Gynecol. Oncol.* **130**, 426-430 (2013).
128. Martin, M.M. & Lindqvist, L. Ph-Dependence of Fluorescein Fluorescence. *J Lumin* **10**, 381-390 (1975).
129. Gottesman, M.M., Fojo, T. & Bates, S.E. Multidrug resistance in cancer: role of ATP-dependent transporters. *Nature Reviews Cancer* **2**, 48-58 (2002).
130. Goldstein, L.J., *et al.* Expression of multidrug resistance gene in human cancers. *J. Natl. Cancer Inst.* **81**, 116-124 (1989).
131. Szakács, G., Paterson, J.K., Ludwig, J.A., Booth-Genthe, C. & Gottesman, M.M. Targeting multidrug resistance in cancer. *Nature reviews Drug discovery* **5**, 219-234 (2006).

132. Cheng, W., Liu, T., Wan, X., Gao, Y. & Wang, H. MicroRNA-199a targets CD44 to suppress the tumorigenicity and multidrug resistance of ovarian cancer-initiating cells. *Febs Journal* **279**, 2047-2059 (2012).
133. Li, Z., *et al.* MiR-27a modulates MDR1/P-glycoprotein expression by targeting HIPK2 in human ovarian cancer cells. *Gynecol. Oncol.* **119**, 125-130 (2010).
134. Lage, H. An overview of cancer multidrug resistance: a still unsolved problem. *Cell. Mol. Life Sci.* **65**, 3145-3167 (2008).
135. Dolmans, D.E.J.G.J., Fukumura, D. & Jain, R.K. Photodynamic therapy for cancer. *Nature Reviews Cancer* **3**, 380-387 (2003).
136. Dougherty, T.J., *et al.* Photodynamic therapy. *J. Natl. Cancer Inst.* **90**, 889-905 (1998).
137. Allison, R.R. & Sibata, C.H. Oncologic photodynamic therapy photosensitizers: a clinical review. *Photodiagnosis Photodyn. Ther.* **7**, 61-75 (2010).
138. Ormond, A.B. & Freeman, H.S. Dye sensitizers for photodynamic therapy. *Materials* **6**, 817-840 (2013).
139. Perun, S., Tatchen, J. & Marian, C.M. Singlet and Triplet Excited States and Intersystem Crossing in Free-Base Porphyrin: TDDFT and DFT/MRCI Study. *Chemphyschem* **9**, 282-292 (2008).
140. Gouterman, M. Spectra of porphyrins. *J. Mol. Spectrosc.* **6**, 138-163 (1961).
141. Brückner, C., *et al.* A spectroscopic and computational study of the singlet and triplet excited states of synthetic β -functionalized chlorins. *Chem. Phys.* **294**, 285-303 (2003).
142. Bonnett, R. & Martinez, G. Photobleaching of sensitizers used in photodynamic therapy. *Tetrahedron* **57**, 9513-9547 (2001).
143. Couzin-Frankel, J. Cancer immunotherapy. *Science* **342**, 1432-1433 (2013).
144. Pardoll, D.M. The blockade of immune checkpoints in cancer immunotherapy. *Nature Reviews Cancer* **12**, 252-264 (2012).
145. Sharma, P. & Allison, J.P. The future of immune checkpoint therapy. *Science* **348**, 56-61 (2015).
146. Zou, W. Immunosuppressive networks in the tumour environment and their therapeutic relevance. *Nature Reviews Cancer* **5**, 263-274 (2005).
147. Uyttenhove, C., *et al.* Evidence for a tumoral immune resistance mechanism based on tryptophan degradation by indoleamine 2, 3-dioxygenase. *Nat. Med.* **9**, 1269-1274 (2003).

148. Muller, A.J., DuHadaway, J.B., Donover, P.S., Sutanto-Ward, E. & Prendergast, G.C. Inhibition of indoleamine 2, 3-dioxygenase, an immunoregulatory target of the cancer suppression gene Bin1, potentiates cancer chemotherapy. *Nat. Med.* **11**, 312-319 (2005).
149. Munn, D.H., *et al.* Inhibition of T cell proliferation by macrophage tryptophan catabolism. *The Journal of experimental medicine* **189**, 1363-1372 (1999).
150. Muller, A.J. & Scherle, P.A. Targeting the mechanisms of tumoral immune tolerance with small-molecule inhibitors. *Nature Reviews Cancer* **6**, 613-625 (2006).
151. Munn, D.H., *et al.* Prevention of allogeneic fetal rejection by tryptophan catabolism. *Science* **281**, 1191-1193 (1998).
152. Yue, E.W., *et al.* Discovery of potent competitive inhibitors of indoleamine 2, 3-dioxygenase with in vivo pharmacodynamic activity and efficacy in a mouse melanoma model. *J. Med. Chem.* **52**, 7364-7367 (2009).
153. Khleif, S., *et al.* First-in-human phase 1 study of the novel indoleamine-2, 3-dioxygenase (IDO) inhibitor NLG-919. in *ASCO Annual Meeting Proceedings*, Vol. 32 TPS3121 (2014).
154. Tang, C., *et al.* Combining radiation and immunotherapy: a new systemic therapy for solid tumors? *Cancer immunology research* **2**, 831-838 (2014).
155. Crittenden, M., *et al.* Current clinical trials testing combinations of immunotherapy and radiation. in *Semin. Radiat. Oncol.*, Vol. 25 54-64 (Elsevier, 2015).
156. Cook, A.M., Lesterhuis, W.J., Nowak, A.K. & Lake, R.A. Chemotherapy and immunotherapy: mapping the road ahead. *Curr. Opin. Immunol.* **39**, 23-29 (2016).
157. Fire, A., *et al.* Potent and specific genetic interference by double-stranded RNA in *Caenorhabditis elegans*. *Nature* **391**, 806-811 (1998).
158. Hamilton, A.J. & Baulcombe, D.C. A species of small antisense RNA in posttranscriptional gene silencing in plants. *Science* **286**, 950-952 (1999).
159. Elbashir, S.M., *et al.* Duplexes of 21-nucleotide RNAs mediate RNA interference in cultured mammalian cells. *Nature* **411**, 494-498 (2001).
160. Hannon, G.J. & Rossi, J.J. Unlocking the potential of the human genome with RNA interference. *Nature* **431**, 371-378 (2004).
161. Iorns, E., Lord, C.J., Turner, N. & Ashworth, A. Utilizing RNA interference to enhance cancer drug discovery. *Nature reviews Drug discovery* **6**, 556-568 (2007).

162. Pecot, C.V., Calin, G.A., Coleman, R.L., Lopez-Berestein, G. & Sood, A.K. RNA interference in the clinic: challenges and future directions. *Nature Reviews Cancer* **11**, 59-67 (2011).
163. Whitehead, K.A., Langer, R. & Anderson, D.G. Knocking down barriers: advances in siRNA delivery. *Nature reviews Drug discovery* **8**, 129-138 (2009).
164. Haussecker, D. Current issues of RNAi therapeutics delivery and development. *J. Control. Release* **195**, 49-54 (2014).
165. Malone, R.W., Felgner, P.L. & Verma, I.M. Cationic liposome-mediated RNA transfection. *Proceedings of the National Academy of Sciences* **86**, 6077-6081 (1989).
166. Zimmermann, T.S., *et al.* RNAi-mediated gene silencing in non-human primates. *Nature* **441**, 111-114 (2006).
167. Akinc, A., *et al.* A combinatorial library of lipid-like materials for delivery of RNAi therapeutics. *Nat. Biotechnol.* **26**, 561-569 (2008).
168. Lungwitz, U., Breunig, M., Blunk, T. & Göpferich, A. Polyethylenimine-based non-viral gene delivery systems. *Eur. J. Pharm. Biopharm.* **60**, 247-266 (2005).
169. Rozema, D.B., *et al.* Dynamic PolyConjugates for targeted in vivo delivery of siRNA to hepatocytes. *Proceedings of the National Academy of Sciences* **104**, 12982-12987 (2007).
170. Panyam, J. & Labhasetwar, V. Sustained cytoplasmic delivery of drugs with intracellular receptors using biodegradable nanoparticles. *Mol. Pharm.* **1**, 77-84 (2004).
171. Davis, M.E., *et al.* Evidence of RNAi in humans from systemically administered siRNA via targeted nanoparticles. *Nature* **464**, 1067-1070 (2010).
172. Stewart, S.A., *et al.* Lentivirus-delivered stable gene silencing by RNAi in primary cells. *RNA* **9**, 493-501 (2003).
173. Moffat, J., *et al.* A lentiviral RNAi library for human and mouse genes applied to an arrayed viral high-content screen. *Cell* **124**, 1283-1298 (2006).
174. Chen, A.A., Derfus, A.M., Khetani, S.R. & Bhatia, S.N. Quantum dots to monitor RNAi delivery and improve gene silencing. *Nucleic Acids Res.* **33**, e190-e190 (2005).
175. Rosi, N.L., *et al.* Oligonucleotide-modified gold nanoparticles for intracellular gene regulation. *Science* **312**, 1027-1030 (2006).
176. Medarova, Z., Pham, W., Farrar, C., Petkova, V. & Moore, A. In vivo imaging of siRNA delivery and silencing in tumors. *Nat. Med.* **13**, 372-377 (2007).

Chapter 2. A Porphyrin-Based Nanoscale Metal-Organic Framework for Photodynamic therapy

2.1 Rationale of the nMOF design

Selective localization of PSs in tumors is critical for effective PDT. However, many PSs are hydrophobic in nature, which not only leads to insufficient tumor localization but also causes PS aggregation to diminish the PDT efficacy.¹ We hypothesized that the incorporation of a porphyrin-derived bridging ligand into a robust and porous UiO nMOF structure with proper morphologies and dimensions would have several advantages over existing nanoparticle PDT agents: first, the PS molecules are well-isolated in the framework to avoid aggregation and self-quenching of the excited states; second, coordination of porphyrin ligands to heavy Hf centers via the carboxylate groups can promote intersystem crossing to enhance ROS generation efficiency; third, the porous nMOF structure provides a pathway for facile diffusion of ROS (such as $^1\text{O}_2$) out of the nMOF interior to exert their cytotoxic effects on cancer cells. In this nMOF design, an unprecedentedly high PS loading can be achieved to enable highly effective PDT of difficult-to-treat cancers.

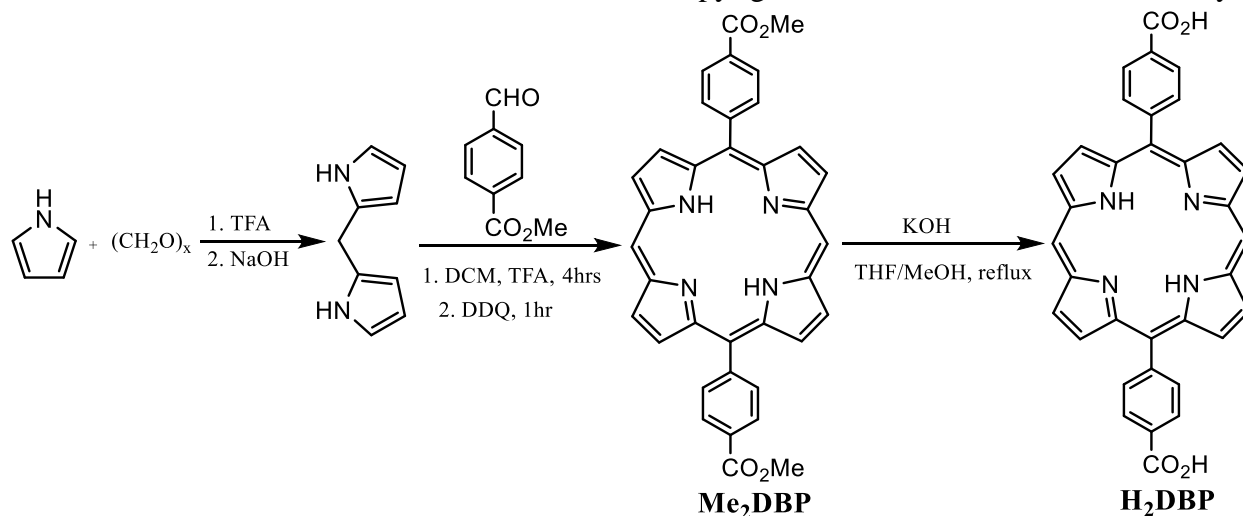
This chapter reports our efforts on the design of the first porphyrin-based nMOF, DBP-Hf, as an efficient photosensitizer for PDT of resistant head and neck cancer. DBP-Hf efficiently generates $^1\text{O}_2$ owing to site isolation of porphyrin ligands, enhanced intersystem crossing by heavy Hf centers, and facile $^1\text{O}_2$ diffusion through porous DBP-Hf nanoplates. Consequently, DBP-Hf displayed greatly enhanced PDT efficacy both *in vitro* and *in vivo*, leading to complete tumor eradication in half of the mice receiving a single DBP-Hf dose and a single light exposure.

2.2 Results and Discussion

2.2.1 Synthesis and characterization of the H₂DBP ligand

The new porphyrin derivative with linearly aligned dicarboxylate groups, 5,15-di(p-benzoato)porphyrin (H₂DBP), was synthesized in 3 steps as shown in Scheme 2-1.

Scheme 2-1 Synthesis of the 5,15-di(p-benzoato)porphyrin ligand. Reprinted with permission from *J. Am. Chem. Soc.*, **2014**, *136*, 16712–16715. Copyright 2014 American Chemical Society.



Dipyrromethane was synthesized based on a modified literature procedure.² To a 1-liter flask 500 mL of distilled pyrrole (7.2 mol) was added. To the flask paraformaldehyde (1.74 g, 58 mmol by formaldehyde) was added and the mixture was degassed for 15 minutes. The mixture was then heated at 60 °C to dissolve most of the solid. After cooling to room temperature, 0.53 mL of trifluoroacetic acid (TFA) was added slowly to the solution. The reaction mixture was stirred for an hour before the addition of 812 mg of sodium hydroxide, then the mixture was stirred for another 45 minutes. Pyrrole was distilled off under vacuum and the remaining solid was extracted with dichloromethane from water and washed with water twice. The crude product was purified by silica gel column chromatography with chloroform as eluent to afford the off-

white product. Yield: 4.94 g, 33.8 mmol (58%). $^1\text{H-NMR}$ (500 MHz, chloroform-D, ppm, Figure 2-1): $\delta=7.72$ (s, 2H), 6.61 (d, 2H), 6.15 (d, 2H), 6.03 (s, 2H), 3.94 (s, 2H).

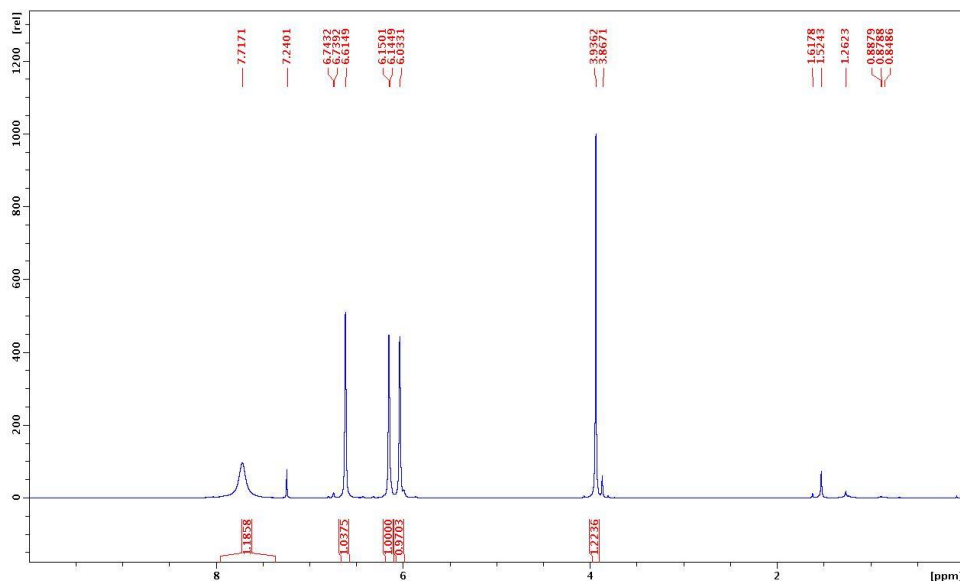


Figure 2-1 ^1H NMR spectrum of dipyrromethane in chloroform-D. Reprinted with permission from *J. Am. Chem. Soc.*, **2014**, *136*, 16712–16715. Copyright 2014 American Chemical Society.

4-(Methoxycarbonyl)benzaldehyde (1.20 g, 7.3 mmol) and dipyrromethane (1.07 g, 7.3 mmol) were added to a round bottom flask. To the flask 1 L of anhydrous dichloromethane (DCM) was added. Trifluoroacetic acid (0.34 mL, 4.4 mmol) was added dropwise via a syringe. The mixture was stirred at room temperature for 4 hours. To the reaction mixture, 2.49 g 2,3-dichloro-5,6-dicyano-1,4-benzoquinone (DDQ, 11.0 mmol) was then added and the mixture was stirred for another hour. Triethylamine was added to neutralize the reaction mixture. The solvent was removed with a rotary evaporator, and the 5,15-di(p-methyl-benzoato)porphyrin (Me_2DBP) product was purified by column chromatography with chloroform as the eluent. Yield: 810 mg, 1.40 mmol (38%). $^1\text{H-NMR}$ (500 MHz, chloroform-D, ppm, Figure 2-2): $\delta=10.38$ (s, 2H), 9.45 (d, 4H), 9.06 (d, 4H), 8.52 (d, 4H), 8.39 (d, 4H), 4.16 (s, 6H), -3.12 (s, 2H).

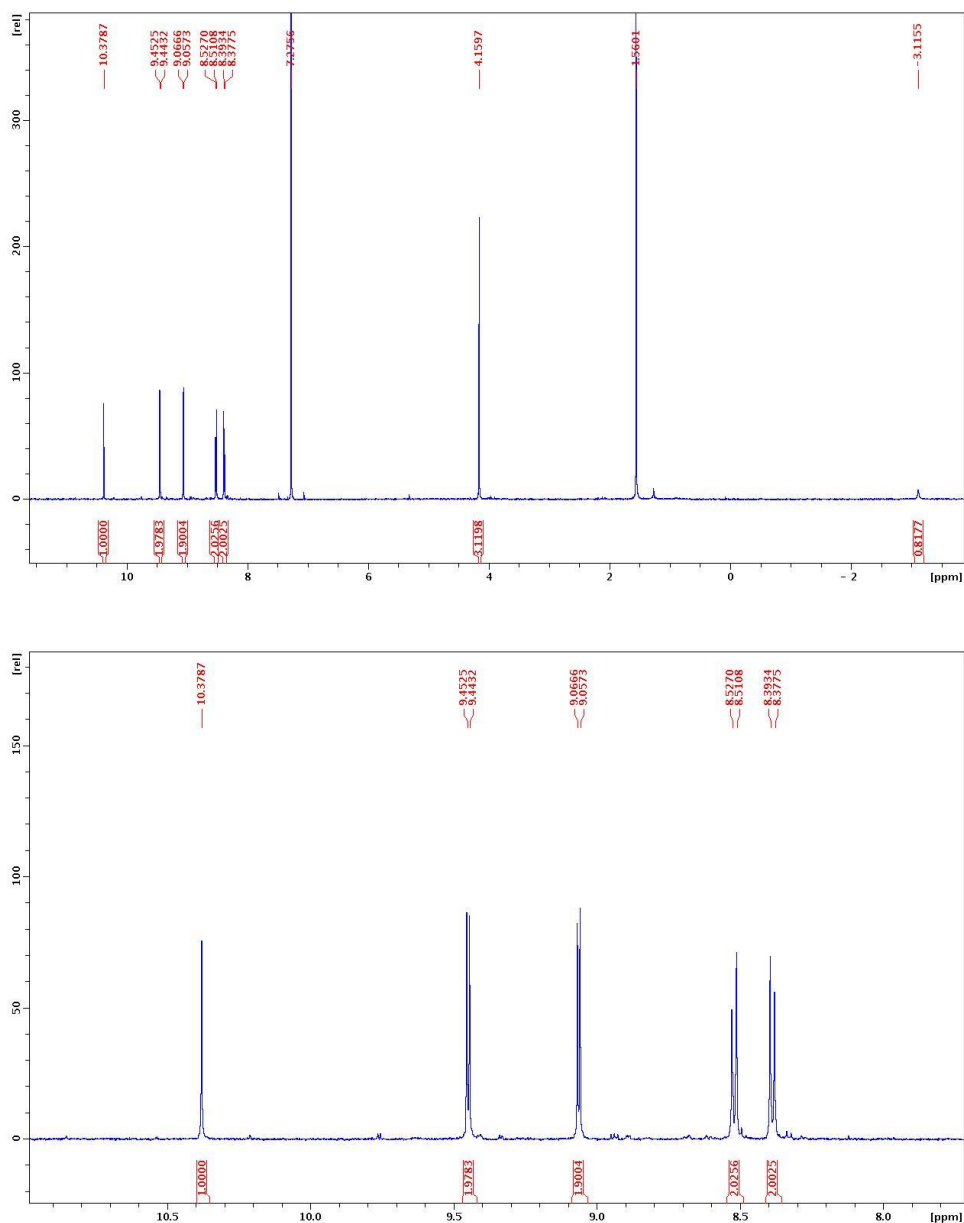


Figure 2-2 ¹H NMR spectrum of 5,15-di(p-methylbenzoato)porphyrin in chloroform-D. The full view (top) and an expanded view of a portion of the spectrum (bottom). Reprinted with permission from *J. Am. Chem. Soc.*, **2014**, *136*, 16712–16715. Copyright 2014 American Chemical Society.

The aforementioned Me₂DBP (399 mg, 0.69 mmol) was dissolved in a mixture of tetrahydrofuran (THF) and methanol (90 mL, 1:1 vol/vol). A potassium hydroxide aqueous

solution (14 mL, 2 M) was then added. The solution was heated to reflux under nitrogen protection overnight. Half of the solvent was removed with a rotary evaporator before the solution was neutralized to pH=3 with trifluoroacetic acid. The dark purple product was collected by centrifugation and washed with water and ether. The solid residue was dried under vacuum to give the pure H₂DBP product in 95% yield (362 mg, 0.66 mmol). ¹³C-NMR (125 MHz, DMSO-D₆, ppm, Figure 2-3): δ= 168.05 (a), 145.36 (f), 135.35, 133.46, 131.22, 130.78 (b-e), 128.67 (g, j), 118.19 (k), 106.62 (h, i). ¹H-NMR (500 MHz, DMSO-D₆, ppm, Figure 2-4): δ=13.35 (s, 2H), 10.71 (s, 2H), 9.71 (d, 4H), 9.08 (d, 4H), 8.45 (m, 8H), -3.26 (s, 2H). ESI-MS for [H₂DBP+H]⁺: 551.1 calc; 551.2 found (Figure 2-5).

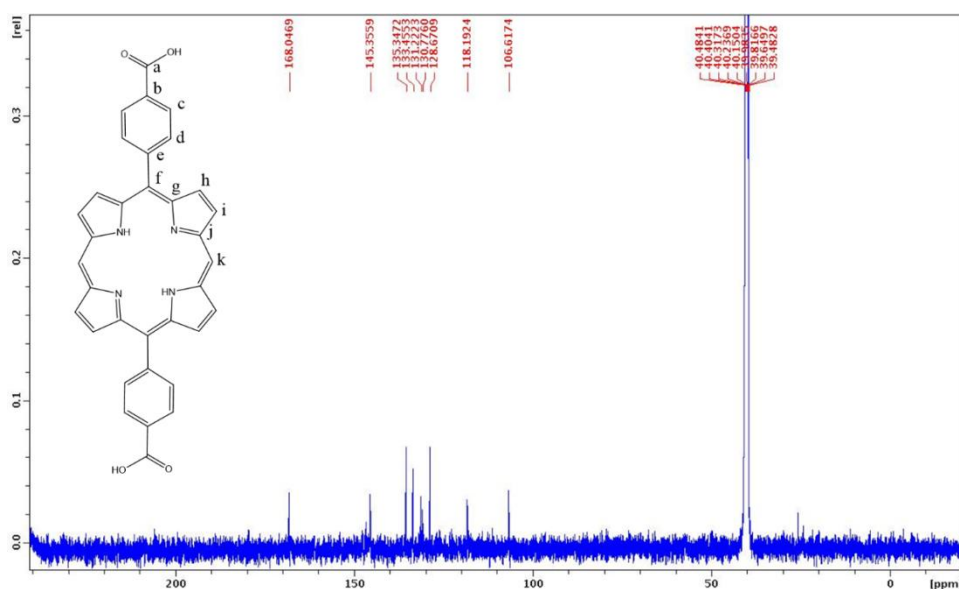


Figure 2-3 ¹³C NMR spectrum of 5,15-di(p-benzoato)porphyrin in DMSO-D₆. Reprinted with permission from *J. Am. Chem. Soc.*, **2014**, *136*, 16712–16715. Copyright 2014 American Chemical Society.

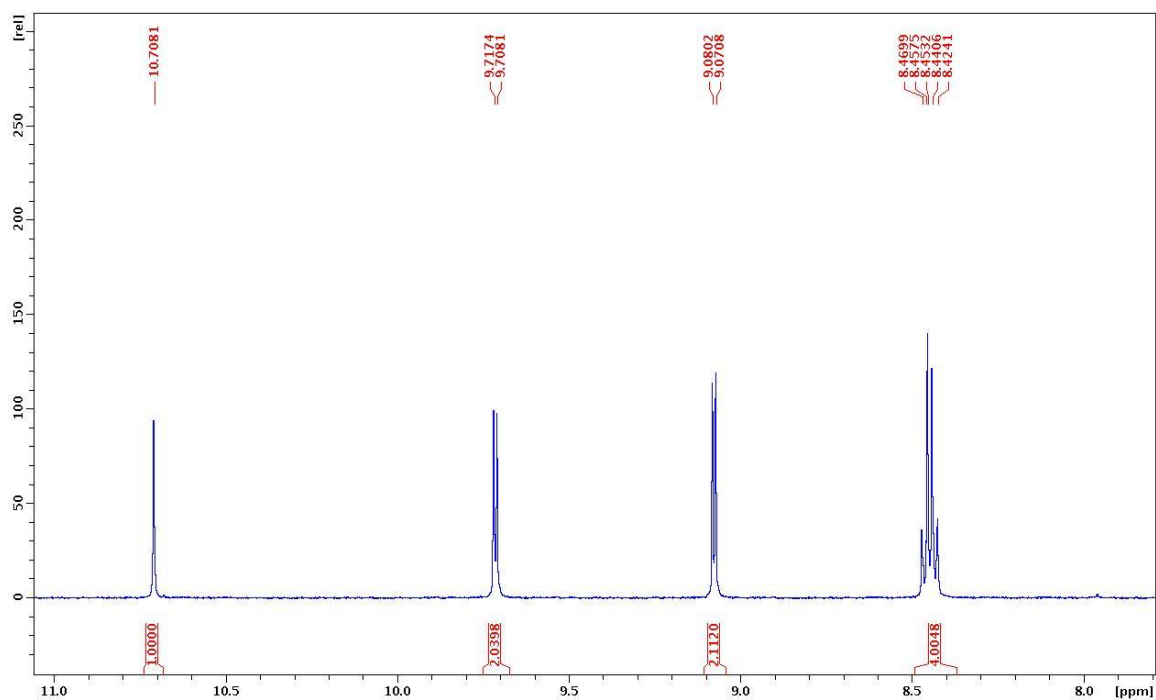
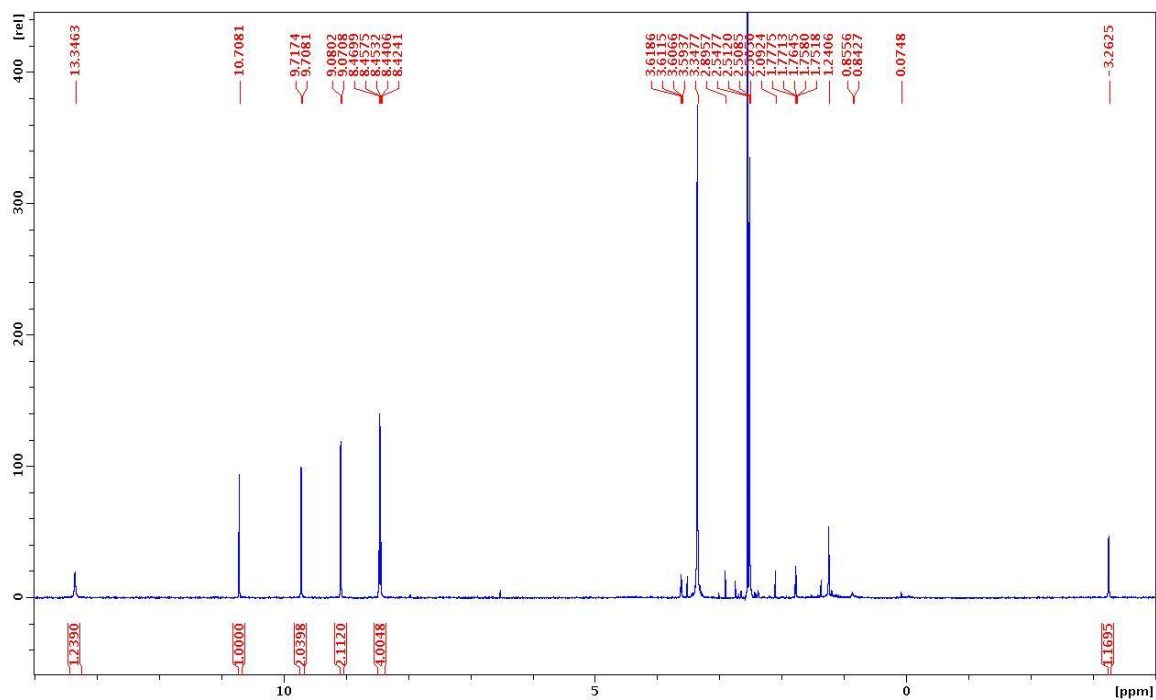


Figure 2-4 ^1H NMR spectrum of 5,15-di(p-benzoato)porphyrin in DMSO-D_6 . The full view (top) and an expanded view of a portion of the spectrum (bottom). Reprinted with permission from *J. Am. Chem. Soc.*, **2014**, *136*, 16712–16715. Copyright 2014 American Chemical Society.

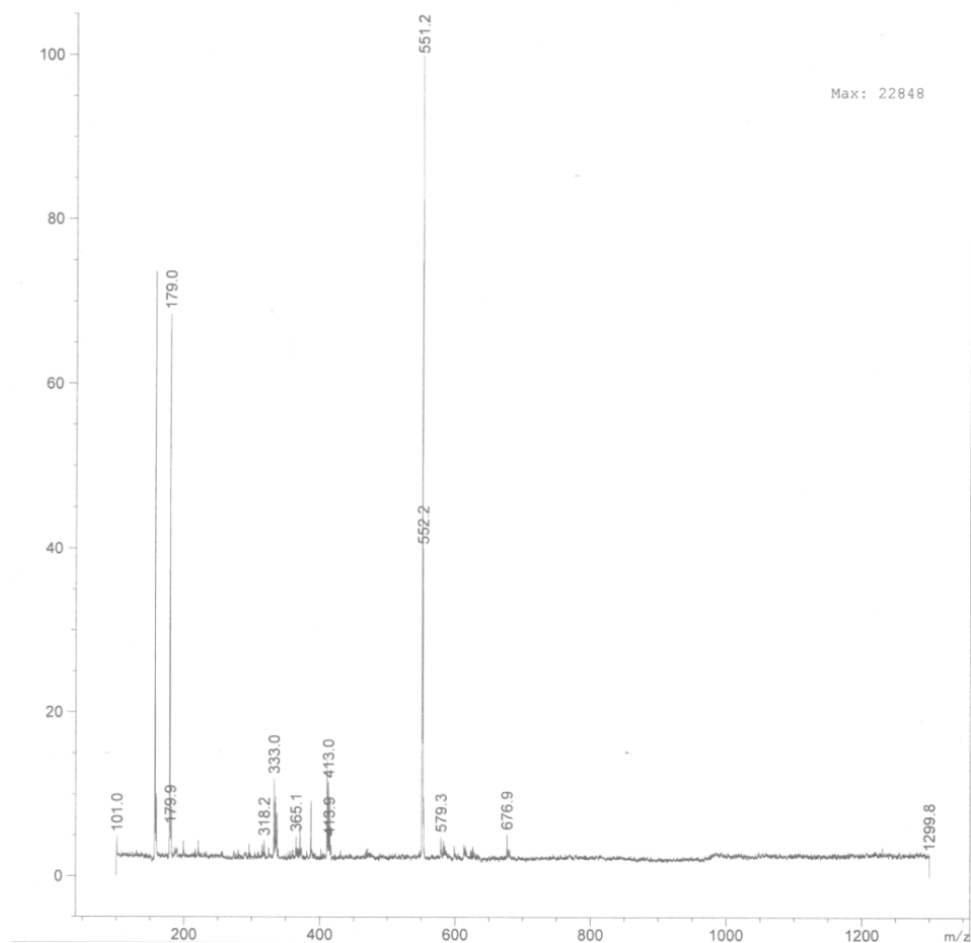
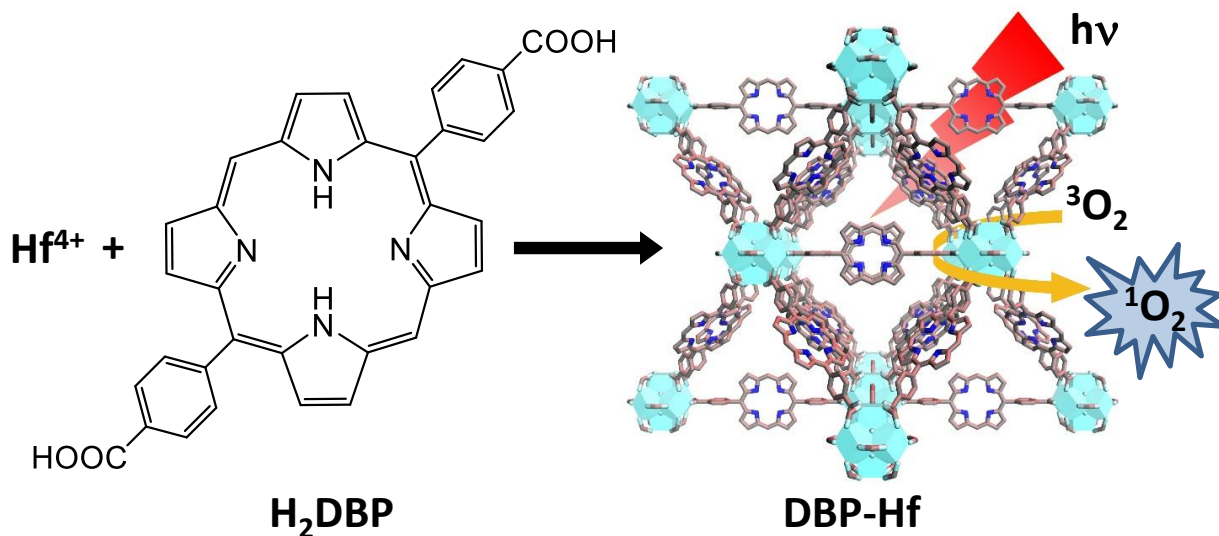


Figure 2-5 Mass spectrum of 5,15-di(p-benzoato)porphyrin. The sample was prepared in DMSO as a 40 mg/L solution and was delivered by methanol. Reprinted with permission from *J. Am. Chem. Soc.*, **2014**, *136*, 16712–16715. Copyright 2014 American Chemical Society.

2.2.2 Synthesis and characterization of DBP-Hf

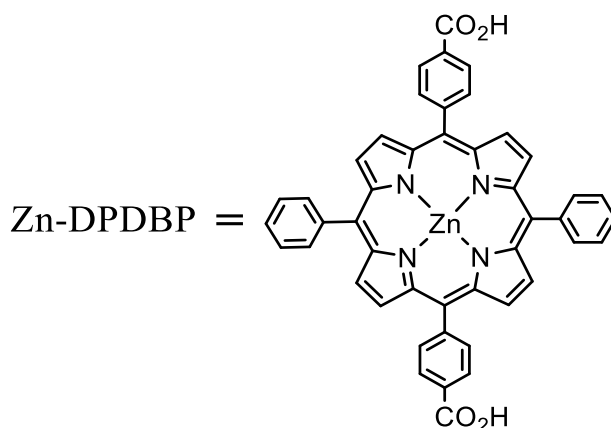
DBP-Hf was synthesized by a solvothermal reaction between HfCl_4 and H_2DBP in N, N-dimethylformamide (DMF) at 80 °C (scheme 2-2). The resulting dark purple powder was washed with copious amounts of DMF, 1% triethylamine in ethanol (v/v), and ethanol successively before being dispersed in ethanol as a stock suspension.

Scheme 2-2 Synthesis of DBP-Hf and the schematic description of singlet oxygen generation process. Reprinted with permission from *J. Am. Chem. Soc.*, **2014**, *136*, 16712–16715. Copyright 2014 American Chemical Society.



The attempts to grow DBP-Hf crystals suitable for single-crystal X-ray diffraction are not successful likely due to the poor solubility of the ligand. Fortunately, the single crystal structure of an analog of DBP-Hf, $\text{Zr}_6(\mu_3\text{-O})_4(\mu_3\text{-OH})_4(\text{Zn-DPDBP})_6$ (Zn-DPDBP-Zr, where DPDBP is 5,15-di(p-benzoato)-10,20-diphenyl-porphyrin and has the same length as DBP), is determined (Table 2-1 & Figure 2-6) and the powder X-ray diffraction (PXRD) pattern matches that of DBP-Hf (Figure 2-6a). DBP-Hf thus adopts a UiO-type MOF structure that is built from 12-connected $\text{Hf}_6(\mu_3\text{-O})_4(\mu_3\text{-OH})_4(\text{carboxylate})_{12}$ secondary building units (SBUs) and DBP bridging ligands.³ DBP-Hf has a very open framework structure with triangular channels of 1.6 nm in dimensions as well as octahedral and tetrahedral cavities of 2.8 nm and 2.0 nm in dimensions, respectively, which facilitates the diffusion of ROS during PDT process.

Table 2-1 Chemical structure of Zn-DPDBP and crystal structure information of Zn-DPDBP-Zr.



Formula	Zr ₆ (O) ₄ (OH) ₄ (Zn-DPDBP) ₆	Absorption coeff. (mm ⁻¹)	0.223
Fw	5263.82	F(000)	10640.0
Temperature (K)	293	θ range data collection	1.01 – 13.00
Wavelength (Å)	0.41328	Limiting indices	-39 ≤ h ≤ 41, -42 ≤ k ≤ 32, -38 ≤ l ≤ 41
Crystal system	cubic	Reflection collected	81986
Space group	<i>Fm</i> $\bar{3}$ <i>m</i>	Independent reflections	1987
<i>a</i> , Å	38.758(2)	R(int)	0.0936
<i>b</i> , Å	38.758(2)	Data/restraints/parameters	1987/35/59
<i>c</i> , Å	38.758(2)	Goodness-of-fit on <i>F</i> ²	2.324
α °	90	Final R indices [<i>I</i> > 2σ(<i>I</i>)]	R1 = 0.0896, wR2 = 0.2592
β °	90	R indices (all data)	R1 = 0.0940, wR2 = 0.2644
γ °	90		
<i>V</i> , Å ³	58224(5)		
<i>Z</i>	4		
Density (calcd. g/cm ³)	0.600		

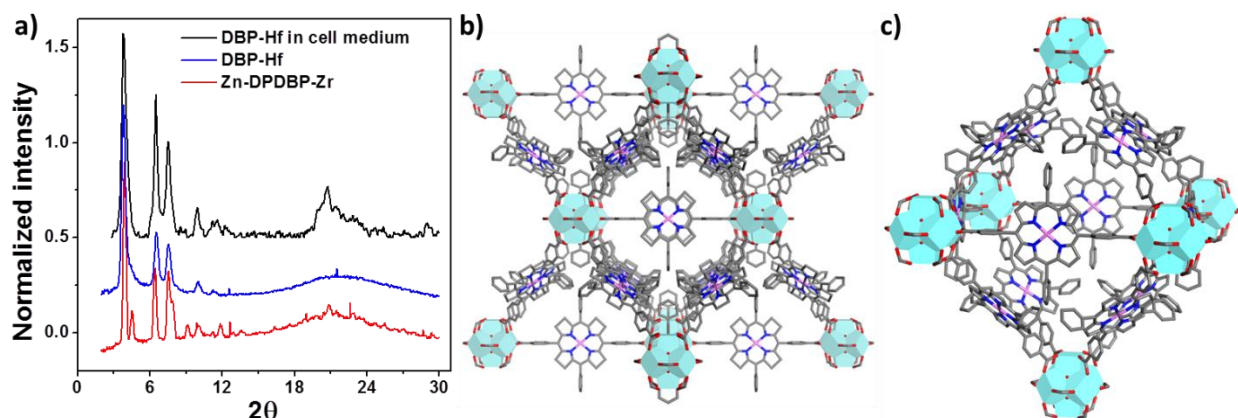


Figure 2-6 Structural confirmation of DBP-Hf. (a) Powder X-ray diffraction patterns of DBP-Hf comparing to Zn-DPDBP-Zr. (b) The structure of Zn-DPDBP-Zr viewed from the [110] direction; (c) the octahedral cavity in the structure. Adapted with permission from *J. Am. Chem. Soc.*, **2014**, *136*, 16712–16715. Copyright 2014 American Chemical Society.

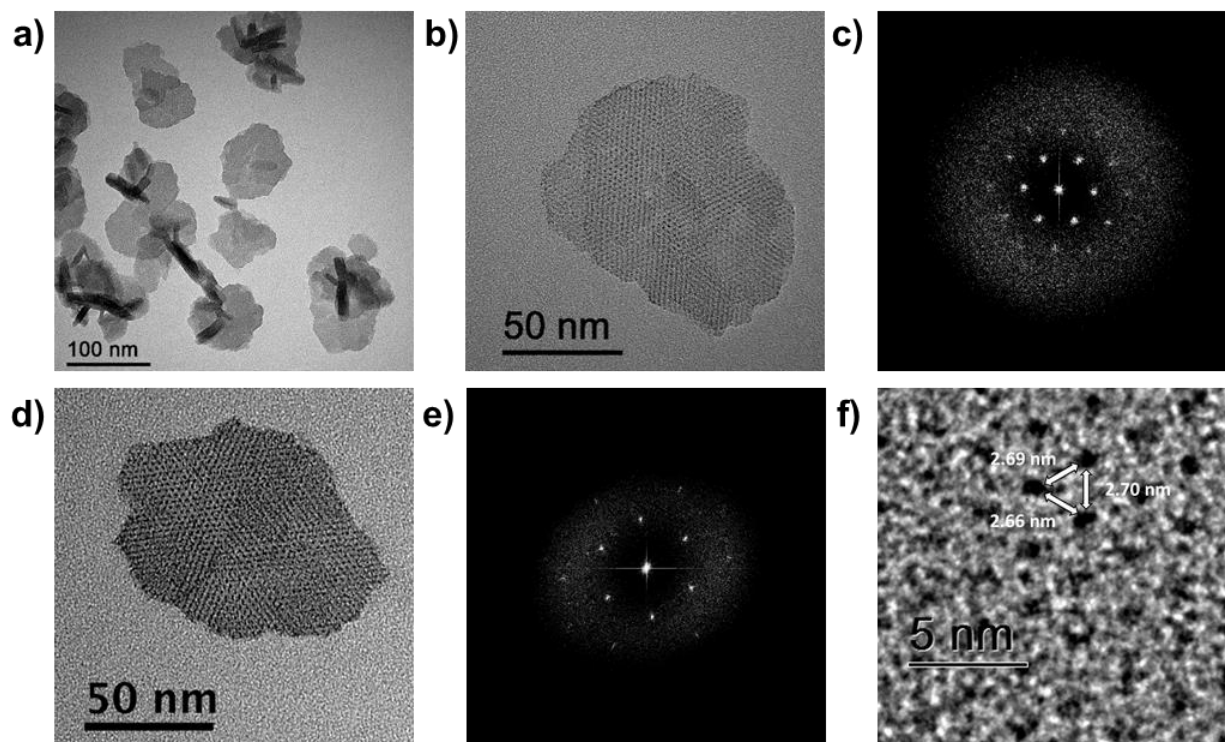


Figure 2-7 TEM images of DBP-Hf. (a) TEM image to show the plate morphology of DBP-Hf; High-resolution TEM images of DBP-Hf samples before (b) and after (d) cell-medium cultivation and their fast Fourier transform pattern are shown in (c) and (e), respectively. (f) A zoomed-in image showing the distances between SBUs. Adapted with permission from *J. Am. Chem. Soc.*, **2014**, *136*, 16712–16715. Copyright 2014 American Chemical Society.

Transmission electron microscopy (TEM) confirms that DBP-Hf particles display a plate morphology (Figure 2-7). Nitrogen adsorption measurements gave a BET surface area of 558 m²/g for the nMOF (Figure 2-8a). Thermogravimetric analysis (Figure 2-8b) shows a weight loss of 77% from 150-600 °C (calculated 73%). Inductively coupled plasma-mass spectrometry (ICP-MS) confirms a Hf content of 24.3% (calculated 23.7%).

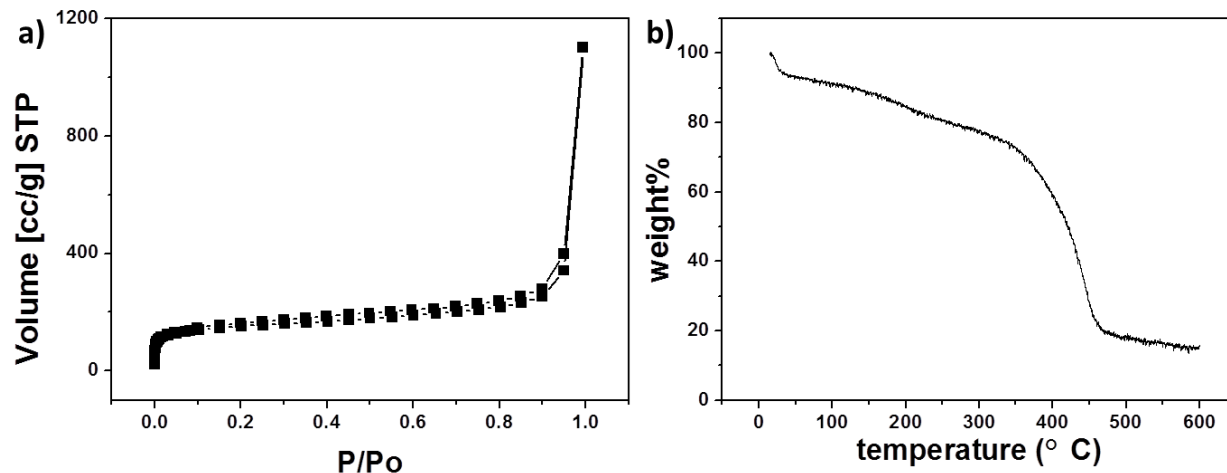


Figure 2-8 (a) Nitrogen adsorption isotherm of DBP-Hf at 77K and (b) Thermogravimetric analysis of DBP-Hf. Adapted with permission from *J. Am. Chem. Soc.*, **2014**, *136*, 16712–16715. Copyright 2014 American Chemical Society.

Individual SBUs are clearly visible in high-resolution TEM images of DBP-Hf (Figure 2-7b). The distances between SBUs are measured to be approximately 2.7 nm (Figure 2-7f), which are consistent with the calculated distance of 2.77 nm based on the X-ray structure model. Fast Fourier transform (FFT) of the high-resolution TEM image displays a 3-fold symmetry for the nanoplates (Figure 2-7c), consistent with the symmetry along (111) direction of the cubic structure of DBP-Hf. The dimensions of the nanoplates are measured to be ~100 nm in diameter and ~10 nm in thickness. Such thin plates consist of only 4-5 sets of (111) packing layer ($d_{111}=2.2$ nm). Dynamic light scattering (DLS) measurements gave an average diameter of 76.3 nm for the particles (Figure 2-9). Notably, the nanoplate morphology is particularly advantageous for generating ROS for PDT. The diffusion length of $^1\text{O}_2$ is no more than 90-120 nm in aqueous environment⁴⁻⁸ and was estimated to be 20-220 nm inside cells.⁹ Therefore, the nanoplates as thin as 10-nm in thickness are ideally suited for transporting $^1\text{O}_2$ from the nMOF interior to the cell cytoplasm to exert cytotoxic effects.

DBP-Hf displays high stability in physiological environment. After incubation in RPMI 1640 cell culture medium for 12 h, the DBP-Hf morphology remained unaltered by TEM observation (Figure 2-7d). The remained crystallinity of the nMOFs was also confirmed by the FFT of the TEM images and the unchanged PXRD pattern (Figure 2-7a,e).

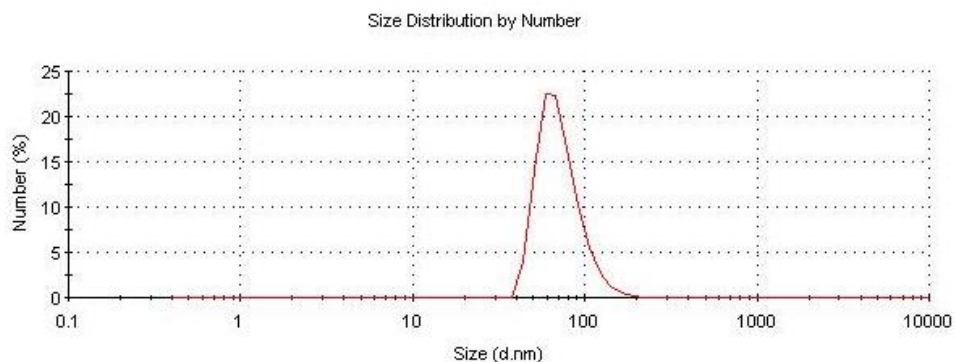


Figure 2-9 DLS plot showing the particle size of DBP-Hf. Reprinted with permission from *J. Am. Chem. Soc.*, **2014**, *136*, 16712–16715. Copyright 2014 American Chemical Society.

2.2.3 Photophysics and photochemistry of H₂DBP and DBP-Hf

The UV-visible absorption spectra of H₂DBP and DBP-Hf in phosphate buffered saline (PBS) buffers (pH=7.4) are compared in Figure 2-10. H₂DBP shows a Soret band at 402 nm and four Q-bands at 505, 540, 566, and 619 nm. The absorption of standard solutions of H₂DBP at concentrations of 0.2, 0.4, 0.6, 0.8, 1, 1.5, 4 and 8 mg/L were acquired and the extinction coefficients of H₂DBP at 402 nm and 619 nm are determined to be 2.2×10^5 and 1.7×10^3 M⁻¹cm⁻¹, respectively (Figure 2-10b). DBP-Hf shows slight red shifts for all Q-bands, with the peaks appearing at 510, 544, 579, and 634 nm, probably due to the coordination of the carboxylate groups of DBP ligands to Hf centers. The presence of four Q-bands and their red shifts support the presence of free-base porphyrin ligands in DBP-Hf. The Soret band of DBP-Hf is

significantly broadened, presumably due to inequivalent ligand environments in thin nanoplates as well as potential framework distortion in thin MOF structures.

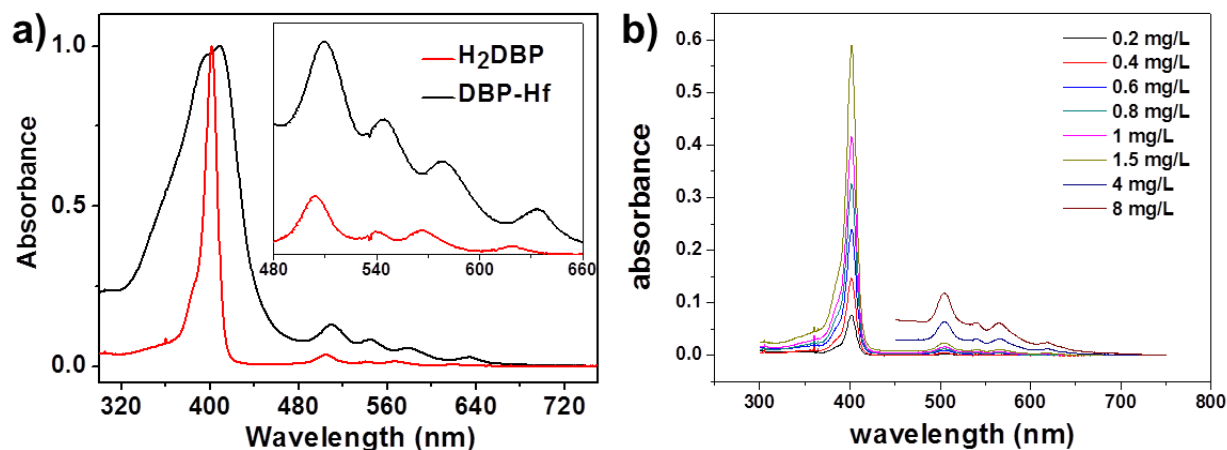


Figure 2-10 UV-visible spectra of H₂DBP and DBP-Hf. Adapted with permission from *J. Am. Chem. Soc.*, **2014**, *136*, 16712–16715. Copyright 2014 American Chemical Society.

The coordination of the porphyrin ligand to Hf will enhance the intersystem crossing from ¹DBP excited state to ³DBP state,¹⁰ which decreases the fluorescence emission and increases the singlet oxygen generation quantum yield. The fluorescence spectra of H₂DBP ligand and DBP-Hf were taken on a spectrofluorophotometer (RF-5301PC, Shimadzu, Japan, Figure 2-11). The ligand fluorescence appears at 630 nm (strong) and 690 nm (weak) with excitation at 405 nm, while DBP-Hf emission at 640 nm greatly diminished by a factor of 250. The fluorescence lifetimes reduction from 10.9 ns for H₂DBP to 0.26 ns for DBP-Hf also confirms such effect (Figure 2-12 and Table 2-2).

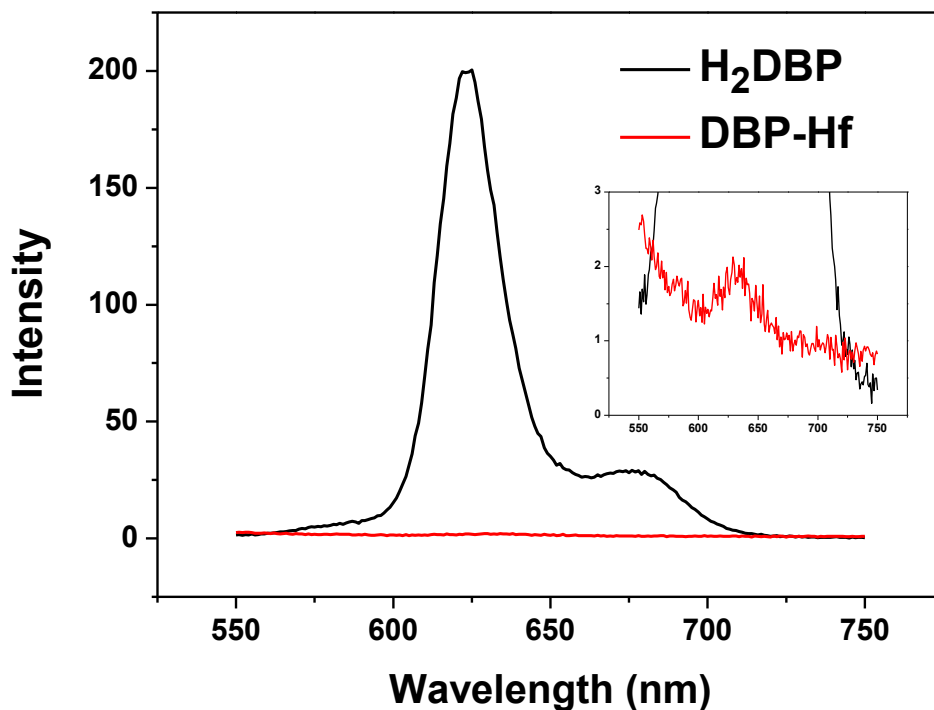


Figure 2-11 Fluorescence of H₂DBP and DBP-Hf in PBS (excitation: 405 nm). The expanded view for the DBP-Hf is shown in the inset. Reprinted with permission from *J. Am. Chem. Soc.*, **2014**, *136*, 16712–16715. Copyright 2014 American Chemical Society.

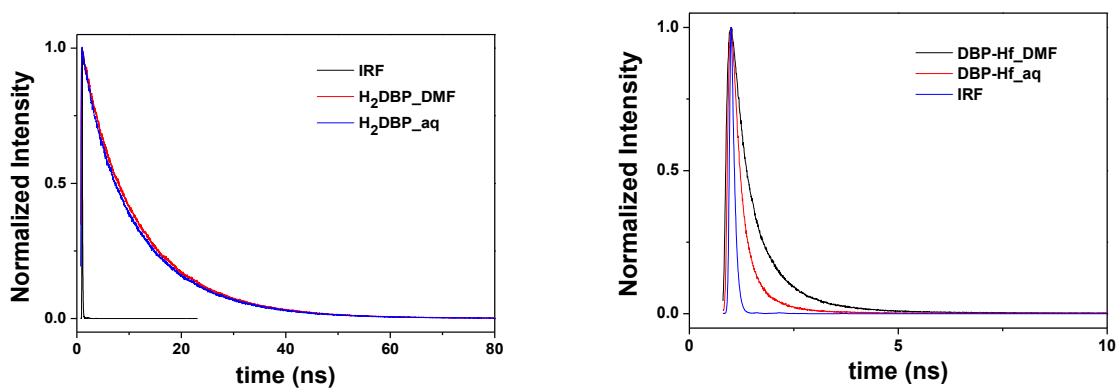


Figure 2-12 Time-resolved fluorescence decay traces of H₂DBP (left) and DBP-Hf (right) in different media, together with instrument response function (excitation/emission 403/640 nm). Reprinted with permission from *J. Am. Chem. Soc.*, **2014**, *136*, 16712–16715. Copyright 2014 American Chemical Society.

Table 2-2 Lifetimes of H2DBP and DBP-Hf fluorescence in different medium, fitted by software.

sample	τ_1 (ns)	τ_2 (ns)	$\bar{\tau}$ (ns)
IRF	0.0074	N/A	N/A
H ₂ DBP_DMF	11.3	N/A	N/A
H ₂ DBP_aq	12.4	7.86	10.9
DBP-Hf_DMF	0.44	1.31	0.54
DBP-Hf_aq	0.21	0.70	0.26

Singlet oxygen generation efficiencies of H₂DBP and DBP-Hf were determined using Singlet Oxygen Sensor Green (SOSG, Life Technologies). After exposure to a LED light source (peak emission at 640 nm, energy irradiance of 100 mW/cm²), the produced ¹O₂ react with chemiluminescent reagent SOSG to generate green fluorescence, and the change of fluorescence signal was quantified with a fluorimeter. The fluorescence intensity was plotted against irradiation time (Figure 2-13). The ¹O₂ generation was depicted with an exponential function that corresponded to a pseudo first-order process.

As the light intensity and photosensitizer concentration are fixed, for the photoreaction, we can assume that [PS*] (the concentration of the excited state of the photosensitizer) is a constant. Therefore, we have singlet oxygen generation rate equation:

$$\frac{d[{}^1O_2]}{dt} = -\frac{d[O_2]}{dt} = k[PS^*][O_2] = k^*[O_2]$$

Where $k^* = k[PS^*]$. Here we have a coupled reaction of SOSG to consume singlet oxygen:

$$\frac{d[SOSG^*]}{dt} = k_2[{}^1O_2][SOSG]$$

Where [SOSG*] is the concentration of reacted form of SOSG.

Applying steady state assumption on [1O_2], we have

$$\frac{d[{}^1O_2]}{dt} = k^*[O_2] - k_d[{}^1O_2] - k_2[{}^1O_2][SOSG] = 0$$

$$[{}^1O_2] = \frac{k^*[O_2]}{k_d + k_2[SOSG]}$$

Where k_d is the rate constant of singlet oxygen loss (due to relaxation or quenched by other species in the solution). When $k_2[SOSG] \ll k_d$ and $[O_2]$ is high,

$$[{}^1O_2] \approx \frac{k^*[O_2]}{k_d} = \text{constant}$$

$$\frac{dI_F}{dt} \propto \frac{d[SOSG^*]}{dt} = k_1[SOSG]$$

Where $k_1 = k_2 k^*[O_2]/k_d$, and the fluorescence intensity is proportional to $[SOSG^*]$:

$$I_F = I_0 \varphi_f \varepsilon_S b [SOSG^*]$$

Where I_0 is the incident light intensity, φ_f is the fluorescence quantum yield of $SOSG^*$, ε_S is the extinction coefficient of $SOSG^*$, and b is the light path length. We can integrate the equation to obtain the correlation of fluorescence intensity I_F and irradiation time t :

$$\ln \frac{[SOSG]}{c_0(SOSG)} = -k_1 t$$

$$I_F = A[1 - e^{-kt}]$$

Where A and k are fitting parameters,

$$A = \varphi_f I_0 \varepsilon_S b c_0(SOSG)$$

$$k = \varphi_{\Delta} N_{ir} \varepsilon_{PS} b c(PS) k_2 / k_d$$

Where $c_0(SOSG)$ is the initial SOSG concentration; φ_{Δ} is the quantum yield of singlet oxygen generation, N_{ir} is the irradiation light intensity by photons per second, ε_{PS} is the extinction coefficient of photosensitizer at LED emission wavelength, $c(PS)$ is the photosensitizer concentration. Linear approximations are applied in above equations.

Note that for H₂DBP+HfCl₄ sample, singlet oxygen generation rate is very low, SOSG consumption becomes negligible. Then the equation could be simplified to

$$I_F = Akt$$

Thus we can compare the linear regression slope to product of Ak in the other groups.

The fitted equations for H₂DBP and DBP-Hf are (Table 2-3):

$$I_{H_2DBP} = 68 \times (1 - e^{-0.0015t})$$

$$I_{DBP-Hf} = 88 \times (1 - e^{-0.0033t})$$

The product of Ak in the equation is proportional to the initial rate of the reaction that indicates the ¹O₂ generation efficiency. DBP-Hf is thus at least twice as efficient as H₂DBP in generating ¹O₂.

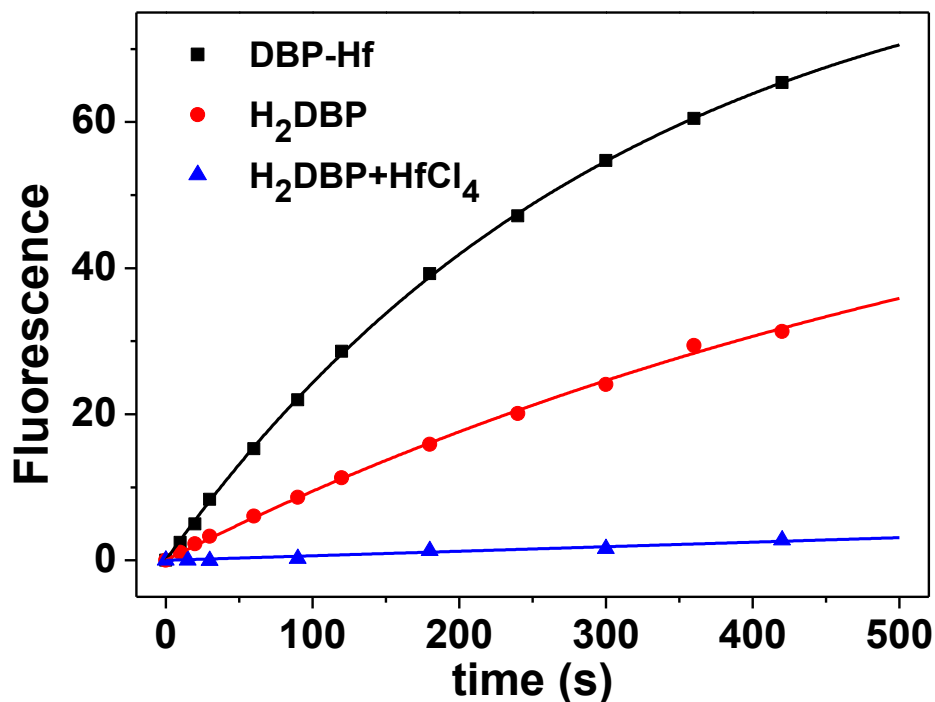


Figure 2-13 Singlet oxygen generation by DBP-Hf, H₂DBP, and H₂DBP+HfCl₄. The dots are experimental data and the solid lines are fit curves. Reprinted with permission from *J. Am. Chem. Soc.*, **2014**, *136*, 16712–16715. Copyright 2014 American Chemical Society.

Table 2-3 Fitting parameters of singlet oxygen generation rate.

	A	k (s ⁻¹)	r ²	Ak
H ₂ DBP	68	1.5×10 ⁻³	0.998	0.102
DBP-Hf	88	3.3×10 ⁻³	0.999	0.290
H ₂ DBP+HfCl ₄			0.97	0.0062

2.2.4 *In vitro* and *in vivo* efficacy

Encouraged by the excellent ¹O₂ generation efficiency, we tested the PDT efficacy of DBP-Hf on resistant head and neck cancer models. The tumor cell uptake of DBP-Hf was first evaluated by incubating human head and neck cancer cells SQ20B with DBP-Hf (30 μg/mL) for

4 h or 12 h (Figure 2-14). The Hf concentrations in the cells were determined by ICP-MS. No significant difference was observed between the uptake amount after 4 h and 12 h incubation, indicating rapid internalization of DBP-Hf to the cancer cells.

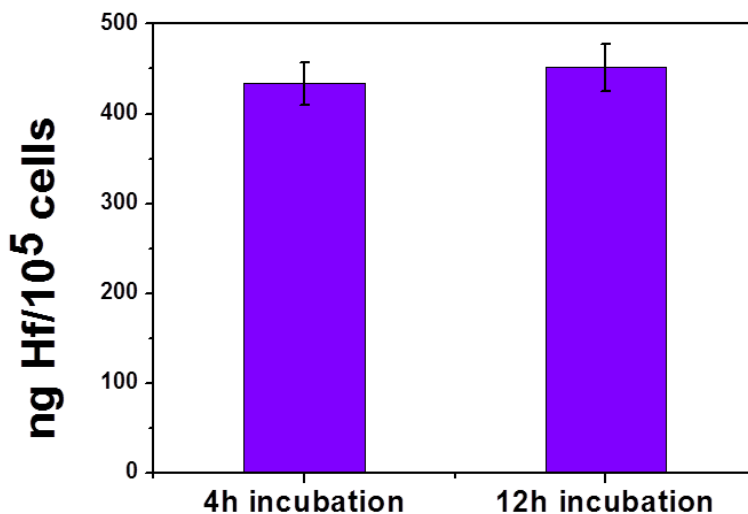


Figure 2-14 Cellular uptake of DBP-Hf after 4 or 12 hour incubation. Reprinted with permission from *J. Am. Chem. Soc.*, **2014**, *136*, 16712–16715. Copyright 2014 American Chemical Society.

To further confirm the PDT efficacy of DBP-Hf, SQ20B cancer cells were treated with H₂DBP, DBP-Hf, or PpIX at various concentrations (5, 10, 20, 50 and 100 μ M based on ligand concentrations), the cells were irradiated with LED light (640 nm, 100 mW/cm²) for 15 min (total light dose 90 J/cm²) or 30 min (total light dose 180 J/cm²), respectively. Significant PDT efficacy was observed in DBP-Hf treated groups, even for the group receiving 5 μ M PS dose and 15 min irradiation (Figure 2-15). H₂DBP-treated groups show moderate PDT efficacy only at 20 μ M dose with 30 min light irradiation while no cytotoxicity was observed in dark control or blank control groups. In comparison, PpIX is much less photocytotoxic than DBP-Hf under similar conditions. Cells incubated with PBS after irradiation for 15 min and 30 min did not show appreciable viability changes (95.2 \pm 2.2% for 15 min and 96.1 \pm 5.2% for 30 min) compared

with cells incubated with PBS and received no irradiation, suggesting that irradiation alone will not induce any cytotoxicity. There was also no cytotoxicity observed in cells treated with H₂DBP or DBP-Hf without irradiation. This result indicated that H₂DBP and DBP-Hf alone are non-toxic to cells at tested concentrations up to 100 μM.

We carried out proof-of-concept *in vivo* experiments on SQ20B subcutaneous xenograft murine models to evaluate the PDT efficacy of DBP-Hf. The mice were treated with PBS control, DBP-Hf (3.5 mg DBP/kg) or H₂DBP (3.5 mg/kg) by intratumoral injection. Twelve hours post injection, each mouse was irradiated at the tumor site with light (180 J/cm²) for 30 min. For comparison from literature, photofrin® is administrated by intraperitoneal injection at 10 mg/kg in tumor bearing mice and with light irradiation of 135 J/cm².¹¹ As depicted in Figure 2-16, the tumors of mice treated with DBP-Hf started shrinking 1 day post PDT treatment. Most importantly, among the four tumors in the DBP-Hf group, two tumors were completely eradicated by single nMOF administration and single light irradiation while the sizes of the other two tumors decreased from ~150 mm³ to ~3 mm³. The tumor growth of mice treated with H₂DBP was slightly suppressed after PDT, however accelerated after 5 days and exhibited no difference to the control group at the endpoint. After local administration, DBP-Hf could be efficiently internalized by the tumor cells and induce cytotoxicity upon irradiation while the free ligand might be cleared away from the tumor sites before irradiation. No skin/tissue damage was observed after PDT treatment on all mice (Figure 2-16c). The histologies of tumor slices of all three groups were observed after PDT treatment (Figure 2-17). The dominant normal tumor cells are observed in control and ligand treated groups. Prevailing apoptosis/necrosis of tumor cells were observed in tumor slices from nMOF group and massive inflammatory cells indicated the

immunoresponse after PDT. The blood vessels in tumor tissue in nMOF treated group are destroyed after PDT while not disturbed in control and ligand treated groups.

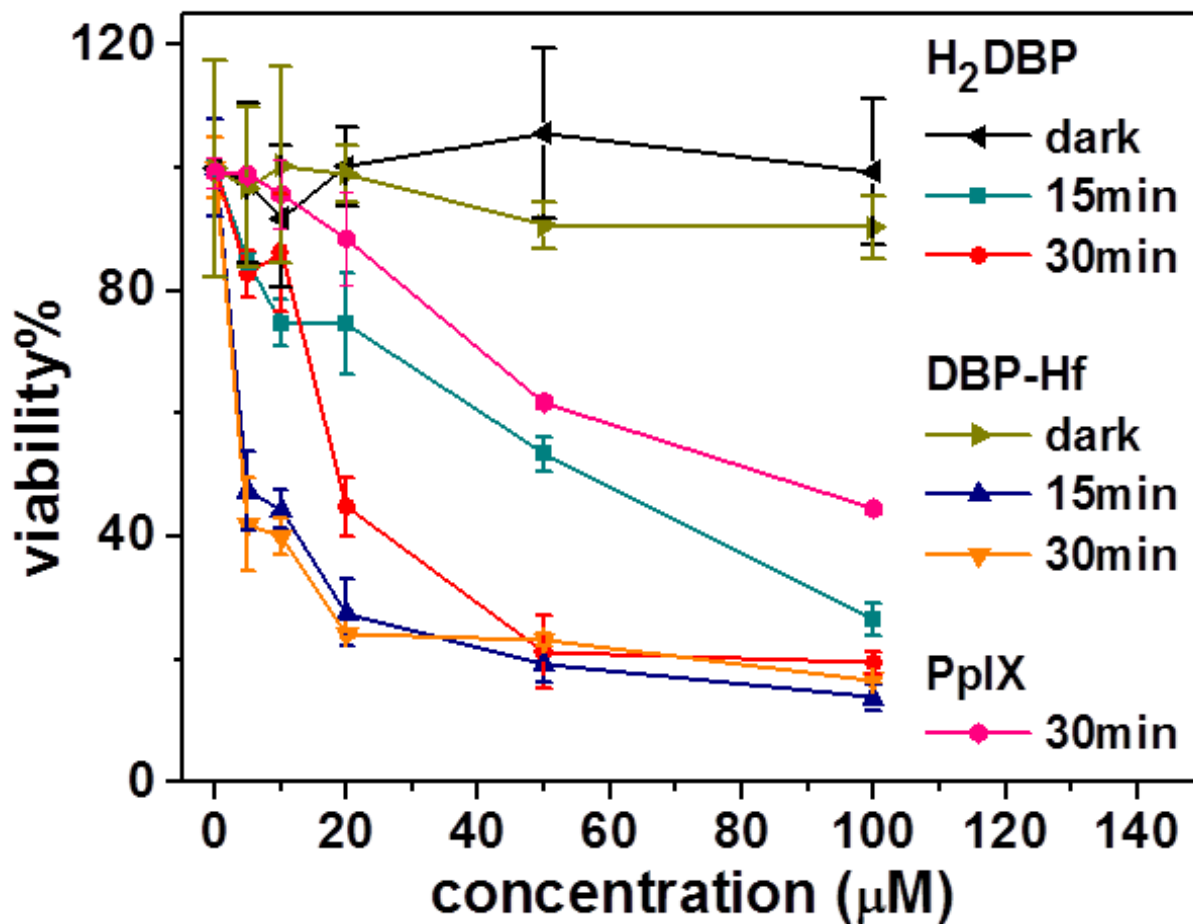


Figure 2-15 *In vitro* PDT cytotoxicity of H₂DBP, DBP-Hf, and PpIX at different PS concentrations and irradiation doses. Adapted with permission from *J. Am. Chem. Soc.*, **2014**, *136*, 16712–16715. Copyright 2014 American Chemical Society.

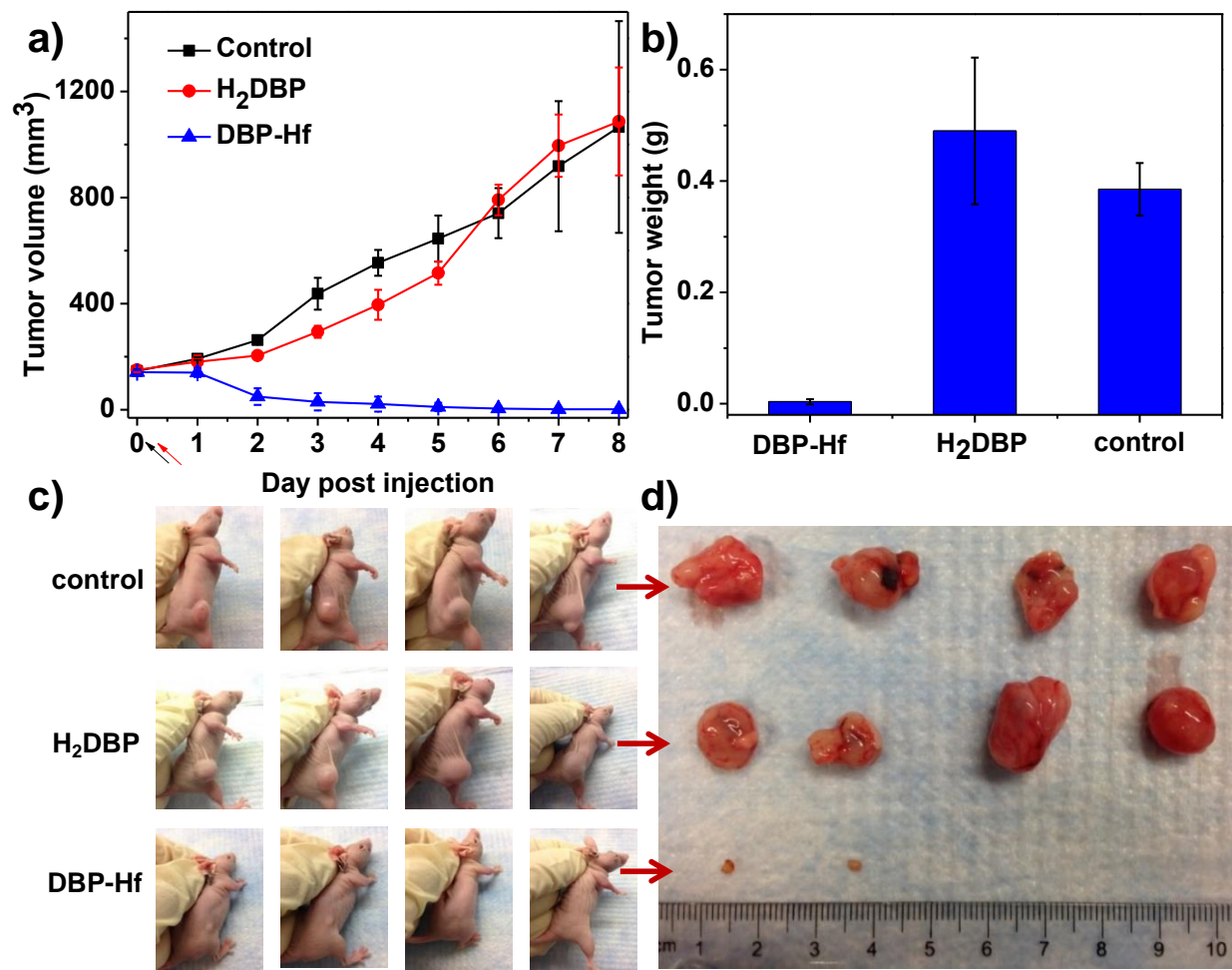
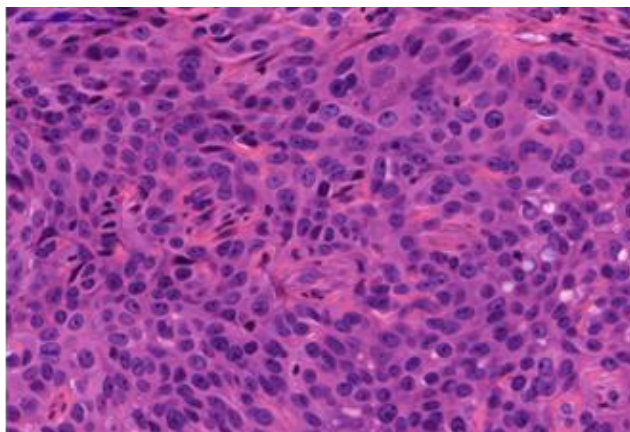
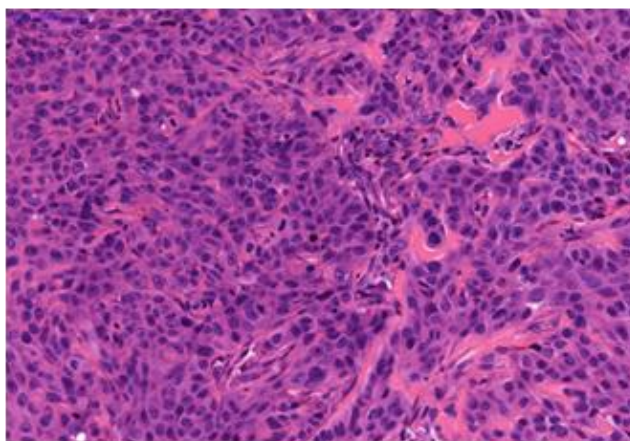


Figure 2-16 *In vivo* efficacy of PDT on SQ20B tumor bearing mice. (a) Tumor growth inhibition curve after PDT treatment. Black and red arrow refer to injection and irradiation time point, respectively. (b) Tumor weight after PDT treatment. (c) Photos of the mice on Day 8. (d) Photo of tumors of each group after PDT. Two tumors in the DBP-Hf group were completely eradicated at the endpoint. Adapted with permission from *J. Am. Chem. Soc.*, **2014**, *136*, 16712–16715. Copyright 2014 American Chemical Society.

control



H₂DBP



DBP-Hf

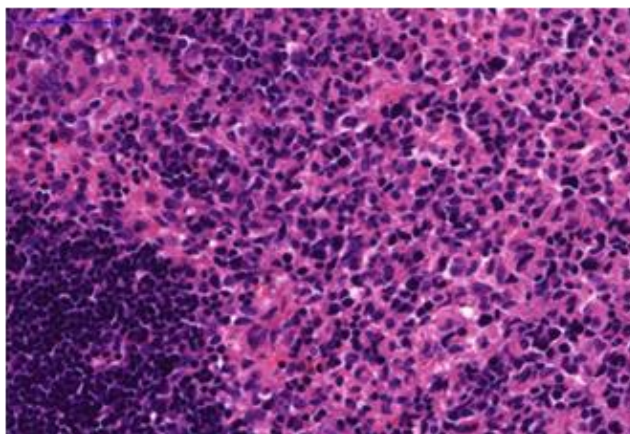


Figure 2-17 Histology of tumor slices of mice after PDT treatment. Adapted with permission from *J. Am. Chem. Soc.*, **2014**, *136*, 16712–16715. Copyright 2014 American Chemical Society.

2.3 Conclusion

In this chapter, we have designed and synthesized a stable and porous DBP-Hf nMOF with an ideal combination of structural regularity and nanoplate morphology for highly effective PDT of resistant head and neck cancer. As a result of site isolation of DBP ligands, enhanced intersystem crossing by Hf clusters, and facile $^1\text{O}_2$ diffusion out of a porous nanoplate, the nMOF works as an efficient PDT photosensitizer, as demonstrated by both $^1\text{O}_2$ generation efficiency measurements and *in vitro* cytotoxicity assays. *In vivo* PDT efficacy studies with subcutaneous xenograft murine models demonstrated 50 times tumor volume reduction in half of the mice and complete tumor eradication in the other half of mice that were treated with DBP-Hf. In comparison, no therapeutic effect was observed in the mice treated with H₂DBP. The facile structural and compositional tunability of nMOFs should allow further tuning of other properties to afford a new generation of highly potent PDT agents for treating resistant cancers in the clinic.

2.4 Methods

UV-visible absorption: The UV-vis absorption spectra of H₂DBP and DBP-Hf were acquired with a UV-vis spectrophotometer (UV-2401PC, Shimadzu, Japan). The H₂DBP solution and DBP-Hf nMOF suspension were prepared in 0.67 mM phosphate buffer saline (PBS). The absorption of standard solutions of H₂DBP at concentrations of 0.2, 0.4, 0.6, 0.8, 1, 1.5, 4 and 8 mg/L were acquired and the standard curve was plotted by linear fitting of the absorbance at 402 nm.

Fluorescence lifetime measurement: Time-domain lifetimes were measured on a ChronosBH lifetime fluorimeter (ISS, Inc.) using Time-Correlated Single Photon Counting (TCSPC)

methods. The fluorimeter contained Becker-Hickl SPC-130 detection electronics and an HPM-100-40 Hybrid PMT detector. Tunable picosecond pulsed excitation was provided by a Fianium SC400-2 supercontinuum laser source with integrated pulse picker and AOTF. Emission wavelengths were selected with bandpass filters (Semrock and Chroma). The Instrument Response Function (IRF) was measured to be approximately 120ps FWHM in a 1% scattering solution of Ludox LS colloidal silica. Lifetimes were fit via a forward convolution method in the Vinci control and analysis software.

Singlet Oxygen generation test: A light-emitting diode (LED) array with peak emission at 640 nm was used as the light source of singlet oxygen generation. The irradiance of LED is 100 mW/cm². Singlet oxygen sensor green (SOSG) reagent (Life Technologies) was employed for the detection of singlet oxygen. H₂DBP and DBP-Hf samples were prepared in 5 μM solutions/suspensions in HBSS buffer (for DBP-Hf samples, the concentration was calculated as ligand equivalents). To 2 mL each of these solutions/suspensions, SOSG stock solution (5 μL at 5 mM) was added (final concentration=12.5 μM) before fluorescence measurement.

For a typical measurement, fluorescence intensity was acquired on a spectrofluorometer (RF-5301PC, Shimadzu, Japan) with excitation at 504 nm and emission at 525 nm (slit width 1.5 nm/3 nm for ex/em). Fluorescence was measured after irradiation by LED for 0 (as background), 10 s, 20 s, 30 s, 1 min, 1.5 min, 2 min, 2.5 min, 3 min, 3.5 min, 4 min, 4.5 min, 5 min, 6 min and 7 min.

Cellular uptake: SQ20B cells were seeded on 6-well plates at 5×10^5 cells/well and further incubated for 24 h. The DBP-Hf samples were added to the cells at a concentration of 30 mg/L. After incubating for 4 h and 12 h, the cells were collected and the cell numbers were counted by

hemocytometer. The cells were digested with concentrated nitric acid and subjected to ICP-MS for the determination of the Hf concentration. The cellular uptake amounts were expressed as Hf (ng) per 10^5 of cells.

***In vitro* cytotoxicity:** The cytotoxicities of DBP-Hf, H₂DBP, and PpIX were evaluated in human head and neck cancer cells SQ20B which are resistant to cisplatin and conventional radiotherapy. SQ20B cells were seeded on 96-well plates at 2000 cells/well. The cells were treated with DBP-Hf and H₂DBP at various ligand concentrations (5, 10, 20, 50 and 100 μ M base on ligand concentrations) after a 24-h incubation. A further incubation of 4 h was allowed, followed by replacing the culture medium with 100 μ L of fresh DMEM/F12 medium. The cells were irradiated with LED light (640 nm) at 100 mW/cm² for 15 min (total light dose 90 J/cm²) or 30 min (total light dose 180 J/cm²), respectively. The cells without irradiation treatment served as controls. The cells were further incubated to achieve a total incubation time of 72 h with DBP-Hf, H₂DBP or PpIX. The cell viability was detected by (3-(4,5-dimethylthiazol-2-yl)-5-(3-carboxymethoxyphenyl)-2-(4-sulfophenyl)-2H-tetrazolium) (MTS) assay (Promega, USA).

***In vivo* efficacy:** The PDT efficacy of DBP-Hf was investigated using SQ20B subcutaneous xenograft murine models. Tumor bearing mice were established by subcutaneous inoculation of SQ20B cell suspension (5×10^6 cells per mouse) into the right flank region of 6-week athymic female nude mice. Three groups were included for comparison: PBS as control, H₂DBP, and DBP-Hf. When tumors reached 100 mm³, PBS, H₂DBP, and DBP-Hf were intratumorally injected to animals at a DBP dose of 3.5 mg/kg. At 12 h post-injection, mice were anesthetized with 2% (v/v) isoflurane and tumors were irradiated with a 640 nm LED for 30 min. The light intensity was measured as 100 mW/cm², and the total light dose was 180 J/cm². Both injection and PDT were performed once.

To evaluate the therapeutic efficacy, tumor growth and body weight evolution were monitored. The tumor size was measured with a digital caliper every day. Tumor volumes were calculated as follows: $(\text{width}^2 \times \text{length})/2$. Finally, all mice were sacrificed on Day 8, and the excised tumors were photographed and weighed. Tumors were fixed with formalin. Paraffin-embedded 5 μm tumor sections were stained with hematoxylin and eosin (H&E) and observed with light microscopy (Pannoramic Scan Whole Slide Scanner, Perkin Elmer, USA).

2.5 References

1. Bechet, D., *et al.* Nanoparticles as vehicles for delivery of photodynamic therapy agents. *Trends Biotechnol.* **26**, 612-621 (2008).
2. Wang, Q.M. & Bruce, D.W. One-step synthesis of β , meso-unsubstituted dipyrromethane. *Synlett* **1995**, 1267-1268 (1995).
3. Cavka, J.H., *et al.* A new zirconium inorganic building brick forming metal organic frameworks with exceptional stability. *J. Am. Chem. Soc.* **130**, 13850-13851 (2008).
4. Kanofsky, J.R. Measurement of Singlet-Oxygen In Vivo: Progress and Pitfalls. *Photochem. Photobiol.* **87**, 14-17 (2011).
5. Stdenis, C.E. & Fell, C.J.D. Diffusivity of Oxygen in Water. *Can J Chem Eng* **49**, 885-& (1971).
6. Merkel, P.B. & Kearns, D.R. Radiationless Decay of Singlet Molecular-Oxygen in Solution - Experimental and Theoretical Study of Electronic-to-Vibrational Energy-Transfer. *J. Am. Chem. Soc.* **94**, 7244-& (1972).
7. Rodgers, M.A.J. & Snowden, P.T. Lifetime of O-2(1delta-G) in Liquid Water as Determined by Time-Resolved Infrared Luminescence Measurements. *J. Am. Chem. Soc.* **104**, 5541-5543 (1982).
8. Snyder, J.W., Skovsen, E., Lambert, J.D.C. & Ogilby, P.R. Subcellular, time-resolved studies of singlet oxygen in single cells. *J. Am. Chem. Soc.* **127**, 14558-14559 (2005).
9. Moan, J. & Berg, K. The Photodegradation of Porphyrins in Cells Can Be Used to Estimate the Lifetime of Singlet Oxygen. *Photochem. Photobiol.* **53**, 549-553 (1991).

10. Scandola, F., Chiorboli, C., Prodi, A., Iengo, E. & Alessio, E. Photophysical properties of metal-mediated assemblies of porphyrins. *Coordination chemistry reviews* **250**, 1471-1496 (2006).
11. Henderson, B.W., Waldow, S.M., Potter, W.R. & Dougherty, T.J. Interaction of photodynamic therapy and hyperthermia: tumor response and cell survival studies after treatment of mice in vivo. *Cancer Res.* **45**, 6071-6077 (1985).

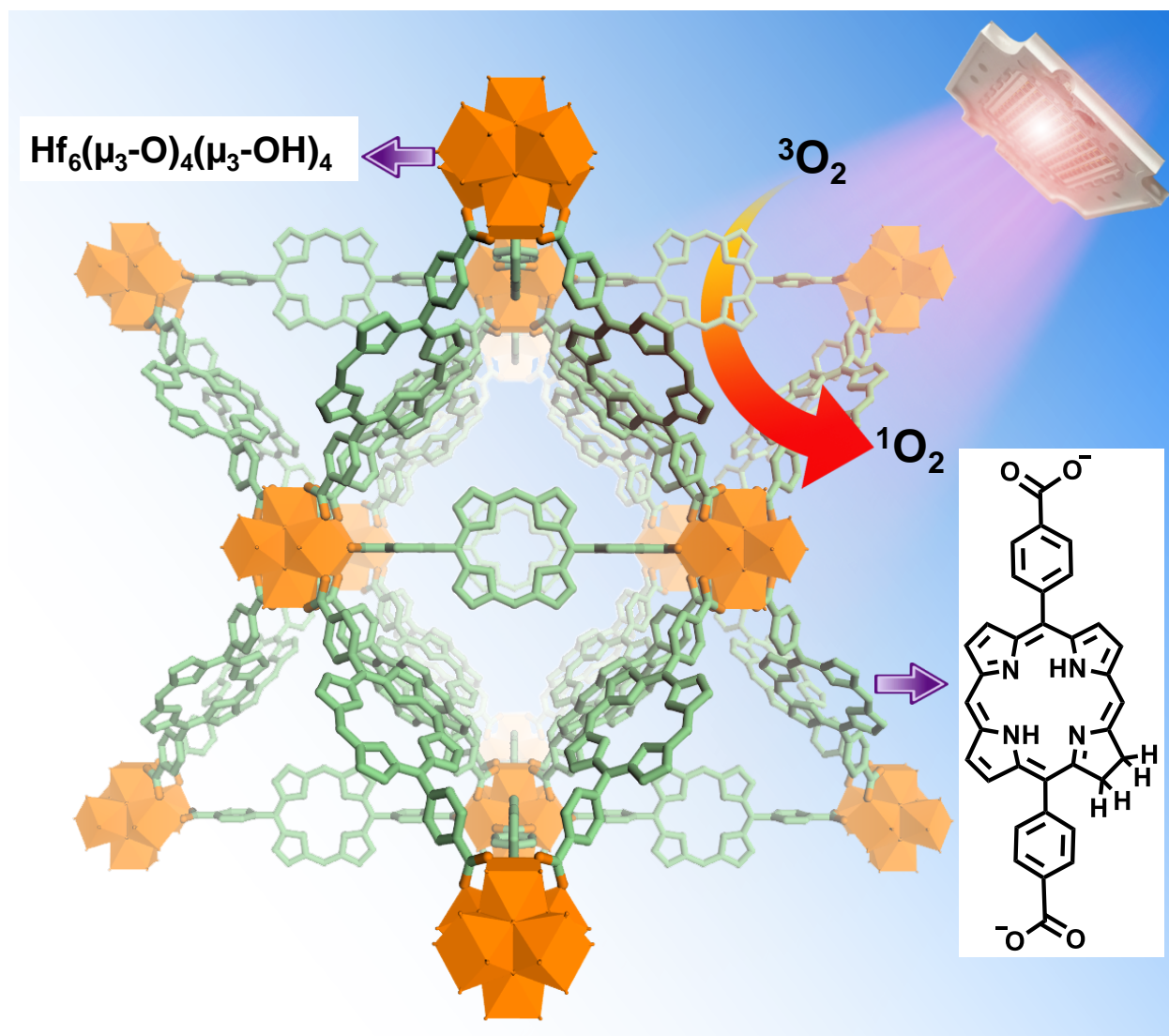
Chapter 3. A Chlorin-Based Nanoscale Metal-Organic Framework for Photodynamic therapy

3.1 Rationale of the nMOF design

After the first successful attempt to use the porphyrin-based nMOF, DBP-Hf, as a photosensitizer (PS) for PDT, we wish to further optimize the nMOF system. Despite the excellent performance in pilot animal studies, the photophysical properties of DBP-Hf are not optimal. The lowest energy absorption at 634 nm and the relatively small extinction coefficient (ϵ) of $2200 \text{ M}^{-1} \text{ cm}^{-1}$ indicate a low energy conversion efficiency. In this chapter, we report the design of the first chlorin-based nMOF, DBC-Hf, with much improved photophysical properties and PDT efficacy.

Hematoporphyrin derivatives were developed as the first generation PSs, leading to the clinical application of the first PDT agent photofrin® in 1993.¹ However, the photophysical properties of porphyrins are non-ideal with the absorption peaks typically near the high energy edge of the tissue-penetrating window (600-900 nm) and small ϵ values. In molecular PS design, reduction of porphyrins to chlorins has been shown to shift the absorption to a longer wavelength with a concomitant increase in ϵ .^{2,3} For example, reduction of 5,10,15,20-tetra(hydroxyphenyl)porphyrin to its chlorin derivative red-shifts the last Q-band from 644 to 650 nm along with a dramatic enhancement in ϵ from $3400 \text{ M}^{-1} \text{ cm}^{-1}$ to $29600 \text{ M}^{-1} \text{ cm}^{-1}$. We hypothesized that a chlorin-based nMOF would have improved photophysical properties over DBP-Hf to lead to more effective cancer treatment by PDT.

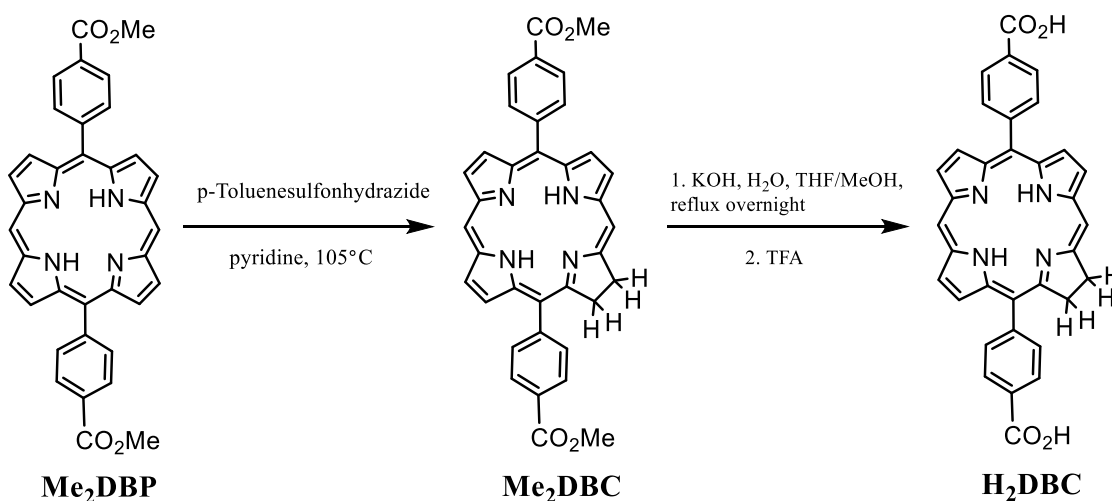
Scheme 3-1 Schematic description of the singlet oxygen generation by DBC-Hf photosensitization with LED light. Reprinted with permission from *J. Am. Chem. Soc.*, **2015**, *137*, 7600–7603. Copyright 2015 American Chemical Society.



3.2 Results and Discussion

3.2.1 Synthesis and characterization of the H₂DBC ligand

Scheme 3-2 Synthesis of the 5,15-di(p-benzoato)chlorin (H₂DBC). Reprinted with permission from *J. Am. Chem. Soc.*, **2015**, *137*, 7600–7603. Copyright 2015 American Chemical Society.



The synthesis of H₂DBC ligand follows the route in scheme 3-2. 5,15-di(p-methylbenzoato)porphyrin (Me₂DBP) was synthesized following the protocol in Chapter 2. Me₂DBP was reduced to 5,15-di(p-methylbenzoato)chlorin (Me₂DBC) following a modified procedure from the literature.⁴ To a 2-neck round bottom flask were added Me₂DBP (239 mg, 0.41 mmol) and anhydrous potassium carbonate (520 mg, 3.76 mmol). Under nitrogen protection 30 mL of anhydrous pyridine was added. The solution was heated to 105 °C before the addition of 3 mL of p-toluenesulfonylhydrazide solution (0.275 M in anhydrous pyridine). The reaction mixture was kept at 105 °C for another 8 hours during which 4 fractions of p-toluenesulfonylhydrazide solutions (0.275 M in anhydrous pyridine, 3 mL for each fraction) were added every 2 h. The reaction mixture was then stirred at 105 °C in the dark for another 12 h. The product was extracted with 2:1 ethyl acetate/water and washed with 2 M HCl, 2 M phosphoric acid (twice), water, and saturated sodium bicarbonate solution. The solution was

treated with 2,3-dichloro-5,6-dicyano-benzoquinone (via slow addition of 1 mg/mL solution in chloroform) until the characteristic absorption of the over-reduced product at 735 nm disappeared. Silica gel chromatography with chloroform as eluent afforded pure Me₂DBC. Yield: 26% (62 mg, 0.11 mmol). ESI-MS for [Me₂DBC+H]⁺: 581.1 calcd; 581.2 found (Figure 3-1). ¹H-NMR (500 MHz, chloroform-D, ppm, Figure 3-2): δ=9.89 (s, 1H), 9.14 (dd, 1H), 9.06 (s, 1H), 8.99 (d, 1H), 8.85 (d, 1H), 8.77 (d, 1H), 8.59 (d, 1H), 8.44 (t, 4H), 8.35 (dd, 1H), 8.27 (d, 2H), 8.04 (d, 2H), 4.72 (t, 2H), 4.36 (t, 2H), 4.13 (s, 3H), 4.12 (s, 3H), -1.42 (s, 1H), -1.91 (s, 1H).

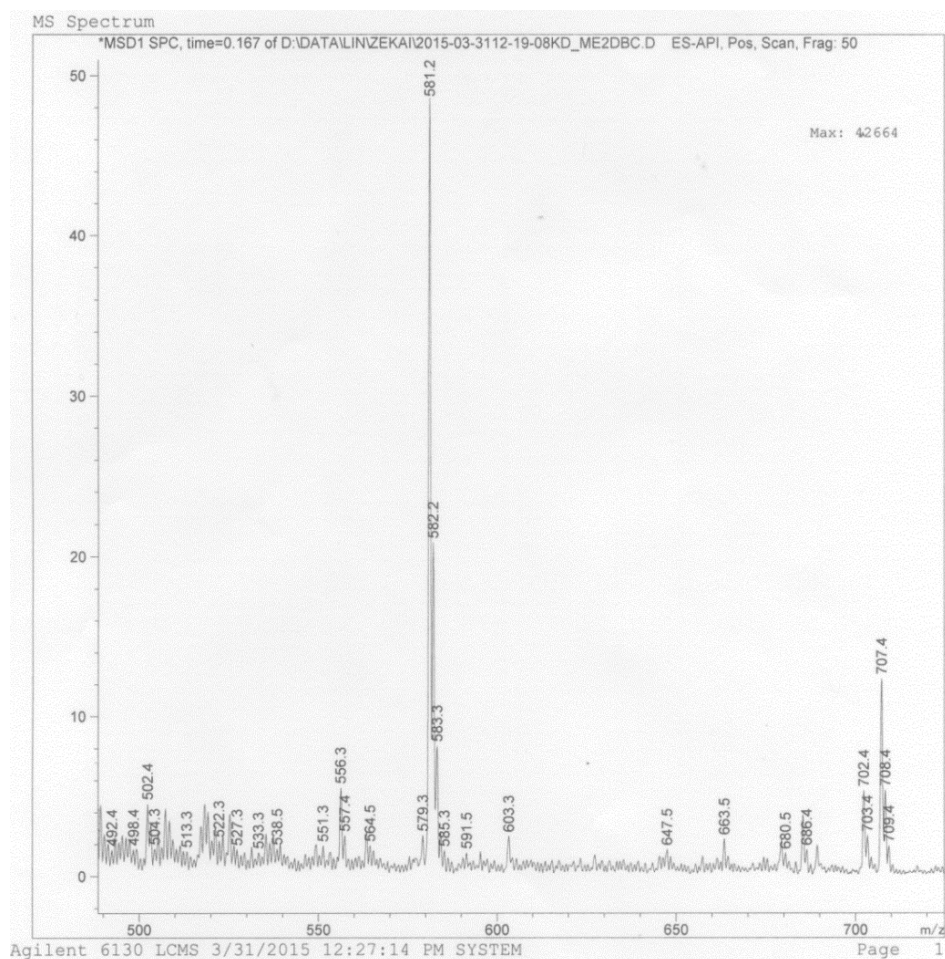


Figure 3-1 ESI-MS of 5,15-di(p-methylbenzoato)chlorin. The sample was prepared in dichloromethane as a 40 mg/L solution and was delivered by dichloromethane. Reprinted with permission from *J. Am. Chem. Soc.*, **2015**, *137*, 7600–7603. Copyright 2015 American Chemical Society.

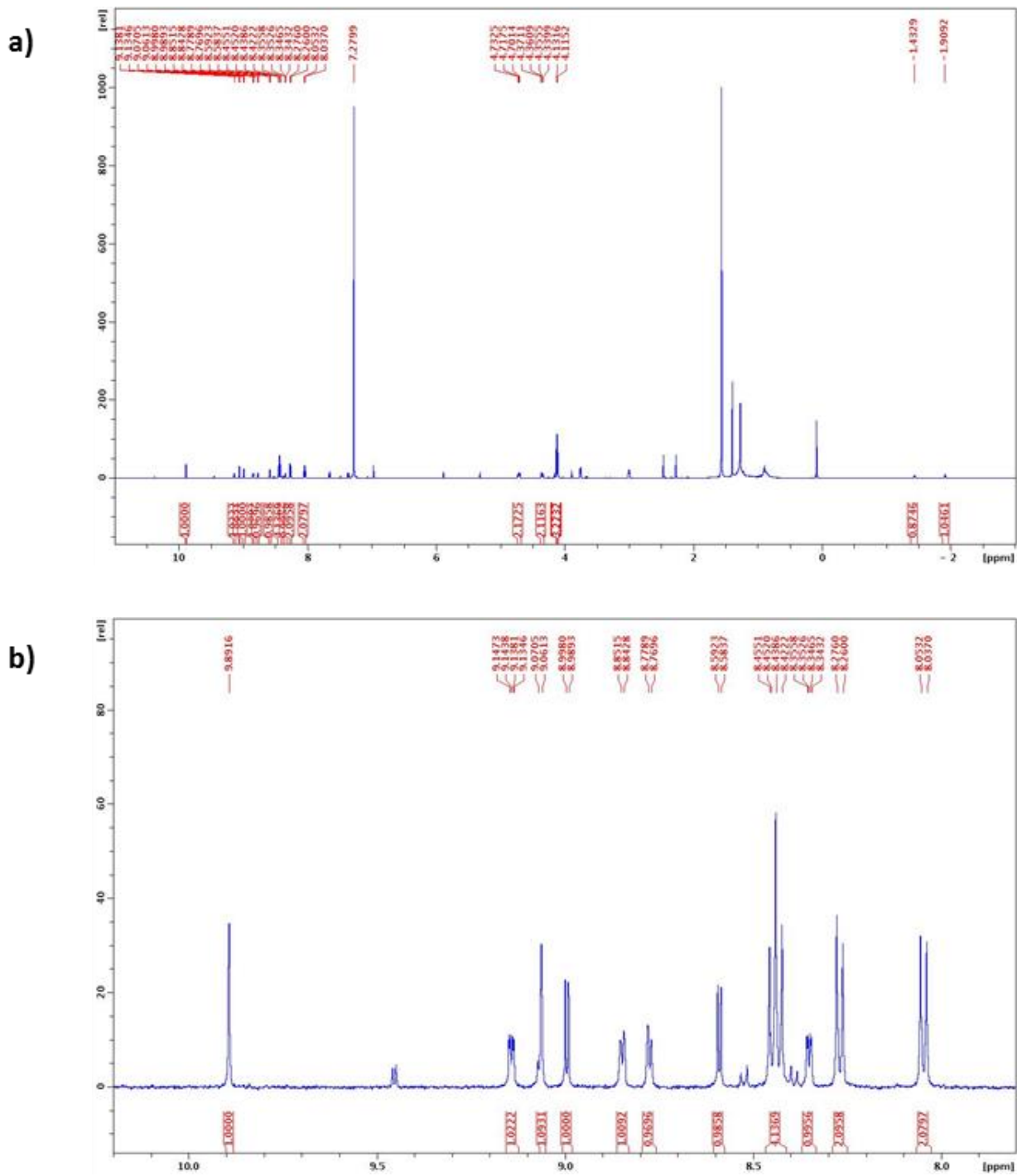


Figure 3-2 ^1H NMR spectra of 5,15-di(p-methylbenzoato)chlorin in chloroform-D. The full spectrum (a) and the expanded view of different portions of the spectrum (b-d) are presented.

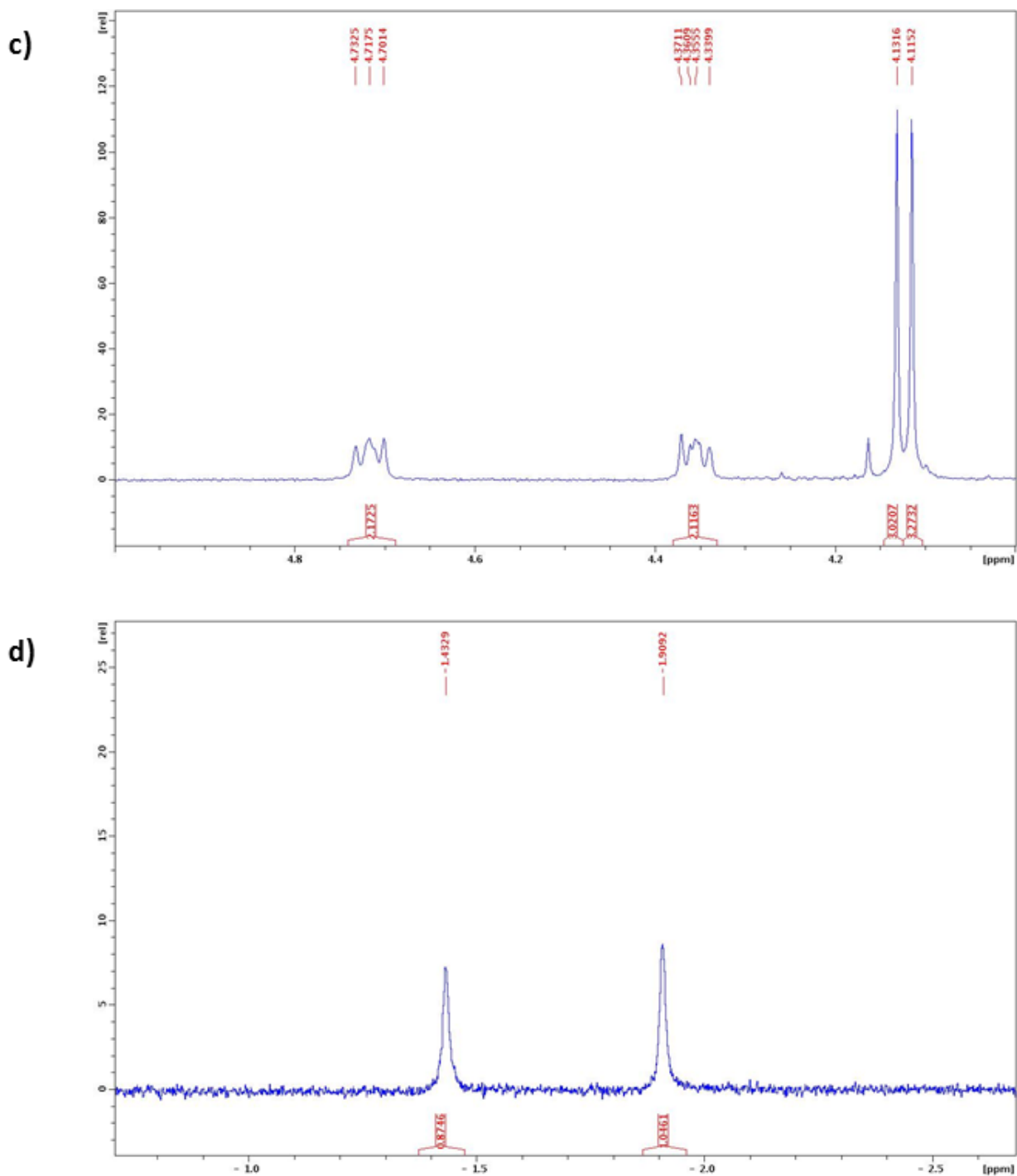


Figure 3-2 (Continued) ^1H NMR spectra of 5,15-di(p-methylbenzoato)chlorin in chloroform-D. The full spectrum (a) and the expanded view of different portions of the spectrum (b-d) are presented. Reprinted with permission from *J. Am. Chem. Soc.*, **2015**, *137*, 7600–7603. Copyright 2015 American Chemical Society.

Me₂DBC (62 mg, 0.11 mmol) was dissolved in a mixture of tetrahydrofuran (THF) and methanol (24 mL, 1:1 vol/vol). A potassium hydroxide aqueous solution (2.5 mL, 2 mol/L) was then added. The solution was heated to reflux under nitrogen protection overnight. Half of the solvent was removed by a rotary evaporator before the pH was adjusted to pH=3 with the addition of trifluoroacetic acid. The dark brownish product was collected by vacuum filtration, washed with water and ether, and dried under vacuum to afford the desired product in 88% yield (52 mg, 0.094 mmol). ¹H-NMR (500 MHz, DMSO-D₆, ppm, Figure 3-3): δ=13.25 (s, 2H), 10.11 (s, 1H), 9.40 (d, 1H), 9.28 (s, 1H), 9.08 (m, 2H), 8.79 (d, 1H), 8.48 (d, 1H), 8.35 (m, 5H), 8.27 (d, 2H), 8.12 (d, 2H), 4.70 (t, 2H), 4.32 (t, 2H), -1.50 (s, 1H), -2.03 (s, 1H). ESI-MS for [H₂DBC+H]⁺: 553.1 calcd; 553.2 found (Figure 3-4).

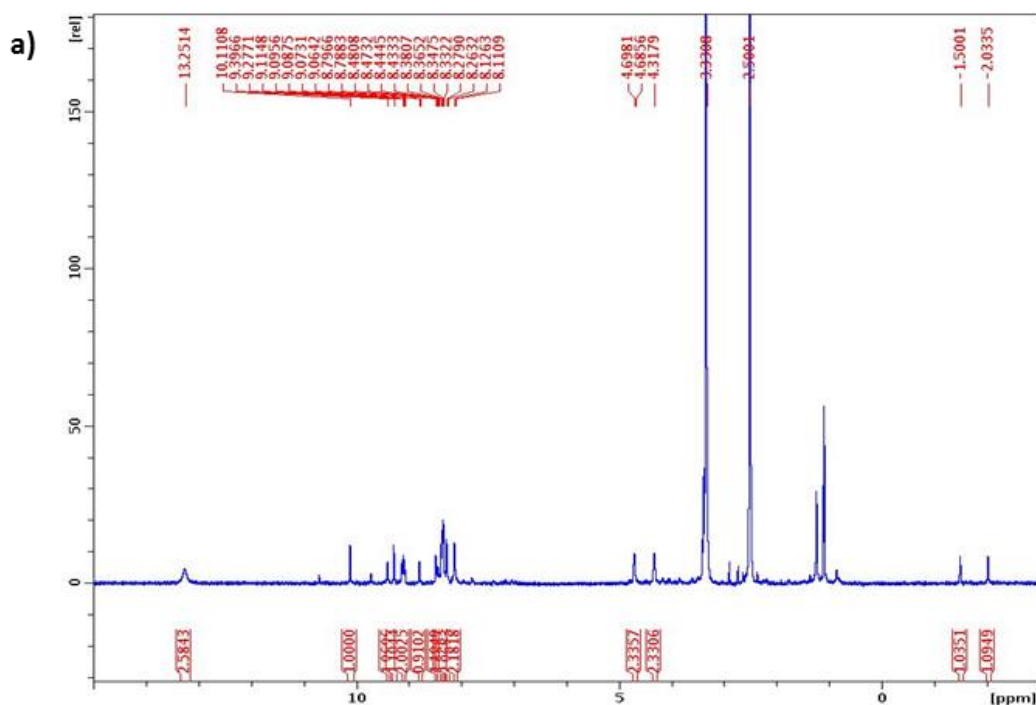


Figure 3-3 ¹H NMR spectrum of 5,15-di(p-benzoato)chlorin in DMSO-D₆. The full spectrum (a) and the expanded view of different portions of the spectrum (b, c) are presented.

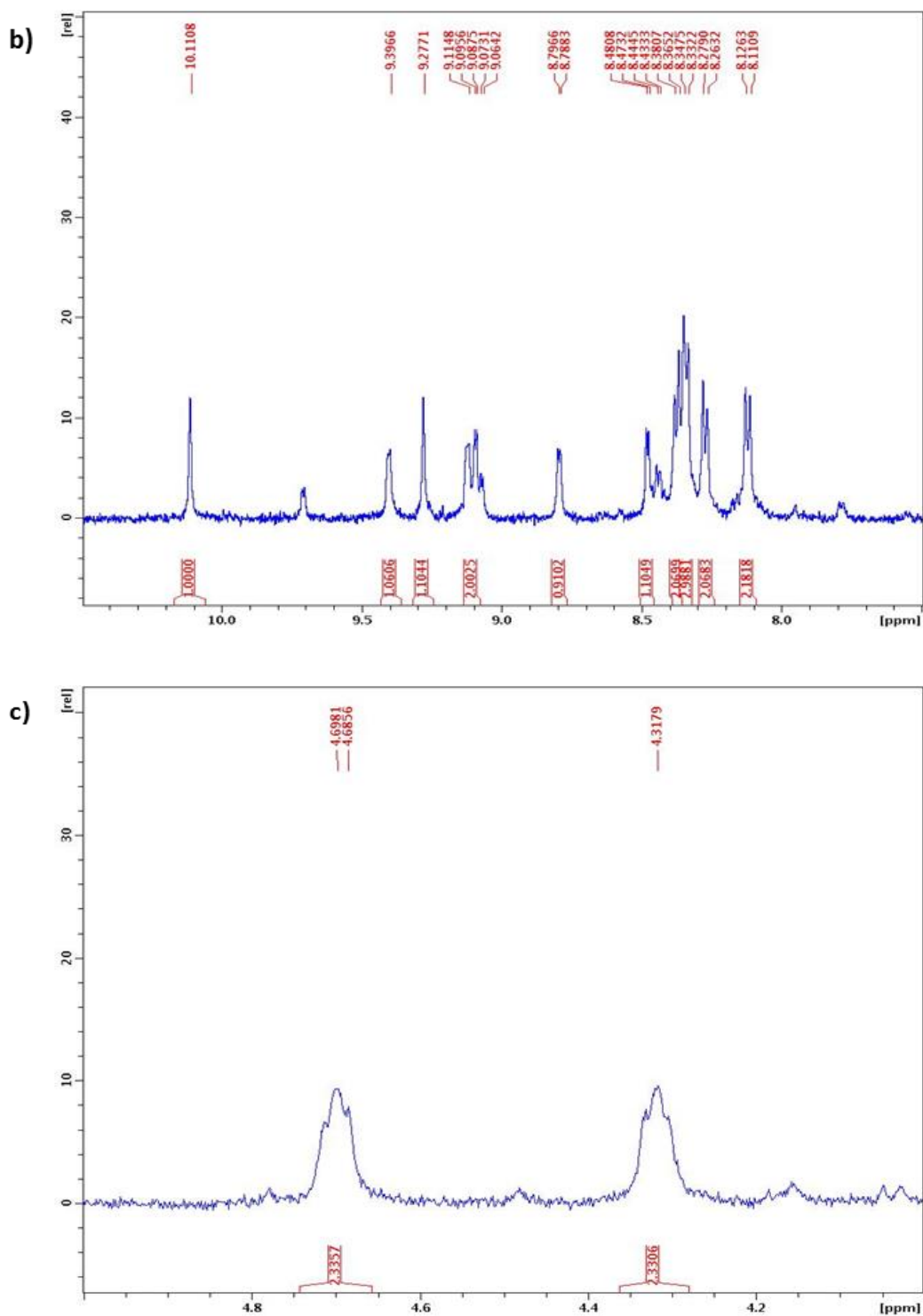


Figure 3-3 (Continued) ^1H NMR spectrum of 5,15-di(p-benzoato)chlorin in DMSO-D_6 . The full spectrum (a) and the expanded view of different portions of the spectrum (b,c) are presented. Reprinted with permission from *J. Am. Chem. Soc.*, **2015**, *137*, 7600–7603. Copyright 2015 American Chemical Society.

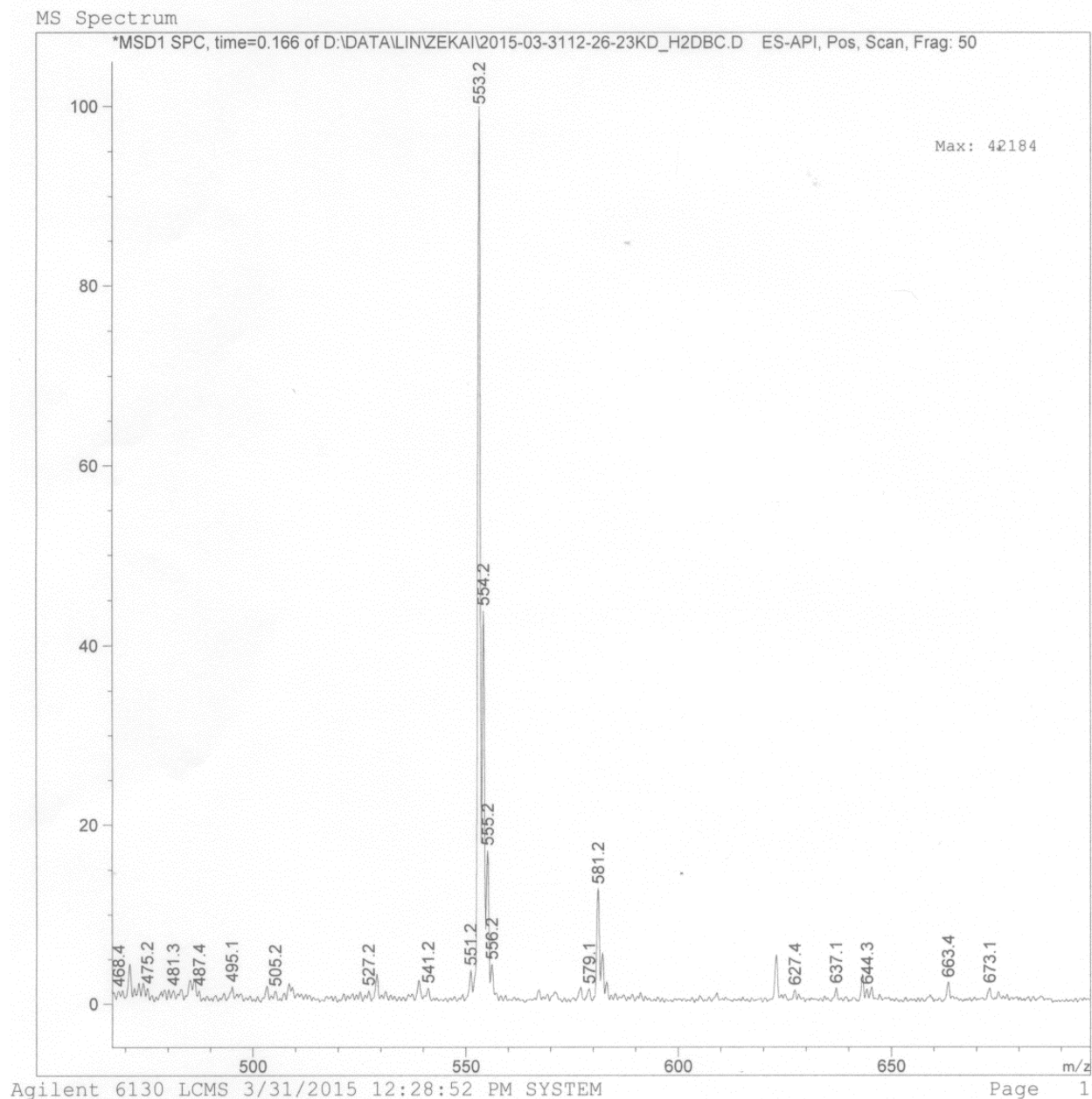


Figure 3-4 ESI-MS of 5,15-di(p-benzoato)chlorin. The sample was prepared in DMSO as a 40 mg/L solution and was delivered by methanol. Reprinted with permission from *J. Am. Chem. Soc.*, **2015**, *137*, 7600–7603. Copyright 2015 American Chemical Society.

3.2.2 Synthesis and characterization of DBC-Hf

A solvothermal reaction between HfCl_4 and H_2DBC in DMF afforded the dark purple powdery product of DBC-Hf. To a 20-mL glass vial was added 3 mL of HfCl_4 solution [2 mg/mL in N,N-dimethylformamide (DMF), 0.018 mmol], 3 mL of the H_2DBC solution (3.5 mg/mL in DMF, 0.018 mmol), and 0.36 mL of acetic acid (6.3 mmol). The reaction mixture was kept in an 80 °C oven for 3 days. The nMOF product was collected by centrifugation and washed with copious amounts of DMF, 1% triethylamine (NEt_3) in ethanol (v/v), and ethanol successively and stored as a stock suspension in ethanol.

Powder X-ray diffraction (PXRD) indicated that DBC-Hf adopts the same UiO-type structure as DBP-Hf, due to the geometric similarity between the DBC and DBP ligands (Figure 3-5a). The $\text{Hf}_6(\mu_3\text{-O})_4(\mu_3\text{-OH})_4$ secondary building units (SBUs) in DBC-Hf are bridged by DBC ligands to construct a UiO framework of $\text{Hf}_6(\mu_3\text{-O})_4(\mu_3\text{-OH})_4(\text{DBC})_6$. The Hf content was determined by inductively coupled plasma-mass spectrometry (ICP-MS, Agilent 7700x, USA) to be 24.0% (23.8% calculated) whereas a DBC weight loss of 64% (72% calculated) was observed in thermogravimetric analysis (Figure 3-5b). The discrepancy of organic weight loss by TGA is presumably a result of the termination of $\text{Hf}_6(\mu_3\text{-O})_4(\mu_3\text{-OH})_4$ SBUs by acetate groups in the ultrathin DBC-Hf nMOF.

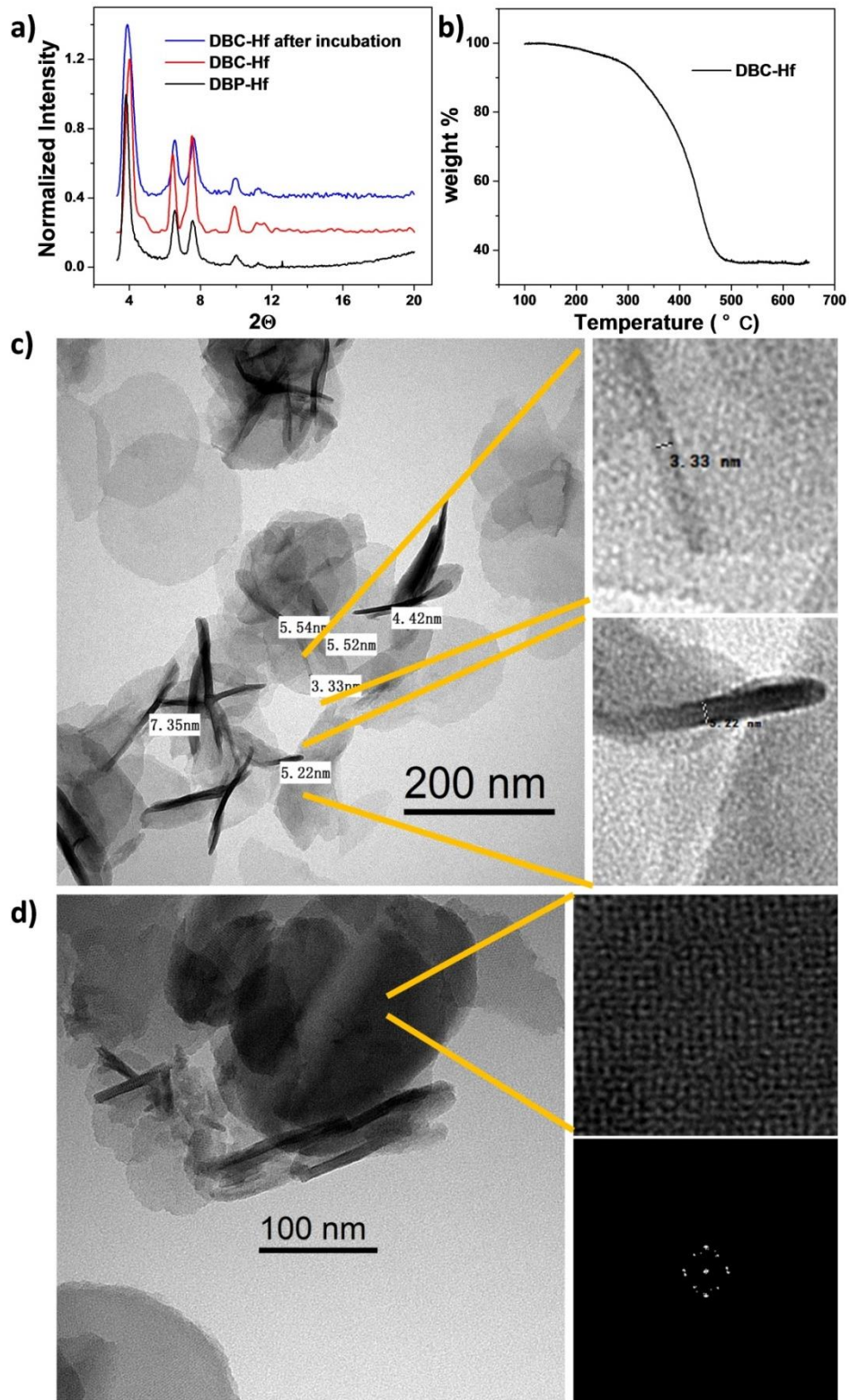


Figure 3-5 Structural characterization of DBC-Hf. (a) PXRD pattern of DBP-Hf and DBC-Hf before and after incubation in cell culture medium. (b) Thermogravimetric analysis of DBC-Hf.

Figure 3-5 (Continued) (c) TEM images of DBC-Hf at different resolutions showing nanoplate morphology and the thickness of the nanoplates lying perpendicular to the grid (left), along with the zoomed-in view of two parts of the image showing the particles constructed from two (top right) or three (bottom right) packing layers. (d) TEM image showing a tilt particle (left) and the zoomed-in view of the particle (top right) and its FFT showing 4-fold symmetry (bottom right). Adapted with permission from *J. Am. Chem. Soc.*, **2015**, *137*, 7600–7603. Copyright 2015 American Chemical Society.

Transmission electron microscopy (TEM) confirms that DBC-Hf adopts a nanoplate morphology similar to that of DBP-Hf (Figure 3-5c). The plate diameters are 100~200 nm, while the thickness varies from 3.3 to 7.5 nm by direct observation of the particles lying perpendicular to the TEM grid (Figure 3-5c,d). Notably, since the calculated distances between neighboring (111) packing layers (d_{111}) of the UiO-type structure are 2.2 nm, the ultra-thin plates consist of only 2-4 sets of (111) packing layers. Such plates are even thinner than DBP-Hf of ~10 nm in thickness, further facilitating the ROS diffusion during PDT. Dynamic light scattering (DLS) measurements of DBC-Hf gave an average diameter of 128.5 nm with a polydispersity index of 0.17 and a ζ potential of -10.2 mV in phosphate buffer saline (PBS) (Figure 3-6).

The stability of DBC-Hf in biological media was confirmed by culturing the nMOF in RPMI 1640 cell culture medium for 12 h. The morphology of nMOFs did not change by TEM (Figure 3-7 a,b), while high resolution TEM images along with their fast-Fourier transform (FFT) patterns indicate the retention of nMOF crystallinity (Figure 3-7 c-f). The PXRD pattern of DBC-Hf did not change after incubation in RPMI 1640 cell medium, further proving the framework stability of DBC-Hf in physiological environments (Figure 1a). (Figure 3-5a).

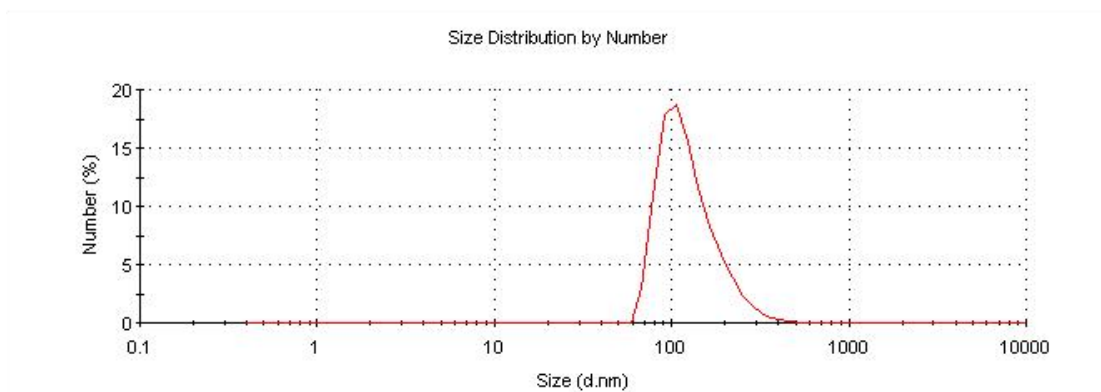


Figure 3-6 DLS plot showing the particle size of DBC-Hf. Adapted with permission from *J. Am. Chem. Soc.*, **2015**, *137*, 7600–7603. Copyright 2015 American Chemical Society.

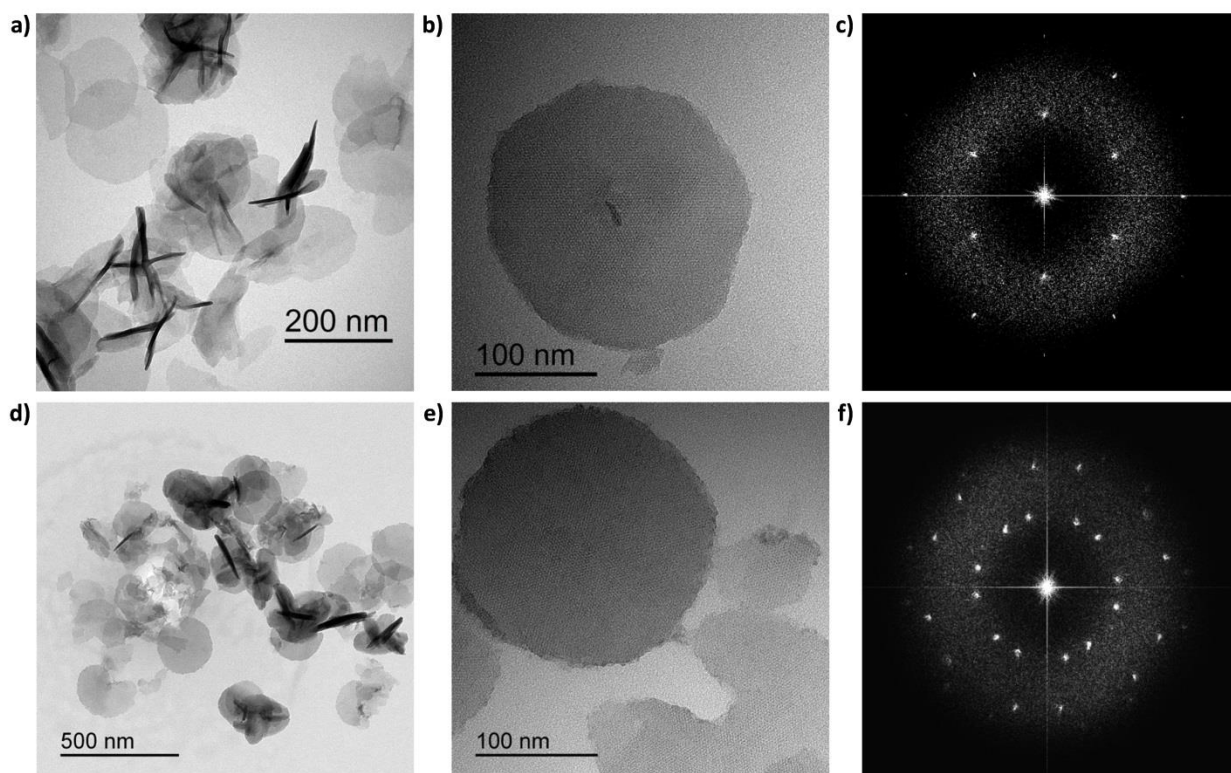


Figure 3-7 TEM images of DBC-Hf at different resolutions before (a-c) and after (d-f) incubation in cell culture medium, along with the corresponding FFT patterns. Adapted with permission from *J. Am. Chem. Soc.*, **2015**, *137*, 7600–7603. Copyright 2015 American Chemical Society.

3.2.3 Photophysics and photochemistry of H₂DBC and DBC-Hf

UV-visible absorption spectroscopy confirmed the improved photophysical properties of chlorin-based PSs (Figure 3-8a). H₂DBC has a split Soret band at $\lambda_{\text{max}}=408$ nm and four Q-bands at 504, 534, 591, and 643 nm. DBC-Hf shows slight red-shifts for all Q-bands compared to H₂DBC, with the peaks at 508, 545, 592, and 646 nm. The lowest energy Q-band of DBC-Hf has thus red-shifted by 13 nm from DBP-Hf, with an ϵ value of $24600 \text{ M}^{-1} \text{ cm}^{-1}$ that is 11-fold greater than that of DBP-Hf. H₂DBC has an ϵ value of $21800 \text{ M}^{-1} \text{ cm}^{-1}$ for the lowest energy Q-band, which is 13-fold greater than that of H₂DBP ($1700 \text{ M}^{-1} \text{ cm}^{-1}$).

The fluorescence peak of H₂DBC shows up majorly at ~641 nm, with a weak peak at ~700 nm (Figure 3-8b). The DBC-Hf fluorescence was ~200 fold weaker than H₂DBC, similar to the case of DBP-Hf and H₂DBP, due to an enhanced intersystem crossing upon coordination of DBC ligands to Hf⁴⁺ ions via the carboxylate groups. Consistent with this, DBC-Hf has a slightly shorter fluorescence lifetime of 7.88 ns compared to H₂DBC (8.15 ns) by Time-Correlated Single Photon Counting measurements (Figure 3-8c and Table 3-1).

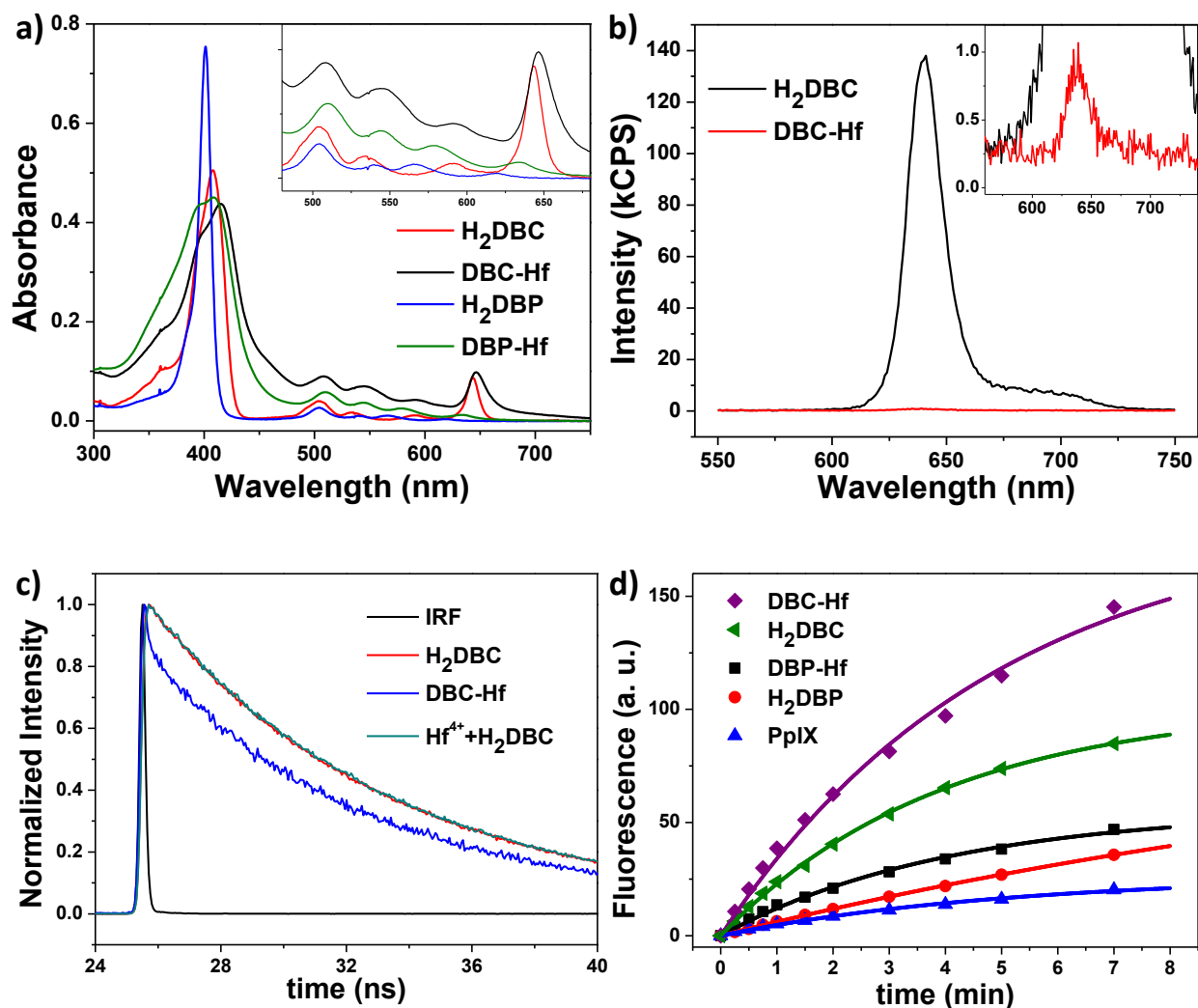


Figure 3-8 Photophysical and photochemical properties of H₂DBC and DBC-Hf. (a) UV-vis absorption spectra of H₂DBC, DBC-Hf, H₂DBP and DBP-Hf in DMF or 0.67 mM PBS. (b) Steady-state fluorescence of 1 μ M H₂DBC and DBC-Hf in aqueous solutions. (c) Time-resolved fluorescence decay traces of H₂DBC, DBC-Hf and a mixture solution of HfCl₄ and H₂DBC as a control in HBSS, together with instrument response function (excitation/emission 408/640 nm). (d) ¹O₂ generation of DBC-Hf, H₂DBC, DBP-Hf, H₂DBP and PpIX at an irradiance of 0.1 W/cm². DBC-Hf and H₂DBC are irradiated with a 650 nm LED, while the others are irradiated with a 640 nm LED. The dots are experimental data and the solid lines are fitted curves. Adapted with permission from *J. Am. Chem. Soc.*, **2015**, *137*, 7600–7603. Copyright 2015 American Chemical Society.

Table 3-1 Fluorescence lifetimes of H₂DBC, DBC-Hf and HfCl₄+H₂DBC control, fitted by software.

sample	τ_1 (ns)	τ_2 (ns)	τ_3 (ns)	$\bar{\tau}$ (ns)
IRF	0.0086	N/A	N/A	N/A
H ₂ DBC	5.80	8.77	N/A	8.15
DBC-Hf	3.27	8.26	0.14	7.88*
HfCl ₄ +DBC	6.12	8.78	N/A	8.13

* The average lifetimes are fitted with only τ_1 and τ_2 , since the τ_3 of this set is likely from scattering.

Singlet Oxygen Sensor Green (SOSG) was employed to determine ¹O₂ generation efficiencies of H₂DBC and DBC-Hf. The fluorescence of SOSG response to ¹O₂ ($\lambda_{\text{ex}} = 504$ nm, $\lambda_{\text{em}} = 525$ nm) was quantified with a fluorimeter. For comparison, ¹O₂ generation efficiency of H₂DBP, DBP-Hf and protoporphyrin IX (PpIX) were also determined. The fluorescence plotted against irradiation time was fitted with an exponential function (Eq 1), indicating a pseudo first-order ¹O₂ generation process (Figure 3-8d). For detailed discussion on the fitting model see chapter 2.

$$I_F = A(1 - e^{-kt}) \quad (\text{Eq 1})$$

Where I_F is fluorescence intensity and t is irradiation time while A and k are fitting parameters (Table 3-2). The total ¹O₂ generation yield was normalized based on that of PpIX to compare the overall photosensitization efficiency. DBC-Hf is ~3 times as efficient as DBP-Hf in generating ¹O₂.

Table 3-2 Fitting parameters for $^1\text{O}_2$ generation curves.

	A	k (min ⁻¹)	Normalized yield
H ₂ DBC	102	0.25	4.3
DBC-Hf	195	0.18	7.3
H ₂ DBP	101	0.06	1.8
DBP-Hf	55.9	0.24	2.4
PpIX	26.6	0.19	1

One of the drawbacks of chlorins comparing to porphyrins is the faster photodegradation.⁵ The photobleaching of DBC-Hf and H₂DBC were monitored under LED irradiation (100 mW/cm², 650 nm, Figure 3-9). Solutions of 7.5 μM ligand or DBP-Hf (base on ligand concentration) were irradiated for 0, 0.5, 1, 2, 3, 5, 7 and 9 minutes and the concentrations were calculated from the characteristic absorption of chlorin species at ~ 650 nm (Figure 3-9a,b). DBC-Hf degraded much slower than the ligand: 87% of DBC-Hf absorption was preserved after 9 min irradiation (54 J/cm² total light dose), comparing to 76% for H₂DBC (Figure 3-9c) under the same conditions. The improved photostability of DBC-Hf is attributed to the rigidification and isolation of the PSs in the nMOF structure. In comparison, DBP-Hf is even less sensitive to light: after 10 min irradiation at 640 nm (60 J/cm² light dose) over 98% of Soret band absorption was retained (Figure 3-9d).

During synthesis of the H₂DBC ligand, we also acquired the bacteriochlorin byproduct, 5,15-di(p-methylbenzoato)bacteriochlorin (Me₂DBB). Bacteriochlorins have strong Q-band absorption at ~ 735 nm, which should be perfect for light penetration for PDT application. Unfortunately, the rapid photobleaching of bacteriochlorins hinders the practical PDT applications that no bacteriochlorin products have been developed to the clinic.⁵ After isolating Me₂DBB by column chromatography, we prepared it into dichloromethane solution and monitored the absorbance at 735 nm upon LED irradiation (100 mW/cm², 740 nm, Figure 3-9e).

With only 2 minute irradiation (12 J/cm^2 light dose) over 90% of Me_2DBB degraded (Figure 3-9f). Due to the unstable nature of the bacteriochlorin upon light irradiation, we abandoned the efforts to grow DBB-based nMOFs.

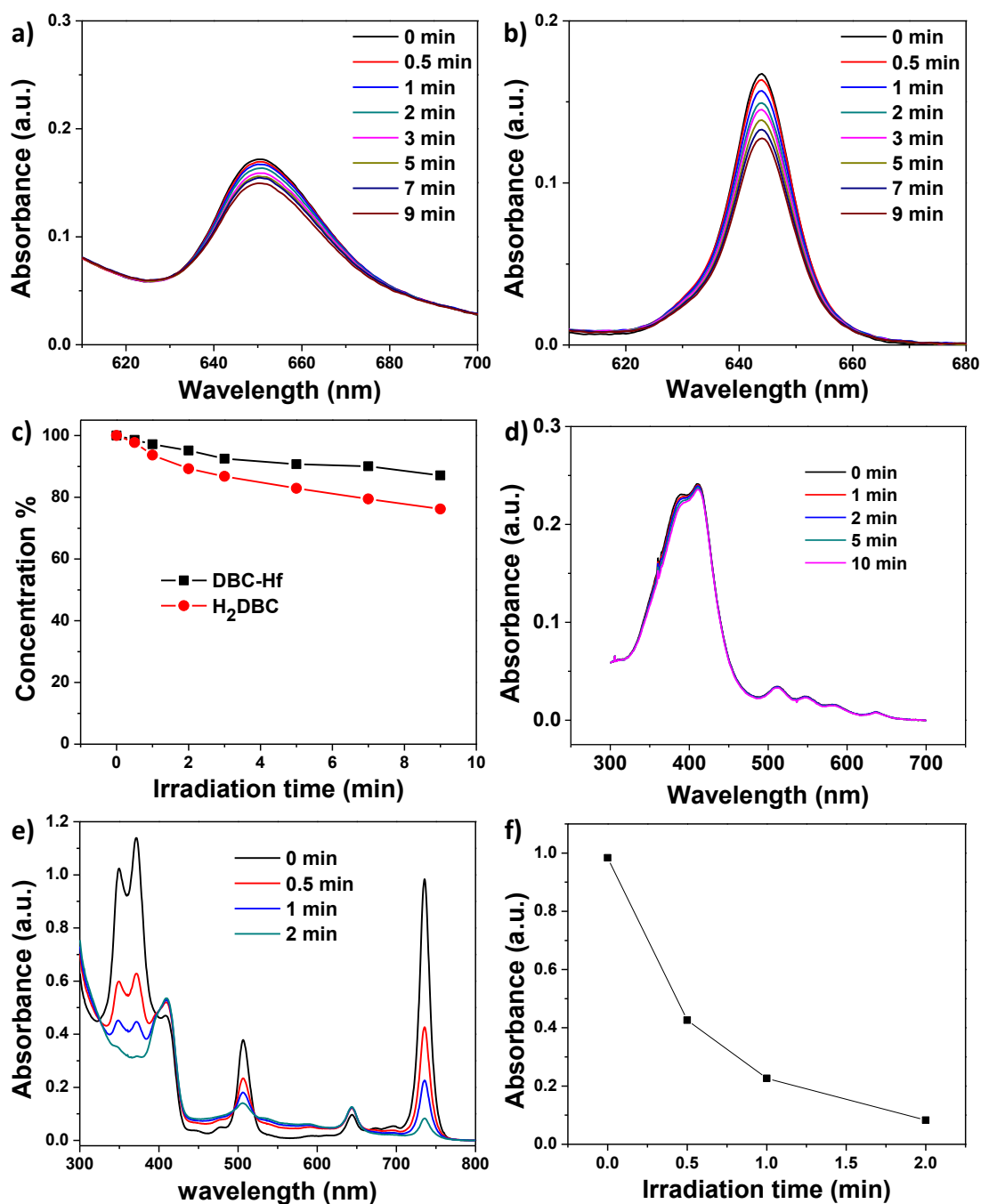


Figure 3-9 Photostability of DBC-Hf, H_2DBC , DBP-Hf, and Me_2DBB . The photobleaching of DBC-Hf (a) and H_2DBC (b) upon LED irradiation. (c) The dependence of the chlorin concentration of both DBC-Hf and H_2DBC on the irradiation time.

Figure 3-9 (Continued) (d) The photobleaching of DBP-Hf upon 640 nm LED irradiation. (e) The photobleaching of Me₂DBB upon 740 nm LED irradiation. (f) The dependence of the bacteriochlorin concentration of Me₂DBB on the irradiation time. Adapted with permission from *J. Am. Chem. Soc.*, **2015**, *137*, 7600–7603. Copyright 2015 American Chemical Society.

3.2.4 *In vitro* and *in vivo* studies

PDT is used in the clinic to treat colon cancer by delivering light through endoscope.^{6,7} It is also known that PDT treatment of primary colon tumors can elicit immunogenic response on metastatic tumors.⁸⁻¹⁰ Encouraged by the improved photophysical properties and increased ¹O₂ generation efficiency of DBC-Hf, we further tested its PDT efficacy against murine and human colorectal cancers in mouse models.

The tumor cell uptake of nMOFs was evaluated by incubating CT26 cells with DBP-Hf or DBC-Hf for 4 h (equivalent Hf concentrations of 50 μM). The Hf contents in CT26 cells were determined to be (3.44±0.13) and (2.35±0.08) nmol/10⁵ cells for DBP-Hf and DBC-Hf, respectively, by ICP-MS. We also compared the cellular uptake of DBC-Hf and H₂DBC in terms of ligand concentrations by UV-vis analysis in CT26 and HT29 (Figure 3-10). The cellular uptake amounts of DBC-Hf and H₂DBC in terms of ligand concentrations were (13.7±0.8) and (20.2±1.7) nmol/10⁶ cells in HT29 cells (Figure 3-10a) and (4.9±0.4) and (0.6±0.1) nmol/10⁶ cells in CT26 cells (Figure 3-10b).

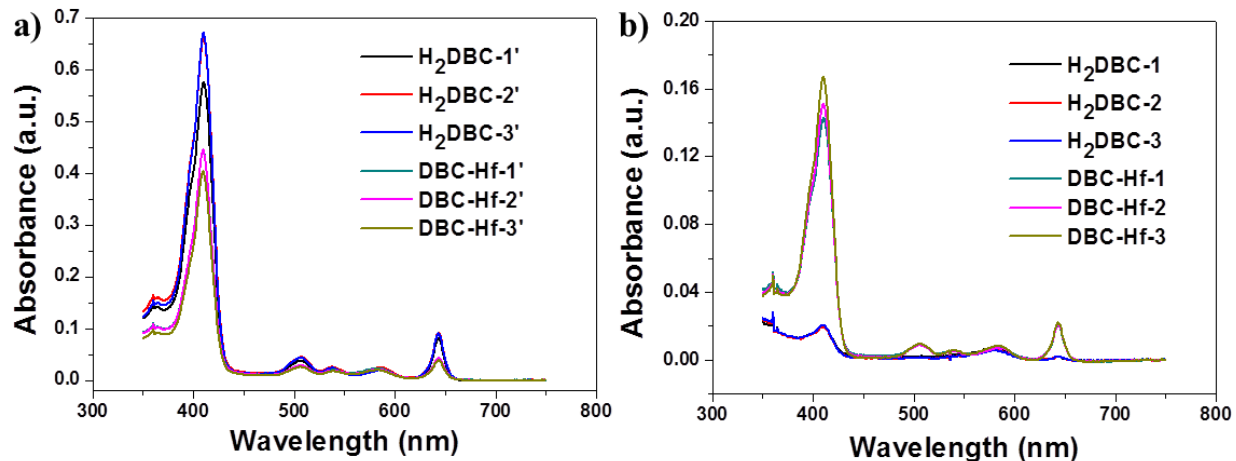


Figure 3-10 Cellular uptake evaluation of H₂DBC and DBC-Hf in HT29 (a) or CT26 (b) cells. Adapted with permission from *J. Am. Chem. Soc.*, **2015**, *137*, 7600–7603. Copyright 2015 American Chemical Society.

The *in vitro* PDT efficacy of DBC-Hf against colon cancer cells were investigated and compared with DBP-Hf and their corresponding free ligands. The nMOFs or free ligands were incubated with CT26 or HT29 cells at various concentrations, and the cells were irradiated with LED light at a total light dose of 90 J/cm². DBC-Hf outperformed DBP-Hf by effectively killing both cancer cell lines at low nMOF and light doses (Figure 3-11). Free ligand treated groups also showed moderate PDT efficacy, while no cytotoxicity was observed in dark control or PBS control groups. The IC₅₀ values of DBC-Hf, H₂DBC, DBP-Hf, and H₂DBP in CT26 cells with irradiation were calculated to be 5.1±0.2, 8.5±0.1, 10.4±0.5, and 20.0±3.1 μM (by ligand concentrations), respectively. The IC₅₀ values of DBC-Hf, H₂DBC, DBP-Hf, and H₂DBP in HT29 cells with irradiation were calculated to be 6.0±1.5, 7.5±2.3, 13.1±2.2, and 17.0±4.0 μM, respectively. These results confirm that DBC-Hf is a more potent PS than DBP-Hf in PDT owing to the enhanced photophysical properties. DBC-Hf showed efficient PDT cytotoxicity in murine

macrophage Raw264.7 cells, but higher ligand concentration ($> 20 \mu\text{M}$) was required to achieve 50% cell killing (Figure 3-11c).

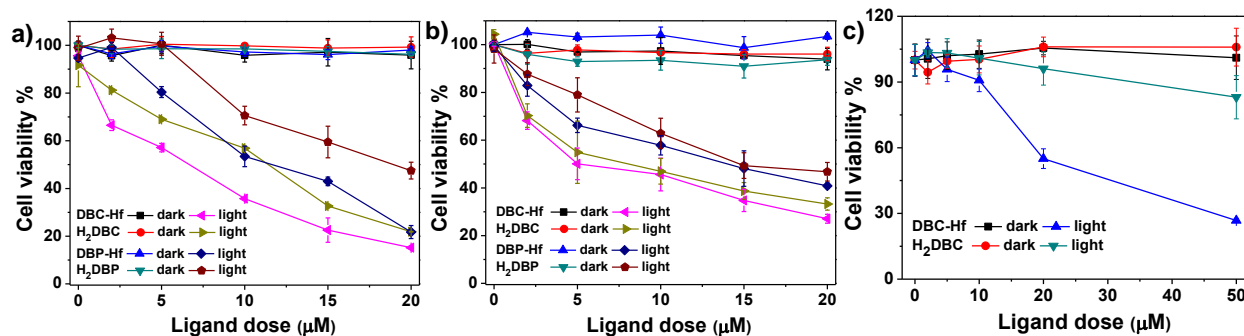


Figure 3-11 *In vitro* PDT efficacies on different cell lines. PDT cytotoxicity of DBC-Hf, H₂DBC, DBP-Hf, and H₂DBP at different PS concentrations in CT26 cells (a) and HT29 cells (b). (c) *In vitro* PDT cytotoxicity of DBC-Hf and H₂DBC at different PS concentrations in murine macrophage Raw 264.7 cells. Adapted with permission from *J. Am. Chem. Soc.*, **2015**, *137*, 7600–7603. Copyright 2015 American Chemical Society.

We further studied the mechanism of PDT cytotoxicity of the DBC-Hf nMOF and the ligand. CT26 cells were incubated with $5 \mu\text{M}$ DBC-Hf or H₂DBC followed by light irradiation at 0.1 W/cm^2 for 15 min (90 J/cm^2). The apoptosis induced by PDT treatment was determined with the Alexa Fluor 488 Annexin V/dead cell apoptosis kit by flow cytometry. No apoptosis or necrosis was observed for cells treated with DBC-Hf or H₂DBC in the dark while significant amounts of cells underwent apoptosis when treated with DBC-Hf or H₂DBC upon light irradiation (Figure 3-12). Calreticulin (CRT) is a distinct biomarker exposed on the surface of cells undergoing immunogenic cell death (ICD).¹¹ The CRT expression was determined by flow cytometry and immunofluorescence to assess the ICD induced by PDT with DBC-Hf (Figure 3-13). Cells treated with DBC-Hf or H₂DBC without light irradiation showed no surface CRT expression

while significant amounts of CRT were detected on the surface of cells upon irradiation. Both apoptosis and ICD therefore contribute to the superior *in vitro* PDT efficacy of DBC-Hf.

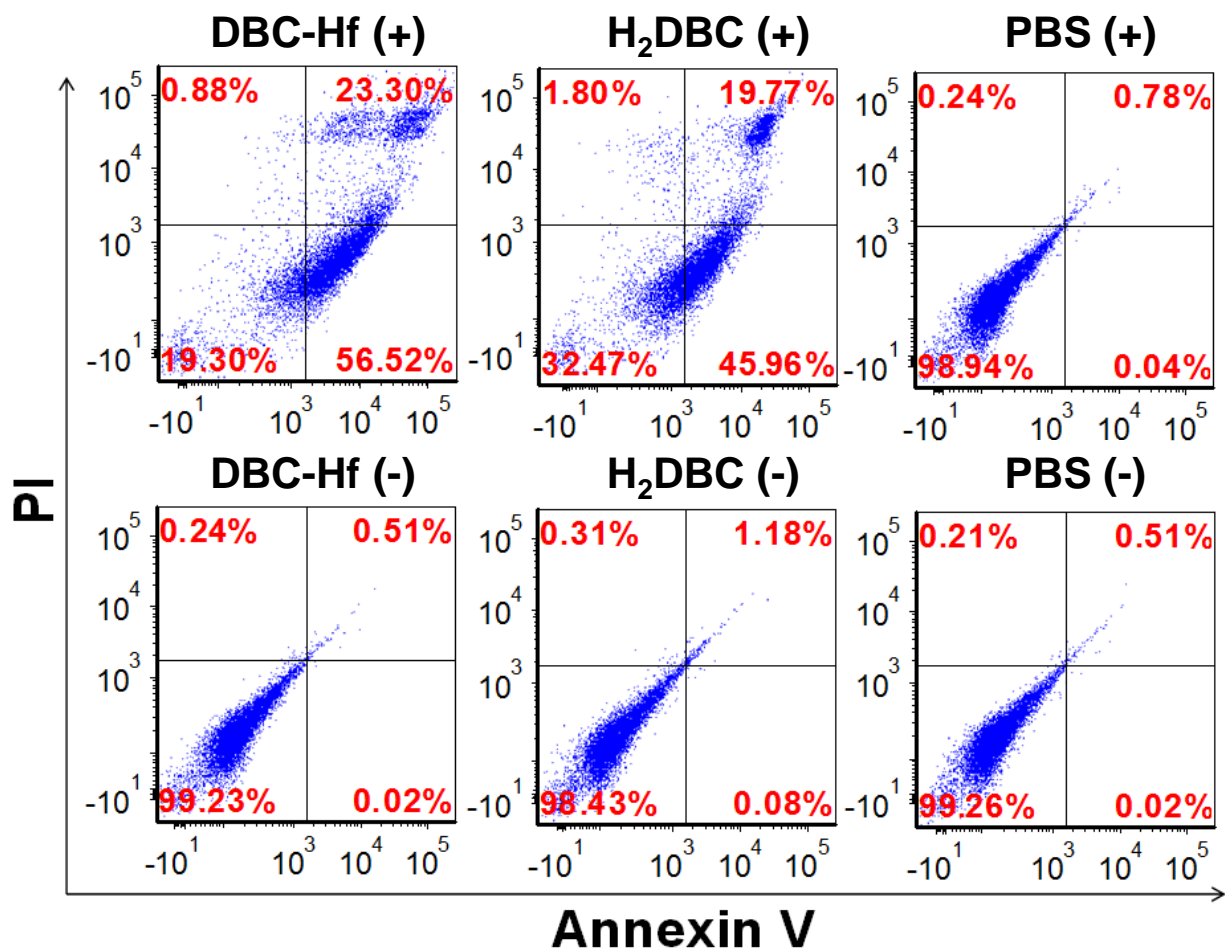


Figure 3-12 Annexin V/PI analysis of CT26 cells incubated with DBC-Hf, H₂DBC or PBS with or without irradiation (90 J/cm²). The quadrants from lower left to upper left (counter clockwise) represent healthy, early apoptotic, late apoptotic, and necrotic cells, respectively. The percentage of cells in each quadrant was shown on the graphs. (+) and (-) refer to with and without irradiation, respectively. Adapted with permission from *J. Am. Chem. Soc.*, **2015**, *137*, 7600–7603. Copyright 2015 American Chemical Society.

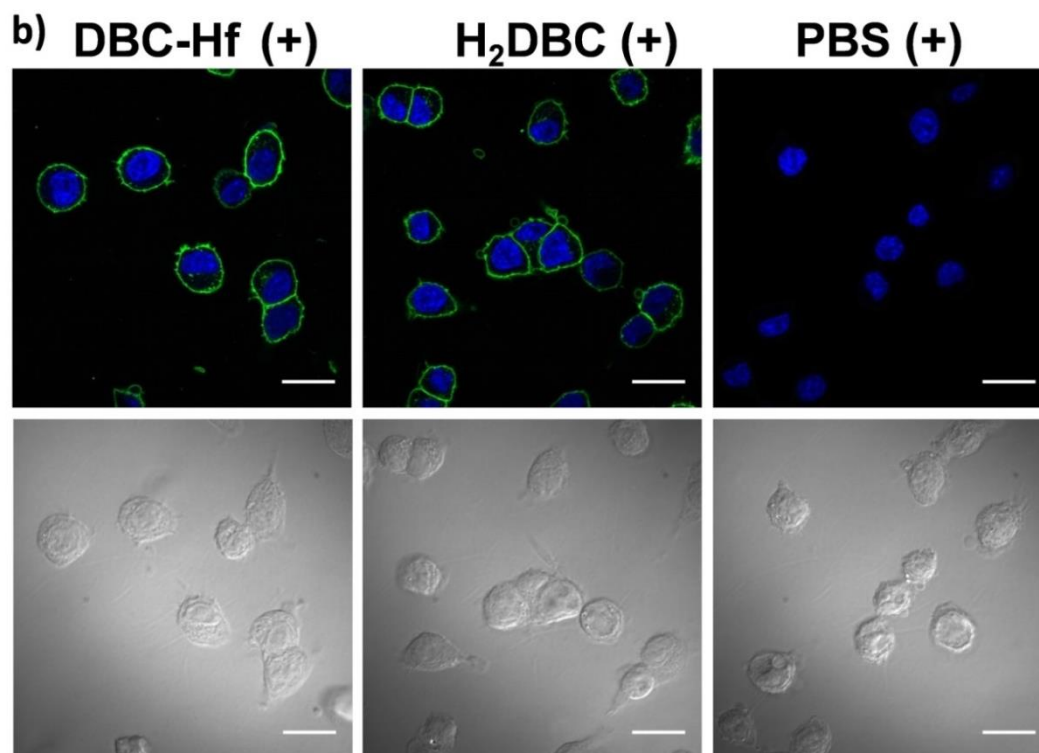
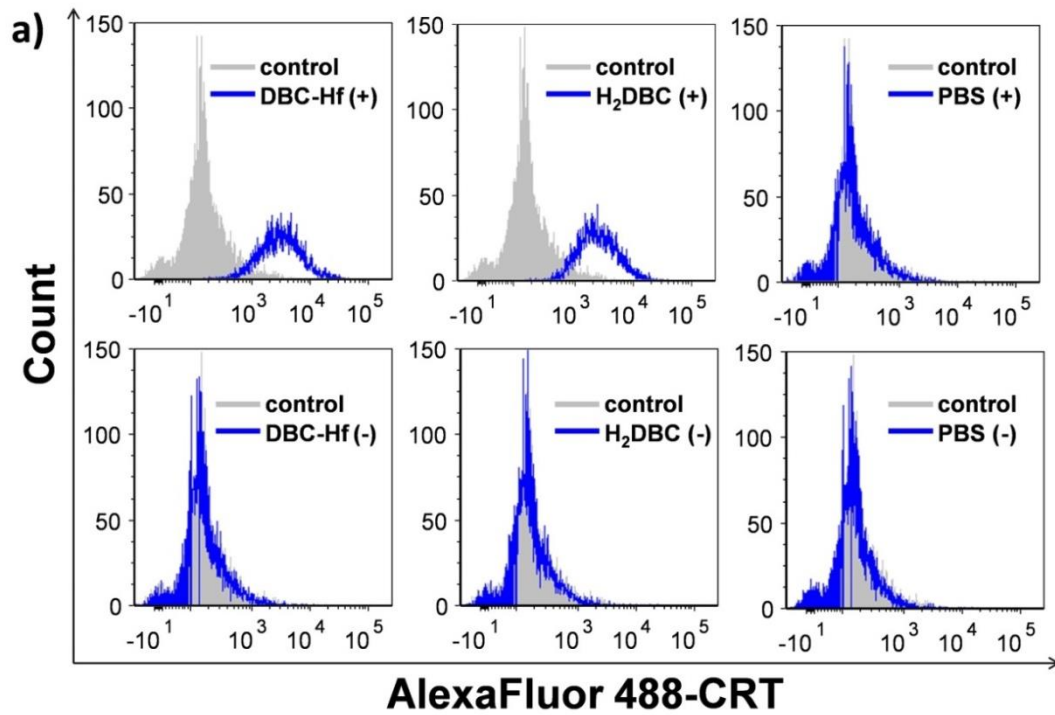


Figure 3-13 Immunogenic cell death detection. (a) CRT exposure on the cell surface of CT26 cells was assessed after incubation with DBC-Hf, H₂DBC or PBS with or without light irradiation (90 J/cm²) by flow cytometry analysis. The fluorescence intensity was gated on PI-negative cells.

Figure 3-13 (Continued) (b) Immunofluorescence microscopy of CRT expression on the cell surface of CT26 cells treated with DBC-Hf, H₂DBC and PBS upon irradiation (90 J/cm²). Blue: DAPI stained nuclei; Green: Alexa Fluor 488-CRT antibody. Bar=20 μm. Adapted with permission from *J. Am. Chem. Soc.*, **2015**, *137*, 7600–7603. Copyright 2015 American Chemical Society.

We carried out *in vivo* anticancer efficacy experiments on subcutaneous flank tumor mouse models of CT26 and HT29. The mice were intratumorally injected with (1) PBS control, (2) DBC-Hf, (3) DBP-Hf, (4) H₂DBC, or (5) H₂DBP at a ligand dose of 1 mg/kg or (6) DBC-Hf at a ligand dose of 3.5 mg/kg. As depicted in Figure 3-14 and 3-15, the tumor growth of mice treated with DBC-Hf (1 mg/kg DBC dose) was effectively inhibited in both models. DBP-Hf and the two PS ligands failed to suppress the tumor growth in either model, due to low PS and light doses. Higher doses of DBC-Hf and light irradiation led to effective tumor regression in HT29 with single treatment and in CT26 with two treatments (Figure 3-14a and 3-15a). The weights and sizes of tumors treated with DBC-Hf at the endpoint were also significantly smaller than the other groups (Figure 3-14 b,d and 3-15 b,d). Histology of frozen tumor slices further confirmed that only DBC-Hf treatment caused apoptosis/necrosis of tumors but not in DBP-Hf or the two PS ligands (Figure 3-16). Along with the *in vitro* PDT results, the superior anticancer efficacies achieved by DBC-Hf in both colorectal cancer models indicate that DBC-Hf is a more efficient photosensitizer than DBP-Hf.

The statistical analysis of tumor weights was run by two-way T-test. For CT26 model, the *P* values of DBC-Hf, DBC-Hf (higher dose), DBP-Hf, H₂DBC, and H₂DBP vs. PBS are 1×10^{-5} , 4×10^{-6} , 0.20656, 0.06635, and 0.43296, respectively. For HT29 model, the *P* values of DBC-Hf, DBC-Hf (higher dose), DBP-Hf, H₂DBC, and H₂DBP vs. PBS are 5×10^{-7} , 8×10^{-9} , 0.43374, 0.07042, and 0.15008, respectively. Significant difference of tumor weights was only observed

between DBC-Hf and PBS control group. DBC-Hf with higher doses of nMOF and light irradiation led to successful tumor regression in both models.

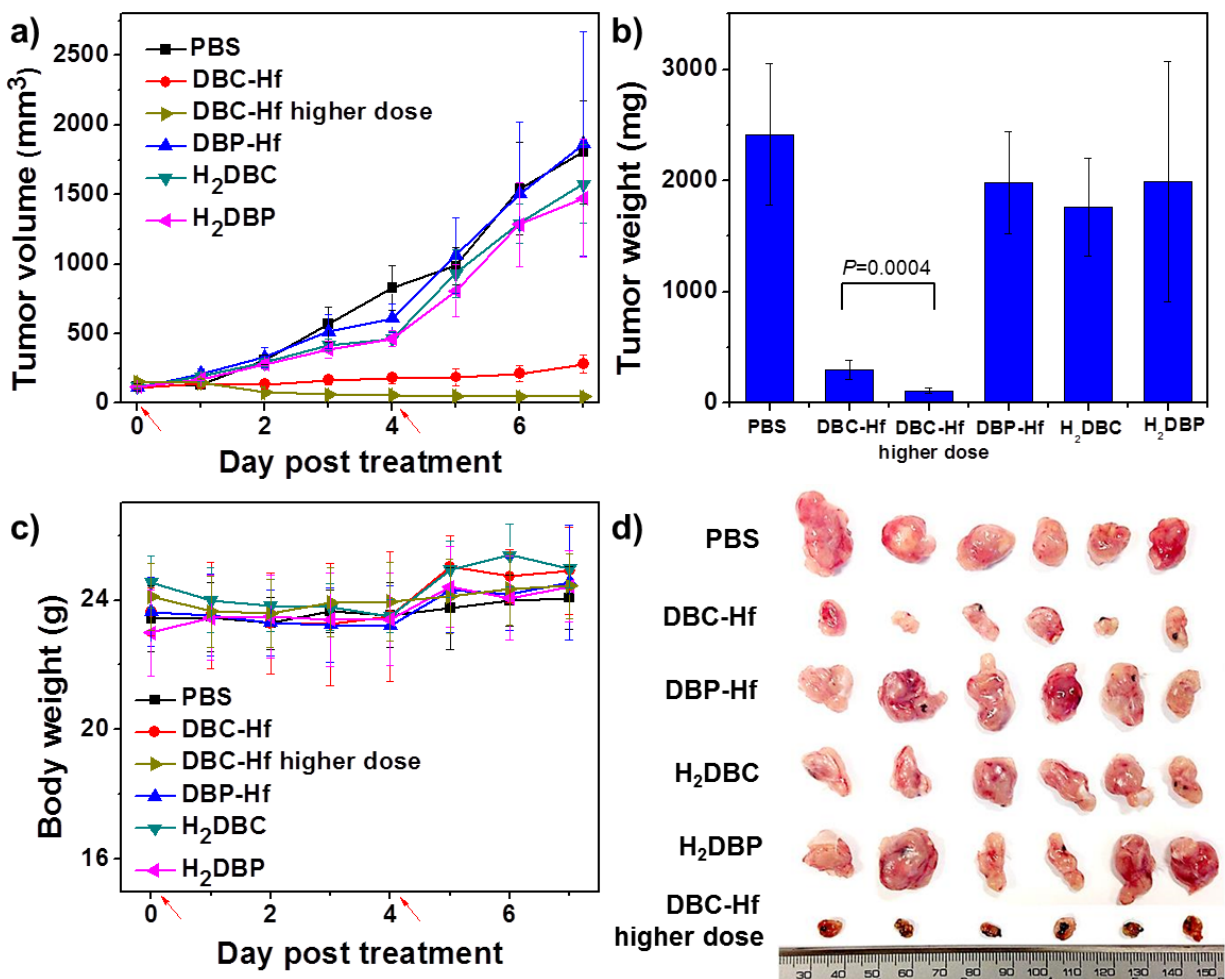


Figure 3-14 *In vivo* PDT efficacy on CT26 mouse tumor model. (a) Tumor growth inhibition curves after PDT treatment. Red arrows refer to treatment time points. (b) Tumor weights after PDT treatment. (c) Body weight evolution of CT26 tumor bearing BALB/c mice treated with nMOFs or ligands ($n=6$). (d) Photos of excised tumors of each group after PDT treatment. Adapted with permission from *J. Am. Chem. Soc.*, **2015**, *137*, 7600–7603. Copyright 2015 American Chemical Society.

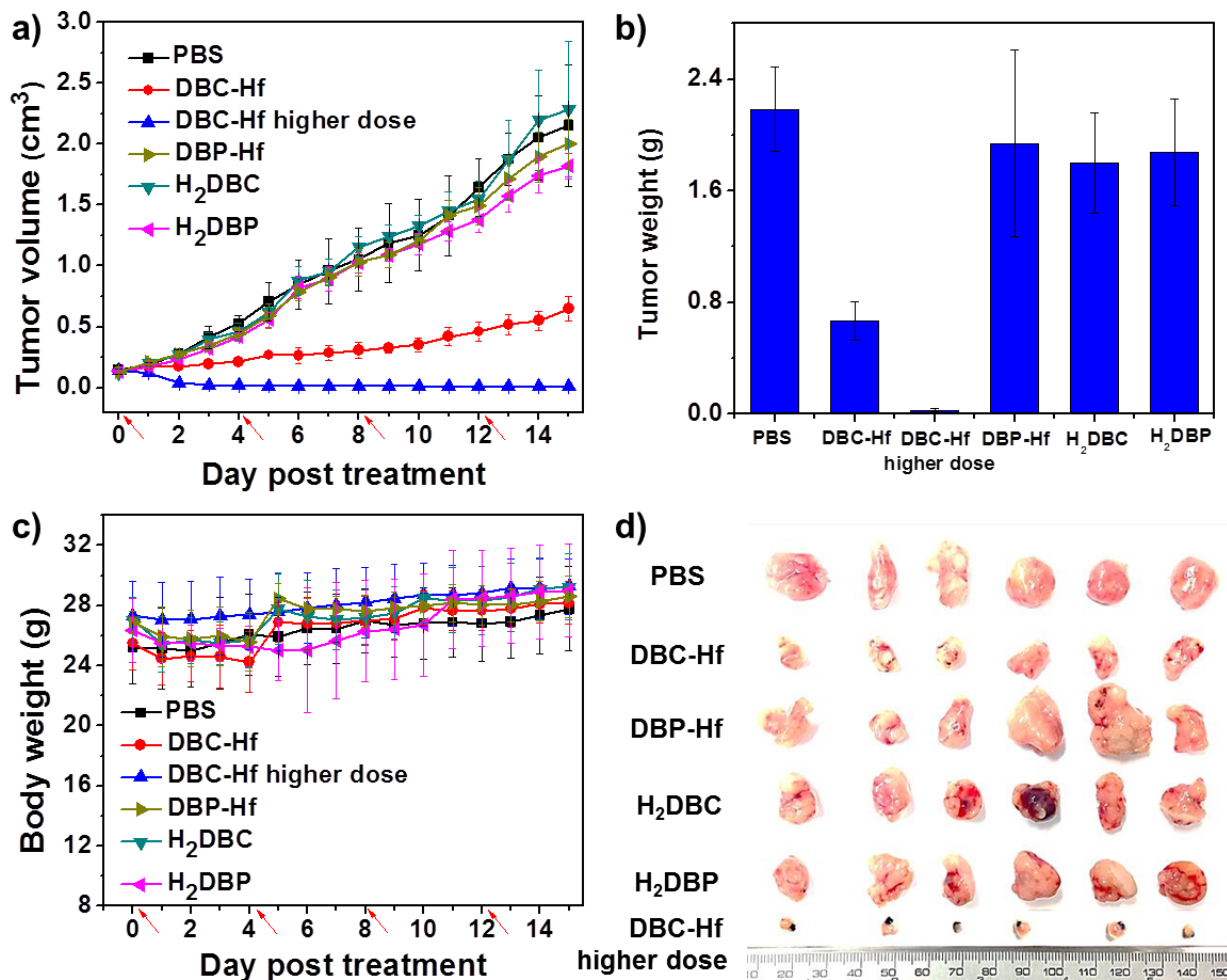


Figure 3-15 *In vivo* PDT efficacy on HT29 subcutaneous xenograft mouse model. (a) Tumor growth inhibition curves after PDT treatment. Red arrows refer to treatment time points. (b) Tumor weights after PDT treatment. (c) Body weight evolution of HT29 tumor bearing nude mice treated with nMOFs or ligands (n=6). (d) Photos of excised tumors of each group after PDT treatment. Adapted with permission from *J. Am. Chem. Soc.*, **2015**, *137*, 7600–7603. Copyright 2015 American Chemical Society.

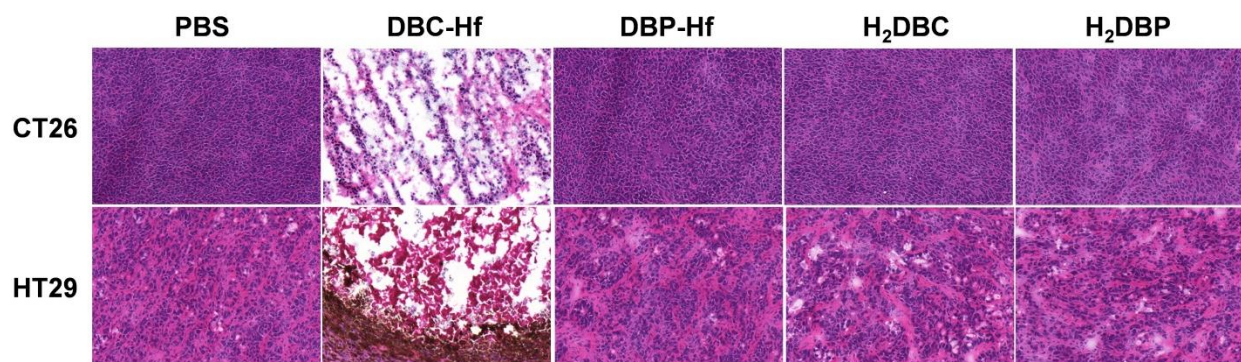


Figure 3-16 Histology of frozen tumor tissue slices after H-E staining. Bar=100 μm . Adapted with permission from *J. Am. Chem. Soc.*, **2015**, *137*, 7600–7603. Copyright 2015 American Chemical Society.

Table 3-3 Statistical analysis of tumor weights by t-test shown with P values.

	CT26 tumor model	HT29 tumor model
DBC-Hf vs. PBS	0.00001	0.0000005
DBP-Hf vs. PBS	0.20656	0.43374
H ₂ DBC vs. PBS	0.06635	0.07042
H ₂ DBP vs. PBS	0.43296	0.15008
DBC-Hf (higher dose) vs. DBC-Hf	0.000004	0.000000008
DBC-Hf vs. DBC-Hf (higher dose)	0.000441	0.000000054

3.3 Conclusion

In this chapter, we have rationally designed the first chlorin-based nMOF, DBC-Hf, with an exceptionally high PS loading, crystallinity, framework stability, porosity, nanoplate morphology, and enhanced intersystem crossing. Importantly, DBC-Hf exhibits a 13 nm red-shift and an 11-fold extinction coefficient increase in the lowest energy Q-band when compared to the previously generation DBP-Hf. As a result, DBC-Hf is three times as efficient as DBP-Hf in generating ¹O₂ and exhibits much higher PDT cytotoxicity in two colon cancer cell lines. The

superior anticancer efficacy of DBC-Hf compared to DBP-Hf was also demonstrated in two colorectal adenocarcinoma mouse models. We further elucidated that both apoptosis and immunogenic cell death contribute to the anticancer efficacy induced by DBC-Hf based PDT. nMOFs thus provide an excellent platform for achieving highly efficient PDT via both apoptosis and immunogenic cell death, and represent a novel class of nanomedicine with significant potential for clinical translation.^{12,13}

3.4 Methods

Digestion for ICP-MS: The nMOF sample was dried on vacuum overnight before being digested by a mixture of concentrate nitric acid and hydrofluoric acid (63% HF/69% HNO₃ 1/100 v/v). The sample was diluted with 2% nitric acid to a total MOF concentration of 80 ppb.

Thermalgravimetric analysis: Thermogravimetric analysis on DBC-Hf nMOF was carried out on Shimadzu TGA-50 thermogravimetric analyzer. The nMOF was collected by centrifugation and dried on the vacuum overnight. The sample was then transferred to a platinum plate and heated at 3 °C/min to 650 °C in air. The weight percentage was plotted against temperature and was normalized to the weight at 100 °C to eliminate the influence of absorbed moisture.

Fluorescence measurement: The fluorescence spectra of H₂DBC ligand and DBC-Hf were taken on a spectrofluorophotometer (Fluorolog-3, Horiba, Japan). H₂DBC was prepared into 1 μM solution in phosphate buffer saline and DBC-Hf was suspended in water to 1 μM by equivalent ligand concentration for the measurement.

Fluorescence lifetime measurement: Time-domain lifetimes were measured on a ChronosBH lifetime fluorometer (ISS, Inc.) using Time-Correlated Single Photon Counting (TCSPC) methods. The fluorometer contained Becker-Hickl SPC-130 detection electronics and an HPM-100-40 Hybrid PMT detector. Excitation was provided by a 403 nm picosecond pulsed laser source (Hamamatsu PLP-10). Emission wavelengths were selected with interference filters (Semrock). The Instrument Response Function (IRF) was measured to be approximately 0.009 ns FWHM in a 1% scattering solution of Ludox LS colloidal silica. Multi-component exponential decay lifetimes were fit via a forward convolution method in the Vinci control and analysis software. DBC-Hf, H₂DBC and a control mixture of HfCl₄ and H₂DBC were prepared into solution/suspensions in Hank's Balanced Saline Solution (HBSS) for the measurement.

Singlet Oxygen generation test: A light-emitting diode (LED) array with peak emission at 650 nm was used as the light source of singlet oxygen generation test for H₂DBC and DBC-Hf while a 640 nm LED was used on H₂DBP, DBP-Hf and protoporphyrin IX (PpIX) samples. The irradiance of LEDs are 100 mW/cm². Singlet Oxygen Sensor Green (SOSG) reagent (Life Technologies) was employed for the detection of singlet oxygen. H₂DBC, DBC-Hf, H₂DBP, DBP-Hf and PpIX samples were prepared in 1 μM solutions/suspensions in diluted HBSS buffer (for DBC-Hf and DBP-Hf, the concentration was calculated as ligand equivalents). To 2 mL each of these solutions/suspensions, SOSG stock solution (5 μL at 5 mM) was added (final concentration=12.5 μM) before fluorescence measurement.

For a typical measurement, fluorescence intensity was acquired on a spectrofluorophotometer (RF-5301PC, Shimadzu, Japan) with excitation at 504 nm and emission at 525 nm (slit width 1.5 nm/3 nm for ex/em). Fluorescence was measured after irradiation by LED for 0 (as background), 15 s, 30 s, 45 s, 1 min, 1.5 min, 2 min, 3 min, 4 min, 5 min and 7 min.

Cellular uptake evaluation: DBP-Hf or DBC-Hf was incubated with CT26 cells at a Hf concentration of 50 μM for 4 h. The cells were collected, counted with a hemocytometer, and digested by concentrated nitric acid. The cellular uptake amounts of Hf were determined by ICP-MS and normalized with cell numbers.

H₂DBC or DBC-Hf was incubated with CT26 cells or HT29 cells at a ligand concentration of 5 μM for 4 h. The cells were collected, counted with a hemocytometer, redispersed in saturated K₃PO₄ aqueous solution, and homogenized with an ultrasound probe. The ligand was further extracted by DMSO followed by centrifugation. The upper phase (organic) was isolated and diluted before UV-vis determination of the ligand concentrations.

***In vitro* cytotoxicity:** The cytotoxicity of DBC-Hf, H₂DBC, DBP-Hf, and H₂DBP was evaluated in murine colorectal cancer cell CT26 and human colorectal cancer cell HT29 cells, respectively. CT26 cells and HT29 cells were seeded on 96-well plates at 1000 cells/well and 2500 cells/well, respectively. The cells were treated with DBC-Hf, H₂DBC, DBP-Hf, and H₂DBP at various ligand concentrations (2, 5, 10, and 20 μM base on ligand concentrations). A further incubation of 4 h was allowed followed by replacing the culture medium with 100 μL of fresh RPMI 1640 medium. The cells were irradiated with LED light (650 nm for DBC-Hf and H₂DBC; 640 nm for DBP-Hf and H₂DBP) at 100 mW/cm² for 15 min (total light dose 90 J/cm²) or kept in dark, respectively. The cells were further incubated to achieve a total incubation time of 72 h. The cell viability was detected by (3-(4,5-dimethylthiazol-2-yl)-5-(3-carboxymethoxyphenyl)-2-(4-sulfophenyl)-2H-tetrazolium) (MTS) assay (Promega, USA).

In vitro cytotoxicity was also carried out in a murine macrophage Raw 264.7 cell line. Raw 264.7 cells were seeded on 96-well plates at 1000 cells/well. The cells were treated with DBC-Hf

and H₂DBC at various ligand concentrations (2, 5, 10, 20, and 50 μM base on ligand concentrations). A further incubation of 4 h was allowed, followed by replacing the culture medium with 100 μL of fresh RPMI 1640 medium. The cells were irradiated with LED light (650 nm) at 100 mW/cm² for 15 min (total light dose 90 J/cm²) or kept in dark, respectively. The cells were further incubated to achieve a total incubation time of 72 h. The cell viability was detected by MTS assay.

Apoptosis and necrosis detection: The apoptosis and necrosis induced by PDT of DBC-Hf and H₂DBC were evaluated by flow cytometry. CT26 cells were seeded at 1×10⁶ cells per well in 6-well plates and further cultured for 24 h. The culture media were replaced by 2 mL of fresh culture media containing 10% FBS. DBC-Hf and H₂DBC were added to the cells, respectively, at an equivalent ligand concentration of 5 μM. Cells incubated with PBS served as control. After 24-h incubation, the cells were irradiated with LED light (650 nm) at 100 mW/cm² for 15 min (90 J/cm²). Following further incubation of 24 h, the floating and adherent cells were collected and stained with Alexa Fluor 488 Annexin V/dead cell apoptosis kit (Invitrogen, USA) according to manufacturer's instructions. The apoptosis and necrosis was examined on a flow cytometer (LSRII Orange, BD, USA).

Immunogenic cell death detection: The immunogenic cell death by PDT of DBC-Hf and H₂DBC were evaluated by immunofluorescence and flow cytometry. For immunofluorescence analysis, CT26 cells were seeded at 5×10⁵ cells per well in 6-well plates and further cultured for 24 h. The culture media were replaced by 2 mL of fresh culture media containing 10% FBS. DBC-Hf and H₂DBC were added to the cells, respectively, at an equivalent ligand concentration of 5 μM. Cells incubated with PBS served as control. After 24-h incubation, the cells were irradiated with LED light (650 nm) at 100 mW/cm² for 15 min (90 J/cm²). Following further

incubation of 4 h, the cells were washed with PBS three times, fixed with 4% paraformaldehyde, incubated with AlexaFluor 488-calreticulin (CRT) antibody for 2 h, stained with DAPI, and observed under CLSM using 405 nm and 488 nm lasers for visualizing nuclei and CRT expression on the cell membrane, respectively.

For flow cytometry analysis, CT26 cells were seeded at 1×10^6 cells per well in 6-well plates and further cultured for 24 h. The culture media were replaced by 2 mL of fresh culture media containing 10% FBS. DBC-Hf and H₂DBC were added to the cells, respectively, at an equivalent ligand concentration of 5 μ M. Cells incubated with PBS served as control. After 24-h incubation, the cells were irradiated with LED light (650 nm) at 100 mW/cm² for 15 min (90 J/cm²). Following further incubation of 4 h, the cells were collected, incubated with AlexaFluor 488-CRT antibody for 2 h, and stained with propidium iodide (PI). The samples were analyzed by flow cytometer (LSRII Orange, BD, USA) to identify cell surface CRT. The fluorescence intensity of stained cells was gated on PI-negative cells.

In vivo efficacy: The PDT efficacy of DBC-Hf was investigated using a flank CT26 mouse tumor model and HT29 subcutaneous xenograft mouse model. Tumor bearing mice were established by subcutaneous inoculation of HT29 cell suspension (2×10^6 cells per mouse) or CT26 cell suspension (1×10^6 cells per mouse) into the right flank region of 6-week athymic male nude mice or 6-week BALB/c male mice, respectively. Six groups were included for comparison: (1) PBS control, (2) DBC-Hf, (3) DBP-Hf, (4) H₂DBC, or (5) H₂DBP at a ligand dose of 1 mg/kg or (6) DBC-Hf at a ligand dose of 3.5 mg/kg. Twelve hours post injection, each mouse in group (1)-(5) was irradiated at the tumor site with light (0.1 W/cm²) for 15 min (90 J/cm²) and the mice in group (6) received light irradiation (0.1 W/cm²) for 30 min (180 J/cm²). For (1) to (5) groups on the CT26 model, mice are treated again 4 days after first treatment, while for (1) to (5)

groups on HT29 model, mice are treated every 4 days for total 4 treatments. When tumors reached 100 mm³, PBS, DBC-Hf, DBP-Hf, H₂DBC, or H₂DBP were intratumorally injected to animals. At 12 h post-injection, mice were anesthetized with 2% (v/v) isoflurane and tumors were irradiated with a 640 nm LED for DBP-Hf/H₂DBP or a 650 nm LED for DBC-Hf/H₂DBC. The light intensity was measured as 100 mW/cm².

To evaluate the therapeutic efficacy, tumor growth and body weight evolution were monitored. The tumor size was measured with a digital caliper every day. Tumor volumes were calculated as follows: (width² × length)/2. Finally, all mice were sacrificed when the tumor size of control group exceeded 2 cm³, and the excised tumors were photographed and weighed. The tumors were embedded in optimal cutting temperature (OCT) medium, sectioned at 5-µm thickness, and subjected to hematoxylin and eosin (H&E) stain for histopathological analysis.

3.5 References

1. Dougherty, T.J. PHOTODYNAMIC THERAPY. *Photochem. Photobiol.* **58**, 895-900 (1993).
2. Ash, D. & Brown, S. New drugs and future developments in photodynamic therapy. *Eur. J. Cancer* **29**, 1781-1783 (1993).
3. Senge, M.O. & Brandt, J.C. Temoporfin (Foscan®, 5, 10, 15, 20-Tetra (m-hydroxyphenyl) chlorin)—A Second-generation Photosensitizer^{†,‡}. *Photochem. Photobiol.* **87**, 1240-1296 (2011).
4. Wang, T.Y., Chen, J.R. & Ma, J.S. Diphenylchlorin and diphenylbacteriochlorin: synthesis, spectroscopy and photosensitising properties. *Dyes and pigments* **52**, 199-208 (2002).
5. Bonnett, R. & Martinez, G. Photobleaching of sensitizers used in photodynamic therapy. *Tetrahedron* **57**, 9513-9547 (2001).

6. Gahlen, J., Probst, R.L. & Stern, J. Photodynamic therapy in the gastro-intestinal tract. Options and limitations. *Chirurg* **73**, 122-131 (2002).
7. Mlkvy, P., Majek, F., Jurgos, L., Makovnik, P. & Durdik, S. Endoscopic treatment of praecancerous colorectal lesions and early colorectal cancer. *Bratisl Med J* **111**, 50-53 (2010).
8. Garg, A.D. & Agostinis, P. ER stress, autophagy and immunogenic cell death in photodynamic therapy-induced anti-cancer immune responses. *Photoch Photobio Sci* **13**, 474-487 (2014).
9. Galluzzi, L., Kepp, O. & Kroemer, G. Enlightening the impact of immunogenic cell death in photodynamic cancer therapy. *EMBO J.* **31**, 1055-1057 (2012).
10. Tanaka, M., Kataoka, H. & Takashi, J. Immunogenic Death of Cells Treated with New Photodynamic Therapy (PDT) with Glucose-Conjugated Chlorin (G-Chlorin). *Dig. Dis. Sci.* **59**, 2018-2018 (2014).
11. Kroemer, G., Galluzzi, L., Kepp, O. & Zitvogel, L. Immunogenic Cell Death in Cancer Therapy. *Annual Review of Immunology, Vol 31* **31**, 51-72 (2013).
12. Lu, K., He, C. & Lin, W. Nanoscale Metal–Organic Framework for Highly Effective Photodynamic Therapy of Resistant Head and Neck Cancer. *J. Am. Chem. Soc.* **136**, 16712-16715 (2014).
13. He, C., Liu, D. & Lin, W. Nanomedicine Applications of Hybrid Nanomaterials Built from Metal–Ligand Coordination Bonds: Nanoscale Metal–Organic Frameworks and Nanoscale Coordination Polymers. *Chem. Rev.* **115**, 11079-11108 (2015).

Chapter 4. A Chlorin-based Nanoscale Metal-Organic Framework Systemically Rejects Colorectal Cancers via Synergistic Photodynamic Therapy and Checkpoint Blockade Immunotherapy

4.1 Rationale of the nMOF design

In Chapters 2 and 3, we demonstrated examples of nMOFs to exert highly efficient photodynamic therapy (PDT).^{1,2} Moreover, we showed in Chapter 3 that nMOF-mediated PDT causes immunogenic cell death (ICD) in tumors. We believe that an immunotherapeutic agent that alters the tumor microenvironment can potentiate the immune activation by PDT and lead to systemic cancer vaccination.

We herein designed a new nMOF, TBC-Hf, constructed from a chlorin derivative, 5,10,15,20-tetra(p-benzoato)chlorin (H₄TBC) and Hf-based SBUs. We took advantage of the highly porous structure of the nMOF to load an IDO inhibitor (IDOi) into TBC-Hf to afford IDOi@TBC-Hf. The IDOi@TBC-Hf system enables a novel cancer treatment strategy by combining nMOF-enabled PDT and IDOi-based immunotherapy (Figure 4-1). Unlike the combination of chemotherapy/radiotherapy with immunotherapy that the treatment dose on major tumor is compromised, the new treatment enjoys the local tumor destruction potency by PDT while eliciting systemic antitumor immune response. Hence, the synergistic combination therapy achieved effective local and distant tumor rejection in colorectal cancer models.

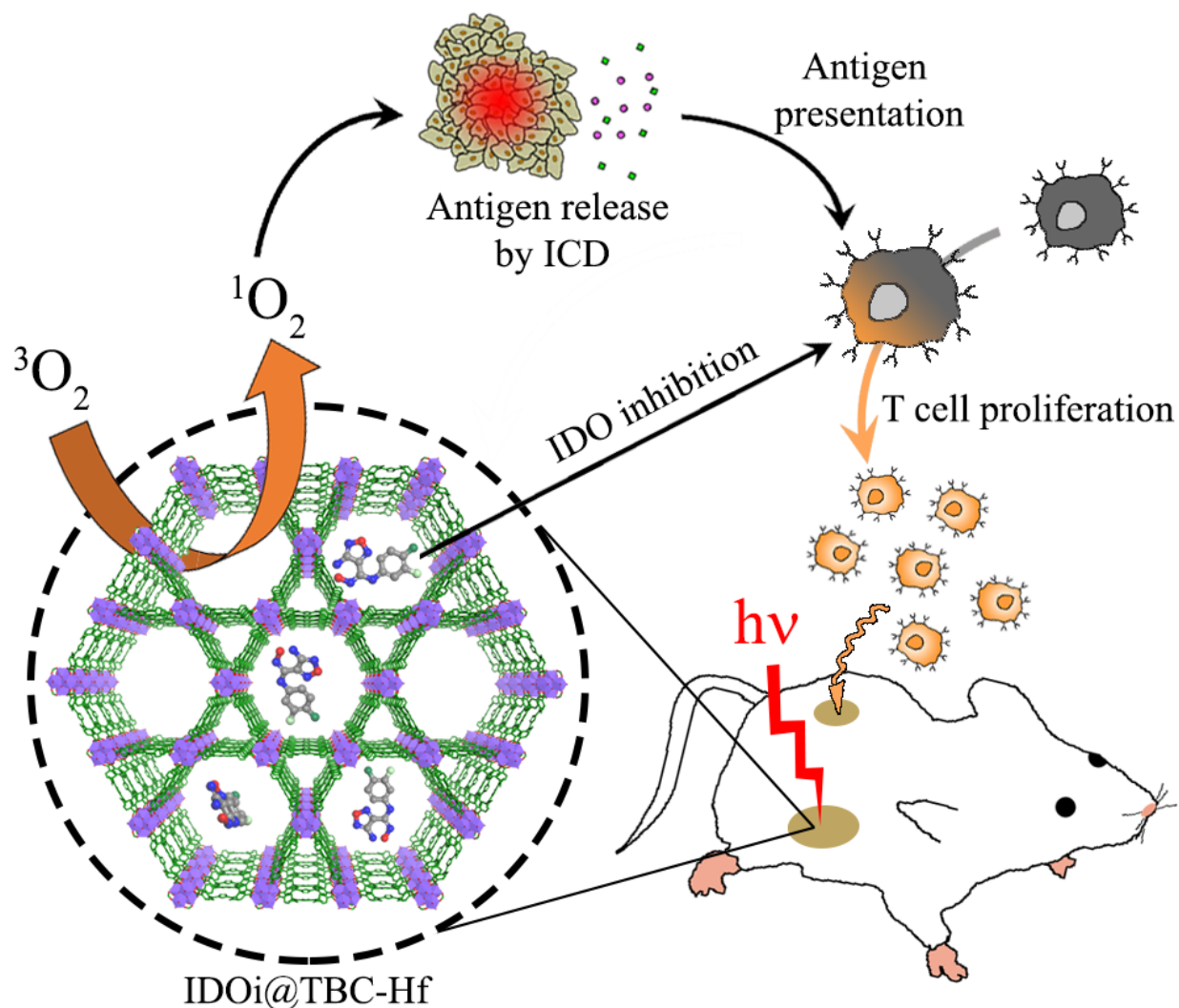


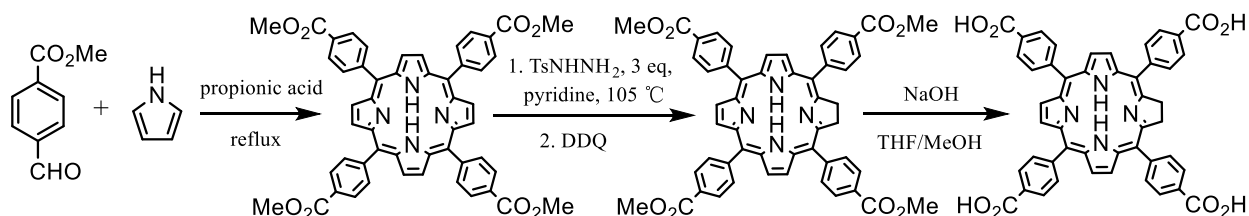
Figure 4-1 Schematic presentation of combined PDT and immunotherapy by IDOi@TBC-Hf. Local injection of IDOi@TBC-Hf and light irradiation generate reactive oxygen species (ROS), causing immunogenic cell death (ICD), and releasing tumor-associated antigens that are presented to T-cells. Meanwhile, the IDO inhibitor released from IDOi@TBC-Hf modulates tryptophan/kynurenine catabolism to activate the immunosuppressive tumor microenvironment. The combination of antigen presentation from PDT and checkpoint blockade by IDO inhibition causes T-cell proliferation and infiltration, leading to not only eradication of local, treated tumors but also rejection of distant, untreated tumors.

4.2 Results

4.2.1 Synthesis and characterization of H₄TBC ligand and TBC-Hf nMOF

The new chlorin derivative 5,10,15,20-tetra(p-benzoato)chlorin (H₄TBC) was synthesized in 3 steps as depicted in scheme 4-1.

Scheme 4-1 Synthesis of 5,10,15,20-tetra(p-benzoato) chlorin (H₄TBC).



Synthesis of 5,10,15,20-tetra(p-methylbenzoato)porphyrin (Me₄TBP)

A mixture of 6.83 g of methylterephthalaldehyde (41.6 mmol) and 2.80 mL of pyrrole (40.4 mmol) was dissolved in 100 mL of propionic acid. The solution was heated to reflux (150 °C) in dark overnight. The purple product was collected by vacuum filtration and was washed with water, methanol and ethyl ether in sequence. Yield: 24.3%. ¹H NMR (500 MHz, CDCl₃, ppm, Figure 4-2): δ=8.84 (s, 8H), 8.47 (d, 8H), 8.32 (d, 8H), 4.14 (s, 12H), -2.79 (s, 2H).

Synthesis of 5,10,15,20-tetra(p-methylbenzoato)chlorin (Me₄TBC)

Me₄TBP (500 mg, 0.59 mmol) and anhydrous potassium carbonate (750 mg, 5.4 mmol) were added to a 2-neck round bottom flask. 40 mL of anhydrous pyridine was added under nitrogen. The solution was heated to 105 °C before the addition of 4.0 mL of p-toluenesulfonylhydrazide solution (0.30 M in anhydrous pyridine). The reaction mixture was kept

at 105 °C for 4 hours during which another 2 fractions of p-toluenesulfonhydrazide solutions (0.30 M in anhydrous pyridine, 4.0 mL for each fraction) were added every 2 h. The reaction mixture was then stirred at 105 °C in the dark for another 12 h. The product was extracted with 2:1 ethyl acetate/water and washed with 2 M HCl, 2 M phosphoric acid, water, and saturated sodium bicarbonate solution. The solution was treated with 2,3-dichloro-5,6-dicyano-benzoquinone (via slow addition of 1 mg/mL solution in chloroform) until the characteristic absorption of the over-reduced product at ~735 nm disappeared. The product was purified by aluminum oxide column chromatography with dichloromethane as the eluent. Yield: 16%. ¹H NMR (500 MHz, CDCl₃, ppm, Figure 4-3): δ=8.57 (d, 2H), 8.40 (m, 10H), 8.20 (m, 6H), 7.99 (d, 4H), 4.18 (s, 4H), 4.11 (s, 6H), 4.09 (s, 6H), -1.45 (s, 2H). ESI-MS for [Me₄TBC+H]⁺: 849.3 calcd, 849.4 found (Figure 4-4).

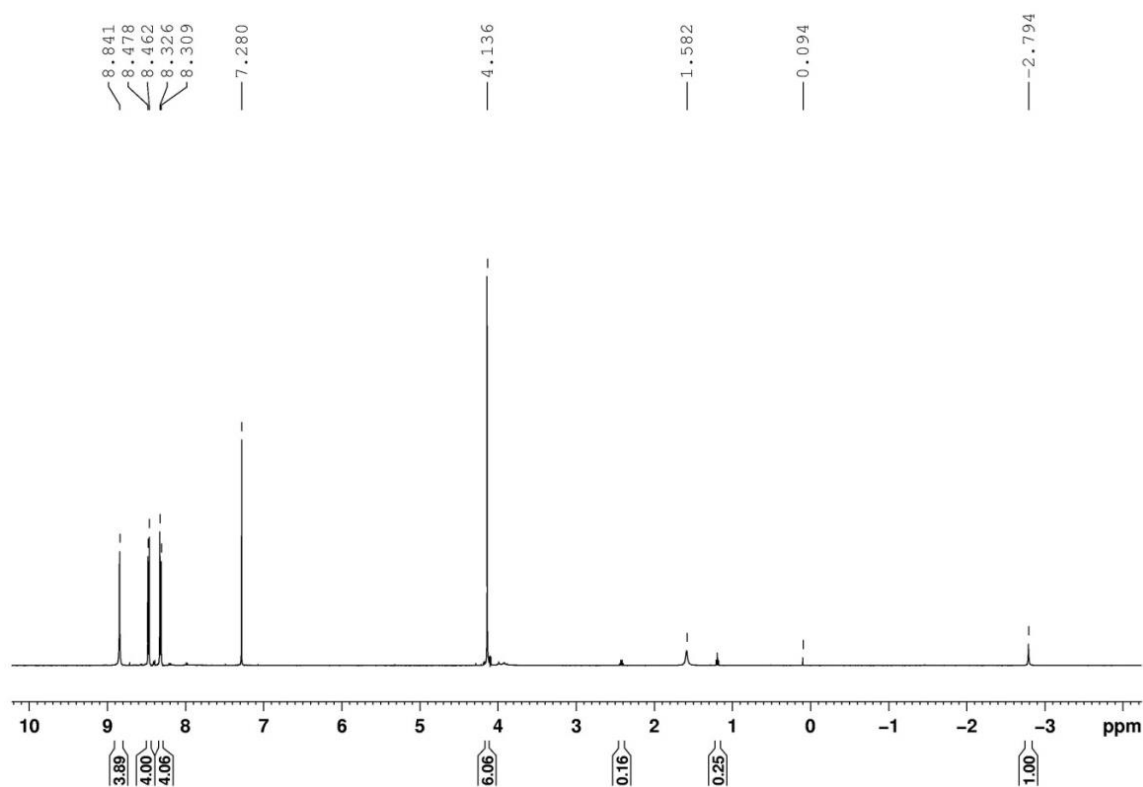


Figure 4-2 ¹H NMR of 5,10,15,20-tetra(p-methylbenzoato)porphyrin.

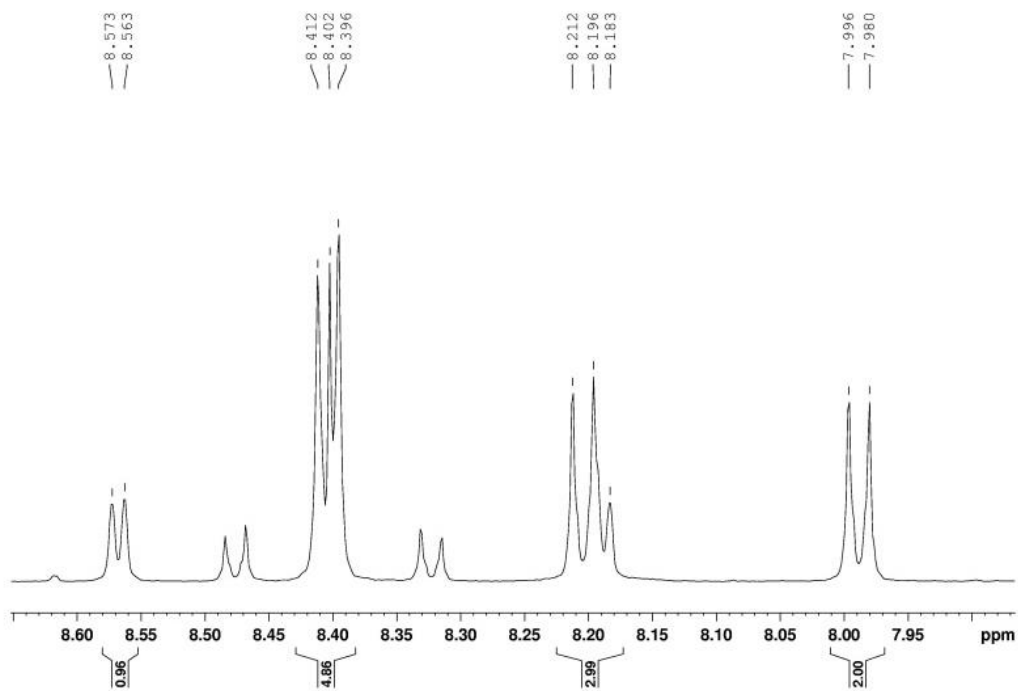
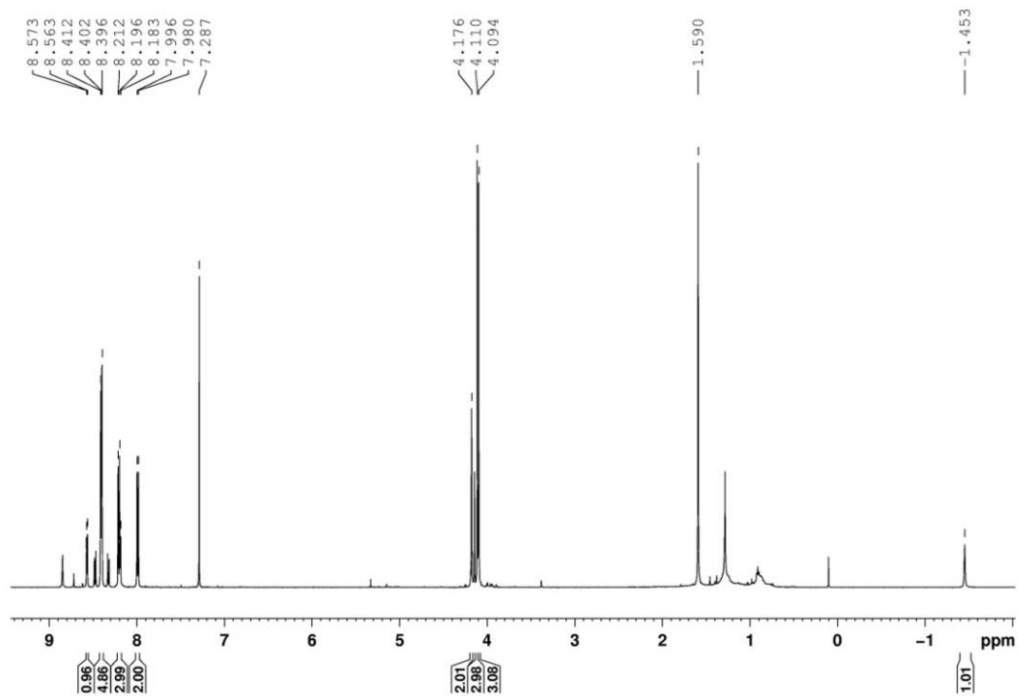


Figure 4-3 ^1H NMR of 5,10,15,20-tetra(p-methylbenzoato)chlorin. (a) The full spectrum and (b) the expanded view of a portion of the spectrum.

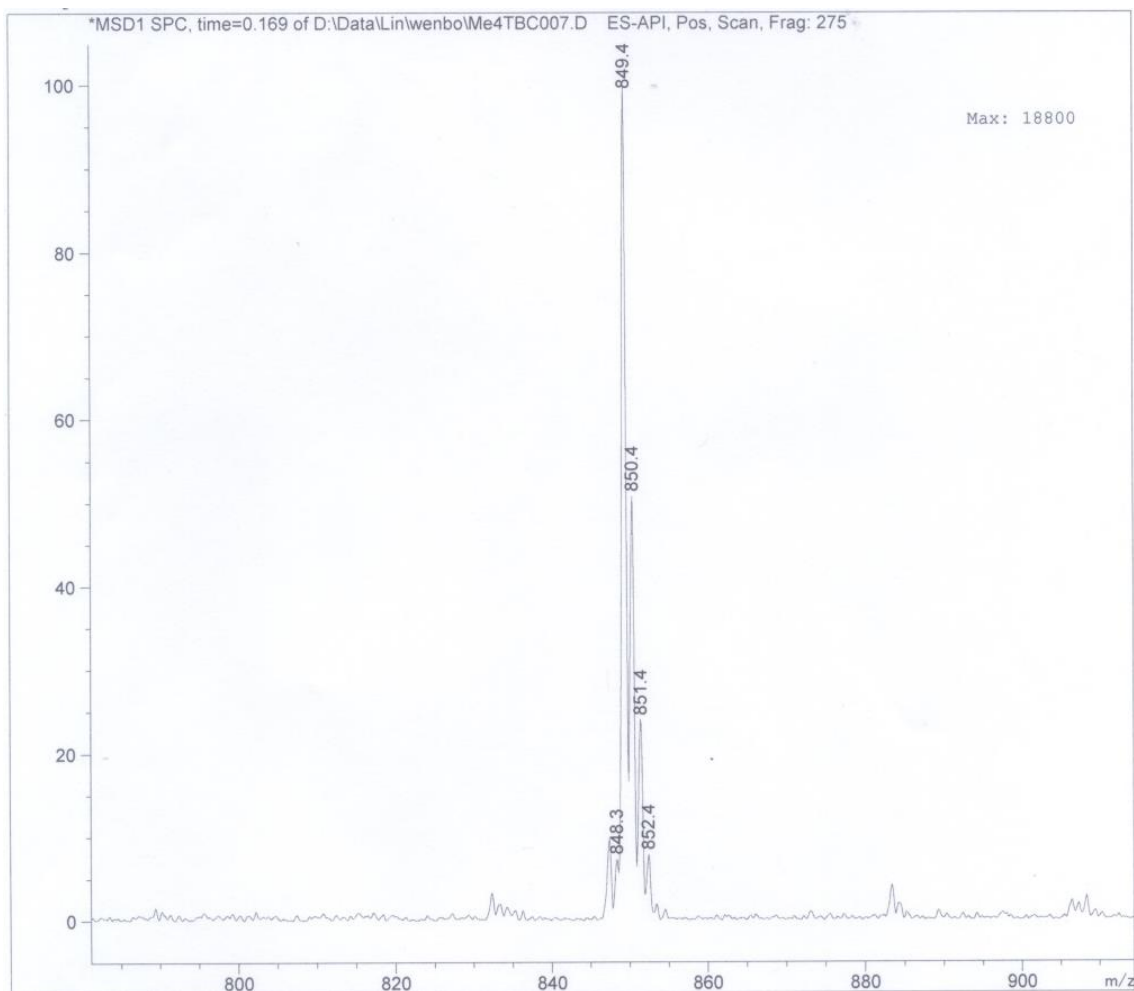


Figure 4-4 ESI-MS of 5,10,15,20-tetra(p-methylbenzoato)chlorin.

Synthesis of 5,10,15,20-tetra(p-benzoato)chlorin (H_4TBC)

The hydrolysis of Me_4TBC was conducted in 1:1 THF/methanol under N_2 . An aqueous NaOH solution (2 mol/L, 40 equiv.) was added to a solution of Me_4TBC after degas with N_2 . The solution was heated at 74 °C (reflux) overnight. After removing most of the organic volatile by a rotary evaporator, the solution was diluted with water and neutralized with HCl (1 M) to pH=3. The product was collected by vacuum filtration and washed with water and methanol before drying on the vacuum. Yield: 78%. 1H NMR (500 MHz, $CDCl_3$, ppm, Figure 4-5): δ =8.60 (d,

2H), 8.31 (m, 10H), 8.19 (m, 6H), 8.01 (d, 4H), 4.10 (s, 4H), -1.56 (s, 2H). ESI-MS for [H4TBC+H]⁺: 793.2 calcd, 793.3 found (Figure 4-6).

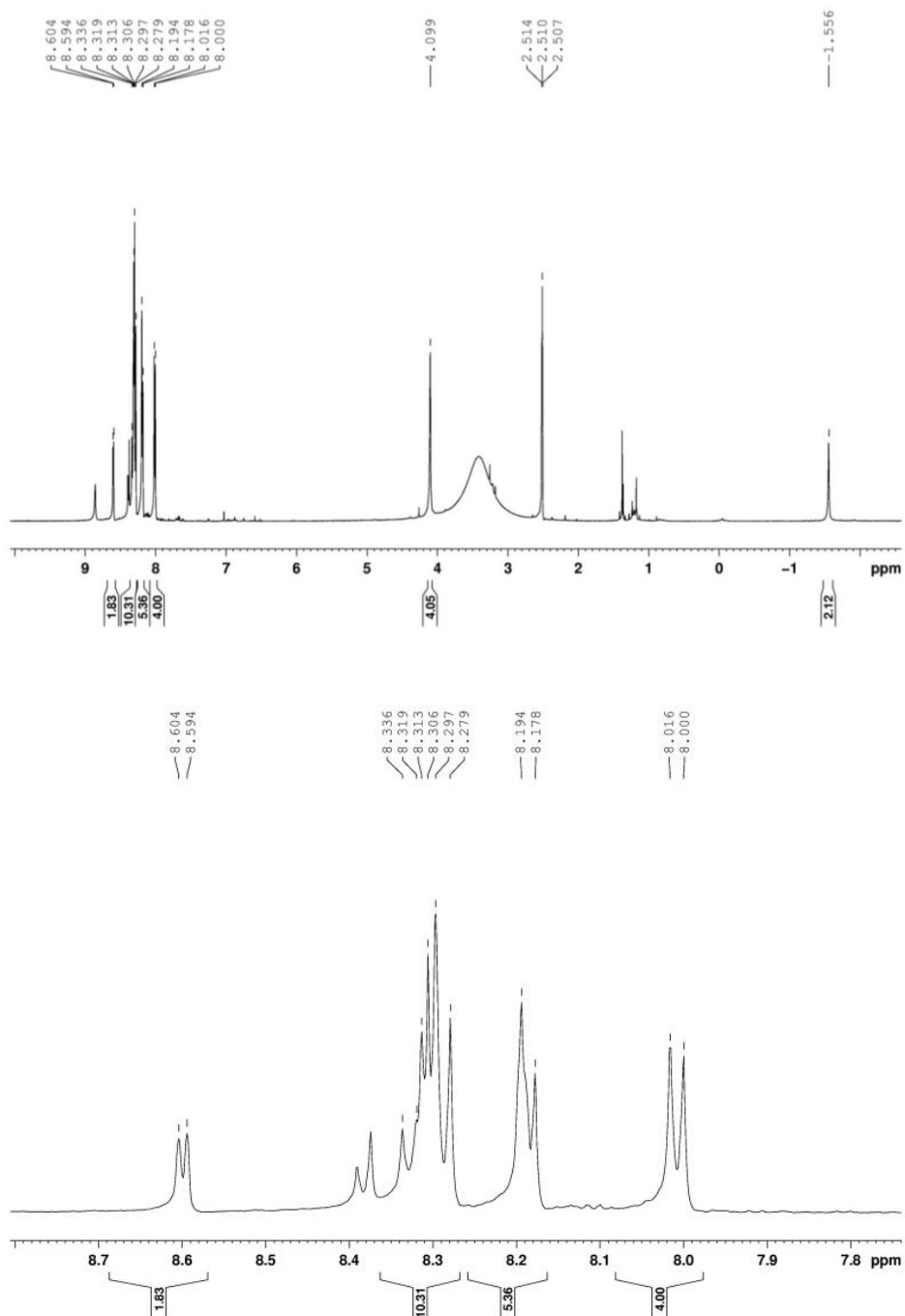


Figure 4-5 ¹H NMR of 5,10,15,20-tetra(p-benzoato)chlorin. (a) The full spectrum and (b) the expanded view of a portion of the spectrum.

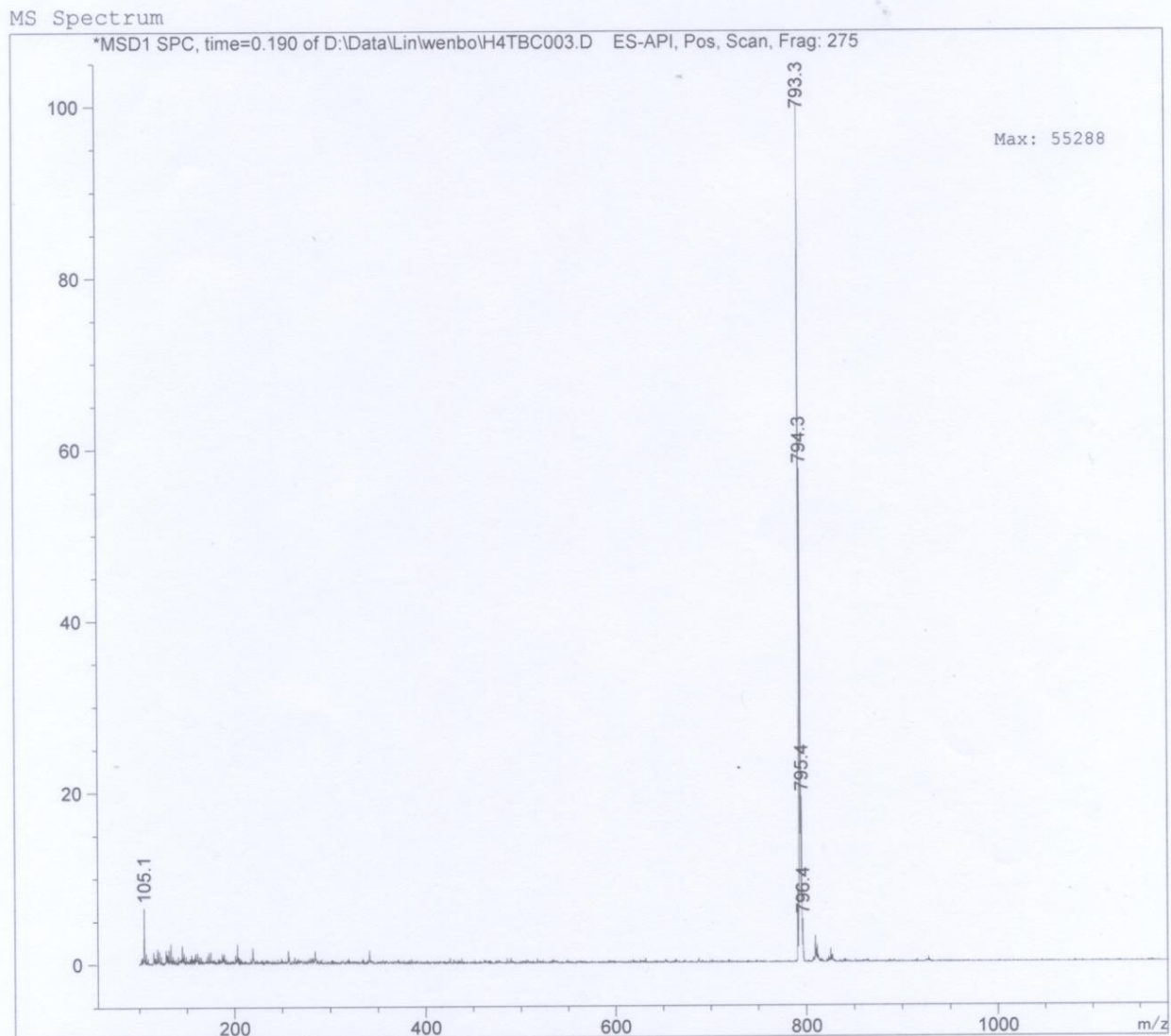


Figure 4-6 ESI-MS of 5,10,15,20-tetra(p-benzoato)chlorin.

Synthesis and characterization of TBC-Hf

A solvothermal reaction between HfCl_4 and H_4TBC in *N,N*-dimethylformamide (DMF) at 80 °C led to the purple powder of TBC-Hf in 87% yield. TBC-Hf was washed with copious amounts of DMF, 1% triethylamine (NEt_3) in ethanol (v/v), and ethanol successively and stored in ethanol as a stock suspension. As a control, TBP-Hf with the corresponding porphyrin ligand

5,10,15,20-tetra(p-benzoato)porphyrin (H₄TBP) was synthesized by a solvothermal reaction between HfCl₄ and H₄TBP in N,N-diethylformamide (DEF) at 120 °C and washed in the same fashion as for TBC-Hf.

TBC-Hf and TBP-Hf adopt the same structure as the previously reported TBP-Zr analog (MOF-545), based on powder X-ray diffraction (PXRD) (Figure 4-7a).³ The carboxylate moieties from the TBC ligands bridge 8 out of 12 edges of octahedral Hf₆(μ₃-O)₄(μ₃-OH)₄ SBUs. The remaining coordination sites on the SBUs are occupied by 4 water and 4 terminal hydroxy groups on the equatorial plane to afford a hexagonal framework of Hf₆(μ₃-O)₄(μ₃-OH)₄(OH)₄(H₂O)₄(TBC)₂ (Figure 4-7b). The nMOFs therefore feature large one-dimensional channels with diameters of 3.5 nm along the *c* axis, along with smaller channels with diameters of 1.0 nm along the *c* axis and 1.1 nm × 0.9 nm windows perpendicular to the *c* axis (Figure 4-7 c,d). TBC-Hf and TBP-Hf exhibit BET surface area of 1077 and 1462 m²/g, respectively (Figure 4-8). During the course of this study, a few reports of TBP-based nMOFs with a cubic structure for PDT have appeared.^{4,5} However, we expect that our highly porous TBP-Hf control will outperform the cubic TBP-based nMOFs due to the enhanced ¹O₂ diffusion through the nMOF channels. In TBC-Hf and TBP-Hf, the porphyrin and chlorin rings are highly rigid in the nMOF structures to minimize energy transfer and self-quenching.

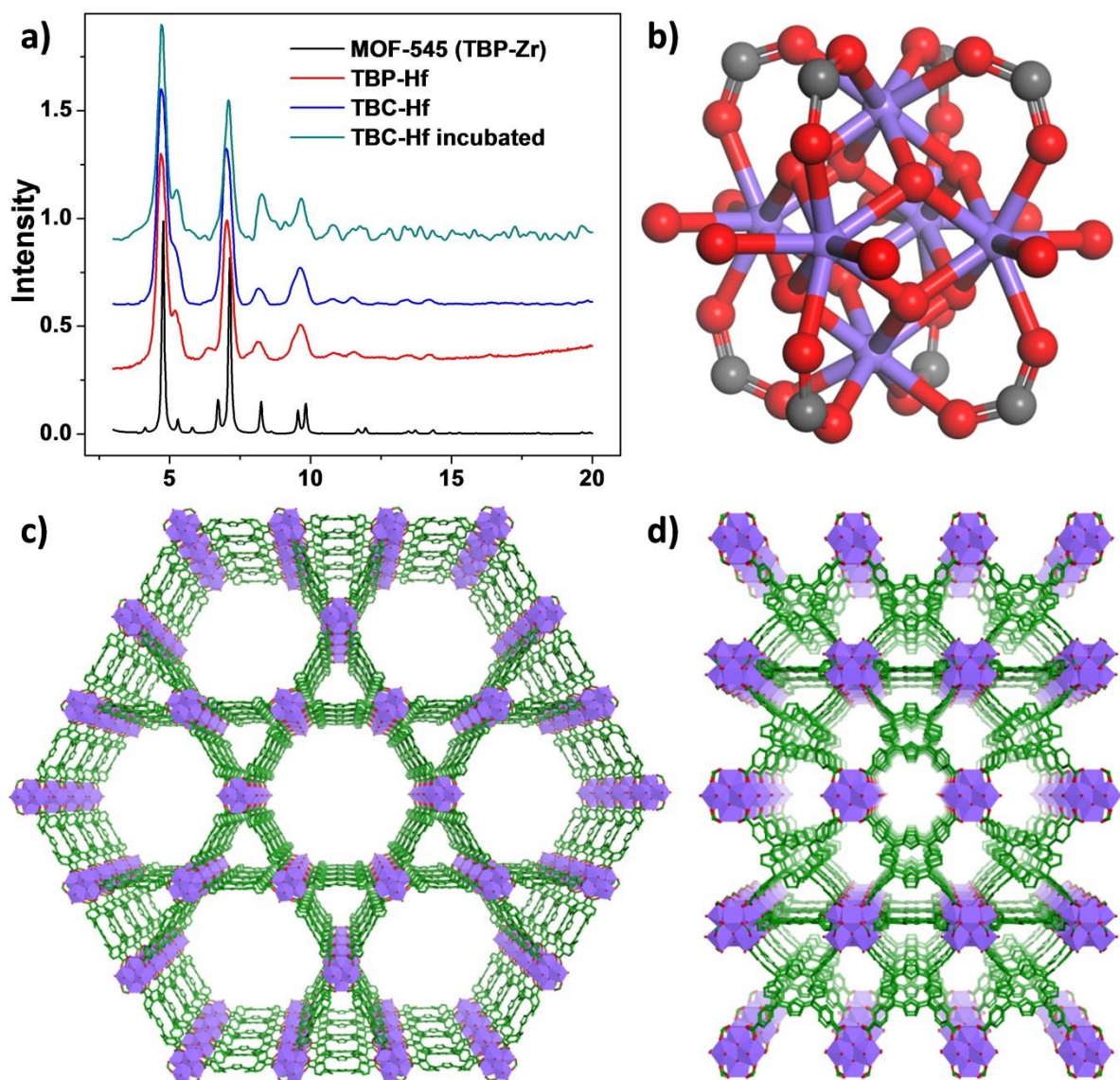


Figure 4-7 Structures of TBC-Hf and TBP-Hf. (a) PXRD patterns of TBP-Hf and TBC-Hf in comparison with MOF-545. (b) The secondary building unit (SBU) of TBC-Hf (Violet, Hf; red, O; gray, C). (c-d) The view of TBC-Hf structure along [001] (c) and [100] (d) direction.

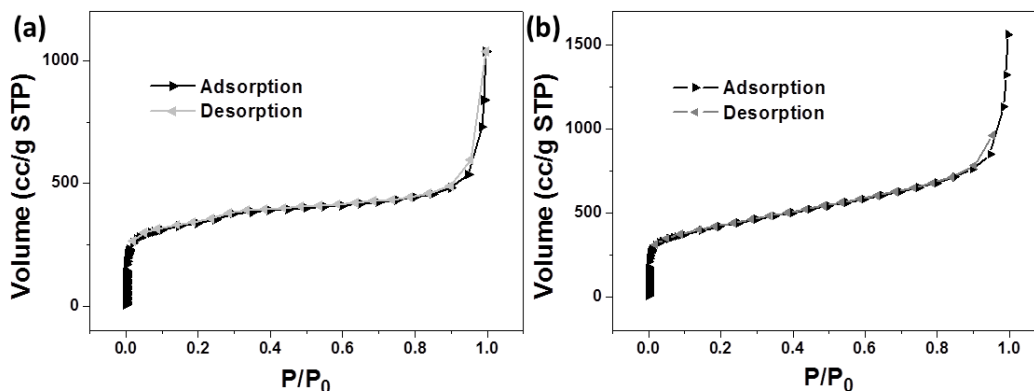


Figure 4-8 Nitrogen adsorption isotherms of TBC-Hf (a) and TBP-Hf (b) at 77K.

Transmission electron microscopy (TEM) revealed nanorod/nanorice morphologies for TBP-Hf and TBC-Hf (Figure 4-9 a,d). The rods are typically 50-100 nm long and 30-60 nm wide for TBC-Hf, and 50-100 nm long and 20-30 nm wide for TBP-Hf. High resolution TEM images show the lattice fringes with the distances matching d_{200} and d_{001} spacings of the crystal structure (Figure 4-9 b,c,e). The average diameter of TBC-Hf and TBP-Hf are 83.2 nm and 72.7 nm, respectively, by dynamic light scattering (DLS) measurements. (Figure 4-10). The nMOFs are stable in biological environments, as evidenced by the lack of significant changes in PXRD pattern or morphology after incubation in Hank's balanced salt solution for 24 h (Figure 4-9f).

The Hf content was determined by inductively coupled plasma-mass spectrometry (ICP-MS) to be 30.4% (36.6% calculated). The TBC weight loss of 61.7% (56.8% calculated) determined by thermogravimetric analysis further confirms the framework formula (Figure 4-11). We encapsulated an INCB24360 analogue IDOi,⁶ 4-amino-N-(3-chloro-4-fluoro-phenyl)-N'-hydroxy-1,2,5-oxadiazole-3-carboximidamide (Figure 4-11b), into the TBC-Hf channels to afford IDOi@TBC-Hf for the co-delivery of IDOi with PSs. The IDOi weight percentage after loading is determined to be 4.7% by TGA.

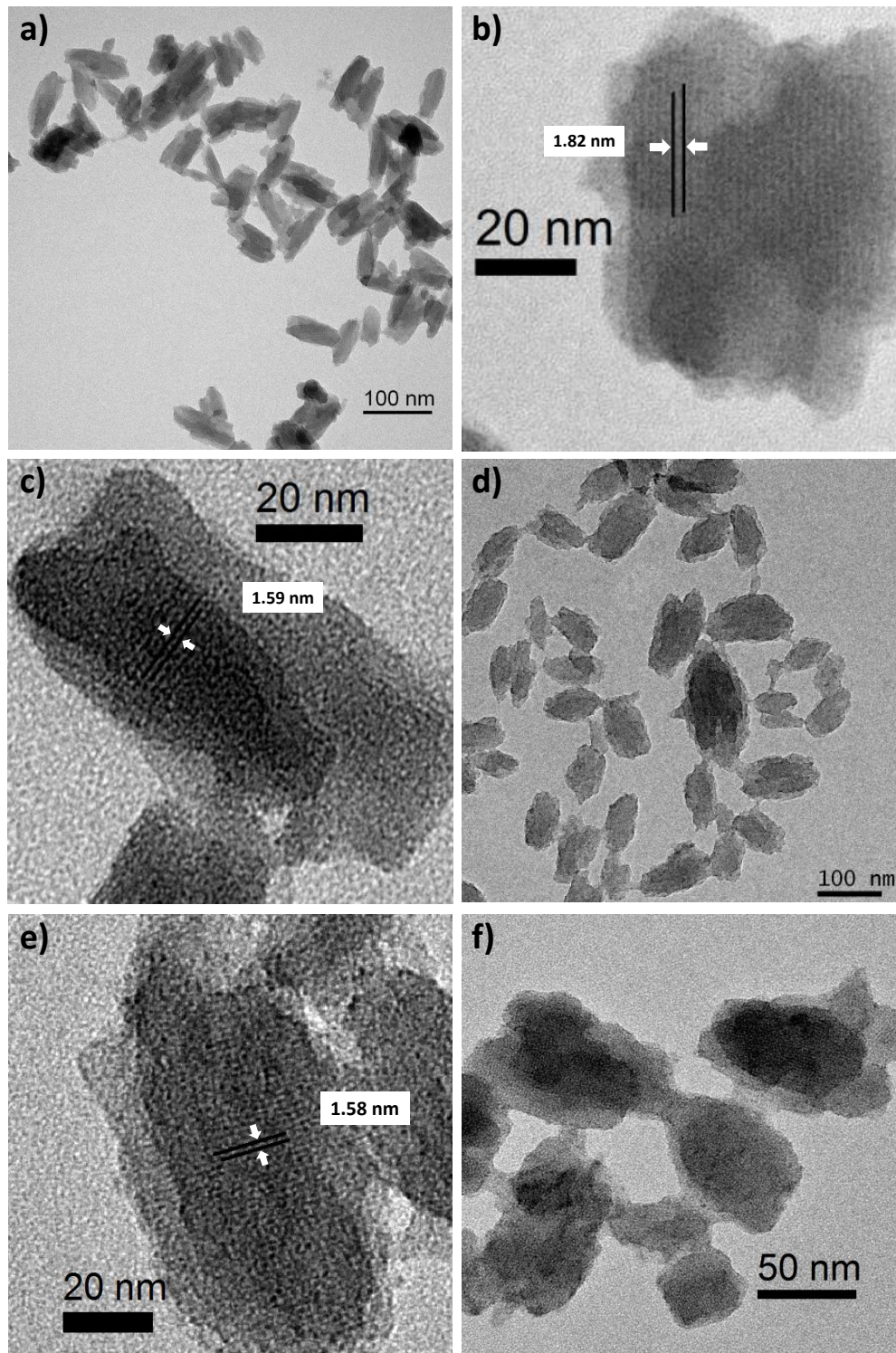
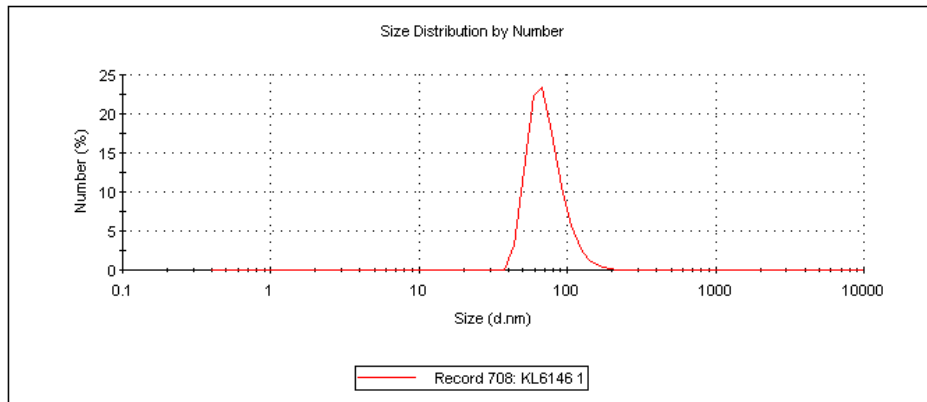


Figure 4-9 TEM images showing the morphology of TBP-Hf and TBC-Hf. (a) TEM images of TBP-Hf. (b-c) High resolution TEM showing the lattice fringes of TBP-Hf in different directions. (d) TEM images of TBC-Hf. (e) High resolution TEM showing the lattice fringes of TBC-Hf. (f) TBC-Hf after incubation in Hank's balanced salt solution for 24 h.

	Size (d.nm):	% Number	Width (d.nm):
Z-Average (d.nm): 103.8	Peak 1: 72.72	100.0	21.29
Pdl: 0.085	Peak 2: 0.000	0.0	0.000
Intercept: 0.935	Peak 3: 0.000	0.0	0.000

Result quality : Good



	Size (d.nm):	% Number	Width (d.nm):
Z-Average (d.nm): 114.9	Peak 1: 83.15	100.0	24.53
Pdl: 0.071	Peak 2: 0.000	0.0	0.000
Intercept: 0.922	Peak 3: 0.000	0.0	0.000

Result quality : Good

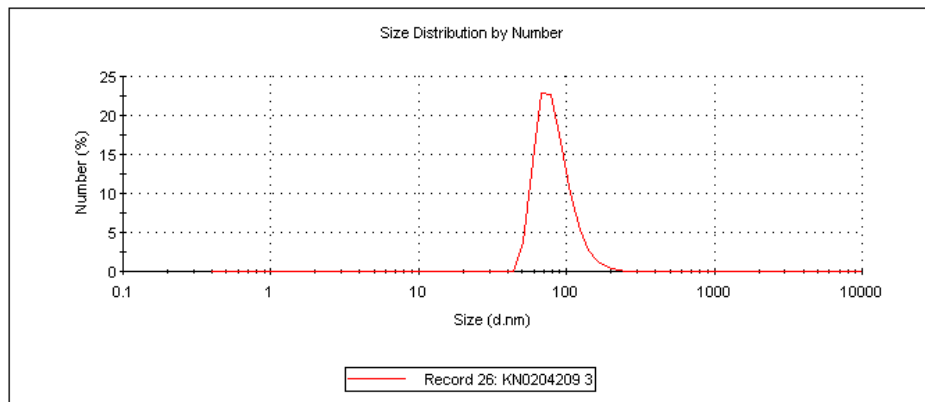


Figure 4-10 DLS plots showing the particle sizes of TBP-Hf (top) and TBC-Hf (bottom).

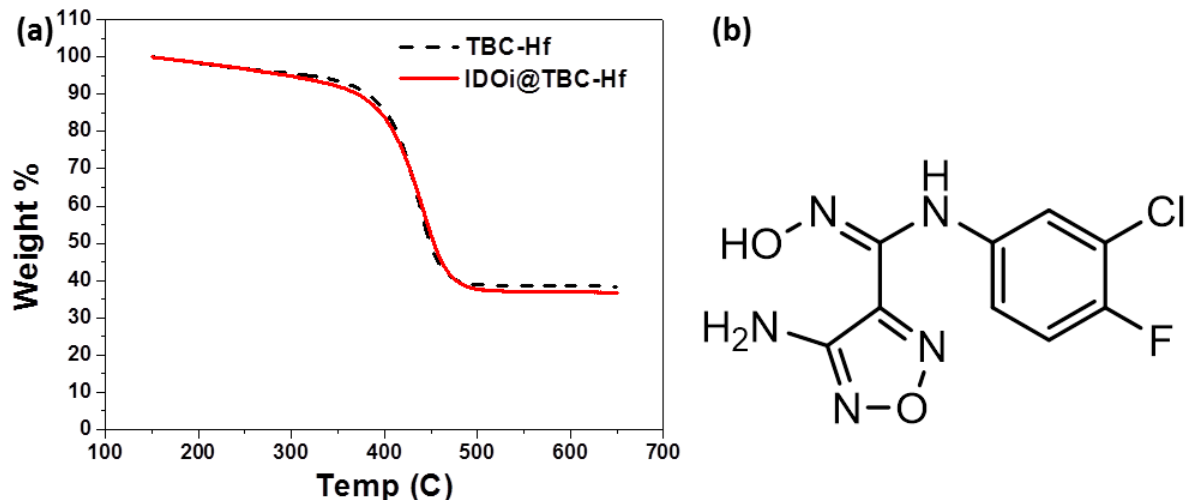


Figure 4-11 (a) TGA of TBC-Hf before and after IDOi loading. (b) The chemical structure of the IDOi, 4-amino-N-(3-chloro-4-fluoro-phenyl)-N'-hydroxy-1,2,5-oxadiazole-3-carboximidamide.

UV-visible absorption spectroscopy indicates that TBC-Hf more effectively absorbs red light compared to TBP-Hf (Figure 4-12a). H_4TBC has a major Soret peak at $\lambda_{max}=420$ nm and four Q-bands at 518, 546, 600, and 652 nm. The Soret absorption of TBC-Hf almost overlaps with that of the free ligand ($\lambda_{max}=421$ nm) while the Q-bands slightly red-shift to 520, 548, 600, and 653 nm. In comparison, the Soret peaks of H_4TBP and TBP-Hf are at $\lambda_{max}=420$ nm and 418 nm, respectively, and the Q-bands are at 516, 549, 592 and 646 nm for H_4TBP and 517, 550, 593 and 647 nm for TBP-Hf. The lowest energy Q-band of the chlorin therefore red-shifts by 6 nm after reduction from the porphyrin counterpart (652 nm compared to 646 nm). The extinction coefficient of H_4TBC at the lowest energy absorption ($\epsilon=44700$ $M^{-1} cm^{-1}$) is ~9 fold greater than that of H_4TBP ($\epsilon=4800$ $M^{-1} cm^{-1}$) while the lowest energy absorption of TBC-Hf ($\epsilon=38500$ $M^{-1} cm^{-1}$) is 6-fold greater than that of TBP-Hf ($\epsilon=6400$ $M^{-1} cm^{-1}$). Notably, the lowest energy absorption of TBC-Hf (653 nm) is at a wavelength of 7-nm longer than that of our previously reported DBC-Hf and the ϵ of TBC-Hf is ~1.6 fold higher than that of DBC-Hf.

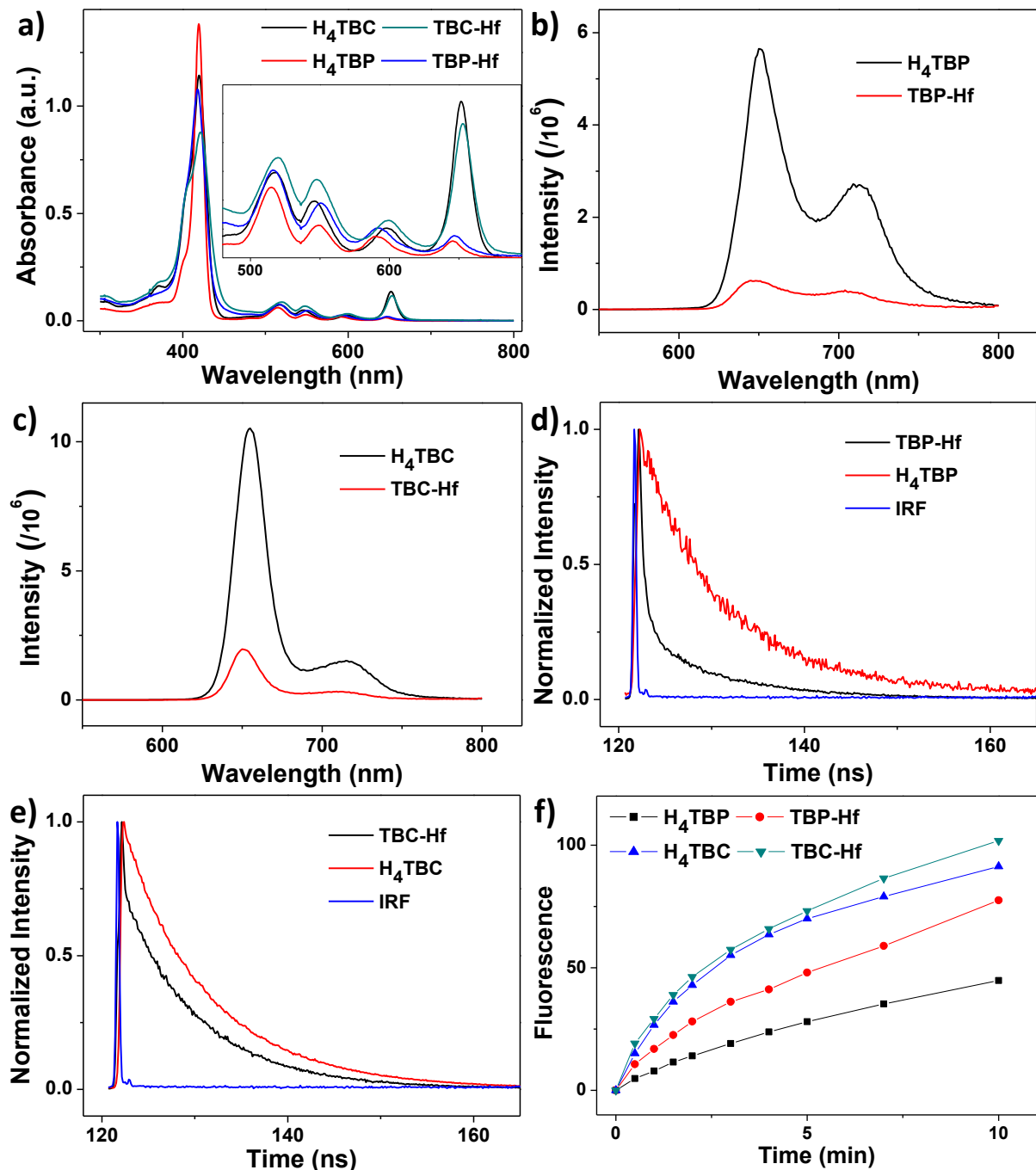


Figure 4-12 Photophysics and photochemistry of the ligands and nMOFs. (a) UV-visible absorption spectra of H_4TBP , H_4TBC , $TBP-Hf$, and $TBC-Hf$. Inset shows expanded views of the Q-band regions. The fluorescence spectra of H_4TBP and $TBP-Hf$ (b), H_4TBC and $TBC-Hf$ (c) with excitation at 420 nm. Time-resolved fluorescence decay traces of H_4TBP and $TBP-Hf$ (d), H_4TBC and $TBC-Hf$ (e) along with instrument response function (IRF). (f) Singlet oxygen generation by H_4TBP , H_4TBC , $TBP-Hf$, and $TBC-Hf$ with a 650 nm LED irradiation at 20 mW/cm^2 , detected by Singlet Oxygen Sensor Green.

H₄TBC exhibits two fluorescence emissions at 655 nm and 715 nm with an intensity ratio of ~6.8 when excited at 420 nm (Figure 4-12c). H₄TBP fluorescence emissions are close to those of H₄TBC, though the 651 nm/713 nm peak intensity ratio is ~2 (Figure 4-12b). After forming nMOFs, the fluorescence intensities drop significantly, consistent with other nMOF systems.^{1,2} For TBC-Hf, the fluorescence peaks slightly blue-shift to 650 nm and 712 nm and the intensities decrease by 5.3-fold and 4.7-fold, respectively; for TBP-Hf, the fluorescence peaks blue-shift to 648 nm and 704 nm and the fluorescence intensities drop by 9.0-fold and 6.5-fold, respectively. The decrease in fluorescence intensity results from the enhanced intersystem crossing after coordination of the chlorin/porphyrin ligands to Hf on the SBUs. Time-Correlated Single Photon Counting measurement results also supported this interpretation: the fluorescence lifetime at 650 nm dropped from 9.56 ns for H₄TBC to 8.25 ns for TBC-Hf and from 9.25 ns for H₄TBP to 8.38 ns for TBP-Hf (Figure 4-12 d, e and Table 4-1).

Table 4-1 Lifetimes of H₄TBP, H₄TBC, TBP-Hf and TBC-Hf fluorescence in different media, fitted by software.

Sample	τ (ns)	χ^2
H ₄ TBP_PBS	9.25±0.05	1.05
TBP-Hf_water	8.38±0.04	1.65
H ₄ TBC_PBS	9.56±0.01	2.22
TBC-Hf_water	8.25±0.01	1.08

4.2.2 Singlet oxygen generation

The $^1\text{O}_2$ generation efficiencies of H_4TBC , TBC-Hf , H_4TBP , and TBP-Hf were determined by Singlet Oxygen Sensor Green (SOSG) assay. The nMOF samples and ligand controls were irradiated with a LED ($\lambda_{\text{max}}=650$ nm, 20 mW/cm 2) and the fluorescence enhancement upon reaction of SOSG with $^1\text{O}_2$ was measured by a fluorimeter (excitation/emission at 504/525 nm). The fluorescence intensity plotted against irradiation time fit exponential decay equations, as we had previously observed in other nMOF systems,^{1,2} indicating a pseudo first-order $^1\text{O}_2$ generation process (Figure 4-12f). TBC-Hf outperforms both TBP-Hf and H_4TBC in terms of $^1\text{O}_2$ generation efficiency.

4.2.3 *In vitro* PDT efficacy and mechanistic study

We first confirmed efficient cellular uptake of TBC-Hf and TBP-Hf by cancer cells. TBC-Hf and TBP-Hf were incubated with colorectal cancer CT26 cells at a ligand concentration of 25 μM for 24 h. The Hf contents inside cells were determined to be (2.07 ± 0.26) and (1.79 ± 0.17) nmol/ 10^4 cells, respectively, by ICP-MS analysis (Figure 4-13). The *in vitro* PDT efficacy of TBP-Hf , TBC-Hf , and both ligands against CT26 cells was next investigated. TBC-Hf outperformed TBP-Hf under 90 J/cm 2 light irradiation. Both nMOFs and ligands outperformed protoporphyrin IX (PpIX) upon irradiation, a commonly used PS, while no cytotoxicity was observed in dark control groups (Figure 4-14). The IC_{50} values of TBC-Hf , TBP-Hf , H_4TBC , H_4TBP and PpIX for CT26 cells were 4.82 ± 0.50 , 7.09 ± 0.39 , 10.04 ± 1.22 , 12.83 ± 1.59 and 23.72 ± 0.60 μM , respectively, at an irradiation dose of 90 J/cm 2 (Figure 4-14c). These results were confirmed by a second colorectal cancer MC38 cell with IC_{50} values of 2.57 ± 0.85 and

17.9±5.0 μM for TBC-Hf and H₄TBC, respectively. The IC₅₀ values exceeded 50 μM for TBP-Hf, H₄TBP, and PpIX for MC38 cells (Figure 4-14d). To demonstrate the versatility of our nMOF system, an unrelated B16F10 melanoma cell were employed to confirm the PDT efficacy, yielding IC₅₀ values of 5.48±0.70, 9.72±0.78, 11.03±1.57, 20.10±4.28 and 16.48±0.77 μM for TBC-Hf, TBP-Hf, H₄TBC, H₄TBP, and PpIX, respectively (Figure 4-14e).

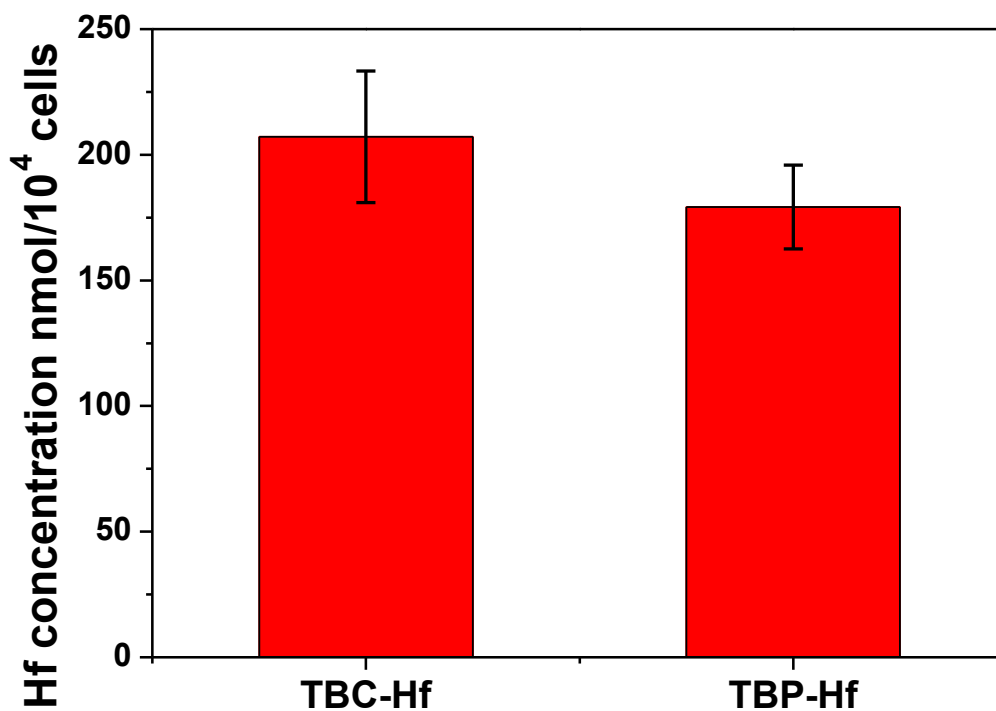


Figure 4-13 Cellular uptake of TBP-Hf and TBC-Hf in CT26 cells.

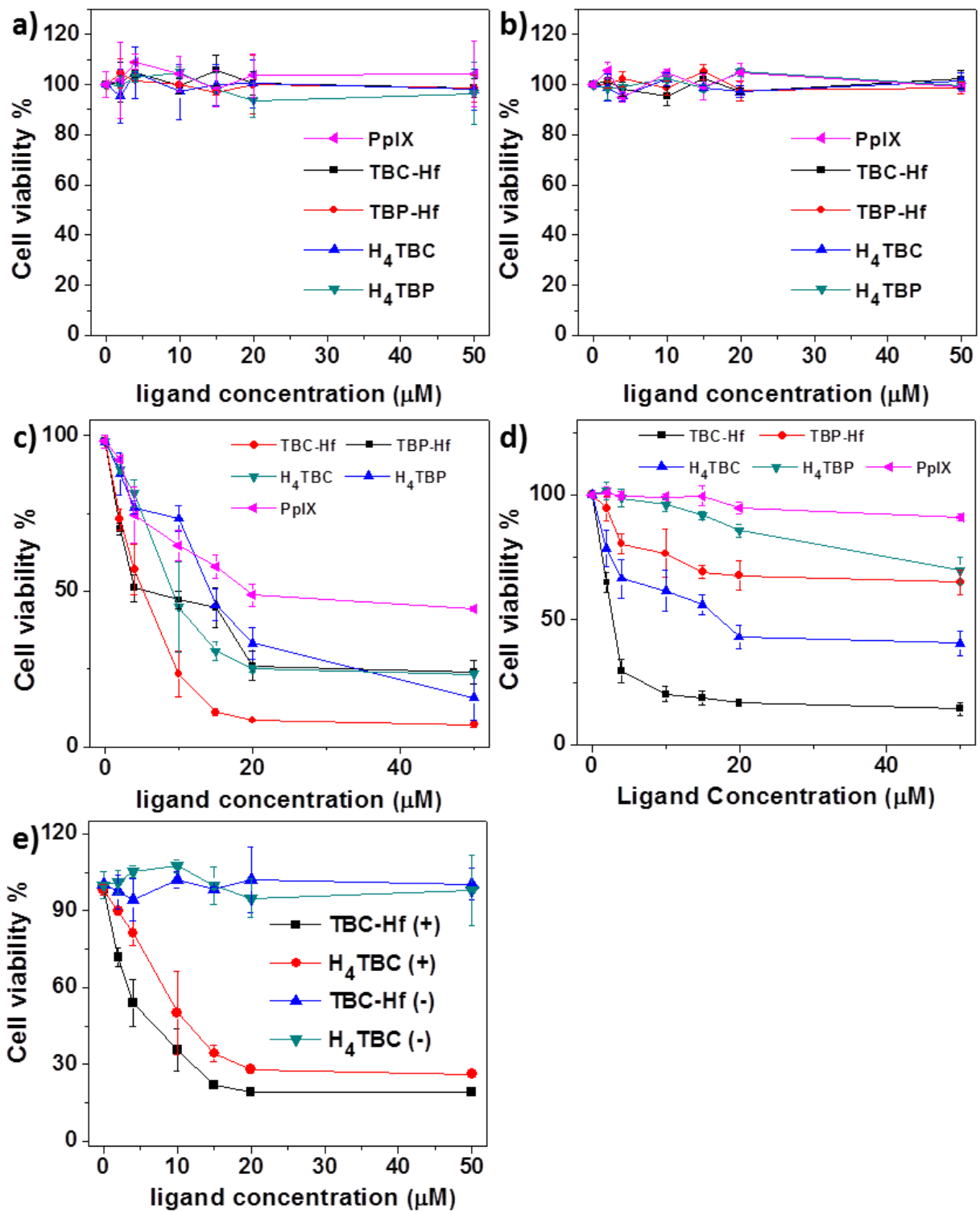


Figure 4-14 *In vitro* PDT efficacy on CT26 (a,c), MC38 (b,d) and B16F10 (e) cells.

Unlike most conventional cytotoxic agents, PDT is known to induce ICD via apoptosis and necrosis, thereby mediating antitumor immune response.⁷ We confirmed that both apoptosis and necrosis occur upon treatment with PDT by flow cytometry of Alexa Fluor 488 Annexin V-labeled dead cells. MC38 cells were incubated with TBC-Hf, TBP-Hf, H₄TBC, and H₄TBP at 1 μ M (ligand concentration of 2 μ M) followed by light irradiation at 90 J/cm² (650 nm, 100 mW/cm²). Significant amounts of cells underwent apoptosis/necrosis when treated with PDT of TBC-Hf, TBP-Hf, H₄TBC, and H₄TBP with only 30.0%, 32.7%, 55.5%, and 57.6% healthy cells, respectively, compared to 80-90% healthy cells in dark control or PBS-treated cells with irradiation (Figure 4-15a). These results were further confirmed in CT26 cells under the same conditions (Figure 4-15b). These results indicate the chlorin-based TBC-Hf is a more efficient PS than the porphyrin-based TBP-Hf at equivalent nMOF and light doses.

We also investigated the ability of PDT treatment to induce ICD by determining cell-surface expression of calreticulin (CRT). MC38 cells were incubated with TBC-Hf, TBP-Hf, H₄TBC, and H₄TBP at 1 μ M (ligand concentration of 2 μ M) followed by light irradiation at 90 J/cm². For flow cytometry analysis, cells were collected and stained with Alexa Fluor 488-CRT antibody and propidium iodide (PI, Figure 4-16). The fluorescence intensity of stained cells was gated on PI-negative cells. For immunostaining analysis, the cells were stained with AlexaFluor 488-CRT and DAPI, and observed under confocal laser scanning microscopy (CLSM, Figure 4-17). In both instances, cells treated with nMOF or ligand showed significant CRT expression on the cell-surface upon irradiation but none with PBS control or without irradiation. Due to the higher ¹O₂ generation efficiency and *in vitro* PDT efficacy of TBC-Hf, we focus our subsequent *in vivo* studies on TBC-Hf and use TBP-Hf as a control wherever appropriate.

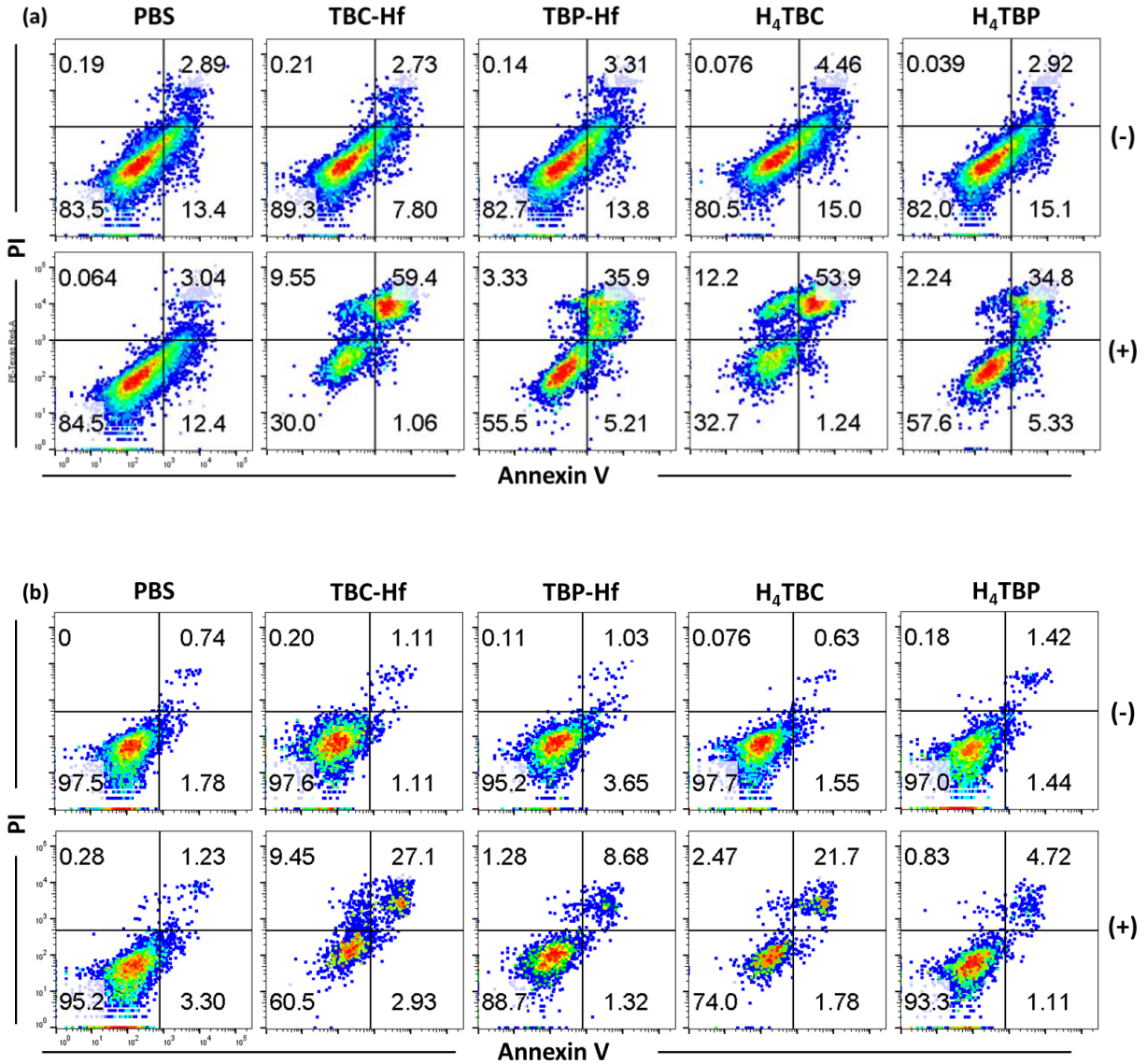


Figure 4-15 Annexin V/PI analysis of CT26 (a) and MC38 (b) cells incubated with PBS, TBC-Hf, TBP-Hf, H₄TBC, and H₄TBP with or without irradiation (90 J/cm²). The quadrants from lower left to upper left (counter clockwise) represent healthy, early apoptotic, late apoptotic, and necrotic cells, respectively. The percentage of cells in each quadrant was shown on the graphs. (+) and (-) refer to with and without irradiation, respectively.

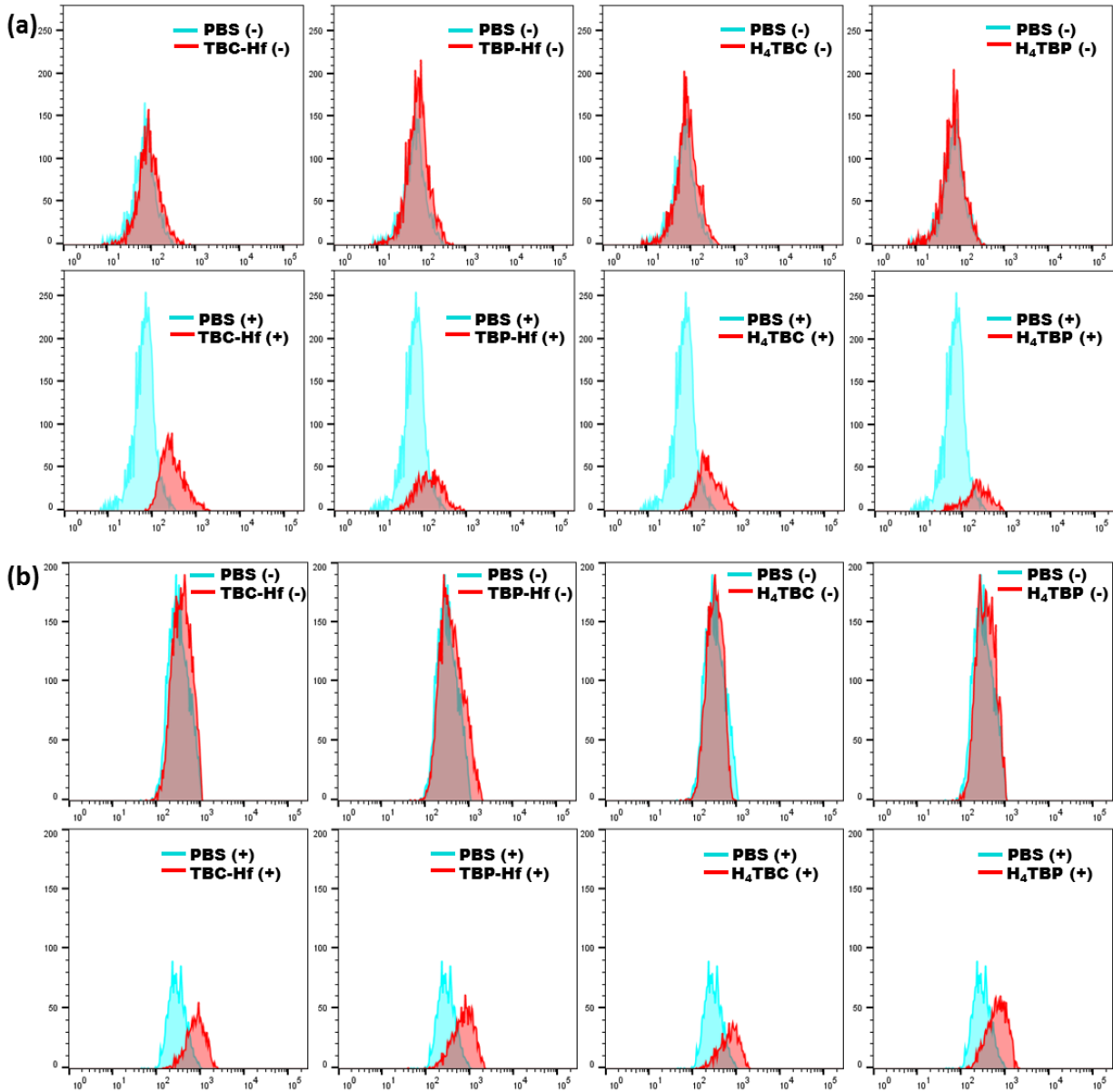


Figure 4-16 CRT exposure on the cell surface. Expression in CT26 (a) and MC38 (b) was assessed after incubation with PBS, TBC-Hf, TBP-Hf, H₄TBC, and H₄TBP, with (+) or without (-) light irradiation (90 J/cm²) by flow cytometry analysis. The fluorescence intensity was gated on PI-negative cells.

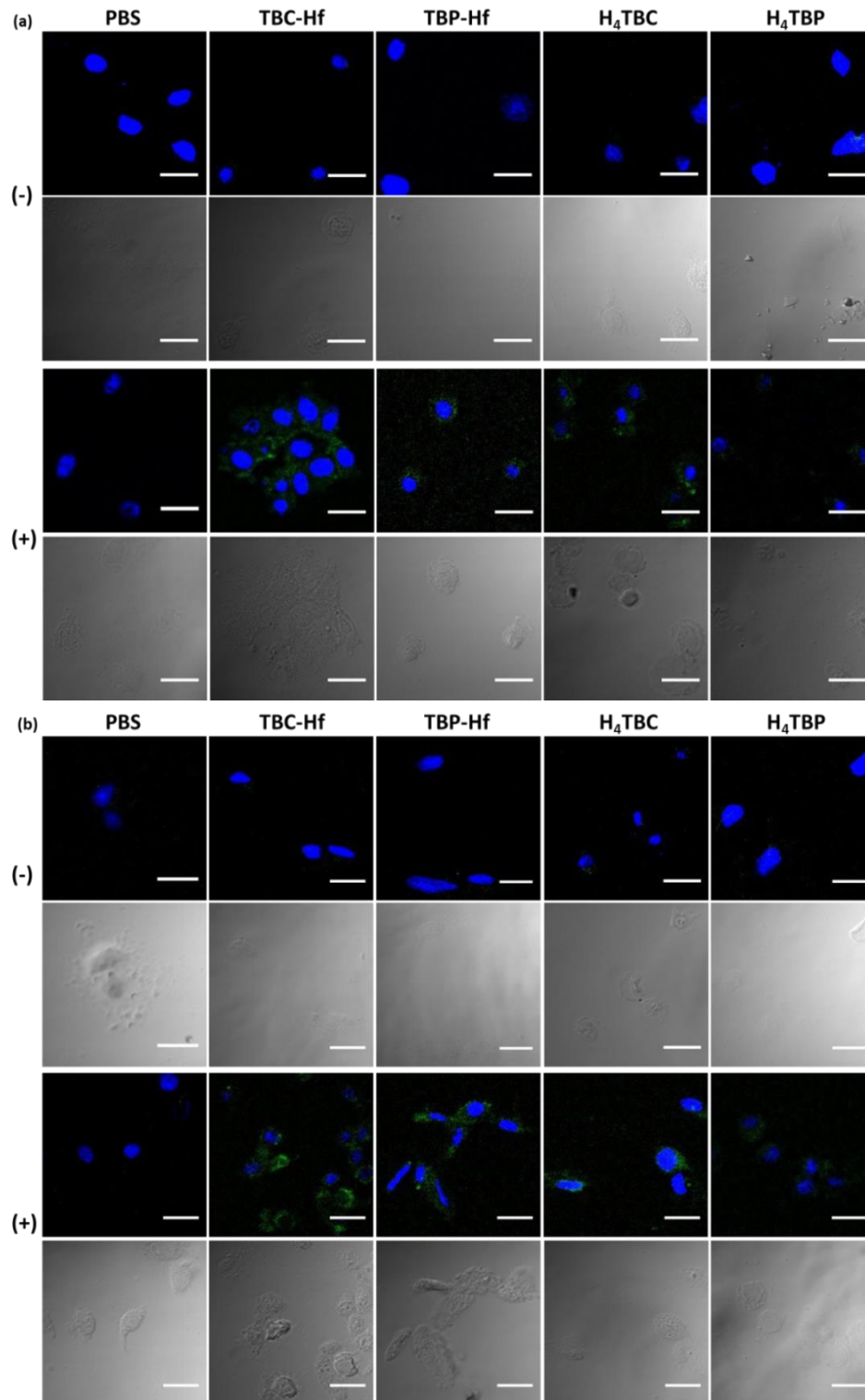


Figure 4-17 Immunofluorescence microscopy of CRT expression on the cell surface. Expression in CT26 (a) and MC38 (b) treated with PBS, TBC-Hf, TBP-Hf, H₄TBC, and H₄TBP with (+) or without (-) irradiation (90 J/cm²). The fluorescence intensity was gated on PI-negative cells. Scale bar = 50 μM.

4.2.4 The abscopal effect of IDOi@TBC-Hf

The immunoregulatory enzyme IDO is often overexpressed in the tumor microenvironment, where it facilitates the survival and growth of tumor cells by suppressing antitumor immune responses.⁸ The small-molecule IDO inhibitor (IDOi) INCB24360, developed by Incyte, can reverse immunosuppression and inhibits tumor growth upon oral administration.⁶ We propose that by encapsulation of IDOi into the nMOF channels, IDOi@TBC-Hf can release IDOi both into the local tumor environment and enter blood circulation for systemic IDO inhibition. The effects of IDOi will alter the suppressive tumor microenvironment of both the treated and untreated tumors. We hypothesize that synergizing local PDT of IDOi@TBC-Hf with checkpoint blockade therapy can promote an efficient abscopal effect, regression of an untreated tumor at a distant site following the local treatment of another tumor in the same organism.

We evaluated the abscopal effect of IDOi@TBC-Hf and light irradiation in two immunocompetent mouse models using bilateral tumor models of colorectal cancers CT26 and MC38 in the flank regions of BALB/c mice and C57BL/6 mice, respectively. When the primary tumors reached $\sim 100 \text{ mm}^3$, mice received a single injection of H₄TBC, H₄TBC plus IDOi, TBC-Hf, or IDOi@TBC-Hf into the primary tumors at a ligand dose of 20 $\mu\text{mol/kg}$ or a corresponding IDOi dose of 1.5 mg/kg. Twelve hours after injection, the primary tumors were irradiated at a light dose of 90 J/cm² (650 nm, 100 mW/cm²). Mice treated with IDOi@TBC-Hf without light irradiation served as dark controls. As depicted in Figure 4-18 and 4-19, local nMOF injection with light irradiation led to near elimination of the treated primary tumors. At the endpoint, CT26 tumor-bearing mice treated with IDOi@TBC-Hf or TBC-Hf and PDT therapy had tumors only (1.1 \pm 0.2)% and (0.7 \pm 0.4)% the size of PBS treated tumors, respectively. Similarly, MC38 tumor-bearing mice had tumors only (0.8 \pm 0.3)% and (0.9 \pm 0.4)% of the size of PBS treated

tumors, respectively. H₄TBC with light irradiation and IDOi@TBC-Hf dark group failed to inhibit the tumor growth while H₄TBC plus IDOi with light irradiation slightly inhibits the tumor growth (Table 4-2). Moreover, only PDT treatment of IDOi@TBC-Hf successfully reduced the sizes of the untreated distant tumors. Tumors began shrinking on Day 6 and 5 after treatment in the CT26 and MC38 models, respectively, suggesting the treatment evoked systemic antitumor immunity in mice (Table 4-2 and 4-3). TBC-Hf with light irradiation and IDOi@TBC-Hf dark control slightly inhibited the distant tumor growth, showing ineffectiveness of monotherapies.

Table 4-2 Statistical analysis of the tumor sizes at the end of treatment on CT26 tumor bearing mice.

	P values	
	Treated tumor	Untreated tumor
PBS vs H ₄ TBC	0.0098	0.0011
PBS vs H ₄ TBC+IDOi	< 0.0001	0.0002
PBS vs TBC-Hf	< 0.0001	< 0.0001
PBS vs IDOi@TBC-Hf (-)	0.34	0.0005
PBS vs IDOi@TBC-Hf	< 0.0001	< 0.0001
TBC-Hf vs IDOi@TBC-Hf	0.17	< 0.0001
IDOi@TBC-Hf (-) vs (+)	< 0.0001	< 0.0001

Table 4-3 Statistical analysis of the tumor sizes at the end of treatment on MC38 tumor bearing mice.

	P values	
	Treated tumor	Untreated tumor
PBS vs TBC-Hf	< 0.0001	0.0005
PBS vs IDOi@TBC-Hf (-)	0.19	< 0.0001
PBS vs IDOi@TBC-Hf	< 0.0001	< 0.0001
TBC-Hf vs IDOi@TBC-Hf	0.81	< 0.0001
IDOi@TBC-Hf (-) vs (+)	< 0.0001	< 0.0001

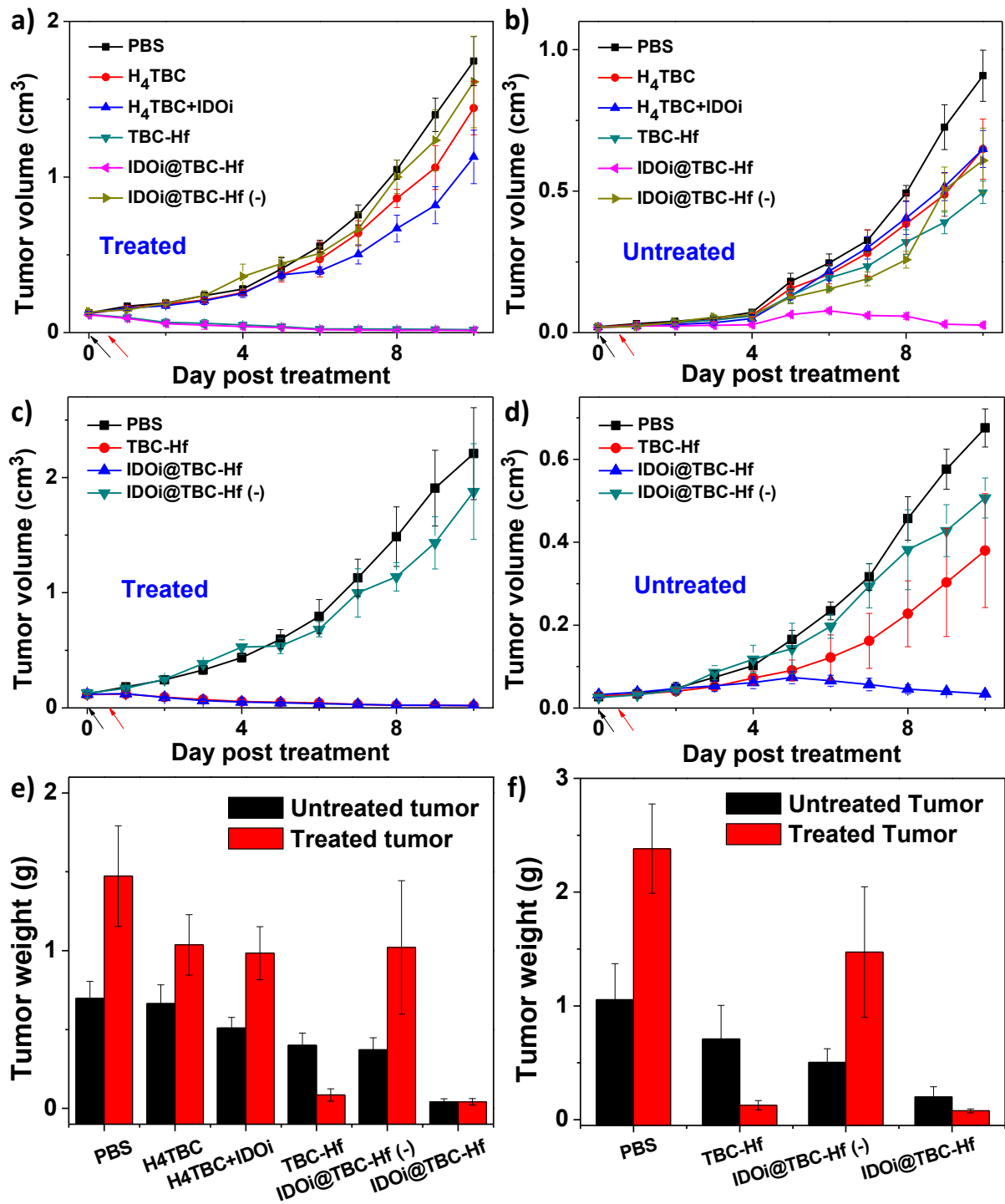


Figure 4-18 *In vivo* anticancer efficacy showing abscopal effect. Growth curves for treated (a and c) and untreated (b and d) tumors of CT26 (a and b) or MC38 (c and d) tumor-bearing mice after PDT treatment. Black and red arrows refer to the time of injection and irradiation, respectively. Tumor weights after PDT treatment on CT26 (e) and MC38 (f) models, collected after euthanizing the mice at day 10.

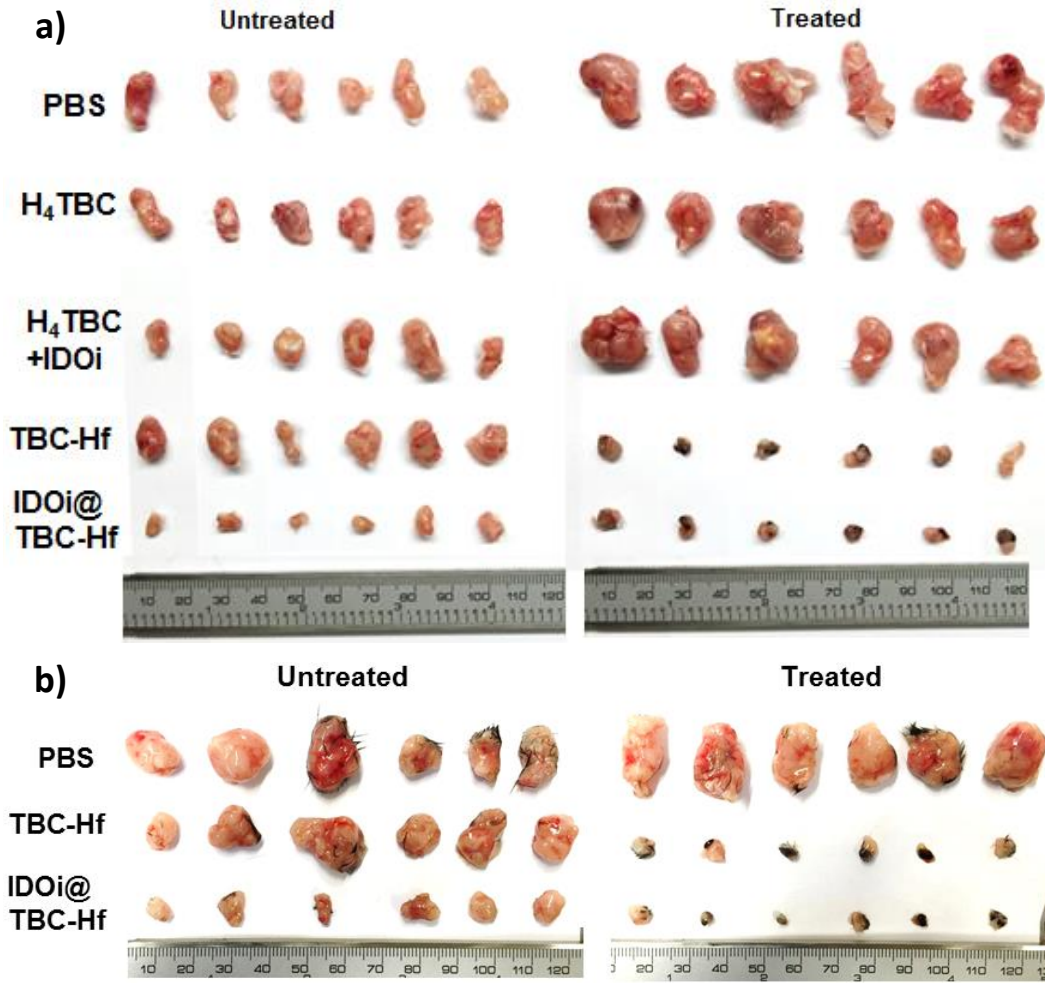


Figure 4-19 Photos of excised tumors of each group after PDT treatment in the CT26 (a) and MC38 (b) models.

4.2.5 Antitumor Immunity

We have shown that PDT of IDOi@TBC-Hf caused effective tumor regression of both primary, treated tumors and distant, untreated tumors in two syngeneic mouse models of colorectal cancer. We further investigated the underlying immunological mechanisms in the MC38 model by Enzyme-Linked ImmunoSpot (ELISPOT) and flow cytometry. We first performed an ELISPOT assay to detect the presence of tumor antigen-specific T cells 14 days after treatment. As shown in Figure 4-20, the number of antigen-specific IFN- γ producing T cells

increased to 799 per million splenocytes in mice treated with IDOi@TBC-Hf (vs. 128 per million splenocytes in PBS group, $P=0.0879$), indicating that PDT of IDOi@TBC-Hf induced *in situ* tumor vaccination to effectively generate tumor-specific T cell response.

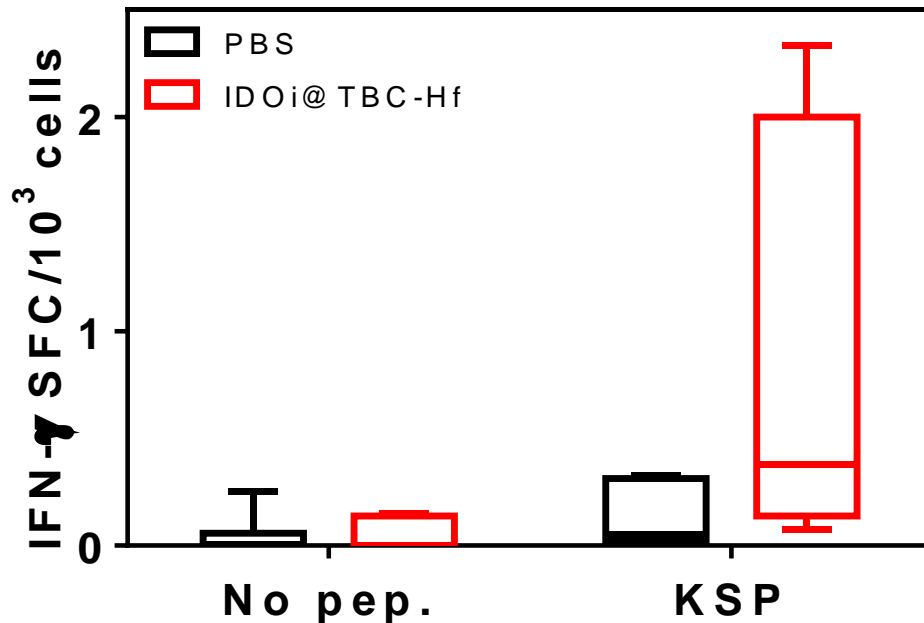


Figure 4-20 Antigen-specific IFN- γ spot forming cells (SFC) at 14 days after IDOi@TBC-Hf PDT treatment.

Further analysis of the immune response was carried out by investigating the tumor-infiltrating leukocyte profiles in each tumor by flow cytometry. Previous research has shown that PDT can evoke acute inflammation,⁷ so we first evaluated the population of leukocytes responsible for innate immune response (neutrophils, B cells, dendritic cells, and macrophages) in both primary and distant tumors 12 hours after PDT treatment. As shown in Figure 4-21, IDOi@TBC-Hf administration and light irradiation led to significant increase in the percentage of tumor-infiltrating neutrophils and B cells with respect to the total number of cells in the tumor compared to PBS (neutrophils: $P=0.0369$ vs. PBS; B cells: $P=0.0215$ vs. PBS). To our surprise,

the percentage of infiltrating dendritic cells (DC) appeared to decrease compared to PBS control in the primary tumor (Figure 4-21c), although the difference is not of statistical significance.

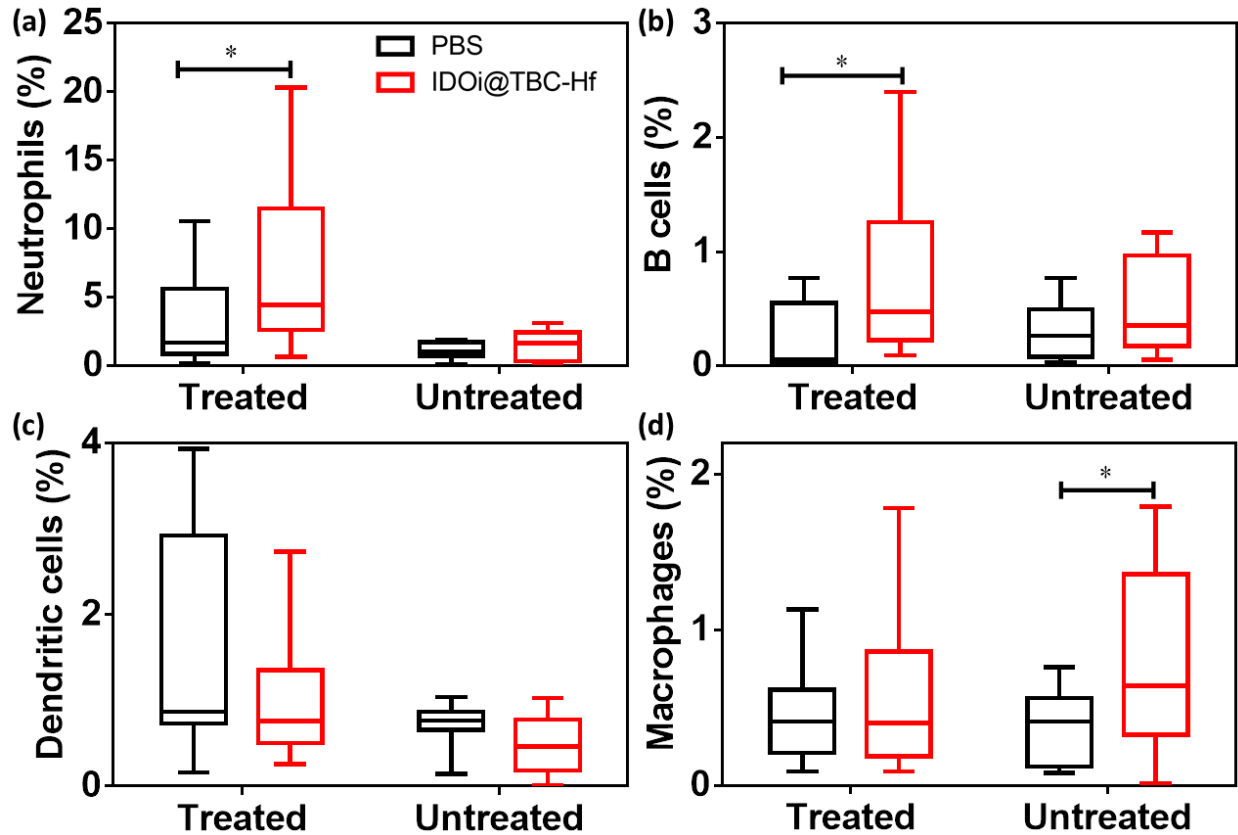


Figure 4-21 Population of leukocytes in the tumor 12 h after IDOi@TBC-Hf PDT treatment. The percentage of tumor-infiltrating neutrophils (a), B cells (b), DCs (c) and macrophages (d), with respect to the total number of cells in the tumor compared to PBS.

To better understand the roles these types of cells played in the antigen presentation after PDT, we further detected the major histocompatibility complex class II (MHC-II) expression on these cells 12 hours after PDT treatment. MHC-II mediates establishment of specific immunity by interacting with CD4 molecules on the surface of helper T cells.⁹ We found a significant decrease in MHC-II expression levels on DCs, macrophages, and neutrophils in the primary treated tumors (DC: $P < 0.0001$ vs. PBS; macrophages: $P = 0.0004$ vs. PBS; neutrophils: $P = 0.006$

vs. PBS, Figure 4-22). These results imply that TBC-Hf mediated PDT may have an impact on the mode of antigen presentation, which is typically the role of DCs.

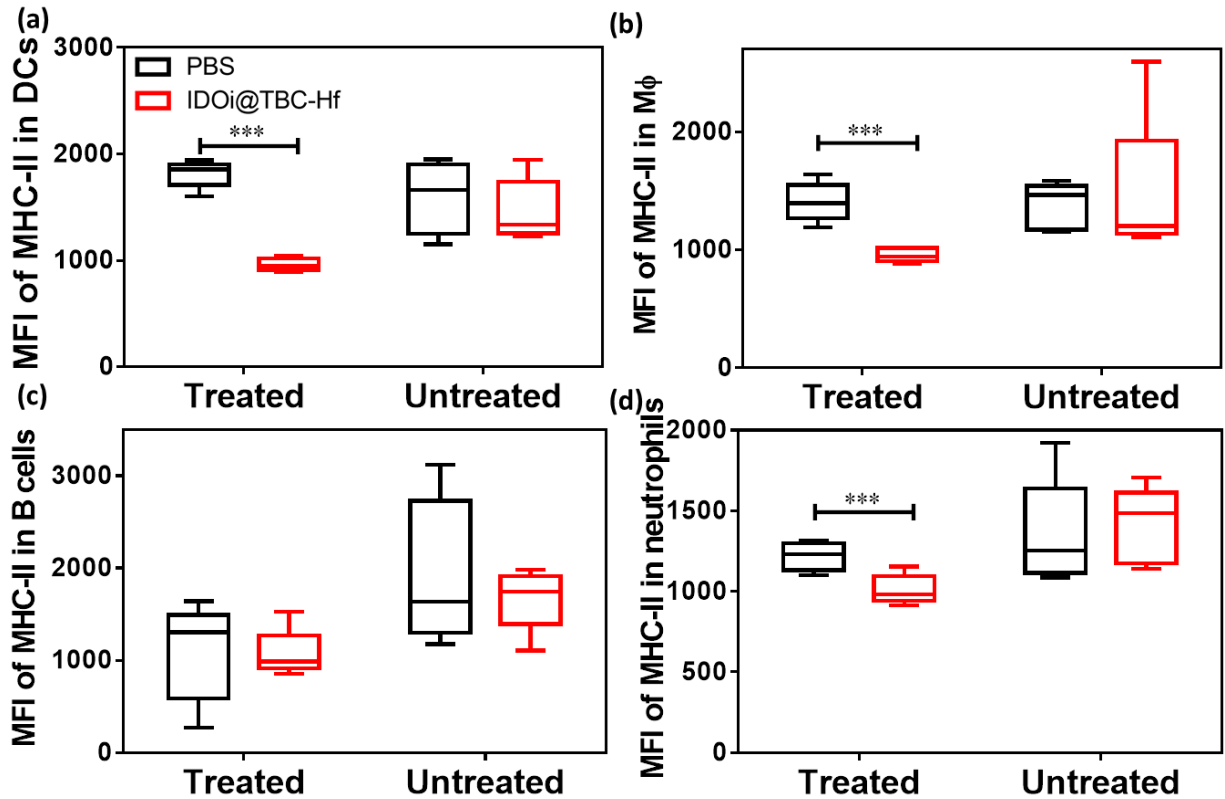


Figure 4-22 The MHC-II expression level in the tumor 12 h after IDOi@TBC-Hf PDT treatment. (a) DCs, (b) macrophages, (c) B cells, and (d) neutrophils.

We also determined the tumor-infiltrating leukocyte profiles 12 days post PDT treatment. As shown in Figure 4-23 a-c, IDOi@TBC-Hf significantly increased the proportion of infiltrating CD8⁺ T cells relative to the total number of cells in the distant tumor (P=0.0012 vs. PBS), an essential step to mounting an antitumor immune response to induce the abscopal effect. In both primary and distant tumors, the percentages of infiltrating CD45⁺ leukocytes and CD4⁺ T cells with respect to the total number of cells in the tumors were significantly increased in mice treated with PDT of IDOi@TBC-Hf (Treated tumor, CD45⁺: P=0.0061 vs. PBS; CD4⁺ T cells:

P=0.0206 vs. PBS. Untreated tumor, CD45⁺: P=0.0001 vs. PBS; CD4⁺ T cells: P=0.0388 vs. PBS). Interestingly, IDOi@TBP-Hf administration and PDT also led to a significant increase in the percentages of tumor-infiltrating B cells and a decrease in the percentages of tumor infiltrating DCs with respect to the total number of cells in the primary tumors 12 days post the treatment (B cells, P=0.0017 vs. PBS; DCs: P=0.0041 vs. PBS, Figure 4-23 d, e).

We also performed T cell blocking experiments to confirm the involvement of T cells in the efficient abscopal response on bilateral subcutaneous MC38 mouse model. MC38 tumor-bearing mice were treated with IDOi@TBC-Hf and light irradiation as described before and received intraperitoneal injection of Mouse IgG, anti-CD4, or anti-CD8 antibody at a dose of 200 µg/mouse/injection on Day 0 and Day 5 post the PDT treatment. While mice treated with Mouse IgG showed regression of both primary and distant tumors, no abscopal effect was observed on mice with blocking of CD4⁺ or CD8⁺ T cells (Figure 4-24). Furthermore, blocking of CD4⁺ and CD8⁺ T cells also diminished the effect of IDOi@TBC-Hf in regressing the primary tumors. These results indicated that CD4⁺ and CD8⁺ T cells were essential not only to abscopal effect but also to primary tumor rejection.

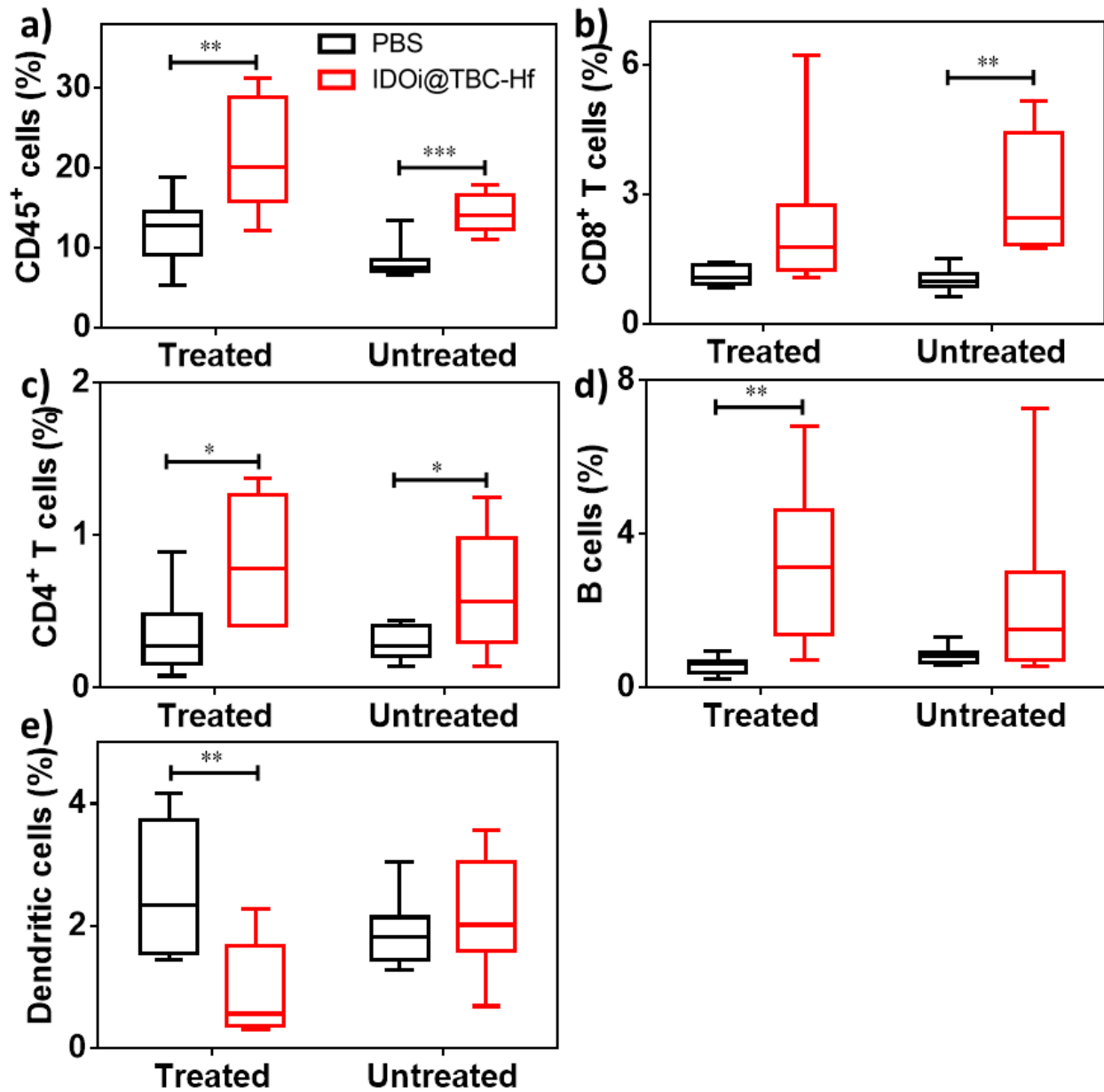


Figure 4-23 Tumor-infiltrating leukocyte profiles in the tumors 12 days after IDOi@TBC-Hf PDT treatment. (a) CD45⁺ T cells, (b) CD8⁺ T cells, (c) CD4⁺ T cells, (d) B cells and (e) DCs, percentages with respect to the total number of cells in the tumors.

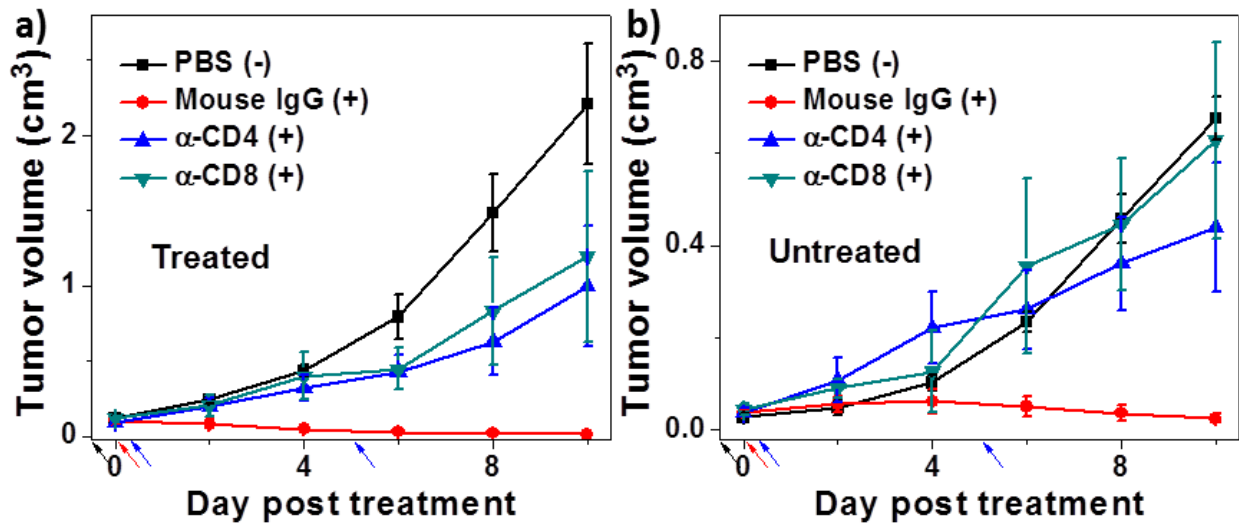


Figure 4-24 *In vivo* T cell blocking experiments. Growth curves for primary, treated (a) and distant, untreated (b) tumors after PDT treatment (+) with IDOi@TBC-Hf and injections of Mouse IgG, anti-CD4, or anti-CD8 antibody, compared to PBS control without PDT treatment (-). Black, red and blue arrows refer to the time of IDOi@TBC-Hf injection, light irradiation and antibody injection, respectively.

4.3 Discussion

In this chapter, we present a new treatment strategy that combines local PDT of a new nMOF, TBC-Hf, in combination with IDO inhibition with nMOF-delivered small molecules to achieve effective and consistent abscopal responses in mouse models of colorectal cancers. We have shown that IDOi released from locally injected IDOi@TBC-Hf reversed the suppressive tumor microenvironment in both treated and untreated tumors, which further synergized with TBC-Hf mediated PDT to stimulate the immune system for activating both acute innate and prolonged adaptive immune response to achieve efficient local tumor regression and a consistent abscopal response. Our treatment method maximizes the benefits of local treatment with systemic immune response for the rejection of both primary and distant tumors while minimizing side effects, potentially affording an effective systemic therapy for metastatic colorectal cancers.

Owing to the outstanding photophysical properties of the chlorin-based TBC ligand, TBC-Hf shows potent PDT efficacy and outperforms its porphyrin counterpart TBP-Hf. The tetracarboxylate ligand constructs a robust framework with very large channels for small molecular inhibitor loading and ROS diffusion, and the coordination to Hf₆ SBUs enhances intersystem crossing of TBC to enhance ¹O₂ generation. As we¹⁰⁻¹³ and others¹⁴⁻¹⁶ have demonstrated the synthetic tunability and potential biomedical applications of nMOFs in the past decade, we believe that the nMOF compositions and structures can be further optimized in order to enhance light absorption and ¹O₂ generation/diffusion. We thus expect nMOF-based synergistic PDT and immunotherapy have the potential for future clinical translation for the treatment of metastatic cancers.

We propose that IDOi@TBC-Hf administration and light irradiation causes highly efficient tumor regression of both primary treated tumors and distant untreated tumors owing to two factors. First, TBC-Hf based PDT causes ICD of cancer cells in the primary tumors, which activates innate immune system and promotes antigen presentation (Figure 4-1). The massive stressed and dying necrotic tumor cells in the PDT-treated primary tumor sites are engulfed by the innate immune effector cells followed by presenting tumor-derived antigenic peptides to T cells, thus stimulating a tumor-specific T cell response. Second, the IDOi is released from intratumorally injected IDOi@TBC-Hf to systemically inhibit IDO activity to reverse the immunosuppressive tumor environments. The two treatment modalities, PDT and IDOi checkpoint blockade therapy, synergize with each other to kill cancer cells locally and create an immunogenic tumor microenvironment systemically, leading to durable and consistent abscopal effects.

Dendritic cells are one of the most important antigen-presenting cells and prevalently believed to play a key role in antitumor immune response.¹⁷ However, we observed a slight decrease of DC population percentage along with a significant decrease of MHC-II expression level on DCs after PDT treatment with IDOi@TBC-Hf, indicating an altered role for DCs after PDT treatment. Meanwhile, the increase of both neutrophils and B cell population percentages implies a compensating effect of other antigen presenting cells to present tumor-associated antigens and initiate the antitumor immune response. Previous studies also suggested that neutrophils, rather than DCs, directly affect T cell proliferation upon PDT treatment.¹⁸ Our future efforts will be directed toward elucidating the roles of neutrophils and B cells in initiating antitumor immune response after the PDT of IDOi@TBC-Hf.

4.4 Conclusion

In this work, we have rationally designed a chlorin-based nMOF with large channels for highly efficient PDT, while simultaneously loaded an IDO inhibitor into its channels to achieve combination therapies of PDT and checkpoint blockade immunotherapy. We consistently observed an abscopal effect in mice receiving treatment with PDT of IDOi@TBC-Hf. The *in situ* vaccination induced by PDT treatment and IDOi immunotherapy synergize with each other and effectively generate systemic antitumor immunity. We believe the present strategy has the potential to significantly increase the durable response rates of checkpoint blockade cancer immunotherapy and lead to clinical benefits for the treatment of metastatic colorectal cancers and other difficult-to-treat cancers.

4.5 Methods

Materials, cell lines, and animals: All of the starting materials were purchased from Sigma-Aldrich and Fisher (USA), unless otherwise noted, and used without further purification.

Murine colon adenocarcinoma cells CT26 and MC38 and murine melanoma cells B16F10 were purchased from the American Type Culture Collection (Rockville, MD, USA) and cultured in Dulbecco's Modified Eagle's Medium (DMEM) medium (Gibco, Grand Island, NY, USA) supplemented with 10% FBS.

C57BL/6 female mice (6 weeks, 20-22 g) and BALB/c female mice (6 weeks, 20-22 g) were provided by Harlan Laboratories, Inc (USA). The study protocol was reviewed and approved by the Institutional Animal Care and Use Committee (IACUC) at the University of Chicago.

Synthesis of TBC-Hf: To a 2-dram glass vial was added 1 mL of HfCl₄ solution [2 mg/mL in N,N-dimethylformamide (DMF), 6.2 μmol], 1 mL of the H₄TBC solution (1.9 mg/mL in DMF, 2.4 μmol), and 60 μL of 88% formic acid (1.4 mmol). The reaction mixture was kept in an 80 °C oven for 2 days. The purple powder was collected by centrifugation and washed with DMF, 1% triethylamine in ethanol (v/v) and ethanol.

Synthesis of TBP-Hf: To a 2-dram glass vial was added 1 mL of HfCl₄ solution [2 mg/mL in N,N-diethylformamide (DEF), 6.2 μmol], 1 mL of the H₄TBP solution (1.9 mg/mL in DEF, 2.4 μmol), and 60 mg of benzoic acid (0.49 mmol). The reaction mixture was kept in a 120 °C oven for 2 days. The violet powder was collected by centrifugation and washed with DMF, 1% triethylamine in ethanol (v/v), and ethanol.

Powder X-ray diffraction: TBC-Hf or TBP-Hf sample was prepared by centrifugation in a capillary tube with one end sealed. The powder X-ray diffraction pattern was acquired on Bruker D8 VENTURE single crystal dual-source diffractometer (Bruker, Germany) and integrated by software.

BET surface area measurement: Nitrogen adsorption of TBC-Hf and TBP-Hf was tested on 3Flex-Surface Characterization Analyzer (Micromeritics, USA) at 77K. The BET surface areas were calculated by software to be 1077 and 1462 m²/g.

Digestion for ICP-MS: The nMOF samples was dried under vacuum overnight before being digested by a mixture of concentrate nitric acid and hydrofluoric acid (63% HF/69% HNO₃ 1/100 v/v). The sample was diluted 35 times and filtered by a PES syringe filter unit before instrument analysis.

Thermogravimetric analysis: Thermogravimetric analysis on TBC-Hf was carried out on a Shimadzu TGA-50 thermogravimetric analyzer. The nMOF was collected by centrifugation and dried under vacuum overnight. The sample was then transferred to a platinum plate and heated at 3 °C/min to 650 °C in air. The weight percentage was plotted against temperature and was normalized to the weight at 150 °C to eliminate the influence of absorbed moisture. The IDOi loading was calculated following the equation below:

$$\text{loading wt\%} = \left(1 - \frac{\text{remaining wt\% after loading}}{\text{remaining wt\% before loading}} \right) \times 100\%$$

Fluorescence measurement: The fluorescence spectra were taken on a spectrofluorophotometer (Fluorolog-3, Horiba, Japan). Samples were prepared as 1 μM solutions in phosphate buffer saline or water by equivalent ligand concentration for the measurements.

Fluorescence lifetime measurement: Time-domain lifetimes were measured on a ChronosBH lifetime fluorometer (ISS, Inc.) using Time-Correlated Single Photon Counting (TCSPC) methods. The fluorometer contained Becker-Hickl SPC-130 detection electronics and an HPM-100-40 Hybrid PMT detector. Excitation was provided by a 403 nm picosecond pulsed laser source (Hamamatsu PLP-10). Emission wavelengths were selected with interference filters (Semrock). The Instrument Response Function (IRF) was measured to be approximately 0.009 ns FWHM in a 1% scattering solution of Ludox LS colloidal silica. Multi-component exponential decay lifetimes were fit via a forward convolution method in the Vinci control and analysis software. Samples were prepared into solution/suspensions in water for the measurement.

Singlet Oxygen Generation: A light-emitting diode (LED) array with peak emission at 650 nm was used as the light source of singlet oxygen generation test. The irradiance of LED is 20 mW/cm^2 . Singlet oxygen sensor green (SOSG) reagent (Life Technologies) was employed for the detection of singlet oxygen. H_4TBP , H_4TBC , TBP-Hf and TBC-Hf samples were prepared in 1 μM solutions/suspensions in water (for the nMOFs, the concentration was calculated as ligand equivalents). To 2 mL each of these solutions/suspensions, SOSG stock solution (5 μL at 5 mM) was added (final concentration=12.5 μM) before fluorescence measurement. For a typical measurement, fluorescence intensity was acquired on a spectrofluorophotometer (RF-5301PC, Shimadzu, Japan) with excitation at 504 nm and emission at 525 nm (slit width 1.5 nm/3 nm for ex/em). Fluorescence was measured after irradiation by LED for 0 (as background), 0.5, 1, 1.5, 2, 3, 4, 5, 7 and 10 min.

Cellular uptake evaluation: TBP-Hf or TBC-Hf was incubated with CT26 cells at a Hf concentration of 150 μM for 24 h. The cells were collected, counted with a hemocytometer, and digested by concentrated nitric acid. The cellular uptake amounts of Hf were determined by ICP-MS and normalized with cell numbers.

IDOi encapsulation: To a suspension of TBC-Hf in ethanol (2.5 mg/mL, 3.0 mL), 3.3 mg of IDOi was added. The mixture was sonicated for 1 minute and 3.0 mL of water was added. The solution was stirred at room temperature in dark for 12 h to afford IDOi@TBC-Hf. IDOi@TBC-Hf was collected by centrifugation and washed with 50% ethanol/water.

***In vitro* PDT efficacy:** The cytotoxicity of TBC-Hf and H₄TBC was evaluated in murine colorectal cancer cell CT26 and murine melanoma cell B16F10, respectively. CT26 cells or B16F10 cells were seeded on 96-well plates at 1000 cells/well. The cells were treated with TBC-Hf and H₄TBC at various ligand concentrations (2, 4, 10, 15, 20, and 50 μM base on ligand concentrations). A further incubation of 4 h was allowed followed by replacing the culture medium with 100 μL of fresh medium. The cells were irradiated with LED light (650 nm) at 100 mW/cm^2 for 15 min (total light dose 90 J/cm^2) or kept in dark, respectively. The cells were further incubated to achieve a total incubation time of 72 h. The cell viability was detected by (3-(4,5-dimethylthiazol-2-yl)-5-(3-carboxymethoxyphenyl)-2-(4-sulfophenyl)-2H-tetrazolium) (MTS) assay (Promega, USA).

Abscopal Effect: The PDT efficacy of IDOi@TBC-Hf was investigated using a bilateral CT26 mouse colorectal cancer model and a bilateral MC38 mouse colorectal cancer model. Tumor bearing mice were established by subcutaneous inoculation of CT26 or MC38 cell suspension (1×10^6 cells per mouse on the right flank and 2×10^5 cells per mouse on the left flank) into 6-

week female BALB/c or 6-week female C57BL/6 mice, respectively. When the right tumors reached 100 mm³, the CT26 tumor bearing mice received intratumoral injection only into the right tumors of PBS, H₄TBC, H₄TBC+IDOi, TBC-Hf, or IDOi@TBC-Hf at a ligand dose of 20 μmol/kg and IDOi dose of 1.5 mg/kg. Twelve hours post injection, CT26 tumor bearing mice were anesthetized with 2% (v/v) isoflurane and right flank tumors were irradiated with a 650 nm LED at 0.1 W/cm² for 15 min (90 J/cm²). IDOi@TBC-Hf without light irradiation served as a dark control. The nMOF injection and light irradiations were performed every three days for a total two injections and irradiations. For MC38 tumor model, mice received intratumoral injection only into the right tumors of PBS, TBC-Hf, or IDOi@TBC-Hf at a ligand dose of 20 μmol/kg and IDOi dose of 1.5 mg/kg. Twelve hours post injection, MC38 tumor bearing mice were anesthetized with 2% (v/v) isoflurane and right flank tumors were irradiated with a 650 nm LED at 0.1 W/cm² for 15 min (90 J/cm²). IDOi@TBC-Hf without light irradiation served as a dark control. The nMOF injection and light irradiations were performed only once on MC38 tumor bearing mice. For both CT26 and MC38 models, no NMOF injection or light irradiation was performed on the left tumors.

To evaluate the therapeutic efficacy, the tumor size was measured with a digital caliper every day. Tumor volumes were calculated as follows: (width² × length)/2. Finally, all mice were sacrificed when the tumor size of control group exceeded 2 cm³, and the excised tumors were photographed and weighed.

T cell blocking: The abscopal effect of IDOi@TBC-Hf was evaluated on bilateral subcutaneous MC38 model on C57BL/6 mice with CD4⁺ T cell or CD8⁺ T cell depletion. When the right tumors reached ~100 mm³, IDOi@TBC-Hf was intratumorally injected to the mice at a dose of 20 μmol/kg. Anti-CD4 (for CD4⁺ T cell depletion), anti-CD8 (for CD8⁺ T cell depletion), or

mouse IgG (control) were intraperitoneally injected to the mice (200 µg/mouse/injection) on Day 0 and Day 5 post the first treatment. Twelve hours post injection, mice were anesthetized with 2% (v/v) isoflurane and the right tumors were irradiated with LED light irradiation (100 mW/cm², 90 J/cm², 650 nm). Single IDOi@TBC-Hf injections followed by single light irradiations were carried out. To evaluate the therapeutic efficacy, the tumor size was measured with a digital caliper every other day. Tumor volumes were calculated as follows: (width² × length)/2.

ELISPOT assay: Tumor-specific immune responses to IFN-γ was measured *in vitro* by ELISPOT assay (Mouse IFN gamma ELISPOT Ready-SET-Go!®; Cat. No. 88-7384-88; eBioscience). A Millipore Multiscreen HTS-IP plate was coated overnight at 4 °C with anti-Mouse IFN-γ capture antibody. Single-cell suspensions of splenocytes were obtained from MC38 tumor-carrying mice and seeded onto the antibody-coated plate at a concentration of 2×10⁵ cells/well. Cells were incubated with or without KSPWFTTL (KSP) stimulation (10 µg/mL; in purity > 95%; PEPTIDE 2.0) for 48 h at 37 °C and then discarded. The plate was then incubated with biotin-conjugated anti-IFN-γ detection antibody at room temperature (r.t.) for 2 h, followed by incubation with Avidin-HRP for 2 h at r.t. AEC substrate solution (Sigma, Cat. AEC101) was added for cytokine spot detection.

Flow Cytometry: Tumors were harvested, treated with 1 mg/mL collagenase I (Gibco™, USA) for 1 h, and ground by the rubber end of a syringe. Cells were filtered through nylon mesh filters and washed with PBS. The single-cell suspension was incubated with anti-CD16/32 (clone 93; eBiosciences) to reduce nonspecific binding to FcRs. Cells were further stained with the following fluorochrome-conjugated antibodies: CD45 (30-F11), CD3e (145-2C11), CD4 (GK1.5), CD8 (53-6.7), Foxp3 (FJK-16s), CD11b (M1/70), Ly6C (HK1.4), Ly6G (RB6-8C5),

F4/80 (BM8), B220 (RA3-6B2) and PI staining solution (all from eBioscience). LSR FORTRESSA (BD Biosciences) was used for cell acquisition, and data analysis was carried out using FlowJo software (TreeStar, Ashland, OR).

MHC-II expression: Tumors were harvested 12 hours after LED irradiation, treated with 1 mg/mL collagenase I, and ground by the rubber end of a syringe. Cells were filtered through nylon mesh filters and washed with PBS. The single cell suspension was incubated with anti-CD16/32 (clone 93; eBiosciences) for 10 minutes and then stained with CD45, CD3e, CD11b, Ly6G, B220, F4/80, CD11c and MHC-II. The expression levels of MHC-II on CD11b+Ly-6G+, CD3e-B220+, CD3e-CD11c+ and CD3e-CD11c-F4/80 populations were determined respectively.

4.6 References

1. Lu, K., He, C. & Lin, W. Nanoscale Metal–Organic Framework for Highly Effective Photodynamic Therapy of Resistant Head and Neck Cancer. *J. Am. Chem. Soc.* **136**, 16712-16715 (2014).
2. Lu, K., He, C. & Lin, W. A Chlorin-Based Nanoscale Metal–Organic Framework for Photodynamic Therapy of Colon Cancers. *J. Am. Chem. Soc.* **137**, 7600-7603 (2015).
3. Morris, W., *et al.* Synthesis, structure, and metalation of two new highly porous zirconium metal–organic frameworks. *Inorg Chem* **51**, 6443-6445 (2012).
4. Liu, J., *et al.* Nanoscale metal– organic frameworks for combined photodynamic & radiation therapy in cancer treatment. *Biomaterials* **97**, 1-9 (2016).
5. Park, J., Jiang, Q., Feng, D., Mao, L. & Zhou, H.-C. Size-Controlled Synthesis of Porphyrinic Metal–Organic Framework and Functionalization for Targeted Photodynamic Therapy. *J. Am. Chem. Soc.* **138**, 3518-3525 (2016).
6. Yue, E.W., *et al.* Discovery of potent competitive inhibitors of indoleamine 2, 3-dioxygenase with in vivo pharmacodynamic activity and efficacy in a mouse melanoma model. *J. Med. Chem.* **52**, 7364-7367 (2009).

7. Castano, A.P., Mroz, P. & Hamblin, M.R. Photodynamic therapy and anti-tumour immunity. *Nature Reviews Cancer* **6**, 535-545 (2006).
8. Uyttenhove, C., *et al.* Evidence for a tumoral immune resistance mechanism based on tryptophan degradation by indoleamine 2, 3-dioxygenase. *Nat. Med.* **9**, 1269-1274 (2003).
9. Janeway, C.A., Travers, P., Walport, M. & Capra, J.D. Immunobiology: the immune system in health and disease. (2005).
10. Huxford, R.C., Della Rocca, J. & Lin, W. Metal–organic frameworks as potential drug carriers. *Curr. Opin. Chem. Biol.* **14**, 262-268 (2010).
11. Lin, W., Rieter, W.J. & Taylor, K.M. Modular synthesis of functional nanoscale coordination polymers. *Angewandte Chemie International Edition* **48**, 650-658 (2009).
12. Della Rocca, J., Liu, D. & Lin, W. Nanoscale Metal–Organic Frameworks for Biomedical Imaging and Drug Delivery. *Accounts Chem Res* **44**, 957-968 (2011).
13. He, C., Liu, D. & Lin, W. Nanomedicine Applications of Hybrid Nanomaterials Built from Metal–Ligand Coordination Bonds: Nanoscale Metal–Organic Frameworks and Nanoscale Coordination Polymers. *Chem. Rev.* **115**, 11079-11108 (2015).
14. Cui, Y., Yue, Y., Qian, G. & Chen, B. Luminescent functional metal–organic frameworks. *Chem. Rev.* **112**, 1126-1162 (2011).
15. Furukawa, H., Cordova, K.E., O’Keeffe, M. & Yaghi, O.M. The chemistry and applications of metal-organic frameworks. *Science* **341**, 1230444 (2013).
16. Horcajada, P., *et al.* Metal–organic frameworks in biomedicine. *Chem. Rev.* **112**, 1232-1268 (2011).
17. Palucka, K. & Banchereau, J. Cancer immunotherapy via dendritic cells. *Nature Reviews Cancer* **12**, 265-277 (2012).
18. Kousis, P.C., Henderson, B.W., Maier, P.G. & Gollnick, S.O. Photodynamic therapy enhancement of antitumor immunity is regulated by neutrophils. *Cancer Res.* **67**, 10501-10510 (2007).

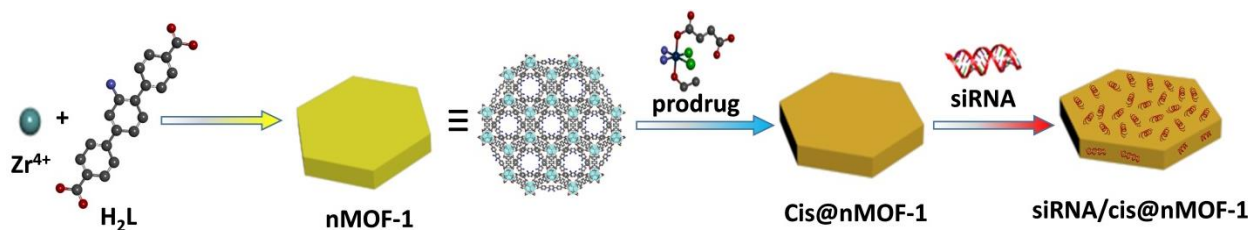
Chapter 5. A Nanoscale Metal-Organic Framework for the Co-delivery of Chemotherapeutic Agents and Nucleic Acid Drugs

5.1 Rationale of the nMOF design

Nanoscale metal-organic frameworks display multifunctionality as a nanocarrier platform for drug delivery, by virtue of their high porosity and structural tunability. In Chapters 2, 3, and 4, we showed examples that directly construct nMOFs with cargo molecules as the struts. In this chapter, we will introduce another work on drug delivery where we employed the large pores of the MOF structure as well as the surface metal coordinate sites for the co-delivery of therapeutic agents to treat resistant cancer.

We surmise that nMOFs can realize the co-delivery of chemotherapeutics and small interfering RNAs (siRNAs) with the following strategy: the large pores of nMOFs can be used to load chemotherapeutics while the metal ions on the nMOF surfaces can be used to bind siRNAs. The simultaneous and efficient delivery of cisplatin and pooled siRNAs to ovarian cancer cells can allow for enhanced anticancer efficacy by blocking multiple drug resistance pathways.

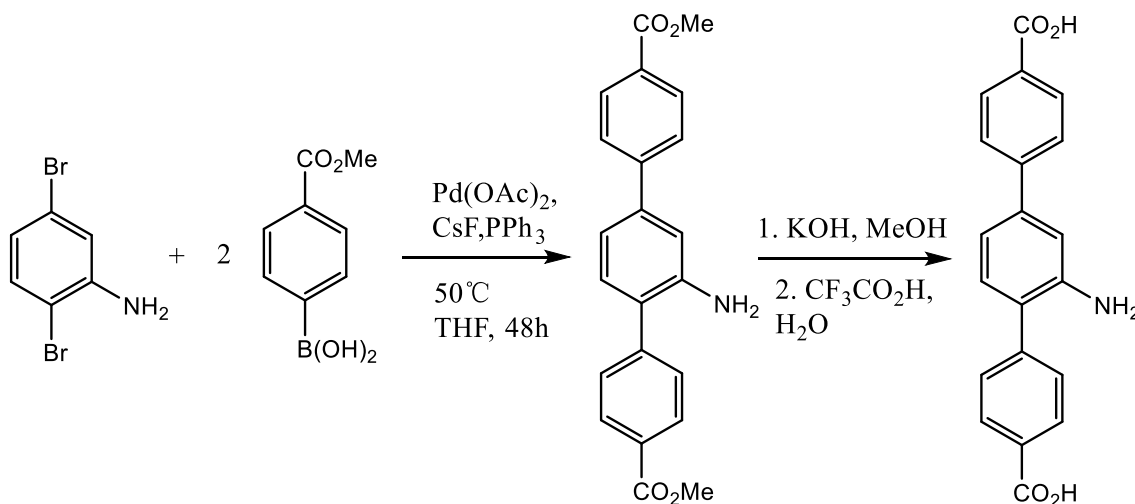
Scheme 5-1 MOF synthesis and drug loading. Adapted with permission from *J. Am. Chem. Soc.*, **2014**, *136*, 5181–5184. Copyright 2014 American Chemical Society.



5.2 Results and Discussion

5.2.1 Synthesis and characterization of the 2'-amino-p-terphenyl-4,4''-dicarboxylate ligand

Scheme 5-2 Synthesis of 2'-amino-p-terphenyl-4,4''-dicarboxylic acid (H_2L). Reprinted with permission from *J. Am. Chem. Soc.*, **2014**, *136*, 5181–5184. Copyright 2014 American Chemical Society.



2'-amino-p-terphenyl-4,4''-dicarboxylic acid (H_2L) was synthesized by the route described in Scheme 5-2 as reported previously.¹ In an 100 mL round-bottom flask 2,5-dibromoaniline (2.00 g, 8.0 mmol), 4-(methoxycarbonyl)-phenylboronic acid (4.40 g, 24.5 mmol) and CsF (5.82 g, 38 mmol) were suspended in 50 mL of anhydrous tetrahydrofuran (THF) under nitrogen protection, followed by addition of palladium acetate (0.60 g, 2.7 mmol) and PPh_3 (1.61 g, 6.1 mmol). The mixture was heated at $50\text{ }^\circ\text{C}$ for 48 h. The methyl ester product (Me_2L) was extracted with water/dichloromethane (DCM) and purified by silica gel column chromatography (DCM: ethyl ether = 50:1 with 0.2% - 0.5% triethylamine). Yield: 58%. 1H NMR (Chloroform- D , Figure 5-1): δ =8.10 (m, 4H), 7.65 (d, 2H), 7.57 (d, 2H), 7.22 (d, 1H), 7.09 (d, 1H), 7.01 (s, 1H), 3.93 (two overlapping singlets, 6H), 3.88 (s, 2H).

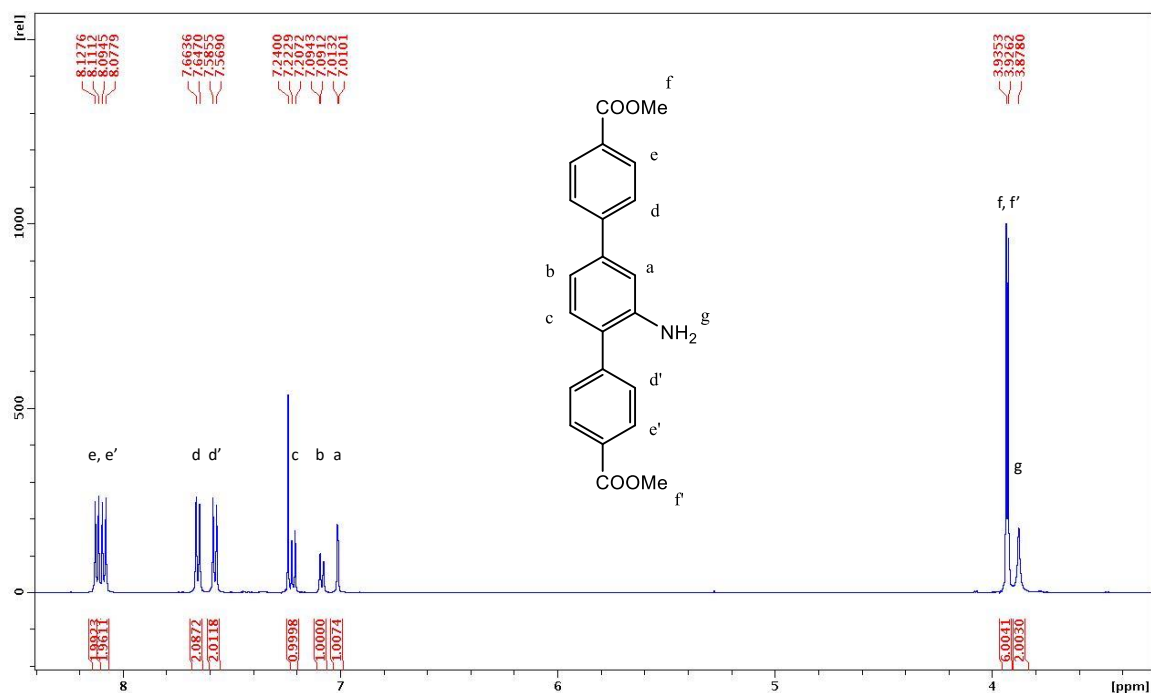


Figure 5-1 ¹H NMR spectrum of Me₂L in chloroform-D. Reprinted with permission from *J. Am. Chem. Soc.*, **2014**, *136*, 5181–5184. Copyright 2014 American Chemical Society.

The Me₂L (1.68 g, 4.65 mmol) was suspended in 200 mL of THF and heated to 40 °C. To the suspension 100 mL of 5.5 M KOH methanol solution was added and the resulting mixture was stirred at 40 °C for 18 hours. A white solid was collected by centrifugation, and then treated with 12 mL of trifluoroacetic acid in 100 mL of THF at room temperature for 2 h. The yellow solid product (H₂L) was isolated by vacuum filtration and washed with THF, methanol and ether. Yield: 80%. ¹H NMR (DMSO-d₆, Figure 5-2): δ=12.97 (br, 2H), 8.03 (m, 4H), 7.74 (d, 2H), 7.61 (d, 2H), 7.16 (d, 2H), 7.02 (dd, 1H), 5.12 (br, 2H). ¹³C NMR (DMSO-d₆, Figure 5-3): δ=167.66, 167.63 (COOH), 146.24 (C1'), 145.00 (C1''), 144.25 (C1), 139.96 (C4'), 131.31 (C6'), 130.40, 130.28 (C3'', C3), 129.98, 129.54 (C4'', C4), 129.19 (C2''), 126.97 (C2), 125.04 (C2'), 115.96 (C5'), 114.26 (C3').

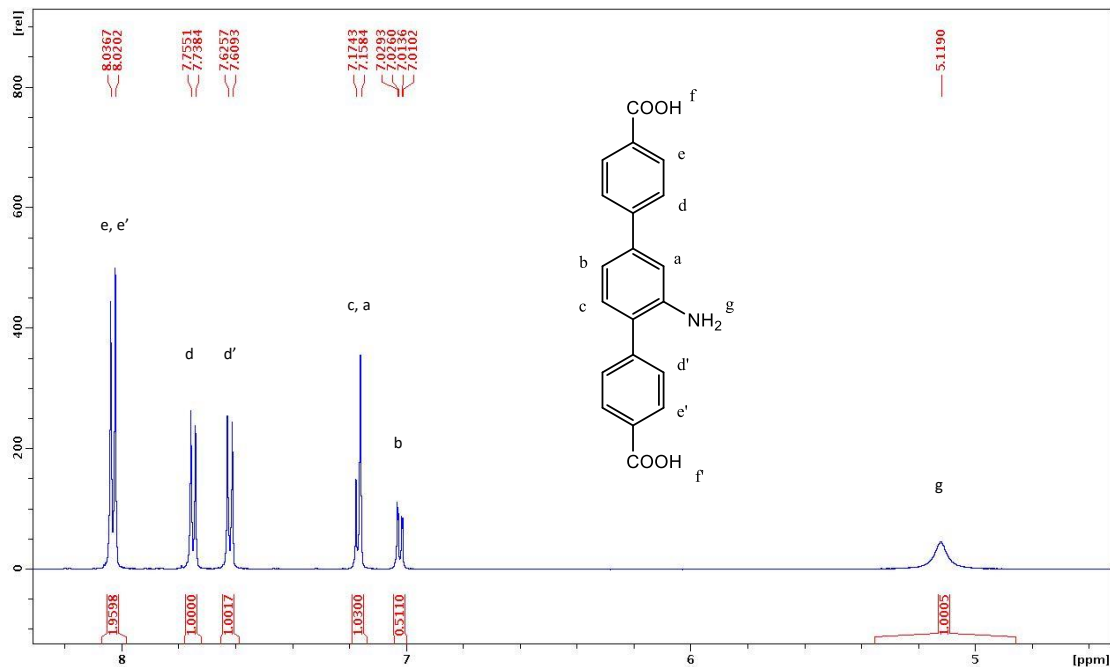


Figure 5-2 ^1H NMR spectrum of H_2L in DMSO-d_6 . Reprinted with permission from *J. Am. Chem. Soc.*, **2014**, *136*, 5181–5184. Copyright 2014 American Chemical Society.

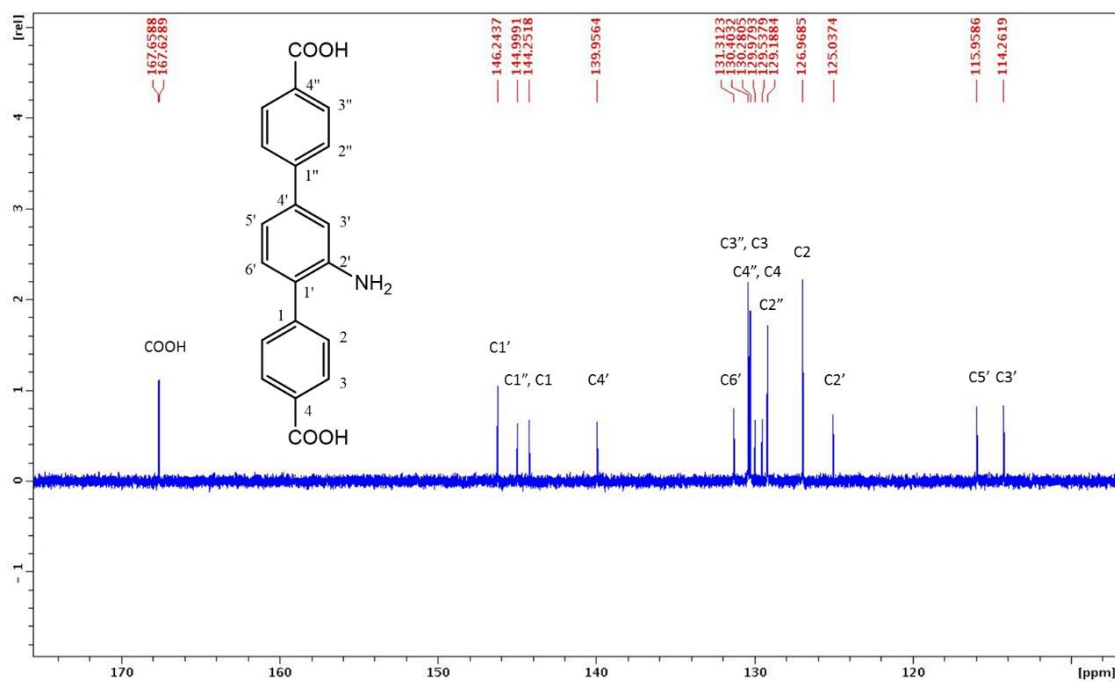
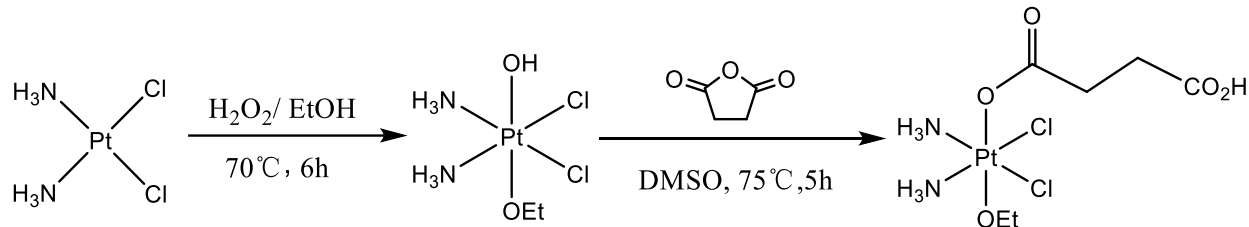


Figure 5-3 ^{13}C NMR spectrum of H_2L in DMSO-d_6 . Reprinted with permission from *J. Am. Chem. Soc.*, **2014**, *136*, 5181–5184. Copyright 2014 American Chemical Society.

5.2.2 Synthesis of the cisplatin prodrug

Scheme 5-3 Synthesis of the cisplatin prodrug. Adapted with permission from *J. Am. Chem. Soc.*, **2014**, *136*, 5181–5184. Copyright 2014 American Chemical Society.



A modified procedure from a previous report was employed to synthesize the cisplatin prodrug $\text{cis,cis,trans-}[\text{Pt}(\text{NH}_3)_2\text{Cl}_2(\text{OEt})(\text{OCOCH}_2\text{CH}_2\text{CO}_2\text{H})]$ (Scheme 5-3).² To an ethanolic suspension of cisplatin (445 mg in 240 mL, 1.48 mmol) 1.00 mL of 30% hydrogen peroxide solution was added. The reaction mixture was heated at 70°C in the dark for 6 h. A yellow product of $\text{cis,cis,trans-}[\text{Pt}(\text{NH}_3)_2\text{Cl}_2(\text{OH})(\text{OEt})]$ was obtained in 76% yield after removal of the solvent in vacuo. $^1\text{H NMR}$ (DMSO-d_6 , Figure 5-4): $\delta=5.55$ (m, 6H), 3.50 (tetra, 2H), 1.05 (t, 3H).

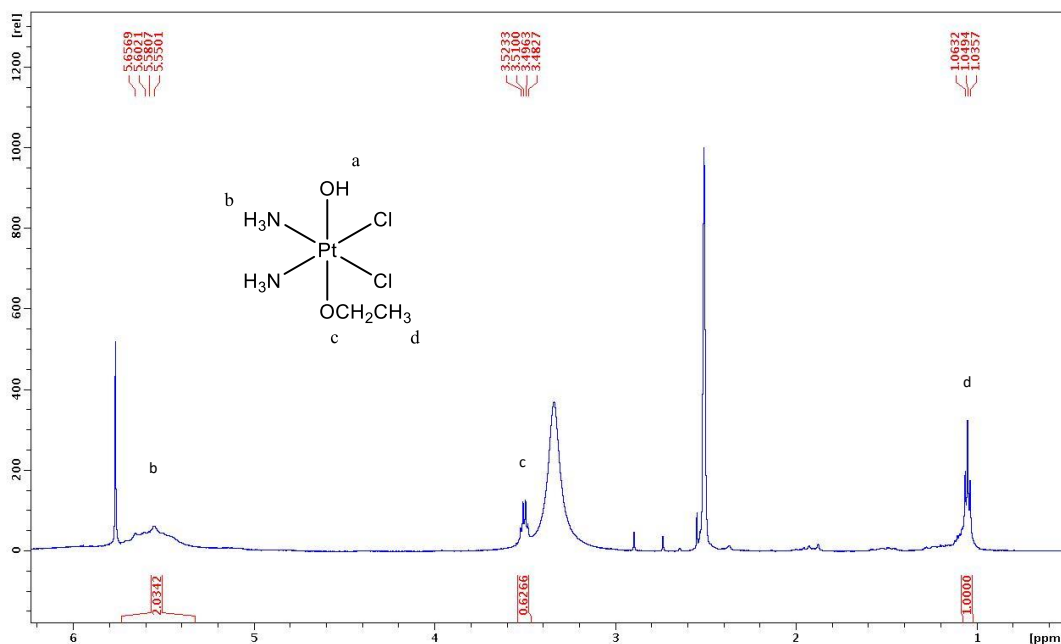


Figure 5-4 $^1\text{H NMR}$ spectrum of $\text{Pt}(\text{NH}_3)_2\text{Cl}_2(\text{OH})(\text{OEt})$ in DMSO-d_6 . Reprinted with permission from *J. Am. Chem. Soc.*, **2014**, *136*, 5181–5184. Copyright 2014 American Chemical Society.

Succinic anhydride (298 mg, 2.98 mmol) and Pt(NH₃)₂Cl₂(OH)(OEt) (107 mg, 0.30 mmol) were dissolved in 3 mL of anhydrous DMSO after drying in vacuo. The mixture was stirred in the dark at 65 °C overnight. Solution volume was reduced under vacuum and the product was crushed out by DCM and was recrystallized in acetone and ethyl ether. Yield: 53%. ¹H NMR (DMSO-d₆, Figure 5-5): δ=12.04 (br, 1H), 5.86 (m, 6H), 3.40 (tetra, 2H), 2.41 (m, 2H), 2.37 (m, 2H), 1.05 (t, 3H). ¹³C NMR (DMSO-d₆, Figure 5-6): δ=180.49, 174.56 (carboxylate), 67.04 (OCH₂), 32.05, 30.67 (-CH₂CH₂-), 17.17 (CH₃). ¹⁹⁵Pt NMR (DMSO-d₆, Figure 5-7): δ= 1001.7 (quintet).

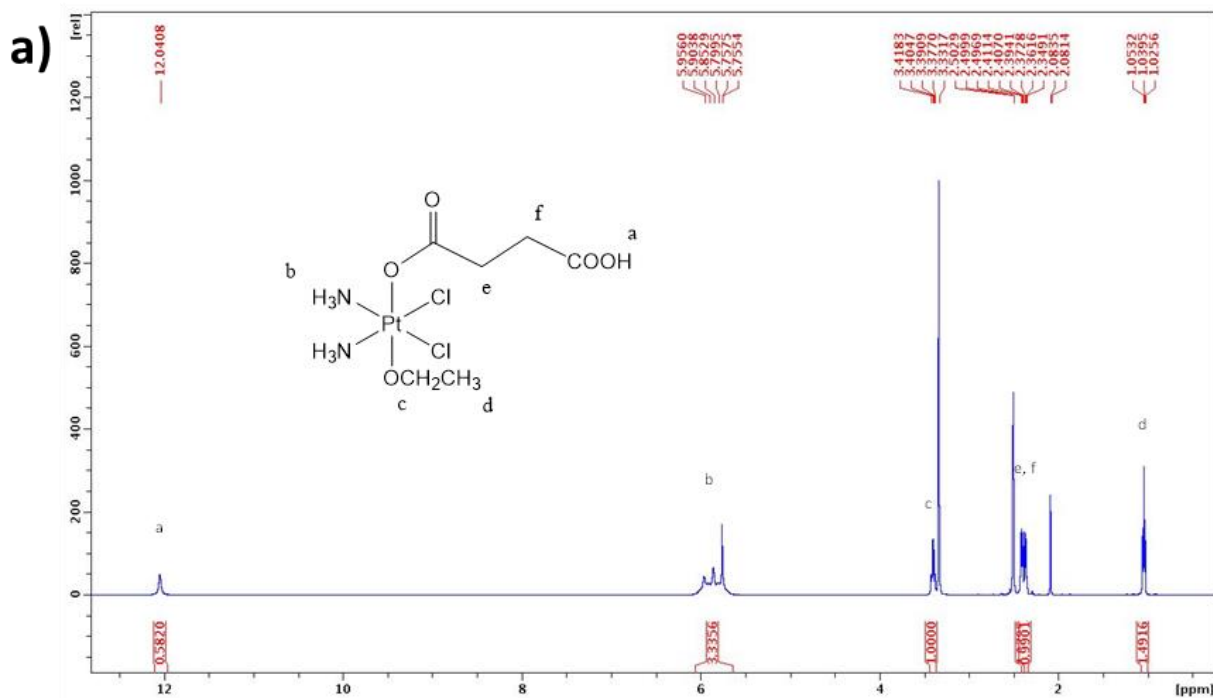


Figure 5-5 ¹H NMR spectra of cis,cis,trans-[Pt(NH₃)₂Cl₂(OEt)(OCOCH₂CH₂CO₂H)] in DMSO-d₆, the full spectrum (a) and expanded view of portions of the spectrum (b,c).

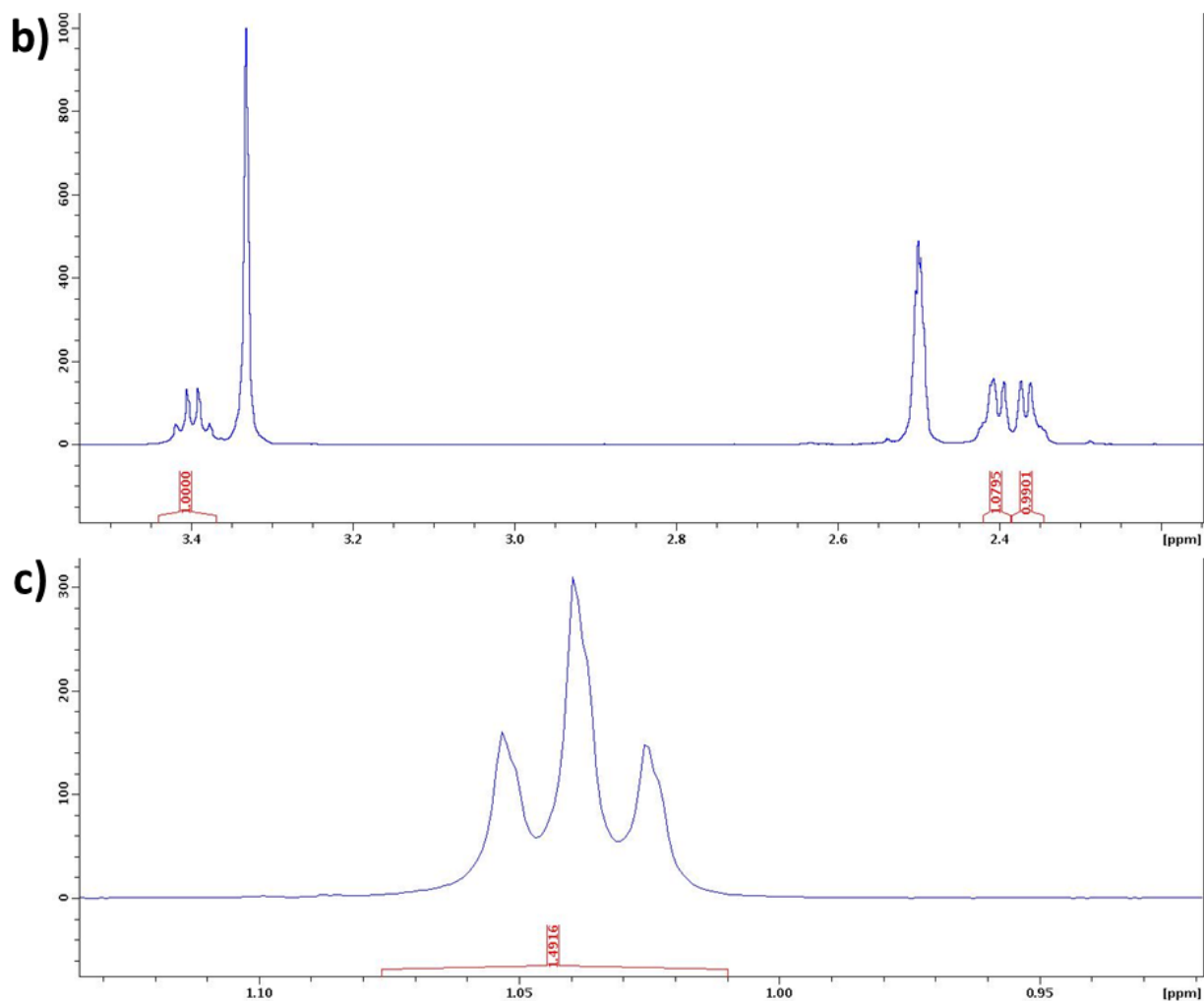


Figure 5-5 (Continued) ^1H NMR spectra of $\text{cis,cis,trans-[Pt(NH}_3)_2\text{Cl}_2(\text{OEt})-(\text{OCOCH}_2\text{CH}_2\text{CO}_2\text{H)]}$ in DMSO-d_6 , the full spectrum (a) and expanded view of portions of the spectrum (b,c). Reprinted with permission from *J. Am. Chem. Soc.*, **2014**, *136*, 5181–5184. Copyright 2014 American Chemical Society.

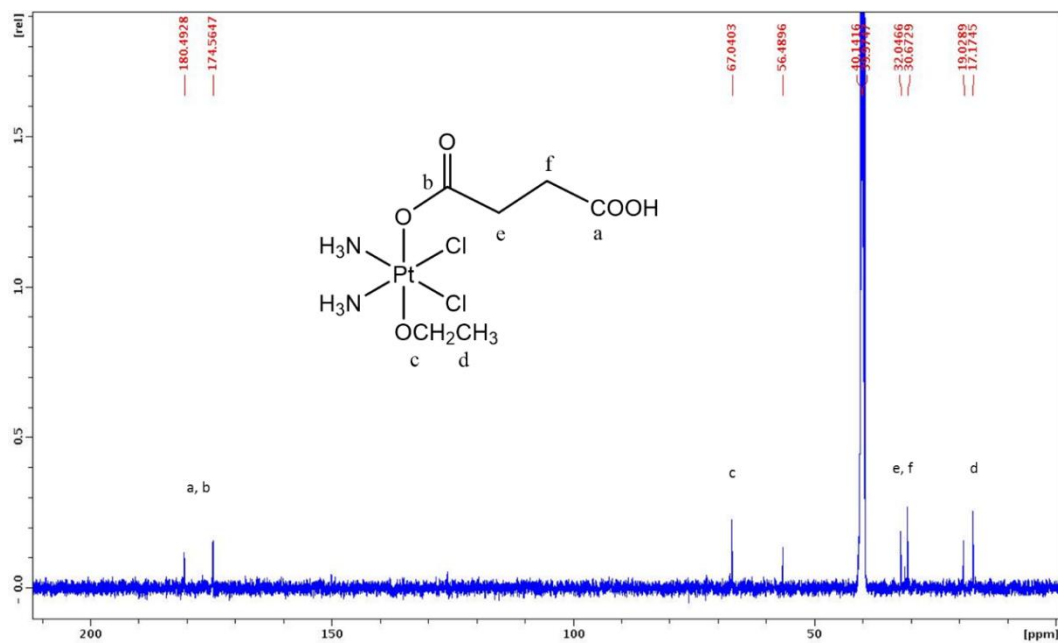


Figure 5-6 ^{13}C NMR spectrum of $\text{cis,cis,trans-[Pt(NH}_3)_2\text{Cl}_2(\text{OEt})-(\text{OCOCH}_2\text{CH}_2\text{CO}_2\text{H})]$ in DMSO-d_6 . Reprinted with permission from *J. Am. Chem. Soc.*, **2014**, *136*, 5181–5184. Copyright 2014 American Chemical Society.

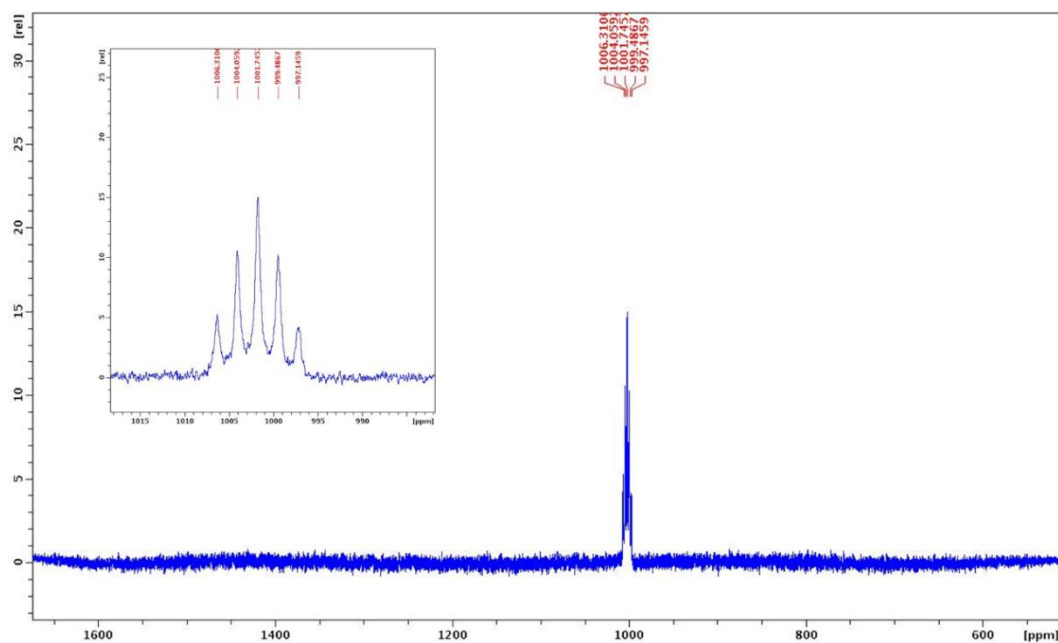


Figure 5-7 ^{195}Pt NMR spectrum of $\text{cis,cis,trans-[Pt(NH}_3)_2\text{Cl}_2(\text{OEt})-(\text{OCOCH}_2\text{CH}_2\text{CO}_2\text{H})]$ in DMSO-d_6 . The coupling to two equivalent ^{14}N nuclei splits the peak to quintet, coupling constant $^1J(^{195}\text{Pt}-^{14}\text{N})=197.0$. Reprinted with permission from *J. Am. Chem. Soc.*, **2014**, *136*, 5181–5184. Copyright 2014 American Chemical Society.

5.2.3 Synthesis and characterization of nMOF-1

nMOF-1 was synthesized by heating a N,N-dimethylformamide (DMF) solution of $ZrCl_4$ and H_2L at 80 °C for 5 days with acetic acid as modulator, which is different from the other reports (Scheme 5-1).³ To our surprise, the as-synthesized **nMOF-1** did not adopt a UiO type structure as predicted, implied by its powder X-ray diffraction (PXRD, Figure 5-8a) from that for a UiO MOF and the hexagonal plate-like morphology by TEM (Tecnai F30, FEI, USA, Figure 5-8b). Instead, a new type of SBU with a formula of $[Zr_6(\mu_3-O)_4(\mu_3-OH)_4]_2(\mu_2-OH)_6$ was formed in which two $Zr_6(\mu_3-O)_4(\mu_3-OH)_4$ SBUs are bridged by 6 μ_2 -hydroxyl groups to construct a new structure as modeled in Figure 5-9. The new structure adopts $P\bar{3}1c$ symmetry and the pore sizes are the same to the UiO type structures with the same ligand. TEM micrographs give the dimensions of the nMOFs to be ~100 nm in diameter of plates and ~30 nm in thickness (Figure 5-8 b,e). High resolution TEM images confirm that the distances between the lattice fringes are 1.83 nm (Figure 5-8e), corresponding to the predicted d_{101} value of 1.87 nm. The fast Fourier transform pattern (FFT) proved a 6-fold symmetry along the observation direction, consistent to the hexagonal symmetry of the structure (Figure 5-8e, inset).

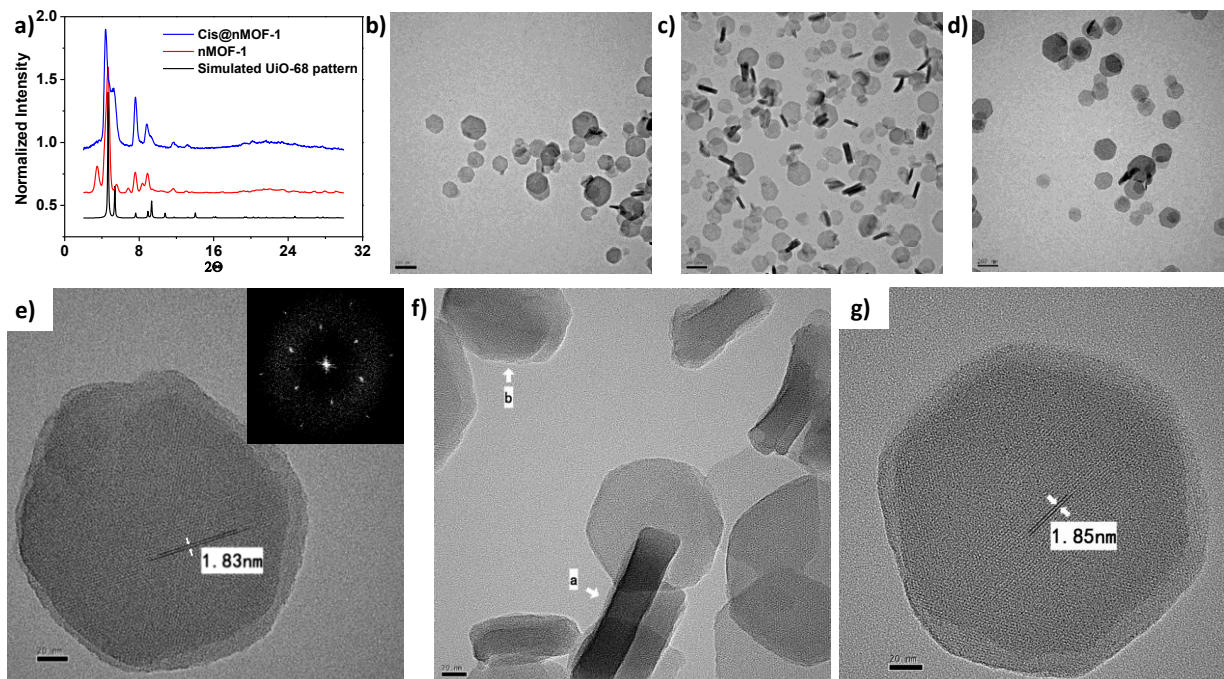


Figure 5-8 Structural characterization of the nMOFs before and after drug loading. (a) PXRD patterns of UiO-68 (black), **nMOF-1** (red), and **Cis@nMOF-1** (blue). TEM images of **nMOF-1** (b), **Cis@nMOF-1** (c), and siRNA/**Cis@nMOF-1** (d). Bars: 200 nm. High resolution TEM image of **nMOF-1** (e), **Cis@nMOF-1** (f), and siRNA/**Cis@nMOF-1** (g). Bar: 20 nm. The inset of (e) is the fast Fourier transform pattern of the high-res TEM image showing the 3-fold symmetry. Adapted with permission from *J. Am. Chem. Soc.*, **2014**, *136*, 5181–5184. Copyright 2014 American Chemical Society.

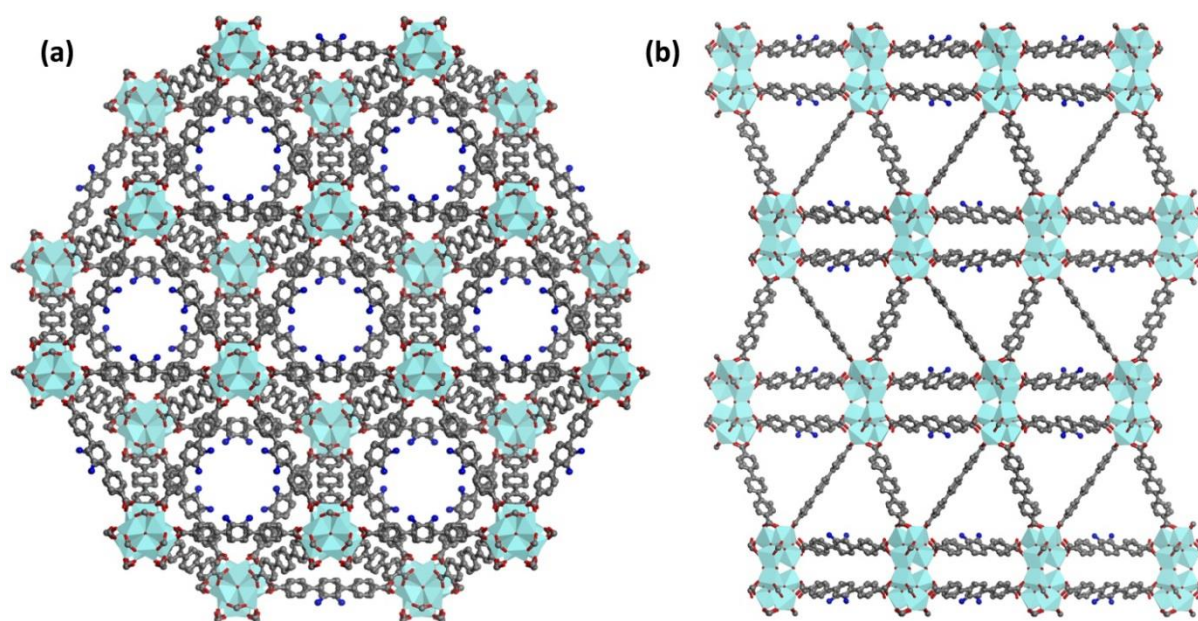


Figure 5-9 Structure models of **nMOF-1**, observed along *c* axis (a) and *a* axis (b).

5.2.4 Cisplatin prodrug and siRNA loading

The cisplatin prodrug, *cis,cis,trans*-[Pt(NH₃)₂Cl₂(OEt)(OCOCH₂CH₂CO₂H)], was loaded into the pores of **nMOF-1** via encapsulation to form **Cis@nMOF-1** (Scheme 5-1). NMR spectroscopy supported the non-covalent encapsulation loading process, as the spectrum appears identical to that was obtained by adding the prodrug to the digested suspension of **nMOF-1** (Figure 5-10). The TEM images of **Cis@nMOF-1** are identical to **nMOF-1** (Figure 5-8c). Interestingly, we observed “standing” particles that align perpendicular to the TEM grid (a) as well as a “leaning” particle stacking on another plate (b) in the high-resolution TEM graph (Figure 5-8f). The cisplatin loading in **Cis@nMOF-1** was determined to be 12.3±1.2 wt% by inductively coupled plasma mass spectrometry (ICP-MS).

The release of the prodrug from **Cis@nMOF-1** is monitored by ICP-MS following dialysis in PBS. The prodrug released slower after encapsulation into **nMOF-1** with a total release of 34% up to 24 h (Figure 5-11). The significantly decreased release rate indicates successful encapsulation of the prodrug and can be attributed to the collapse of nMOF structure in 5 mM PBS to retard the drug release. The cisplatin prodrug was released even much more slowly from **Cis@nMOF-1** in water, with less than 15% release in 24 h. The study shows that negligible amount of cisplatin prodrug was released from **Cis@nMOF-1** during the siRNA loading, which was done in water in 30 min. The released drug was confirmed to be intact cisplatin prodrug by ¹⁹⁵Pt NMR (DMSO-d₆, Figure 5-12): δ= 998.8.

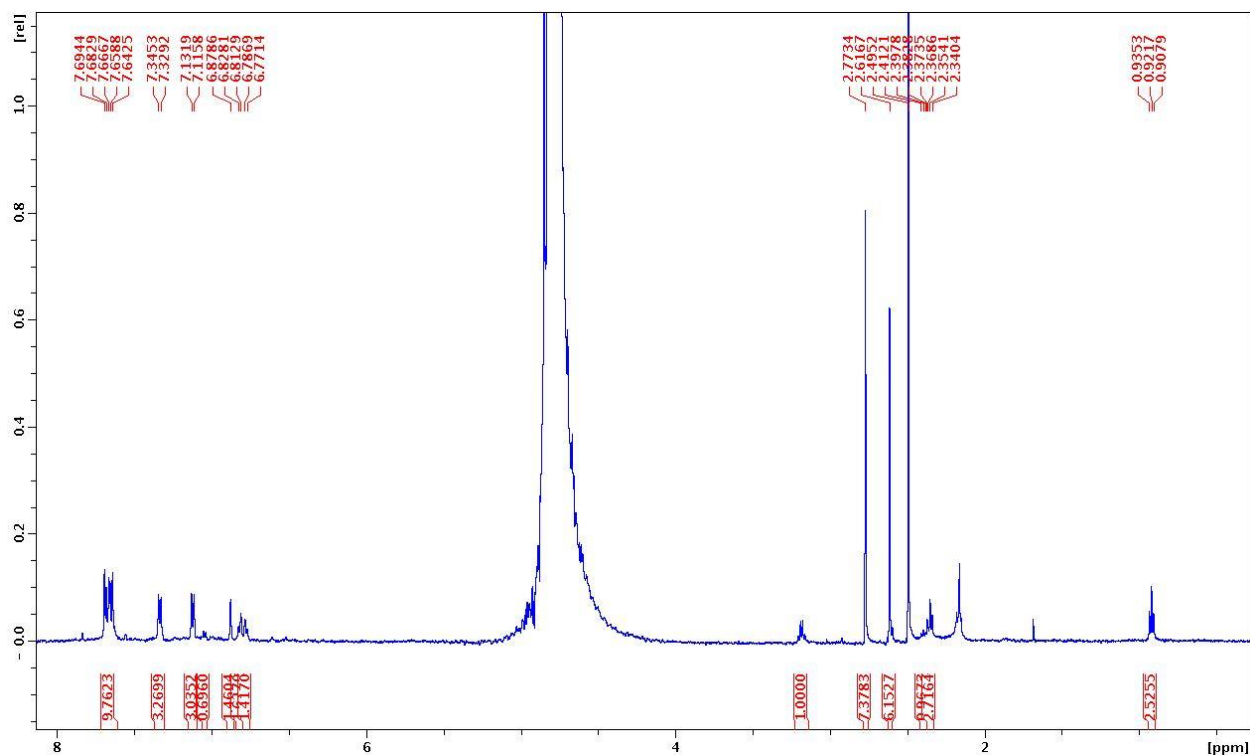


Figure 5-10 ^1H NMR spectrum of Cis@nMOF-1 after digestion. Reprinted with permission from *J. Am. Chem. Soc.*, **2014**, *136*, 5181–5184. Copyright 2014 American Chemical Society.

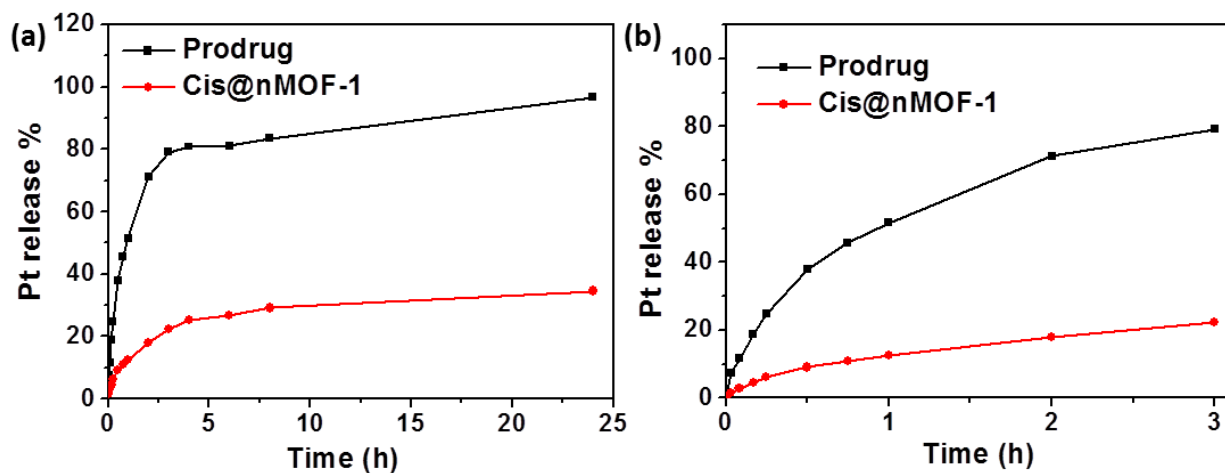


Figure 5-11 Release profiles of cisplatin prodrug from Cis@nMOF-1 in 5 mM PBS by dialysis method. The full plot (a) and the zoomed-in view of the first 3 h (b) are presented. Adapted with permission from *J. Am. Chem. Soc.*, **2014**, *136*, 5181–5184. Copyright 2014 American Chemical Society.

(Figure 5-13). The siRNA loading did not change the morphology of nMOFs as shown by TEM (Figure 5-8 d,g). Dynamic light scattering (DLS, Nano-ZS, Malvern, UK) measurements gave average diameters of 98 ± 11 nm (PDI=0.070), 103 ± 17 nm (PDI=0.124), and 128 ± 3 nm (PDI=0.116) for **nMOF-1**, **Cis@nMOF-1** and **siRNA/Cis@nMOF-1**, respectively (Figure 5-14). The increase in the DLS diameter for **siRNA/Cis@nMOF-1** evidences the presence of siRNA on the **nMOF-1** surface. The siRNA binding capabilities of nMOFs were confirmed by gel electrophoresis, which showed that nMOFs could efficiently “capture” siRNA on the surface as evidenced by the complete retardation of siRNA band migration for **siRNA/Cis@nMOF-1** (Figure 5-15a). The siRNA loading efficiency (LE) was also quantitatively examined by fluorimetry. Fluorescently labeled siRNA (TAMRA-siRNA) was used to form **siRNA/Cis@nMOF-1**, and the LE was determined to be as high as 81.6 ± 0.6 %. As a result of steric hindrance on surfaces, nMOFs protected siRNA from RNase degradation: a siRNA band was clearly visible upon incubating **siRNA/Cis@nMOF-1** in serum for up to 4 h while the naked siRNA was completely degraded under the same condition (Figure 5-15b). Interestingly, siRNA “coating” on the NMOF surface significantly retarded protein adsorption, suggesting possible stabilization of NMOFs via siRNA binding (Figure 5-15c).

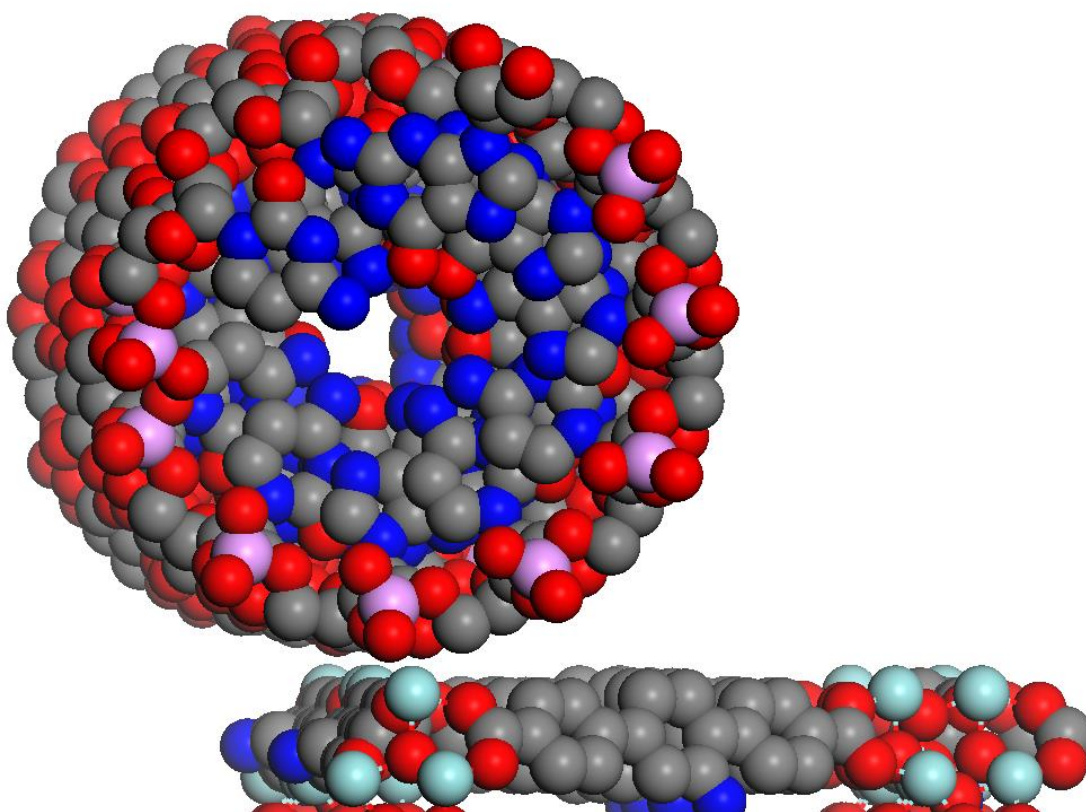


Figure 5-13 Structure model of the interaction between the siRNA and nMOF surface. Gray, C; red, O; cyan, Zr; blue, N; magenta, P.

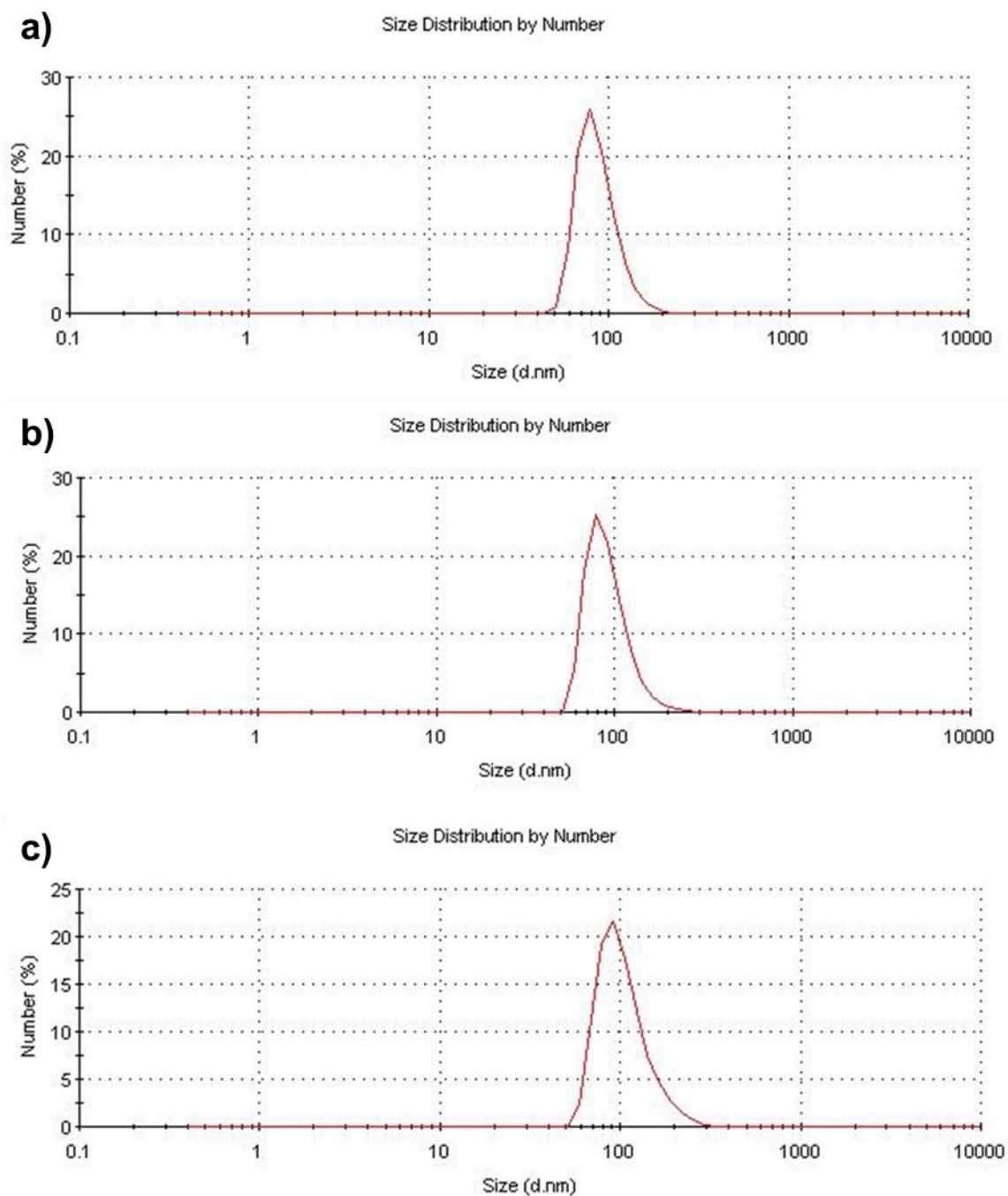


Figure 5-14 DLS plot showing the particle size of **nMOF-1** (a), **Cis@nMOF-1** (b) and **siRNA/Cis@nMOF-1** (c). Reprinted with permission from *J. Am. Chem. Soc.*, **2014**, *136*, 5181–5184. Copyright 2014 American Chemical Society.

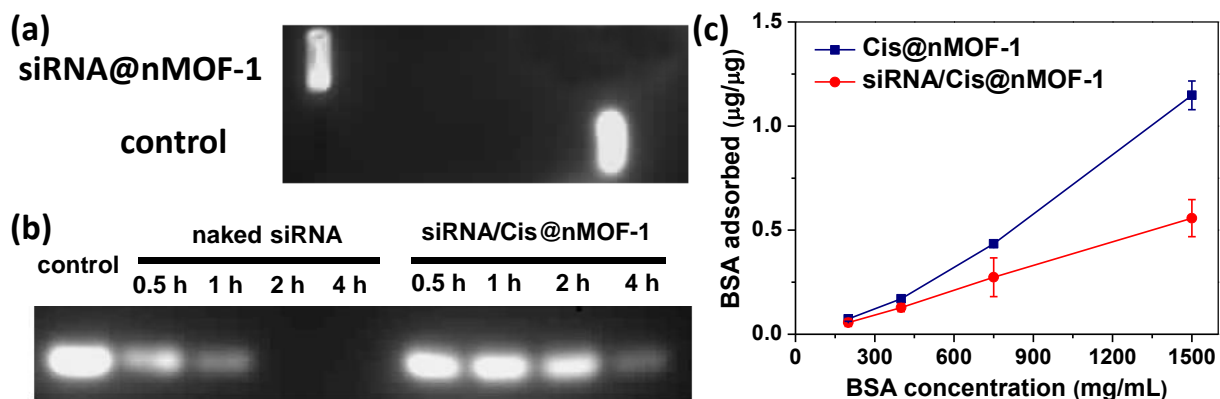


Figure 5-15 Stabilization effect after loading siRNA to the nMOF. (a) Agarose gel electrophoresis of siRNA/Cis@nMOF-1 and naked siRNA showing the siRNA loading into the nMOFs. (b) Serum stability of pooled siRNAs in siRNA/Cis@nMOF-1 as evaluated by electrophoresis. (c) BSA binding to Cis@nMOF-1 with and without siRNA loading. The results were expressed as the amount of BSA (μg) adsorbed to per μg of Cis@nMOF-1. Adapted with permission from *J. Am. Chem. Soc.*, **2014**, *136*, 5181–5184. Copyright 2014 American Chemical Society.

5.2.5 *In vitro* gene silencing study

High siRNA uptake levels and successful endosomal escape are two prerequisites for efficient siRNA-mediated gene silencing.⁷⁻⁹ Compared to the naked siRNA solution, cellular uptake of siRNA/Cis@nMOF-1 were significantly enhanced by more than 11 folds (Figure 5-16a), indicating that the nMOF facilitates the siRNA internalization via endocytosis pathways. The siRNA uptake was also directly observed by confocal laser scanning microscopy (CLSM). As illustrated in Figure 5-16c, large amounts of siRNA (red fluorescence) were located in the cytoplasm of SKOV-3 cells. In addition, zirconium phosphate has extremely low solubility ($K_{\text{sp}}=10^{-134}$), which demonstrates a high affinity of Zr(IV) to phosphate ions. As illustrated in Figure 5-16b, phosphate buffer saline (PBS) containing relatively high phosphate group concentration (2 mM) significantly promoted siRNA release compared to water. It is reasonable

to expect that siRNA could dissociate from Cis@**nMOF-1** by decomposition of nMOF after internalization and entrapment in endosomes due to the presence of much higher concentrations of endogenous phosphate ions in endosomes than in extracellular environments.^{10,11} The dissociated Zr ions can bind to the negatively charged and phosphate-group-enriched endosome membrane to disrupt the endosome structure and facilitate the release of entrapped siRNAs. This hypothesis was supported by CLSM studies and time-dependent endosome/siRNA co-localization studies (Figure 5-17 and 5-18). After 2-hour incubation, siRNA in the siRNA/Cis@**nMOF-1** was able to escape from the endo/lysosome entrapment, as demonstrated by the separation of red (siRNA) and green (Lysotracker Green stained lysosome) fluorescence in the cytoplasm (Figure 5-16d).

We further evaluated the transfection efficiency mediated by siRNA/Cis@**nMOF-1** in SKOV-3 cells. As shown in Figure 5-19, siRNA/Cis@**nMOF-1** evoked potent gene silencing in SKOV-3 cells at 0.4 µg/mL (30 nM) of siRNA as determined by ELISA. Interestingly, by using one-third of the siRNA dose for the pooled siRNAs/Cis@**nMOF-1** compared to single siRNA/Cis@**nMOF-1**, equivalent gene silencing efficiencies were achieved, suggesting the synergistic silencing effects of pooled siRNAs. In comparison, none of the free siRNA solution, Cis@**nMOF-1**, and **nMOF-1** was able to down-regulate the gene expression.

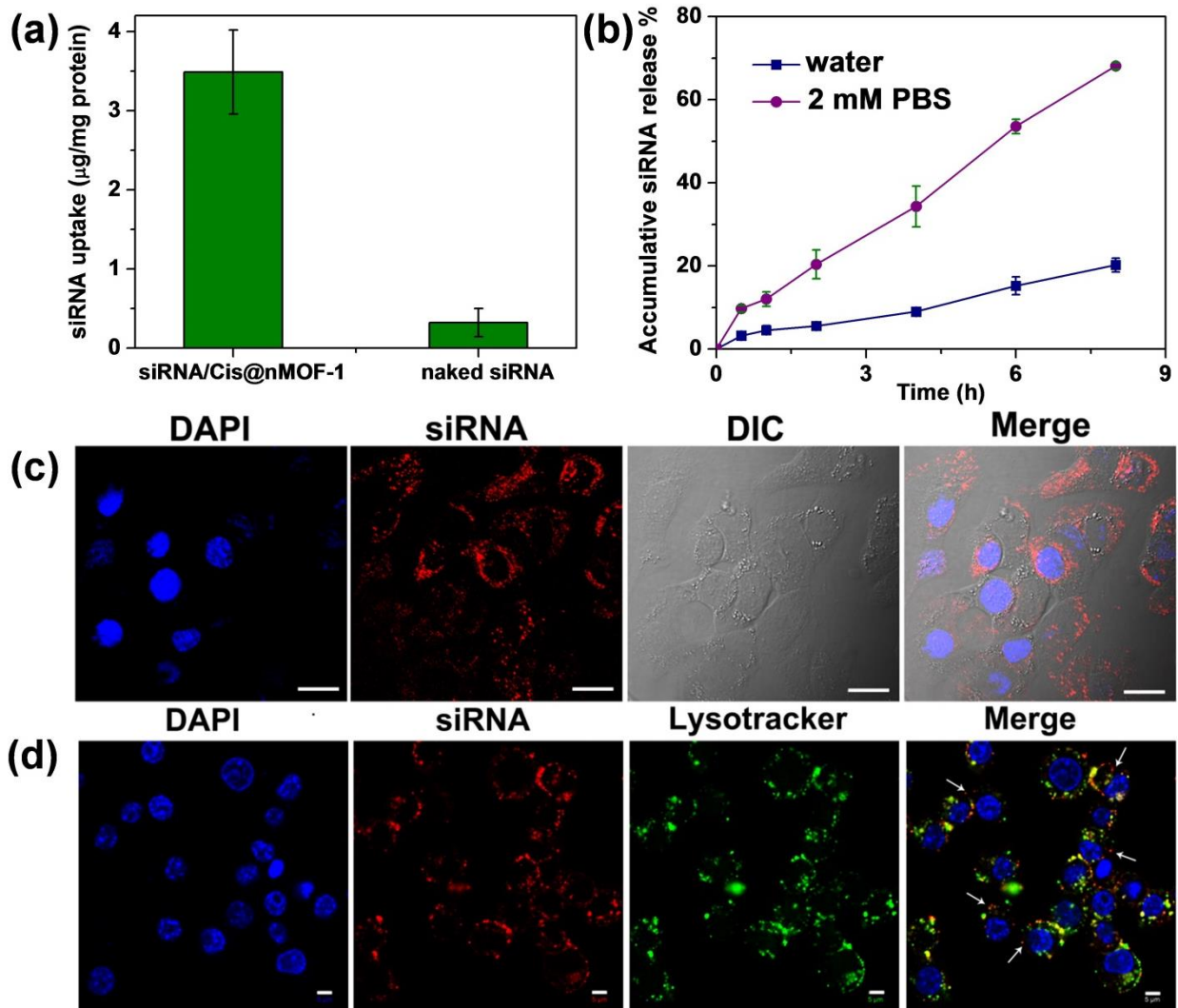


Figure 5-16 Cellular uptake and endosomal escape of siRNA/Cis@nMOF-1 in SKOV-3 cells. (a) Cellular uptake of siRNA/Cis@nMOF-1 in SKOV-3 cells ($n = 3$). (b) siRNA release from nMOFs, dramatically promoted in 2 mM PBS compared to water. (c) CLSM image showing the internalization of siRNA (TAMRA-labeled) into the cytoplasm of SKOV-3 cells. Nuclei were stained with DAPI. Bar represents 20 μm . (d) siRNA (TAMRA-labeled, red) successfully escaped from endosomes as evidenced by the separation of green and red fluorescence (white arrows). Endosome/lysosome and nuclei were stained with LysoTracker Green and DAPI, respectively. Bar represents 5 μm . Adapted with permission from *J. Am. Chem. Soc.*, **2014**, *136*, 5181–5184. Copyright 2014 American Chemical Society.

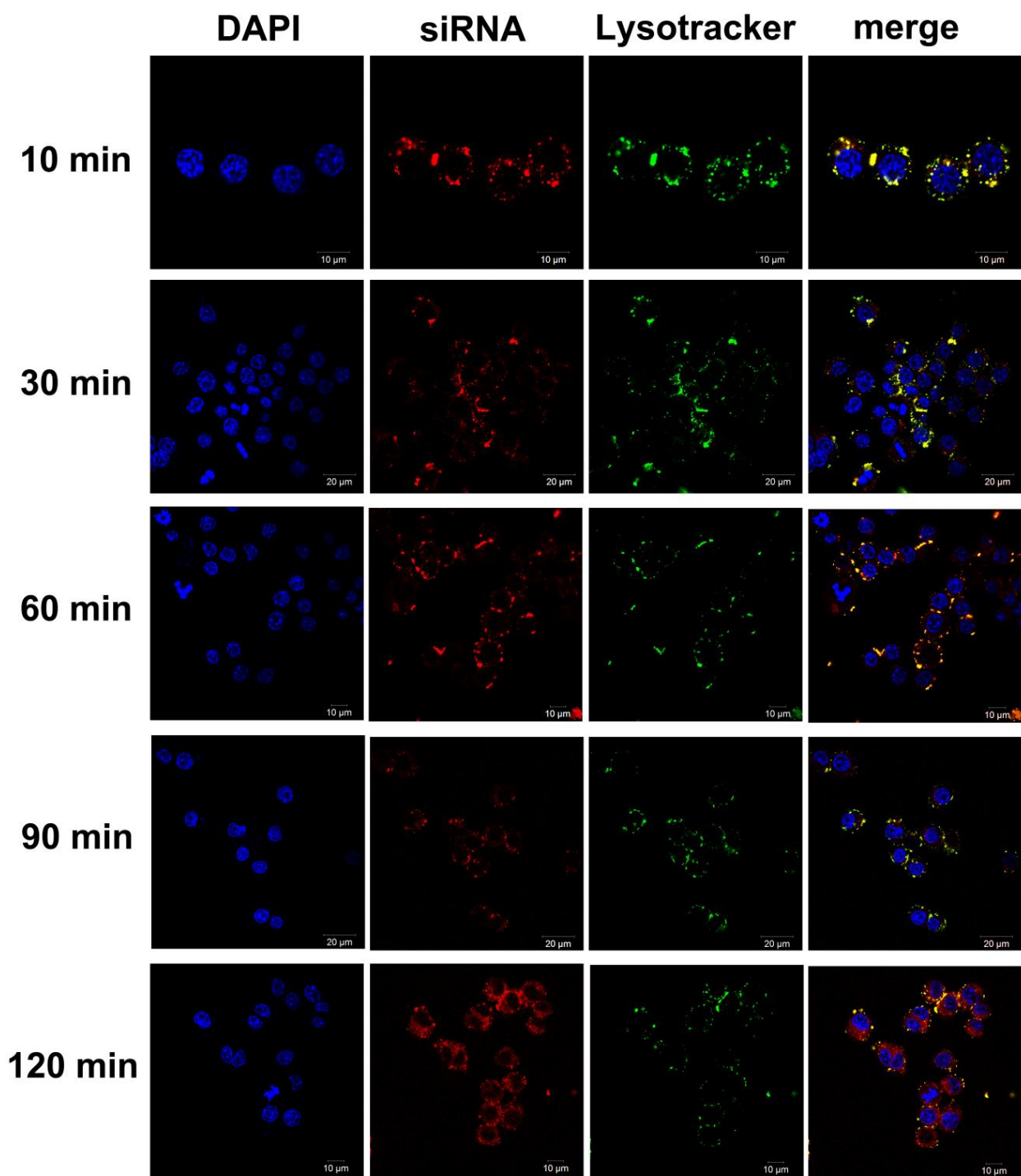


Figure 5-17 CLSM images showing the time-dependent endosomal escape of siRNA in SKOV-3 cells. Endosome/lysosome and nuclei were stained with Lysotracker Green and DAPI, respectively. Bar represented 10 μm . Reprinted with permission from *J. Am. Chem. Soc.*, **2014**, *136*, 5181–5184. Copyright 2014 American Chemical Society.

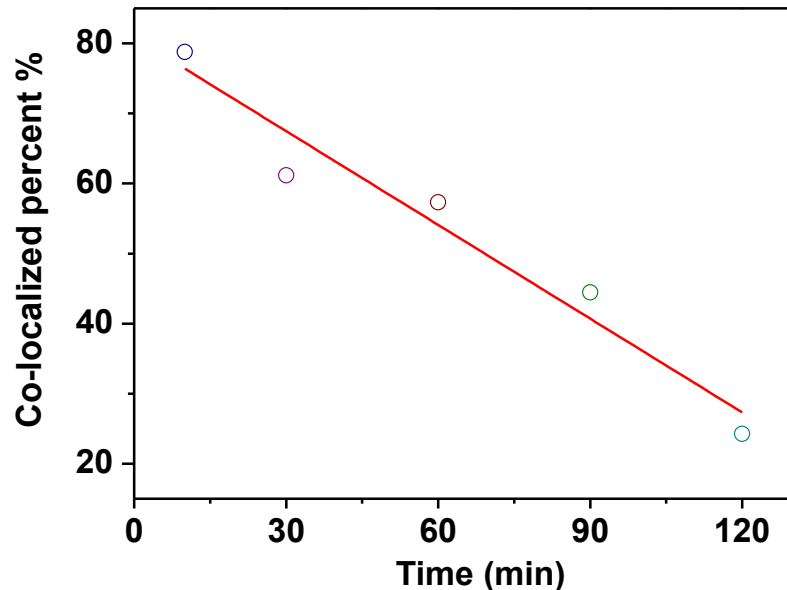


Figure 5-18 Percent co-localization of siRNA and endosome/lysosome quantified by Image J based on the CLSM images. Reprinted with permission from *J. Am. Chem. Soc.*, **2014**, *136*, 5181–5184. Copyright 2014 American Chemical Society.

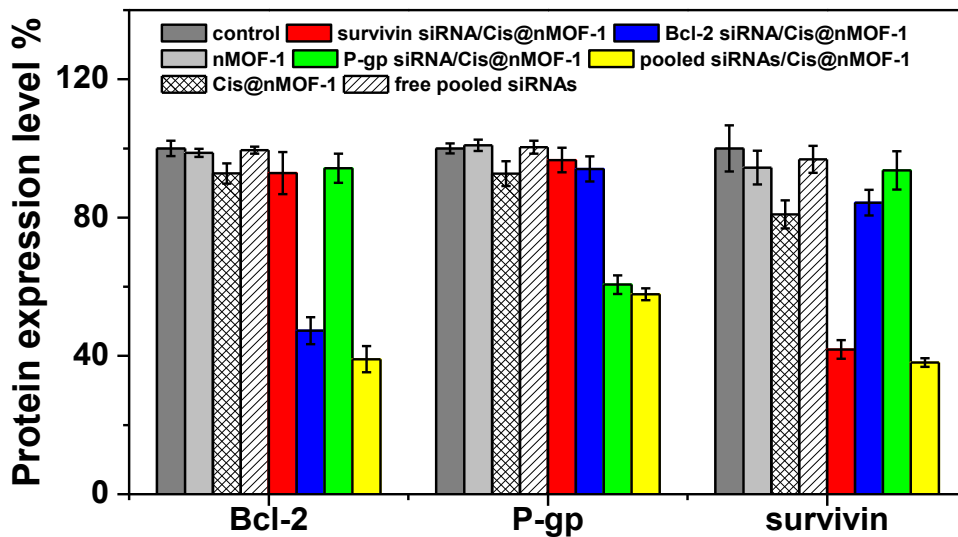


Figure 5-19 siRNA/Cis@nMOF-1 mediated gene silencing in SKOV-3 cells. Silencing efficiency was expressed as percentage values of control group treated with PBS. Adapted with permission from *J. Am. Chem. Soc.*, **2014**, *136*, 5181–5184. Copyright 2014 American Chemical Society.

5.2.6 *In vitro* anticancer efficacy on resistant tumor models

To examine whether the efficient and simultaneous knockdown of three MDR-relevant genes including survivin, Bcl-2, and P-gp could effectively reverse the cisplatin resistance in ovarian cancer cells, the cytotoxicity of free cisplatin, Cis@**nMOF-1**, and siRNA/Cis@**nMOF-1** was assessed by 3-(4,5-dimethylthiazol-2-yl)-5-(3-carboxymethoxyphenyl)-2-(4-sulfophenyl)-2H-tetrazolium (MTS) assay (Figure 5-20a) and by flow cytometry (Figure 5-21). The cisplatin IC₅₀ values of free cisplatin, Cis@**nMOF-1**, pooled siRNAs/Cis@**nMOF-1**, free cisplatin plus free pooled siRNAs, and free cisplatin plus pooled siRNAs/**nMOF-1** were calculated to be 53.9±4.7, 53.2±4.4, 4.7±1.8, 45.1±7.0, and 6.6±0.3 μM, respectively. No cytotoxicity (cell viability of 96.2±3.4%) was observed in SKOV-3 cells when treated with siRNA/**nMOF-1** at 12 times higher siRNA dose. By co-delivering pooled siRNAs and cisplatin utilizing nMOFs, the IC₅₀ value dramatically decreased (by more than 11 fold) compared to free cisplatin and Cis@**nMOF-1**. In control experiments, pooled siRNAs/Cis@**nMOF-1** and Cis@**nMOF-1** exhibited a similar level of cytotoxicity in cisplatin-sensitive cancer cell lines including A2780, PC-3, MCF-7, and H460 cells but significantly lower IC₅₀ values in cisplatin-resistant A2780/CDDP cells (4.2±0.6 vs. 21.4±1.4 μM for pooled siRNAs/Cis@**nMOF-1** and Cis@**nMOF-1**, respectively; Figure 5-20 b-f and Table 5-1). This result suggested that the cisplatin-resistant ovarian cancer cells could be re-sensitized after being transfected with siRNA/Cis@**nMOF-1**, and the synergistic effects of siRNA and cisplatin significantly enhanced the *in vitro* chemotherapeutic efficacy. At 50 times higher **nMOF-1** dose, cell viability was determined to be 98.1±5.4%, indicating a lack of toxicity for **nMOF-1**. We carried out DNA ladder and Annexin V conjugate staining assays in order to demonstrate that the enhanced cytotoxicity of siRNA/Cis@**nMOF-1** was caused by cell apoptosis rather than necrosis. As indicated in Figure

5-22, no DNA fragmentation was detectable in the control, Cis@**nMOF-1**, and free cisplatin groups. Cells treated with siRNA/Cis@**nMOF-1** displayed characteristic DNA fragmentation or laddering, demonstrating that the cytotoxicity induced by siRNA/Cis@**nMOF-1** was associated with apoptosis. Annexin V conjugate staining provided further evidence to the apoptosis induced by siRNA/Cis@**nMOF-1** (Figure 5-23). siRNA (red fluorescence) loaded in the nMOFs were efficiently internalized into the cytoplasm after a 24-h incubation to trigger MDR-relevant gene silencing. Annexin V conjugate (green fluorescence) was clearly visible in cells treated with siRNA/Cis@**nMOF-1** but not in cells treated with siRNA/**nMOF-1** (pooled siRNAs alone) or Cis@**nMOF-1** (cisplatin alone). This result indicates that co-delivery of cisplatin and pooled siRNAs would induce cell apoptosis in cisplatin-resistant cells by combining the synergistic effects of down-regulating the expressions of MDR-relevant genes and chemotherapeutics. Importantly, **nMOF-1** and pooled siRNAs/Cis@**nMOF-1** evoked no immunogenic response in Raw 264.7 macrophage and SKOV-3 cells (Figure 5-24).

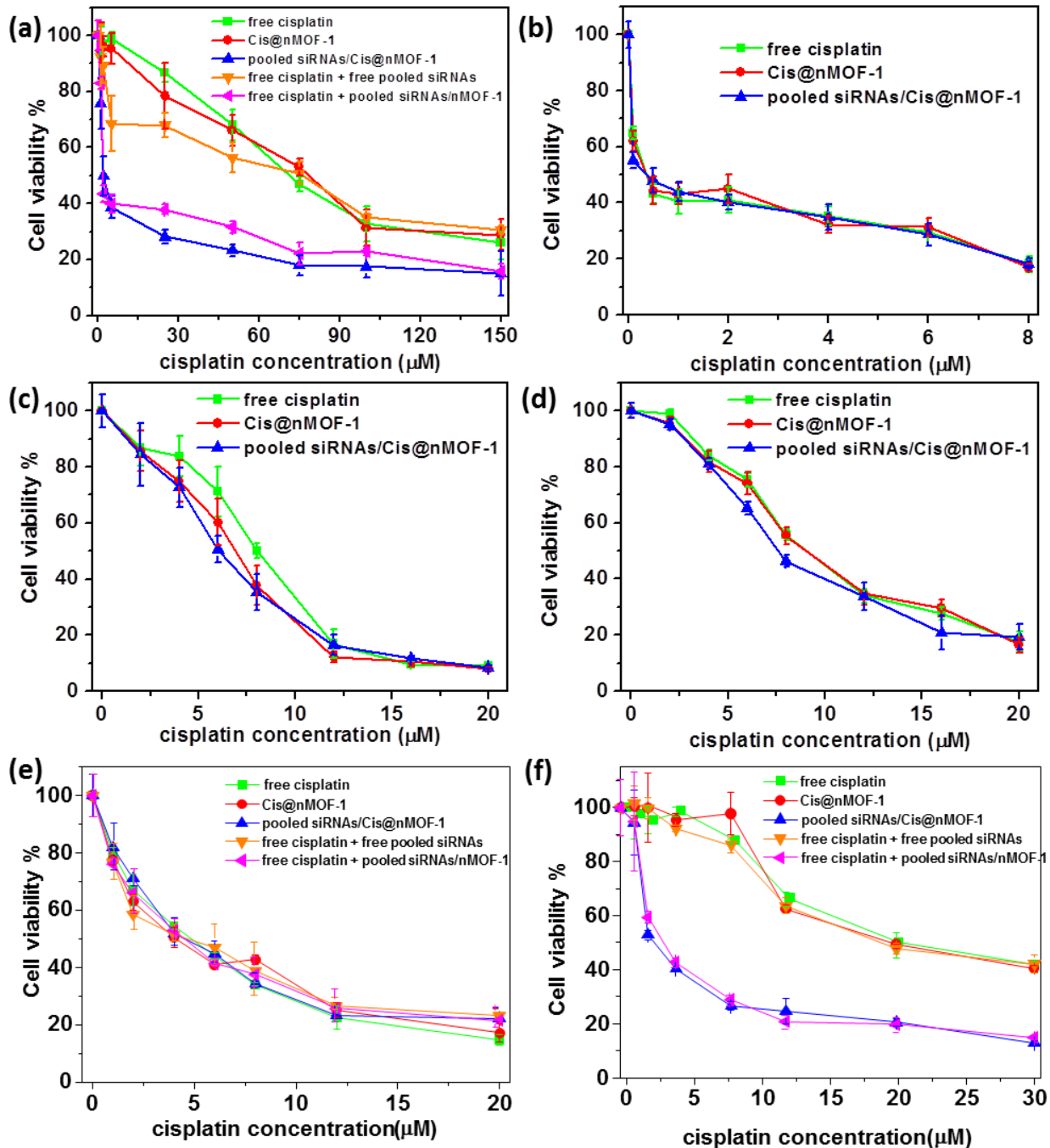


Figure 5-20 *In vitro* cytotoxicity in different cells. (a) SKOV-3 cells; (b) PC-3 cells; (c) MCF-7 cells; (d) H460 cells; (e) A2780 cells; (f) A2780/CDDP cells. Adapted with permission from *J. Am. Chem. Soc.*, **2014**, *136*, 5181–5184. Copyright 2014 American Chemical Society.

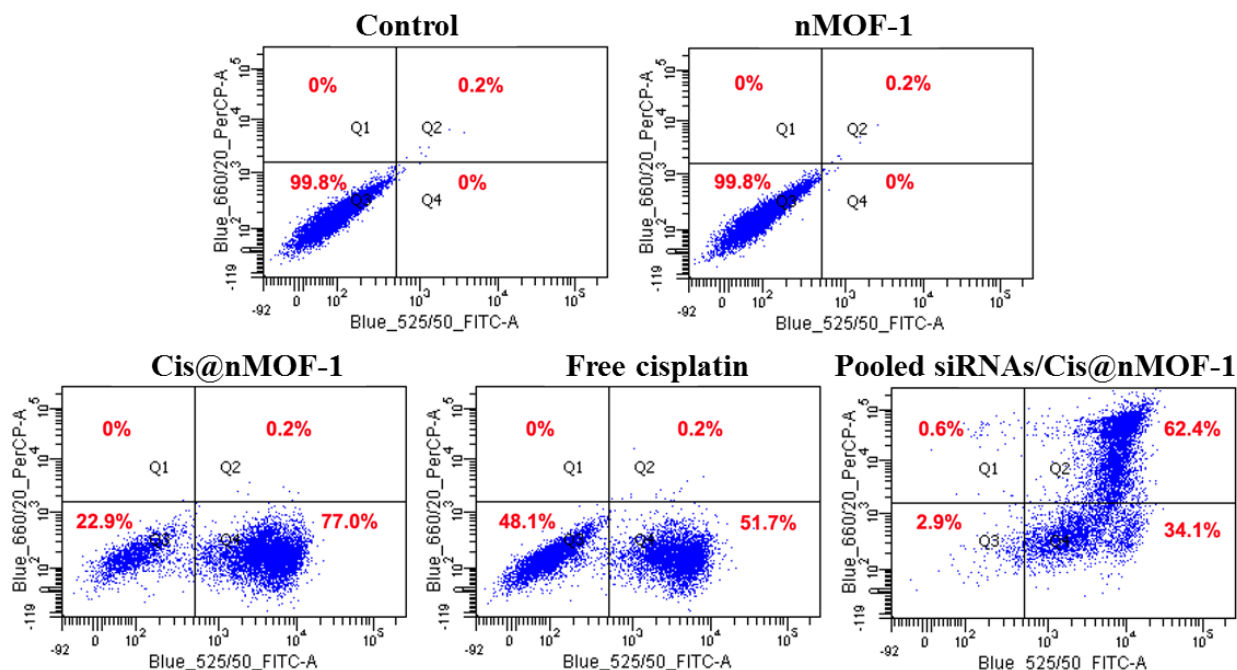


Figure 5-21 Annexin V/PI analysis of SKOV-3 cells after the incubation for 24 h. The Q1-Q4 quadrants represent necrosis, late apoptotic, healthy, and early apoptotic cells, respectively. The percent of cells in each quadrant was shown on the graphs. Adapted with permission from *J. Am. Chem. Soc.*, **2014**, *136*, 5181–5184. Copyright 2014 American Chemical Society.

Table 5-1 IC₅₀ (μM) values in A2780 and A2780/CDDP cells. The cells are incubated for 72 h with free cisplatin solution, Cis@nMOF-1, pooled siRNAs/Cis@nMOF-1, free cisplatin solution plus free pooled siRNA solution (weight ratio of cisplatin to siRNA = 4.5:1), free cisplatin solution plus pooled siRNAs/nMOF-1 (weight ratio of cisplatin to siRNA = 4.5:1).

	A2780	A2780/CDDP
Free cisplatin	4.16±0.21	23.20±0.60
Cis@nMOF-1	4.06±0.20	21.4±1.38
Pooled siRNAs/Cis@nMOF-1	4.49±0.68	4.20±0.61
Free cisplatin+pooled siRNAs	4.18±0.33	22.85±2.30
Free cisplatin+pooled siRNAs/nMOF-1	4.18±0.17	4.87±0.63

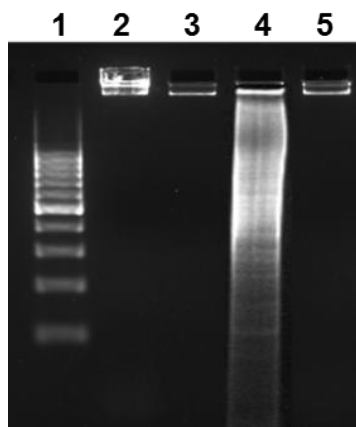


Figure 5-22 DNA ladder analysis. Lane 1-5: DNA marker, control, Cis@nMOF-1, siRNA/Cis@nMOF-1, and free cisplatin. Reprinted with permission from *J. Am. Chem. Soc.*, **2014**, *136*, 5181–5184. Copyright 2014 American Chemical Society.

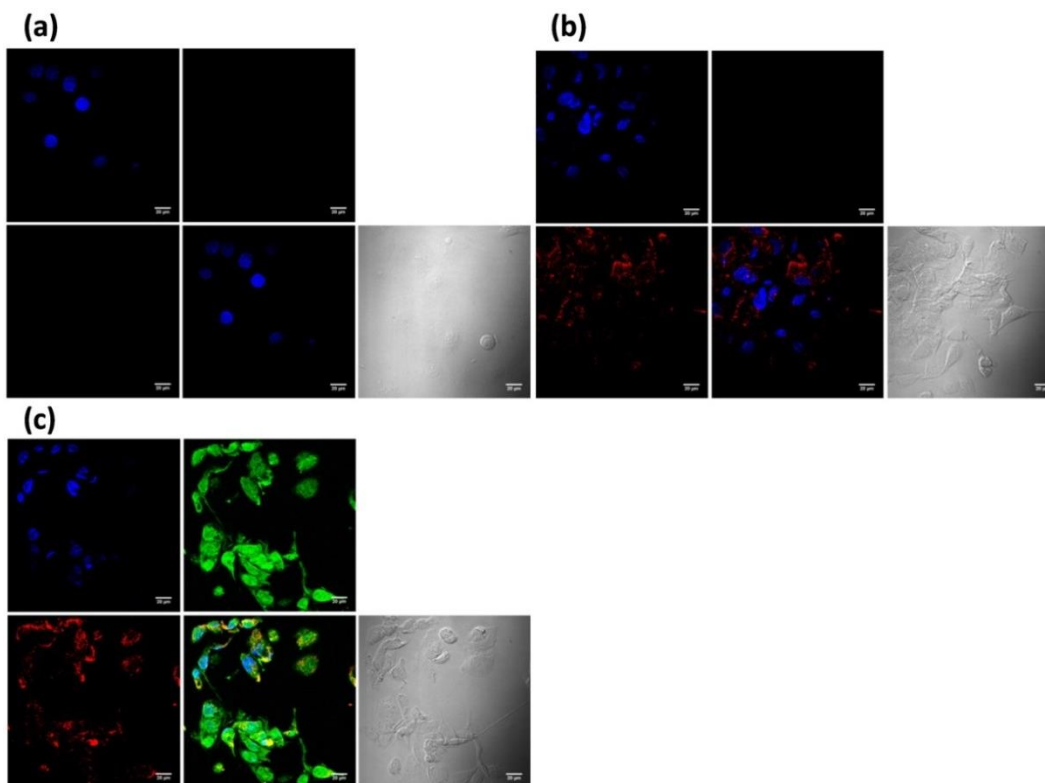


Figure 5-23 CLSM images showing cell apoptosis and siRNA internalization in SKOV-3 cells. The cells are incubated with Cis@nMOF-1 (a), siRNA/nMOF-1 (b), and siRNA/Cis@nMOF-1 (c) for 24 h. The apoptotic cells were stained with Alexa Fluor 488 Annexin V conjugate, and the nuclei were stained with DAPI. Upper left: DAPI stained nuclei; upper right: Alexa Fluor 488 Annexin V conjugate stained apoptotic cells; lower left: TAMRA-labeled siRNA; lower middle: overlay of upper left, upper right, and lower left; lower right: DIC. Bar represented 20 μm . Reprinted with permission from *J. Am. Chem. Soc.*, **2014**, *136*, 5181–5184. Copyright 2014 American Chemical Society.

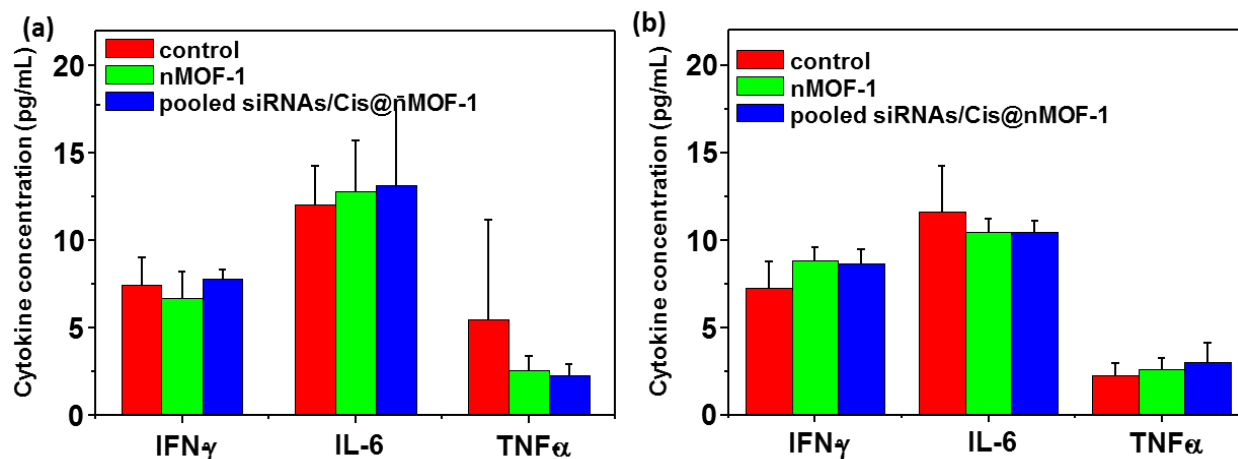


Figure 5-24 Immunogenic response of **nMOF-1** and pooled siRNAs/Cis@**nMOF-1** in SKOV-3 (a) and Raw 264.7 (b) cells. The cells were incubated with **nMOF-1** or pooled siRNAs/ Cis@**nMOF-1** for 72 h followed by the determination of TNF- α , IL-6, and IFN- γ by ELISA. Adapted with permission from *J. Am. Chem. Soc.*, **2014**, *136*, 5181–5184. Copyright 2014 American Chemical Society.

5.3 Conclusion

In this chapter, we have shown that **nMOF-1** with high porosity and surface binding sites represent a unique nanocarrier platform for the co-delivery of chemotherapeutic agents and pooled MDR gene silencing siRNAs to drug-resistant ovarian cancer cells. Cisplatin prodrug was efficiently encapsulated into **nMOF-1** whereas siRNA were loaded by coordinating to metal sites on the nMOF surfaces. **nMOF-1** protects siRNAs from nuclease degradation, enhances siRNA cellular uptake, and promotes siRNA escape from endosomes to silence MDR genes, leading to an order-of-magnitude enhancement in chemotherapeutic efficacy of cisplatin. The simplicity of the present approach makes it amenable to co-delivery of chemotherapeutics and other nucleic acid drugs such as siRNA, microRNA, plasmid DNA by nMOFs. We believe that

this unique nMOF platform holds great promise in the treatment of difficult-to-cure cancers by co-delivering therapeutic cargoes of disparate characteristics and functions.

5.4 Methods

nMOF-1 synthesis: DMF solutions of $ZrCl_4$ (3 mL, 1.4 mg/mL, 18 μ mol) and H_2L (3 mL, 2 mg/mL, 18 μ mol) were added to a 20 mL glass vial. The mixture was diluted to 10 mL, followed by addition of 750 μ L of acetic acid. The mixture was kept in an 80 $^{\circ}C$ oven for 5 days. The light yellow product was collected by centrifugation and washed with DMF, 5% triethylamine ethanolic solution and ethanol in sequence, and preserved in ethanol as a stock suspension. (Yield: ~20%).

Encapsulation of the cisplatin prodrug: Cis,cis,trans-[Pt(NH₃)₂Cl₂(OEt)(OCOCH₂CH₂CO₂H)] (5.0 mg, 0.011 mmol) were dissolved in 2 mL of DMF. To this solution 10.7 mg of **nMOF-1** was suspended. The resulting mixture was stirred at room temperature for 36 hours. The prodrug-loaded **nMOF-1** (Cis@**nMOF-1**) was collected by centrifugation and washed with copious amounts of DMF and ethanol in sequence, and was suspended in ethanol.

nMOF digestion for NMR: Cis@**nMOF-1** (2-3 mg) is collected by centrifugation and dried on vacuum overnight. The yellow powder is then digested in sodium phosphate (tribasic) saturated D₂O by sonication for 10 min and vortex for 2 min. The organic components were extracted by DMSO-d₆ for ¹H NMR analysis.

Cisplatin prodrug release profile: The release of the cisplatin prodrug from Cis@**nMOF-1** was evaluated. Cis@**nMOF-1** was dialyzed in 5 mM phosphate buffer saline (PBS) in a dialysis bag

(MWCO 7000) with stirring (150 rpm) at 37 °C in a beaker. Free cisplatin prodrug solution served as control. Samples were taken at 2 min, 5 min, 10 min, 15 min, 30 min, 45 min, 1 h, 2 h, 3 h, 4 h, 6 h, 8 h, and 24 h to determine the release percentage of cisplatin by ICP-MS.

Loading of siRNA onto Cis@nMOF-1: Survivin siRNA, Bcl-2 siRNA, and P-gp siRNA were dissolved in DEPC-treated water at weight ratio of 1: 1: 1 to achieve a 2 mg/mL pooled siRNA solution. Cis@nMOF-1 (1 mg/mL) dispersed in DEPC-treated water was mixed with siRNA solution (2 mg/mL) at weight ratio of cisplatin : siRNA = 15 : 4, and the mixture was stirred (800 rpm) at room temperature for 30 min to afford siRNA/Cis@nMOF-1. After siRNA loading, the nMOFs were centrifuged at 13000 rpm for 15 min. The supernatant was discarded to remove the free siRNA and the precipitate of nMOFs was collected and re-suspended in aqueous solution for subsequent evaluations.

siRNA protection and release assay: siRNA/Cis@nMOF-1 containing 1 µg of siRNA was mixed with an equal volume of FBS. After incubation for a determined period of time at 37 °C, 100 mM PBS was added to the mixture to disrupt the nMOF structure, and thus the siRNA was dissociated from nMOFs. The mixture was heated to 80 °C to inactivate the nucleases. The siRNA integrity was subsequently evaluated on 4% (w/v) agarose gel electrophoresis. Naked siRNA solution containing 1 µg of siRNA served as control.

As for the evaluation of siRNA release profiles from nMOFs, siRNA/Cis@nMOF-1 containing 1 µg of TAMRA-siRNA were incubated with 1 mL of 2 mM PBS or DEPC-treated water at 37 °C under shaking. At predetermined time intervals (0.5, 1, 2, 4, 6, and 8 h), the suspension was centrifuged at 13,000 rpm for 10 min and 0.5 mL of the supernatant was

quantified for TAMRA-siRNA content by fluorimetry. An equal volume of the release medium was added, and the precipitate was re-suspended before further incubation.

Protein binding assay: Five hundred microliters of siRNA/Cis@nMOF-1 (1 mg/mL) and Cis@nMOF-1 (1 mg/mL) were incubated with 100, 250, 400, 750, and 1500 $\mu\text{g/mL}$ of bovine serum albumin (BSA) at 37 $^{\circ}\text{C}$ for 1 h, respectively. The nMOFs were centrifuged at 13000 rpm for 10 min, and the BSA concentrations in the supernatant were determined by Pierce BCA Protein Assay Kit (Promega, USA) according to the manufacture instructions. The protein binding was expressed as the amount of protein (μg) associated to per μg nMOFs.

siRNA loading efficiency: We quantitatively determined the loading efficiency (LE) of siRNA onto Cis@nMOF-1 by fluorimetry. TAMRA-labeled siRNA was loaded onto Cis@nMOF-1 and the nMOF suspension was centrifuged at 13,000 rpm for 30 min. The amount of free TAMRA-siRNA in the supernatant was determined with fluorimetry based on the standard curve (TAMRA, $\lambda_{\text{ex}} = 565 \text{ nm}$, $\lambda_{\text{em}} = 580 \text{ nm}$). LE was calculated from the following equation:

$$\text{LE (\%)} = \frac{W_0 - W_1}{W_0} \times 100$$

Where W_0 and W_1 stand for the content of total siRNA and free siRNA in the supernatant, respectively.

siRNA cellular uptake: SKOV-3 cells were seeded on a 24-well plate at 1×10^5 cells per well and cultured for 24 h. TAMRA-siRNA-containing nMOFs and naked TAMRA-siRNA solution (2 mg/mL) were added (0.4 μg siRNA/well). Following a 4-h incubation, cells were washed with PBS three times and then lysed with 0.5% (w/v) sodium dodecyl sulfate (SDS, pH 8.0). The

lysate was quantified for TAMRA-siRNA by fluorimetry and protein content by the BCA kit. Uptake level was expressed as the amount of TAMRA-siRNA associated with 1 mg of cellular protein.

The internalization of TAMRA-siRNA/Cis@**nMOF-1** was also directly visualized using confocal laser scanning microscopy (CLSM, Olympus FV1000). SKOV-3 cells were incubated with TAMRA-siRNA/Cis@**nMOF-1** for 4 h at 37 °C. The cells were washed with PBS three times, fixed with 4% paraformaldehyde for 20 min at 4 °C, and stained with 4',6-diamidino-2-phenylindole (DAPI) (10 µg/mL) for 20 min at room temperature before observation on the microscopy.

Endosomal escape observation: To visualize the co-localization of internalized siRNA/Cis@**nMOF-1** with endosomal/lysosomal compartments, cells were incubated with nMOF containing TAMRA-siRNA for 2 h at 37 °C. The cells were washed with PBS three times, fixed with 4% paraformaldehyde for 20 min at 4 °C, and sequentially stained with LysoTracker Green (100 nM) for 2 h at room temperature and DAPI (10 µg/mL) for 20 min at room temperature before observation on CLSM.

A time dependent study of endosomal escape was performed by incubation siRNA/Cis@**nMOF-1** with SKOV-3 cells for 10, 30, 60, 90, and 120 min followed by LysoTracker Green and DAPI staining. The time-dependent co-localization of siRNA/Cis@**nMOF-1** and endosome/lysosome was observed under CLSM, and the co-localization efficiency was quantitatively determined using Image J (co-localization threshold) based on the CLSM images.

***In vitro* transfection efficiency of siRNA/Cis@nMOF-1:** SKOV-3 cells were seeded at 2×10^5 cells per well in 24-well plates and further cultured for 24 h. The culture media were replaced by

1 mL of pre-warmed and fresh culture media containing 10% FBS prior to the experiment. siRNA/Cis@**nMOF-1** containing pooled siRNAs and single siRNA, pooled siRNAs/**nMOF-1**, free siRNA solution, and Cis@**nMOF-1** were added to the cells at a siRNA dose of 0.4 µg (30 nM) per well, corresponding to the cisplatin dose of 1.5 µg per well. Following incubation for 4 h, the culture media were replaced by pre-warmed and fresh culture media containing 10% FBS, and a further 20-h incubation was allowed. The supernatant of the culture media was collected for the determination of extracellular survivin and P-gp production by ELISA (R&D Systems, USA; MyBiosource, USA) following manufacture instructions. The cells were lysed, and the Bcl-2 amount in the lysate was quantified by ELISA (R&D Systems, USA).

***In vitro* cytotoxicity:** SKOV-3 cells were seeded at 5000 cells per well in 96-well plates and further cultured for 24 h. The culture media were replaced by 100 µL of fresh culture media containing 10% FBS. Free cisplatin solution, Cis@**nMOF-1**, pooled siRNA/Cis@**nMOF-1**, free cisplatin solution plus free pooled siRNA solution (weight ratio of cisplatin to siRNA = 4.5:1), free cisplatin solution plus pooled siRNAs/**nMOF-1** (weight ratio of cisplatin to siRNA = 4.5:1), and pooled siRNAs/**nMOF-1** at different siRNA or cisplatin doses are applied. Following incubation for 72 h, the cell viability was determined by (3-(4,5-dimethylthiazol-2-yl)-5-(3-carboxymethoxy-phenyl)-2-(4-sulfophenyl)-2H-tetrazolium) (MTS) assay (Promega, USA) according to manufacture instructions. The concentrations of cisplatin required to inhibit cell growth by 50% (IC₅₀ values) were calculated.

The cytotoxicity of pooled siRNAs/Cis@**nMOF-1** was evaluated on cisplatin-sensitive cancer cell lines. PC-3, MCF-7, and H460 cells were seeded at 1500, 5000, and 2500 cells per well in 96-well plates and further cultured for 24 h. The culture media were replaced by 100 µL of fresh culture media containing 10% FBS. Free cisplatin solution, Cis@**nMOF-1**, pooled

siRNA/Cis@nMOF-1 were added at different cisplatin doses. Following incubation for 72 h, the cell viability was determined by MTS assay. IC₅₀ values were calculated accordingly.

The enhanced *in vitro* anticancer efficacy of pooled siRNAs/Cis@nMOF-1 was further confirmed by carrying out cytotoxicity analysis on cisplatin sensitive and resistant A2780 and A2780/CDDP cells. A2780 and A2780/CDDP cells were seeded at 2500 cells per well in 96-well plates and further cultured for 24 h. The culture media were replaced by 100 µL of RPMI 1640 containing 10% FBS. Free cisplatin solution, Cis@nMOF-1, pooled siRNA/Cis@nMOF-1, free cisplatin solution plus free pooled siRNA solution (weight ratio of cisplatin to siRNA = 4.5:1), free cisplatin solution plus pooled siRNAs/nMOF-1 (weight ratio of cisplatin to siRNA = 4.5:1), and pooled siRNAs/nMOF-1 were added at different cisplatin doses and equivalent siRNA doses. Following incubation for 72 h, the cell viability was determined by MTS assay. IC₅₀ values were calculated accordingly.

DNA ladder: SKOV-3 cells were seeded at 1×10^6 cells per well in 6-well plates and further cultured for 24 h. The culture media were replaced by 2 mL of fresh culture media containing 10% FBS. Free cisplatin solution, Cis@nMOF-1 or siRNA/Cis@nMOF-1 was added to the cells, respectively, at cisplatin concentration of 10 µM. Following incubation for 24 h, total DNA of cancer cells was extracted using DNA ladder isolation kit (Sigma-Aldrich, USA) according to the manufacture instructions and examined for DNA fragmentation on a 2% (w/v) agarose gel electrophoresis at 35 V for 3 h.

Cell apoptosis by Annexin V staining: Coverslips putting in the 6-well plates were seeded with SKOV-3 cells at the density of 1×10^6 cells per well. The cells were incubated at 37 °C and 5% CO₂ for 24 h prior to nanoparticle treatment. siRNA/Cis@nMOF-1, siRNA/nMOF-1 solution,

and Cis@**nMOF-1** were incubated with cells at 37 °C and 5% CO₂ for 24 h. Then, the cells were washed with PBS, stained with Alexa Fluor 488 conjugated Annexin V (Invitrogen, USA) according to the manufacture instructions for 15 min at room temperature, fixed with iced 4% paraformaldehyde for 20 min at 4 °C, and stained with 10 µg/mL of DAPI. The cells were observed using CLSM at excitation wavelength of 405 nm, 488 nm, and 546 nm to visualize nuclei (blue fluorescence), cell apoptosis (green fluorescence) and nanoparticle internalization (red fluorescence), respectively.

Flow cytometry analysis: SKOV-3 cells were seeded at 1×10^6 cells per well in 6-well plates and further cultured for 24 h. The culture media were replaced by 2 mL of fresh culture media containing 10% FBS. Free cisplatin solution, **nMOF-1**, Cis@**nMOF-1**, and pooled siRNAs/Cis@**nMOF-1** were added to the cells, respectively, at cisplatin concentration of 5 µM or equivalent **nMOF-1** concentration of 10 µg/mL. Cells incubated with saline served as control. Following incubating for 24 h, the floating and adherent cells were collected by cell scraper and stained with Alexa Fluor 488 annexin V/dead cell apoptosis kit with Alexa Fluor 488 annexin V and PI (Invitrogen, USA) according to the manufacture instructions. The apoptosis was examined on a flow cytometer (LSRII Blue, BD, USA).

Immunogenic response assay: SKOV-3 cells and Raw 264.7 cells were seeded at 2×10^5 cells per well in 24-well plates and further cultured for 24 h. The culture media were replaced by 1 mL of fresh culture media containing 10% FBS prior to the experiment. **nMOF-1** and pooled siRNA/Cis@**nMOF-1** were added to the cells at a siRNA dose of 0.4 µg (30 nM) per well, corresponding to the **nMOF-1** dose of 10 µg per well. Following incubation for 72 h, the supernatant of the culture media was collected for the determination of TNF-α, IL-6, and IFN-γ

by ELISA (R&D Systems, USA) following manufacturer's instructions. Cells treated with saline served as controls.

5.5 References

1. Carboni, M., Abney, C.W., Liu, S. & Lin, W. Highly porous and stable metal-organic frameworks for uranium extraction. *Chemical Science* **4**, 2396-2402 (2013).
2. Feazell, R.P., Nakayama-Ratchford, N., Dai, H. & Lippard, S.J. Soluble single-walled carbon nanotubes as longboat delivery systems for Platinum(IV) anticancer drug design. *J. Am. Chem. Soc.* **129**, 8438-+ (2007).
3. Schaate, A., *et al.* Modulated Synthesis of Zr-Based Metal-Organic Frameworks: From Nano to Single Crystals. *Chem-Eur J* **17**, 6643-6651 (2011).
4. Xiong, X.B. & Lavasanifar, A. Traceable multifunctional micellar nanocarriers for cancer-targeted co-delivery of MDR-1 siRNA and doxorubicin. *ACS nano* **5**, 5202-5213 (2011).
5. Chen, A.M., *et al.* Co-delivery of doxorubicin and Bcl-2 siRNA by mesoporous silica nanoparticles enhances the efficacy of chemotherapy in multidrug-resistant cancer cells. *Small* **5**, 2673-2677 (2009).
6. Cho, Y.S., *et al.* Targeted Delivery of siRNA-Generating DNA Nanocassettes Using Multifunctional Nanoparticles. *Small* **9**, 1964-1973 (2013).
7. Foged, C. siRNA Delivery with Lipid-based Systems: Promises and Pitfalls. *Curr. Top. Med. Chem.* **12**, 97-107 (2012).
8. Zhang, K., Hao, L.L., Hurst, S.J. & Mirkin, C.A. Antibody-Linked Spherical Nucleic Acids for Cellular Targeting. *J. Am. Chem. Soc.* **134**, 16488-16491 (2012).
9. Cutler, J.I., Auyeung, E. & Mirkin, C.A. Spherical Nucleic Acids. *J. Am. Chem. Soc.* **134**, 1376-1391 (2012).
10. Alfrey, A.C. & Ibels, L.S. Role of phosphate and pyrophosphate in soft tissue calcification. in *Homeostasis of Phosphate and Other Minerals* 187-193 (Springer, 1978).
11. Tanokura, M. & Kazuhiro, Y. Changes in intracellular pH and inorganic phosphate concentration during and after muscle contraction as studied by time-resolved ³¹P-NMR. *FEBS Lett.* **171**, 165-168 (1984).

Chapter 6. Nanoscale Metal-organic Frameworks for Real-Time Intracellular pH Sensing in Live Cells

6.1 Rationale of the nMOF design

Intracellular pH (pH_i) is crucial in regulating cellular behaviors such as vesicle trafficking, cellular metabolism and signaling, and cell proliferation and apoptosis.^{1,2} In eukaryotic cells, the functions of subcellular organelles are highly dependent on the pH values in these individual compartments.³ Endosomes and lysosomes that participate in the secretory and endocytic pathways have a relatively low pH ranging from 4.5-6.5.¹ Real-time sensing and monitoring of pH changes inside live cells are thus important for understanding physiological and pathological processes and the rational design of intracellular drug delivery systems is of great interest. pH_i can be measured with a variety of techniques, including proton-permeable microelectrodes, nuclear magnetic resonance (NMR), absorption spectroscopy, and fluorescence imaging.⁴⁻⁶ Fluorescence-based techniques are among the most powerful tools for pH sensing, owing to their high sensitivity and outstanding spatiotemporal resolution.⁷ In particular, ratiometric sensing by measuring fluorescent signals at two excitation or emission wavelengths of a pH-sensitive probe is not adversely influenced by fluctuation of local probe concentration, allowing accurate and reliable pH_i measurements.⁸ Since Kopelman and co-workers designed PEBBLEs (probes encapsulated by biologically localized embedding) as the first generation of ratiometric fluorescence nanosensors,⁹ a number of polymeric nanoparticles, silica nanoparticles, quantum dots, latex nanobeads, and zeolite-based nanoparticles have been developed for pH_i sensing.^{6,10-15} By taking advantage of the versatility of the nMOFs, we designed the first nMOF-based pH sensor for real-time pH_i measurements in live cells.

Fluorescein and its derivatives (i.e. fluorescein isothiocyanate, FITC) are pH sensitive and exhibit pH-dependent ratiometric fluorescence changes, conferring its ability to sense the pH_i in live cells.¹⁶ However, the application of fluorescein in live cell imaging is severely limited by its rapid release from cells.¹⁷ We expect to change the trafficking pathway of fluorescein moieties by covalent conjugation of FITC to the bridging ligands of **nMOF-1**, the nMOF we reported in Chapter 5, thereby generate a novel nMOF sensor for real-time pH_i measurements in live cells (Figure 6-1). The FITC-conjugated nMOFs promise a few advantages for pH_i sensing include: (1) the periodic and porous structures of nMOFs enable high FITC loadings without dye aggregation, thus preventing deleterious self-quenching; (2) the open channels of nMOFs allow rapid and free diffusion of hydronium ions to afford fast sensor response;¹⁸⁻²⁰ (3) the covalent conjugation of FITC to nMOFs prevents dye leaching, thus eliminating background interference stemming from the released dye during pH_i sensing.

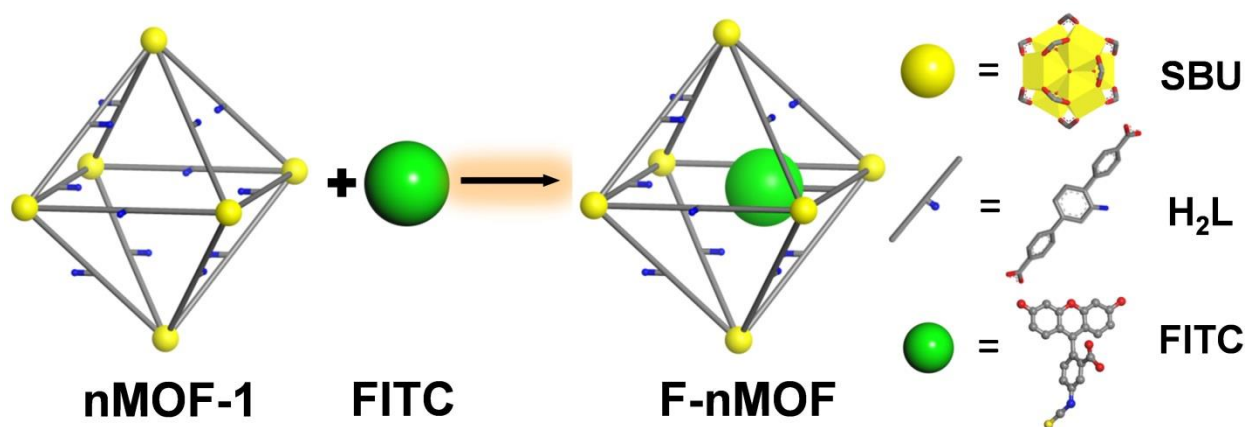


Figure 6-1 Schematic presentation of FITC loading. Adapted with permission from *J. Am. Chem. Soc.*, **2014**, *136*, 12253–12256. Copyright 2014 American Chemical Society.

6.2 Results and Discussion

6.2.1 Preparation and Characterization of F-nMOF

nMOF-1 was synthesized as described in Chapter 5. Transmission electron microscopy (TEM, Tecnai F30 and Tecnai Spirit, FEI, USA) micrographs showed the hexagonal plate-like morphology of **nMOF-1** and gave a diameter of ~100 nm and a thickness of ~30 nm (Figure 6-2 b,c). FITC was covalently conjugated to **nMOF-1** to afford a FITC-conjugated nMOF (**F-nMOF**) by forming a thiourea linkage between the isothiocyanate group on FITC and the amino group of the bridging ligand (Figure 6-1). **F-nMOF** retained the hexagonal plate-like morphology and powder X-ray diffraction (PXRD) pattern of **nMOF-1** as shown in Figure 6-2 a,d,e. Dynamic light scattering (DLS) measurements gave average diameters of 111.8 nm (PDI=0.140) and 123.2 nm (PDI=0.135) for **nMOF-1** and **F-nMOF**, respectively (Figure 6-3).

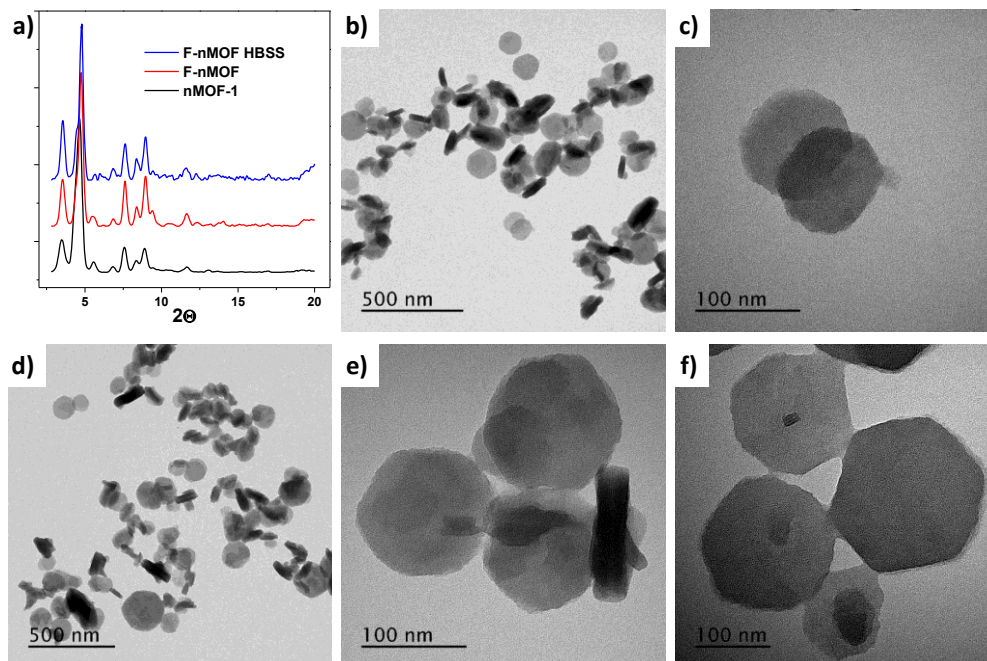


Figure 6-2 Structures and morphologies of **nMOF-1** and **F-nMOF**. (a) Powder X-ray diffraction of **nMOF-1**, **F-nMOF** and **F-nMOF** incubated in HBSS for 12 h. The TEM images of **nMOF-1** (b,c), **F-nMOF** (d,e) and **F-nMOF** incubated in HBSS for 48h (f). Adapted with permission from *J. Am. Chem. Soc.*, **2014**, *136*, 12253–12256. Copyright 2014 American Chemical Society.

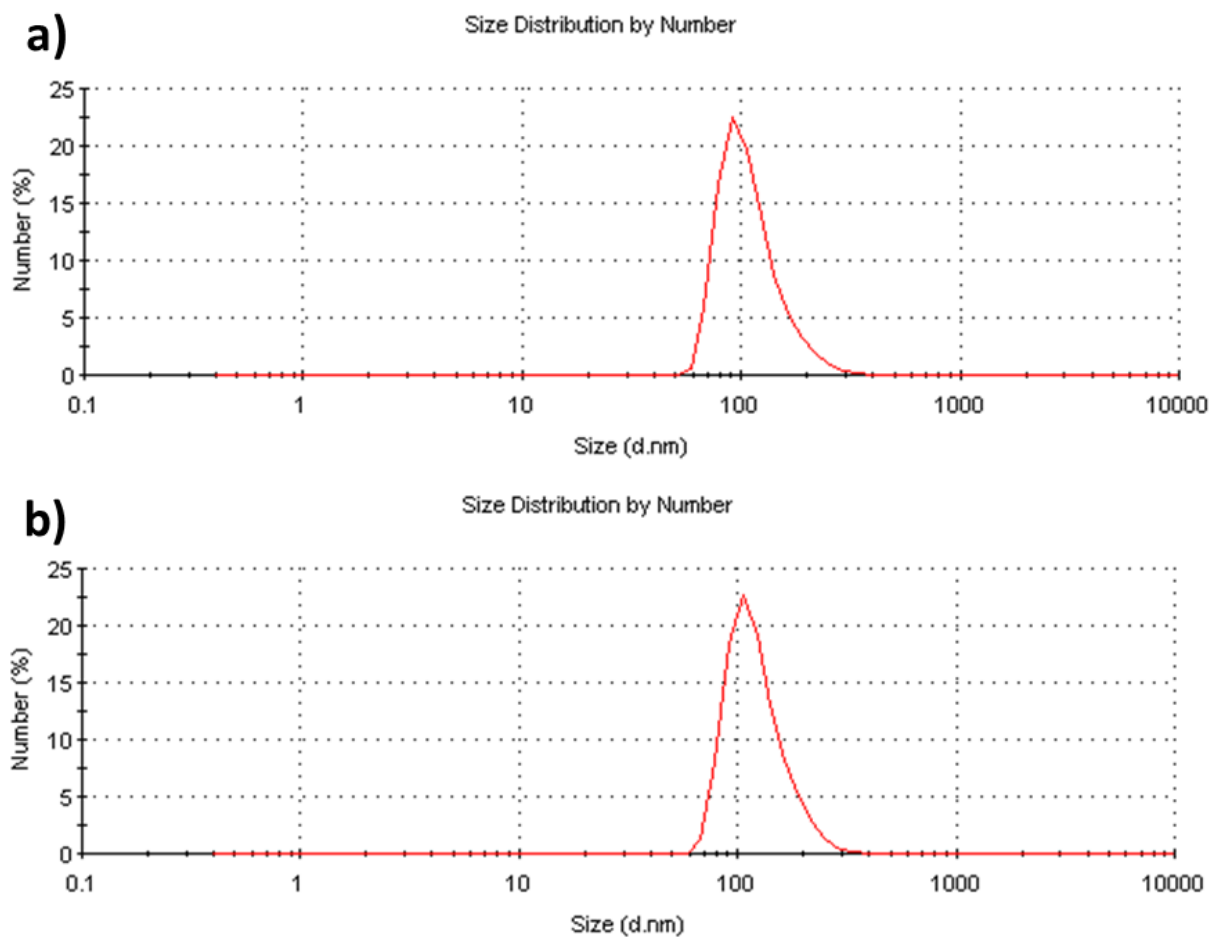


Figure 6-3 DLS measurements of **nMOF-1** (a) and **F-nMOF** (b). Adapted with permission from *J. Am. Chem. Soc.*, **2014**, *136*, 12253–12256. Copyright 2014 American Chemical Society.

The comparison of ^1H NMR spectra of FITC, the conjugated ligand FITC-L, **F-nMOF** and **nMOF-1** confirmed the presence of both free H_2L and FITC-L in **F-nMOF** digestion (Figure 6-4), and mass spectrometry observed both the H_2L ligand (exact mass=333) and conjugated FITC-L (exact mass=722) signals (Figure 6-5).

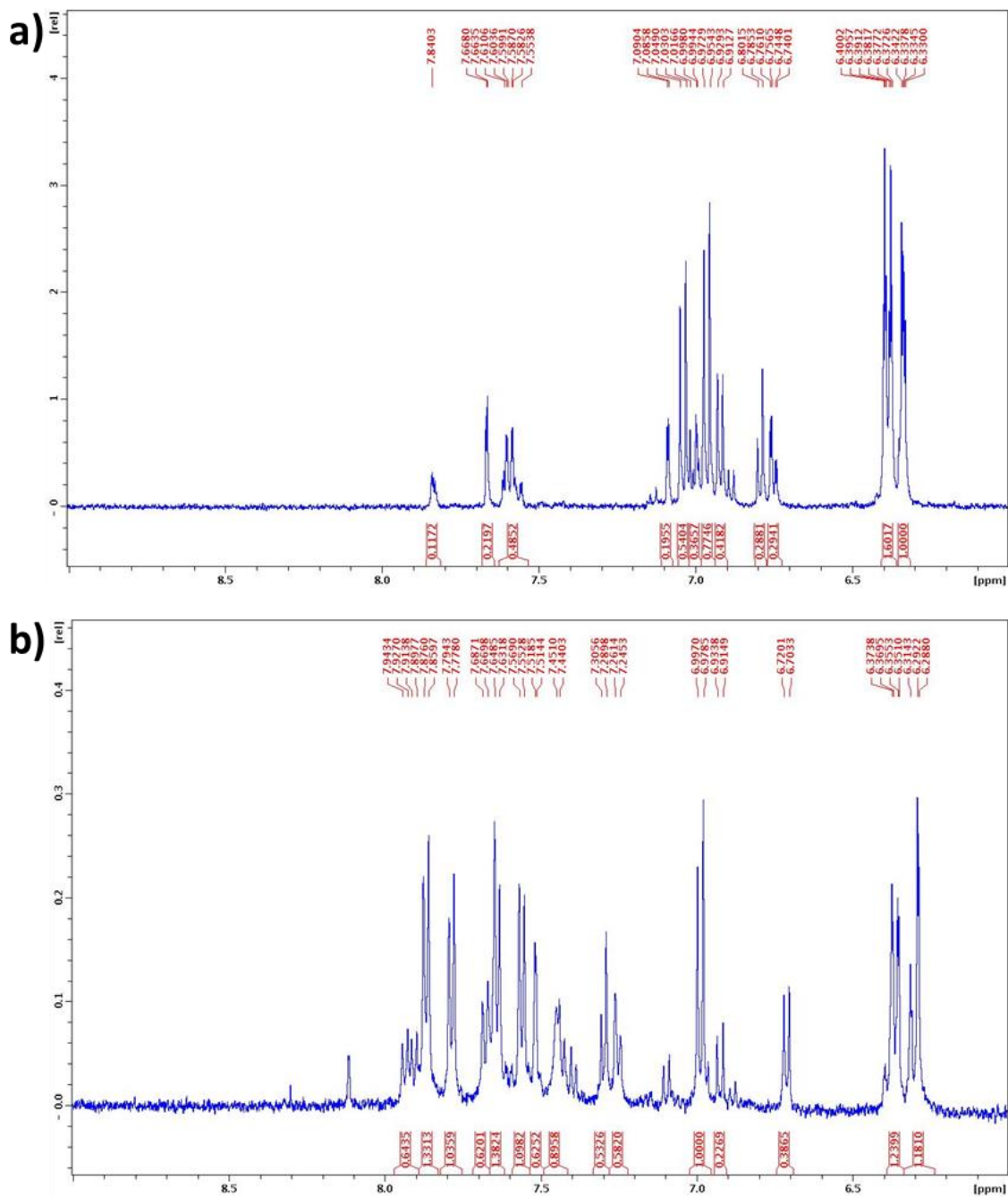


Figure 6-4 ^1H NMR spectra to confirm covalent attachment. The samples of FITC (a), FITC-L (b), F-nMOF (c) and nMOF-1 (d) are prepared or extracted in DMSO- d_6 .

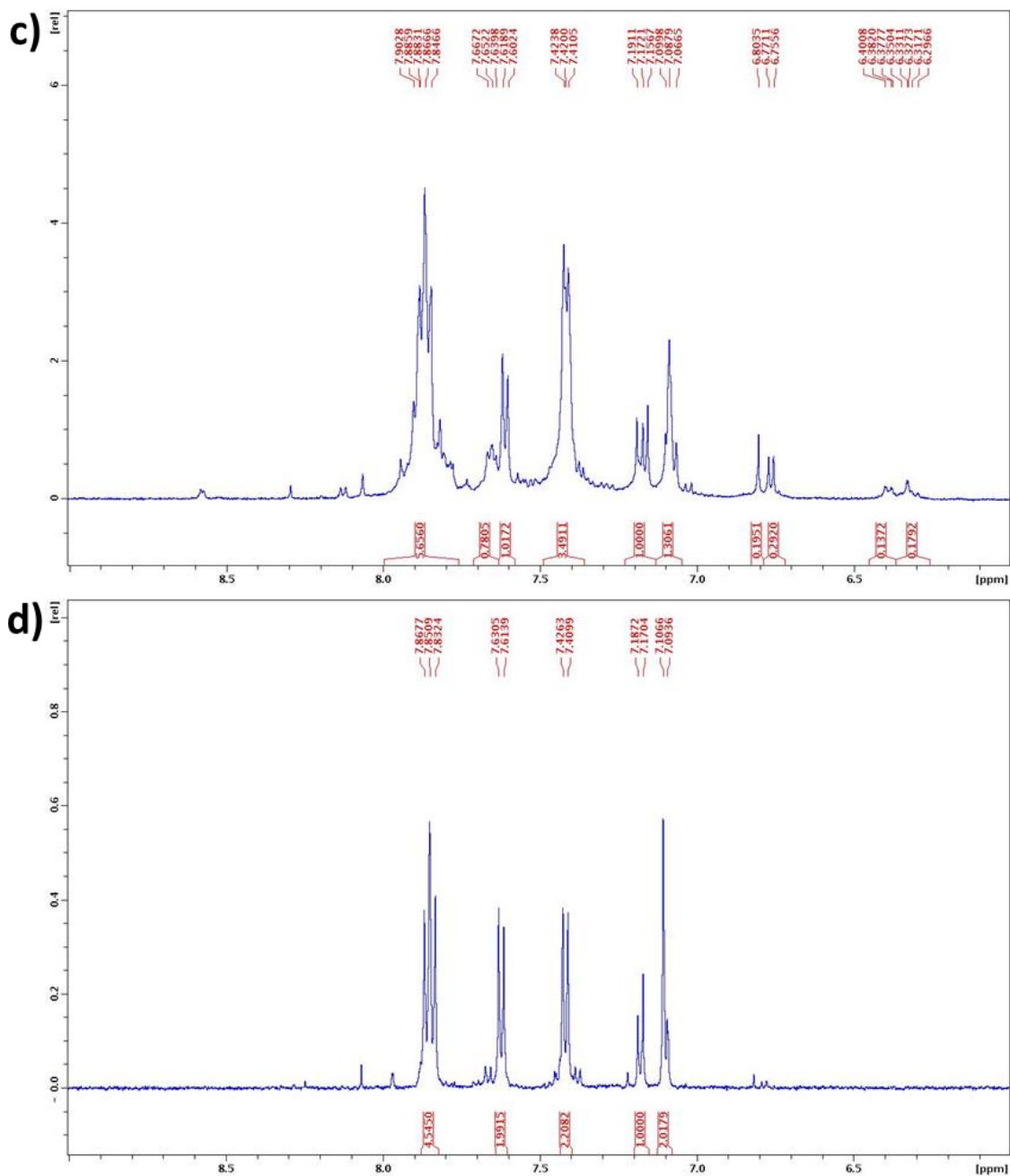


Figure 6-4 (Continued) ¹H NMR spectra to confirm covalent attachment. The samples of FITC (a), FITC-L (b), F-nMOF (c) and nMOF-1 (d) are prepared or extracted in DMSO-d₆. Adapted with permission from *J. Am. Chem. Soc.*, **2014**, *136*, 12253–12256. Copyright 2014 American Chemical Society.

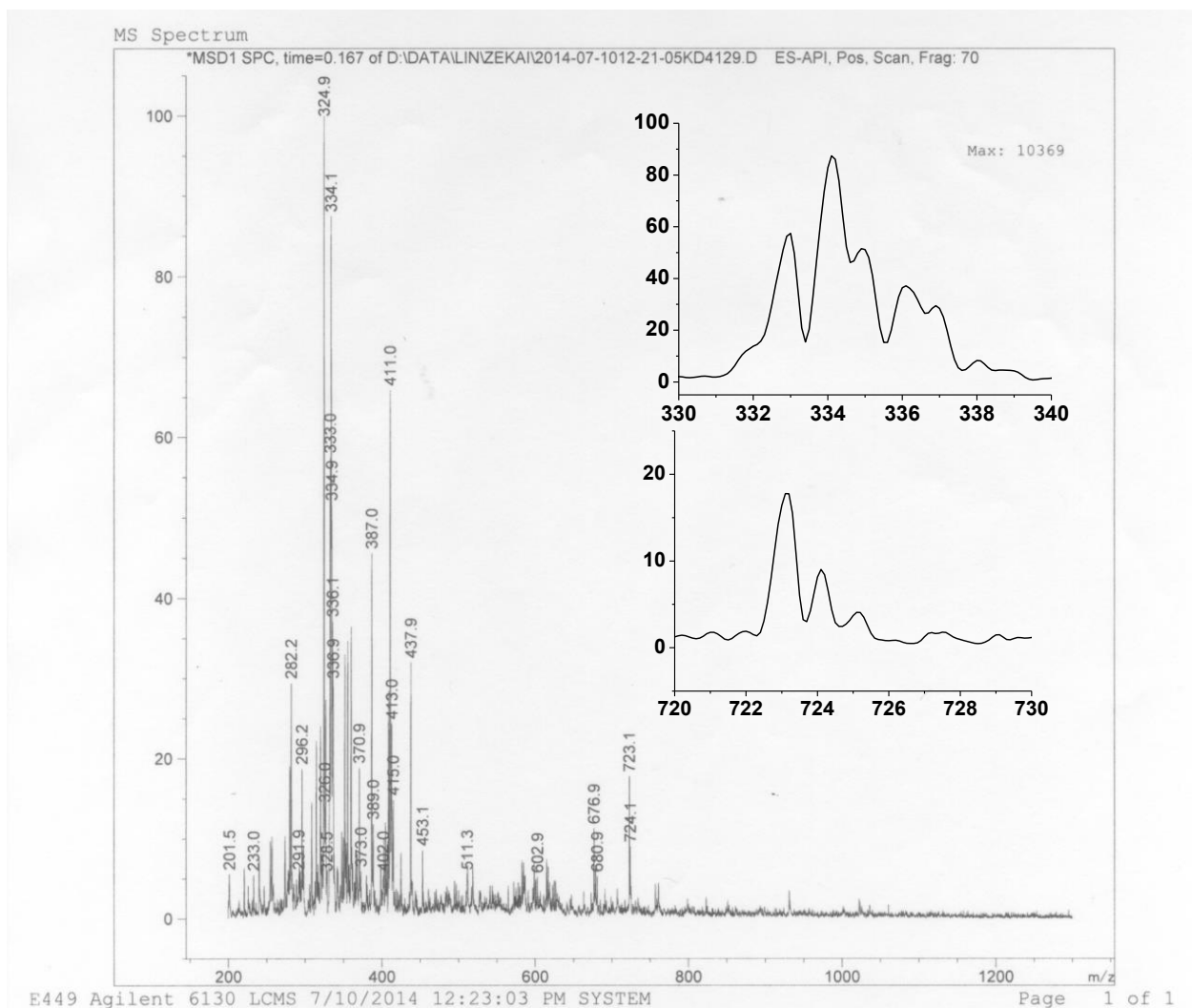


Figure 6-5 Mass spectrum of **F-nMOF** digest. Inset shows the existence of both the free ligand (upper) and the conjugated ligand (bottom). Adapted with permission from *J. Am. Chem. Soc.*, **2014**, *136*, 12253–12256. Copyright 2014 American Chemical Society.

Negligible dye leaching, good structural stability and high quantum efficiency are key factors of ideal fluorescence nanosensors. The covalent conjugation of FITC to **nMOF-1** framework efficiently prevents the dye leaching, which is confirmed by UV-visible spectroscopy. Less than 4.5% of FITC fluorescence was observed in the supernatant after incubating **F-nMOF** in Hanks's Balanced Salt Solution (HBSS) for 24 h (Figure 6-6). After incubation in HBSS for

up to 48 h, **F-nMOF** exhibited unaltered morphology and PXRD patterns (Figure 6-2 a, f, Figure 6-7), indicating its structural stability in the media used for pH_i sensing.

Low fluorescence efficiency is another common issue for dye-loaded nanosensors, which can be attributed to the insufficient dye loading or self-quenching due to dye aggregation. Typical fluorescence dye loadings in amorphous nanosensors range from 0.1-0.5% in order to avoid aggregation-induced self-quenching.^{11,21,22} In contrast, the porous and regular structure of **nMOF-1** allows exceptionally high dye loadings without dye aggregation (see below).

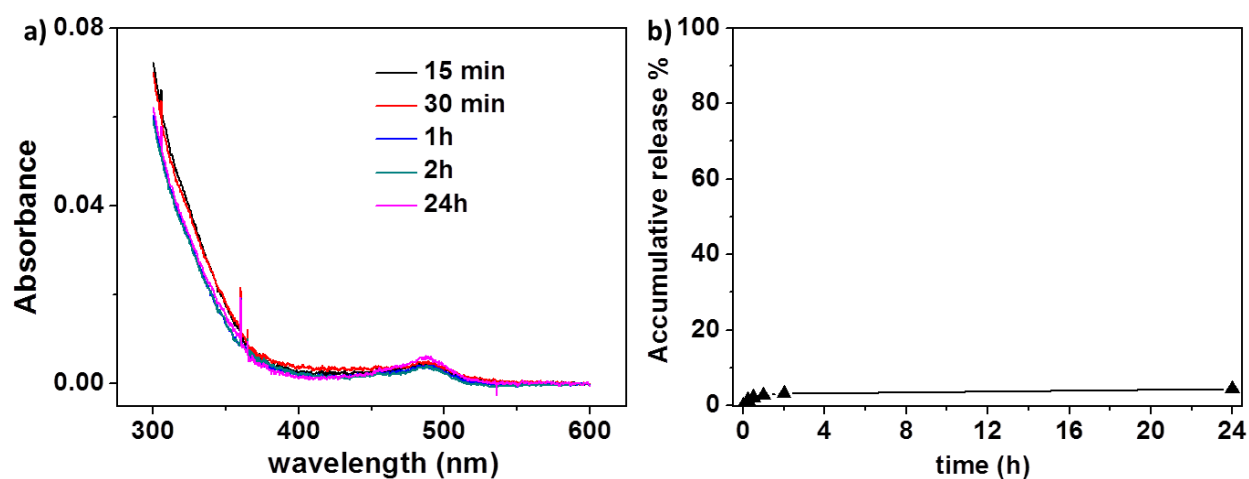


Figure 6-6 Studies of FITC leaching upon HBSS incubation. (a) The UV-vis absorption of supernatant after centrifugation removal of nMOFs at different time point. (b) The accumulative release percentage calculated from absorption at 480 nm. Adapted with permission from *J. Am. Chem. Soc.*, **2014**, *136*, 12253–12256. Copyright 2014 American Chemical Society.

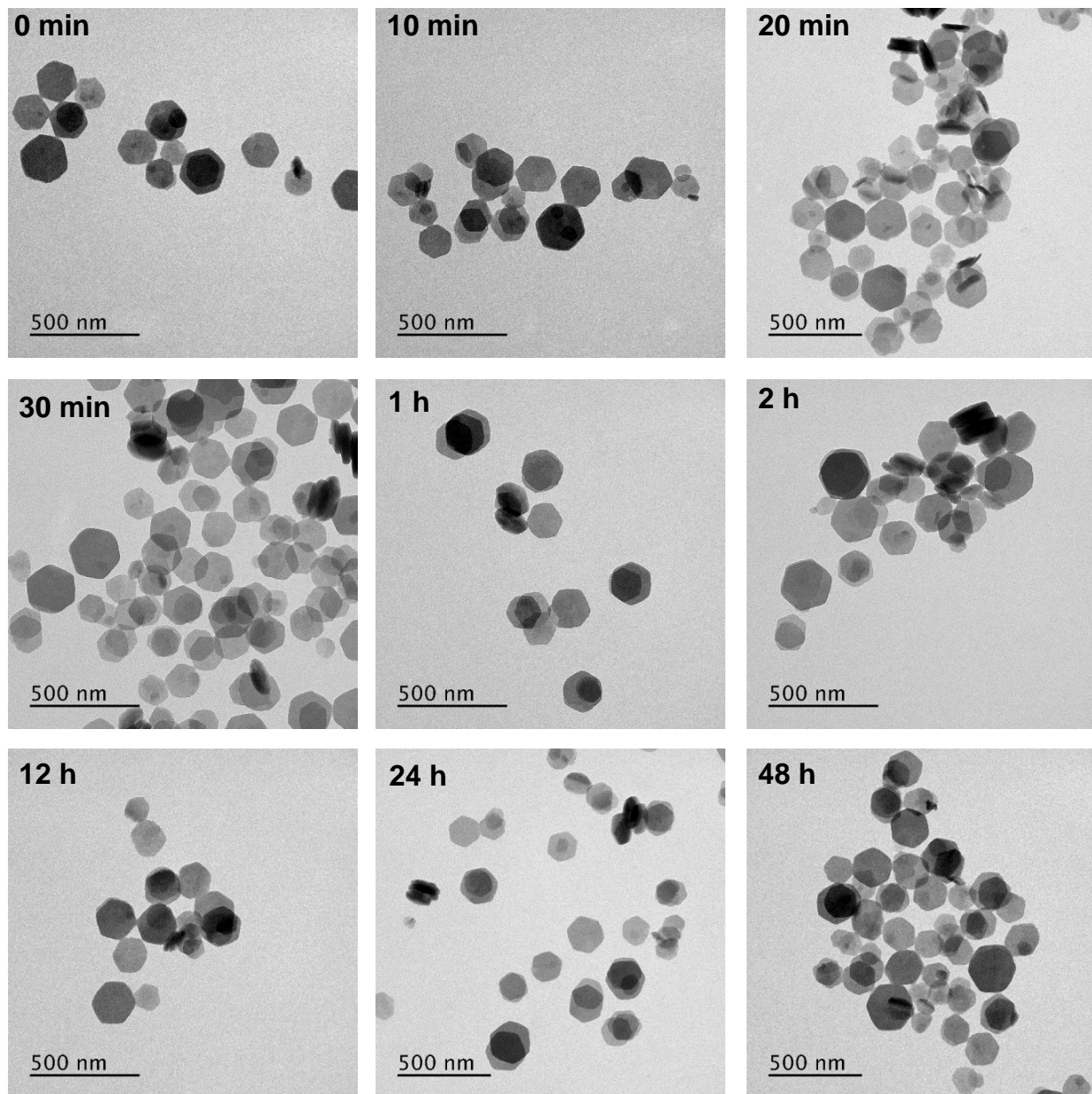


Figure 6-7 TEM images of **F-nMOF** after incubation in HBSS for different time. Reprinted with permission from *J. Am. Chem. Soc.*, **2014**, *136*, 12253–12256. Copyright 2014 American Chemical Society.

We evaluated the fluorescence efficiency of **F-nMOF** with a series of FITC loadings in order to obtain optimal **F-nMOF** for pH_i sensing. The FITC loading increased with the FITC feed amount (1, 3, 5, 8, 12, 17, and 30 wt.%), and exhibited saturation behaviors when FITC feed

reached 12 wt.% (Figure 6-8 and 6-9). The fluorescence efficiency of **F-nMOF** at different FITC loadings was evaluated by comparing the absorbance of **F-nMOF** at 490 nm (Figure 6-10) and the fluorescence intensity of **F-nMOF** at 516 nm (with excitation at 490 nm), respectively. As shown in Figure 6-11, the absorbance of **F-nMOF** increased linearly as the FITC loading increased (after subtracting the light scattering of the blank **nMOF-1**). In contrast, the fluorescence linearly increased as the FITC loading increased up to a FITC loading of ~7 wt.% (corresponding to 8 wt.% of feed amount), and then saturated as the FITC loading further increased, suggesting appreciable self-quenching of FITC dyes at >7 wt.% loading. For subsequent pH_i sensing and imaging studies, we use **F-nMOF** with a FITC loading of 4 wt.% in order to avoid self-quenching of FITC dyes and potential complications from different pH dependence behaviors of dye aggregates.

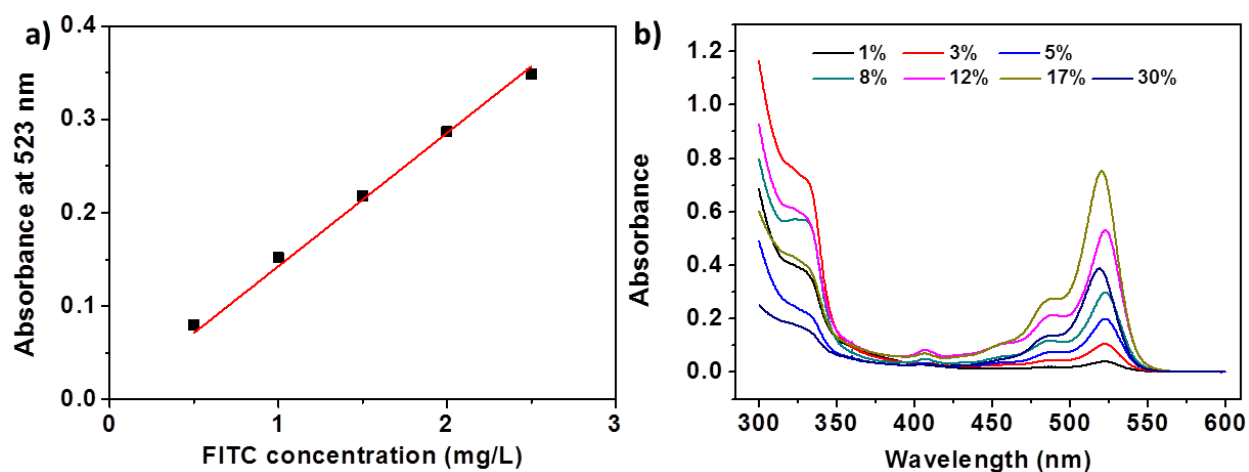


Figure 6-8 FITC loading quantification. (a) The standard curve of FITC UV-vis absorption at 523 nm in the test media. (b) Absorbance spectra of the supernatant collected from each washing step after FITC loading at a series of FITC feed amount percent. Numbers shown in the figure legend represent the FITC feed wt.%. The supernatant collected from FITC loading at a FITC feed of 17 wt.% and 30 wt.% was diluted with triethylamine/DMF (1:9, v/v) solution before determination. Adapted with permission from *J. Am. Chem. Soc.*, **2014**, *136*, 12253–12256. Copyright 2014 American Chemical Society.

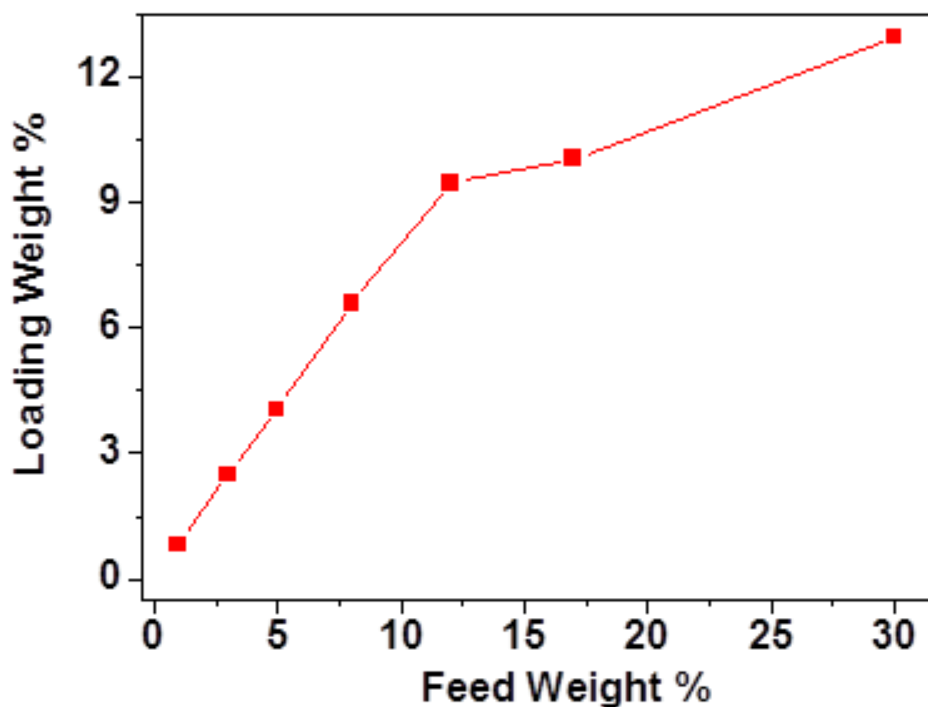


Figure 6-9 Correlation between FITC feed wt.% and FITC loading wt.%. Reprinted with permission from *J. Am. Chem. Soc.*, **2014**, *136*, 12253–12256. Copyright 2014 American Chemical Society.

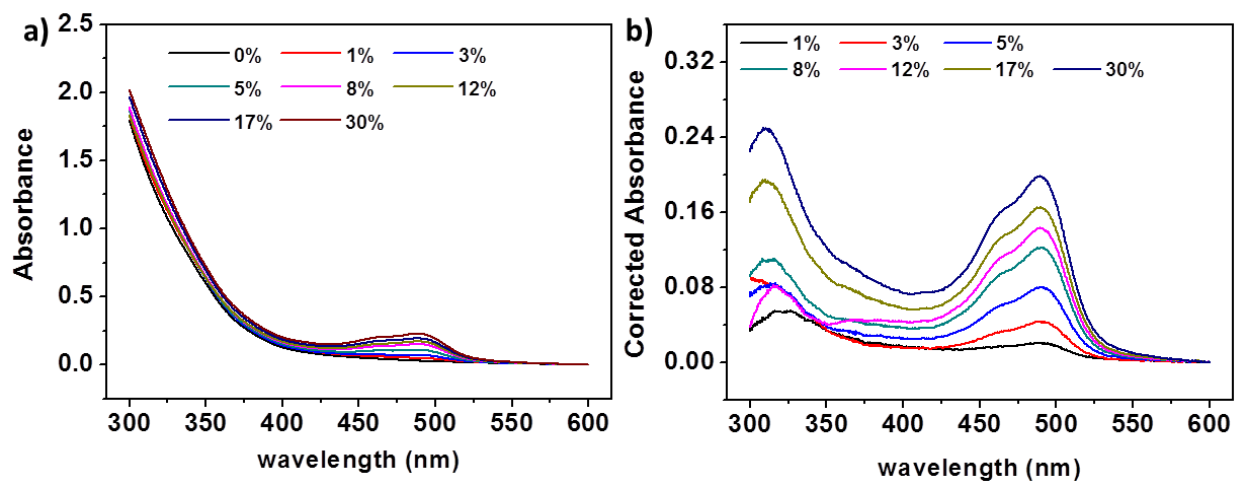


Figure 6-10 Absorption spectra of **F-nMOFs** at a series of FITC loading amounts. (a) The original signal and (b) after subtracting the scattering from **nMOF-1** (0%). Numbers shown in the figure legend represent the FITC feed wt.%. Adapted with permission from *J. Am. Chem. Soc.*, **2014**, *136*, 12253–12256. Copyright 2014 American Chemical Society.

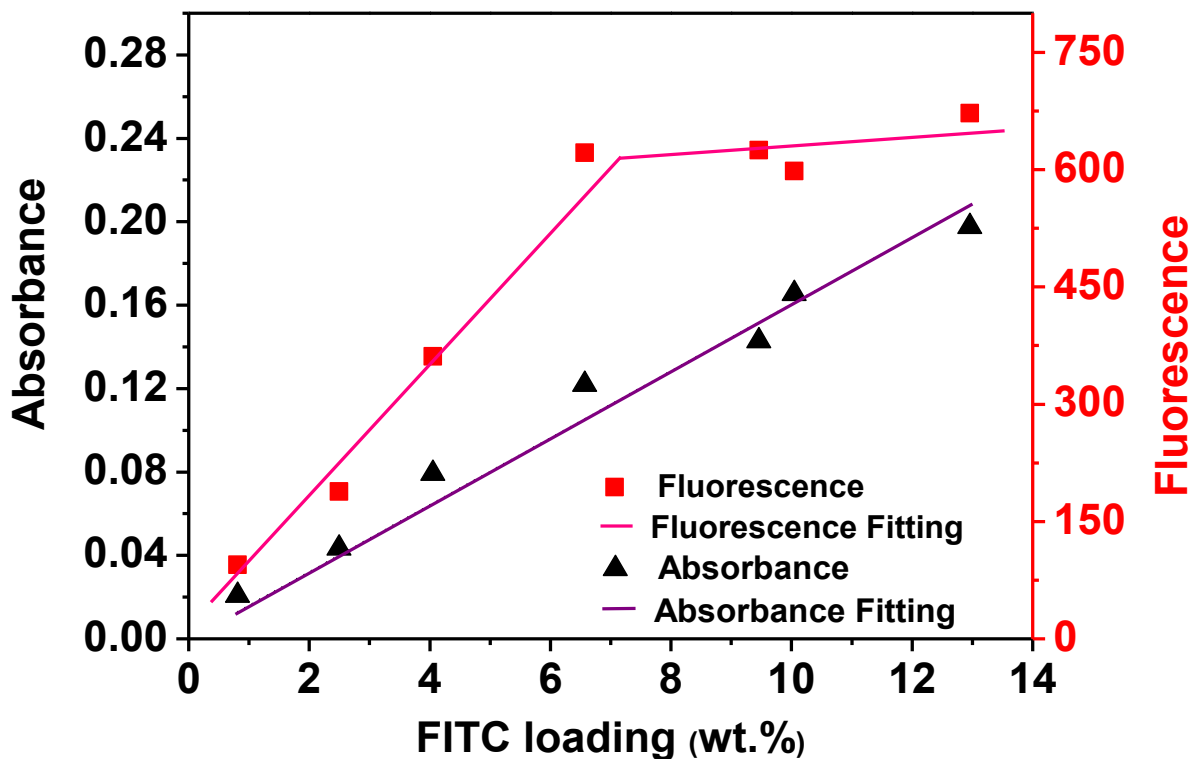


Figure 6-11 Fluorescence efficiency of **F-nMOF**s with different FITC loadings. The absorbance was acquired at 490 nm and the fluorescence intensity was detected at excitation/emission wavelength of 490 nm/516 nm. Reprinted with permission from *J. Am. Chem. Soc.*, **2014**, *136*, 12253–12256. Copyright 2014 American Chemical Society.

6.2.2 Response curve calibration

Ratiometric pH-sensitivity of **F-nMOF** was then determined and compared with free FITC to confirm that **F-nMOF** is an efficient pH sensor with rapid response. FITC acts as a pH sensor by providing pH-specific ratios of fluorescence intensities at 520 nm when excited at 488 nm and 435 nm, respectively. pH calibrations for both free FITC solution and **F-nMOF** suspension were carried out in acetate and PBS buffers with pH values ranging from 4.0 to 8.0 by fluorimetry. The 520 nm fluorescence intensity ratios by exciting at 488 nm and 435 nm ($I_{488/520}:I_{435/520}$) were

calculated and the correlation of fluorescence intensity ratio r to pH was established by non-linear curve fitting (Figure 6-12 a,b), which we will discuss in detail later.

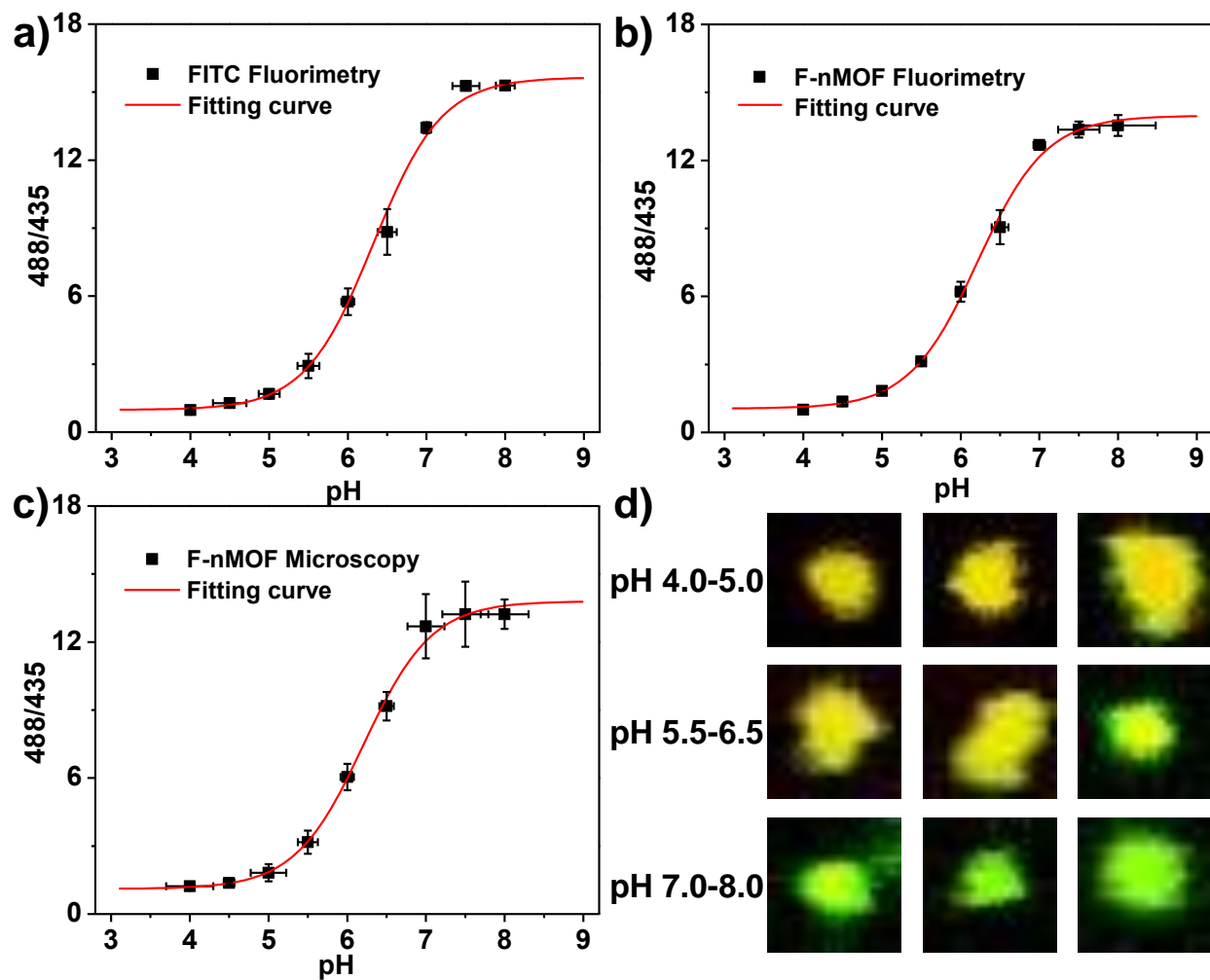


Figure 6-12 Calibration curves of r -pH responses. pH calibration curves of free FITC (a) and **F-nMOF** acquired by fluorimetry (b) and by CLSM (c). 488/435 in the Y-axis represents $r = I_{488/520} : I_{435/520}$. (d) CLSM images showing the overlay of green (488 nm excitation) and red (435 nm excitation) colors of **F-nMOF** particles in HBSS buffers with different pH values. Top, pH=4.0, 4.5 and 5.0; middle, pH=5.5, 6.0 and 6.5; bottom, pH=7.0, 7.5 and 8.0. Adapted with permission from *J. Am. Chem. Soc.*, **2014**, *136*, 12253–12256. Copyright 2014 American Chemical Society.

Moreover, **F-nMOF** was mixed with HBSS buffers with pH values ranging from 4.0 to 8.0 and subjected to confocal laser scanning microscopy (CLSM) imaging. The images of **F-nMOF** were acquired using dual excitation wavelengths, 488 nm and 435 nm, and analyzed by Image J to quantify the fluorescence intensity of **F-nMOF** particles. A calibration curve was generated using the same fitting method as for the fluorimetry data (Figure 6-12 c,d and Figure 6-13).

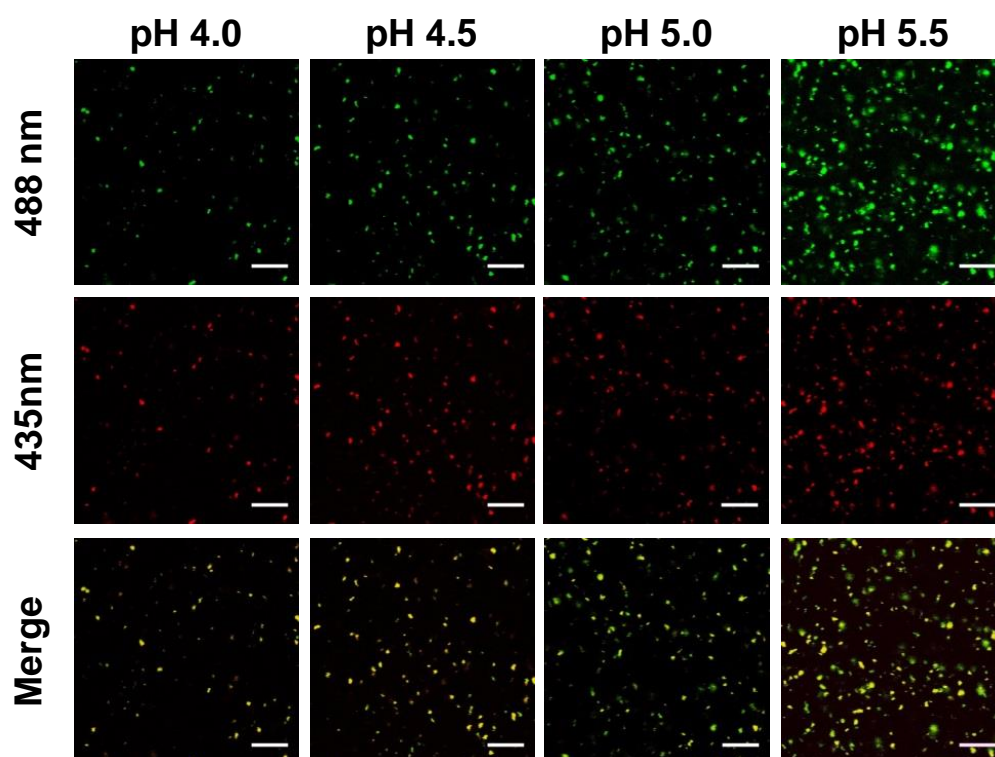


Figure 6-13 Images of **F-nMOF** dispersed in HBSS with a series of pH acquired by CLSM, applied with artificial colors by Image J.

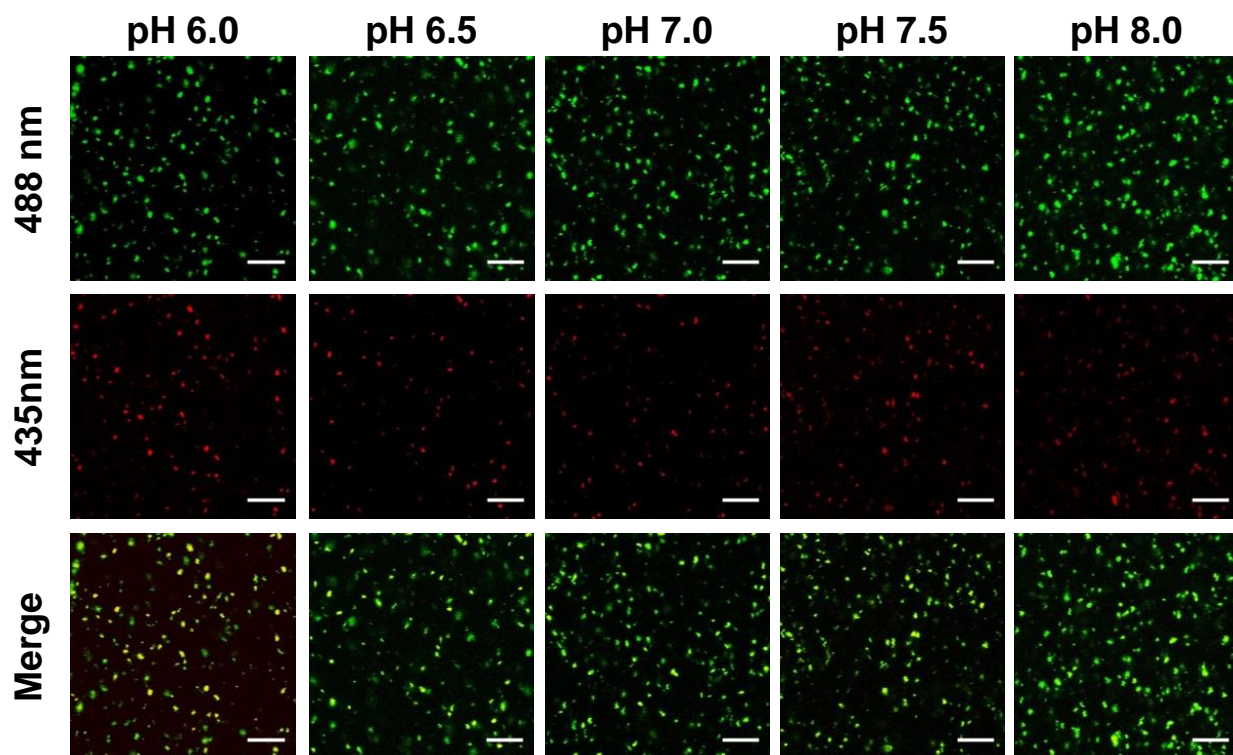


Figure 6-13 (Continued) Images of F-nMOF dispersed in HBSS with a series of pH acquired by CLSM, applied with artificial colors by Image J. The excitation wavelengths are 488 nm (green) and 435 nm (red), respectively, and the same emission wavelength of 520 nm is applied. Bar represented 5 μm . Reprinted with permission from *J. Am. Chem. Soc.*, **2014**, *136*, 12253–12256. Copyright 2014 American Chemical Society.

The dual-excitation fluorescence emission intensity ratio (r) to pH plot was similar to a titration curve, indicating that the pH response likely result from a deprotonation process. The pKa of fluorescein mono-anion is 6.7. The di-anion form of fluorescein has higher absorbance at 490 nm than its mono-anion form while the 435 nm absorption peak disappears.^{23,24} In order to better understand and analyze the correlation between r and pH, a fitting was performed as follows:

HA and A were used herein to refer to mono- and di-anionic forms of FITC, respectively. Since the other proton dissociation processes do not contribute to the ratio change of FITC

fluorescence,²⁴ the other steps of proton dissociation were ignored. The concentration of each species is:

$$[HA] = c_0 \frac{[H^+]}{[H^+] + K}$$

$$[A] = c_0 \frac{K}{[H^+] + K}$$

Where c_0 is the total concentration of FITC, and K is the dissociation constant of the related deprotonation step.

The fluorescence intensity is linearly correlated to FITC specie concentrations:

$$I_f = I_0 \phi_f \varepsilon bc = kc$$

$$I_{488nm} = k_{a1}[HA] + k_{b1}[A]$$

$$I_{435nm} = k_{a2}[HA] + k_{b2}[A]$$

Where I_0 , ϕ_f , ε , b , and c are incident light intensity, quantum yield, extinction coefficient, path length, and the concentration of the solution, respectively.

r can be calculated with the following equation:

$$r = \frac{I_{488nm}}{I_{435nm}} = \frac{k_{a1}[H^+] + k_{b1}K}{k_{a2}[H^+] + k_{b2}K} = \frac{\frac{k_{a1}}{k_{a2}}[H^+] + \frac{k_{b1}}{k_{a2}}K}{[H^+] + \frac{k_{b2}}{k_{a2}}K}$$

$$r = \frac{\frac{k_{a1}}{k_{a2}} e^{-2.303pH} + \frac{k_{b1}}{k_{a2}} K}{e^{-2.303pH} + \frac{k_{b2}}{k_{a2}} K}$$

Therefore, the r against proton activity $[H^+]$ fits a non-linear regression in a form of:

$$y = \frac{P_1x + P_2}{x + Q_1}$$

Where:

$$P_1 = \frac{k_{a1}}{k_{a2}}$$

$$P_2 = \frac{k_{b1}}{k_{a2}} K$$

$$Q_1 = \frac{k_{b2}}{k_{a2}} K$$

Based on this hypothesis, we ran the regression on MatLab, which gave the following results:

(1) For free FITC solution by fluorimetry:

$$r = \frac{0.98[H^+] + 7.42 \times 10^{-6}}{[H^+] + 4.74 \times 10^{-7}}$$

adjusted $r^2=0.99$

(2) For **F-nMOF** by fluorimetry:

$$r = \frac{1.05[H^+] + 8.17 \times 10^{-6}}{[H^+] + 6.14 \times 10^{-7}}$$

adjusted $r^2=0.99$

(3) For **F-nMOF** by CLSM:

$$r = \frac{1.11[H^+] + 8.61 \times 10^{-6}}{[H^+] + 6.24 \times 10^{-7}}$$

adjusted $r^2=0.99$

Additionally, the errors of pH were calculated from the errors of r were based on these equations:

$$[H^+] = Q_1 \left(\frac{H - L}{r - L} - 1 \right)$$

$$\frac{dpH}{dr} = \frac{1}{2.303} \frac{(H-L)}{(r-L)(H-r)}$$

where H and L are upper limit and lower limit of r , respectively,

$$H = \frac{P_2}{Q_1}$$

$$L = P_1$$

As shown in Figure 6-12, the pH-dependent changes in the $I_{488/520}:I_{435/520}$ ratios remain the same for free FITC and **F-nMOF**, indicating that the FITC sensing function was completely preserved in **F-nMOF**. The open channels of **F-nMOF** facilitate the rapid and free diffusion of hydronium ions, allowing rapid pH response of conjugated FITC.¹⁸ The pH calibration curves of **F-nMOF** acquired by fluorimetry and CLSM were similar, verifying the validity of the CLSM quantification method for subsequent live cell imaging studies. The pH response of **F-nMOF** exhibits high sensitivity and relatively small deviations at pH = 5.0-7.0, the typical pH range for cell culture media, cytosol, and endocytic compartments. The standard deviations of pH were below 0.2 pH unit in this pH range. Thus, **F-nMOF** represents an excellent nanosensor for sensing pH_i , and is ideally suited for real-time monitoring of endocytosis of nMOF and endosome maturation.

6.2.3 Live cell pH sensing

pH measurements of live cells at fixed pH values were then performed to confirm the validity of the pH calibration curve *in vitro*. Human non-small cell lung cancer H460 cells were incubated with **F-nMOF** in HBSS for 2 h and then incubated with fresh pH clamping buffers containing 100 μ M nigericin and with fixed pH values ranging from 4.0 to 8.0.²⁵ CLSM images

were obtained with dual excitation wavelengths and the $I_{488/520}:I_{435/520}$ ratios of **F-nMOF** particles inside the cells clamped at different pH values were analyzed by Image J (Figure 6-14). The pH vs. r curve shown in Figure 6-15 fits well with the pH calibration curve presented in Figure 6-12c, which further validates the pH calibration curves established by both fluorimetry and CLSM.

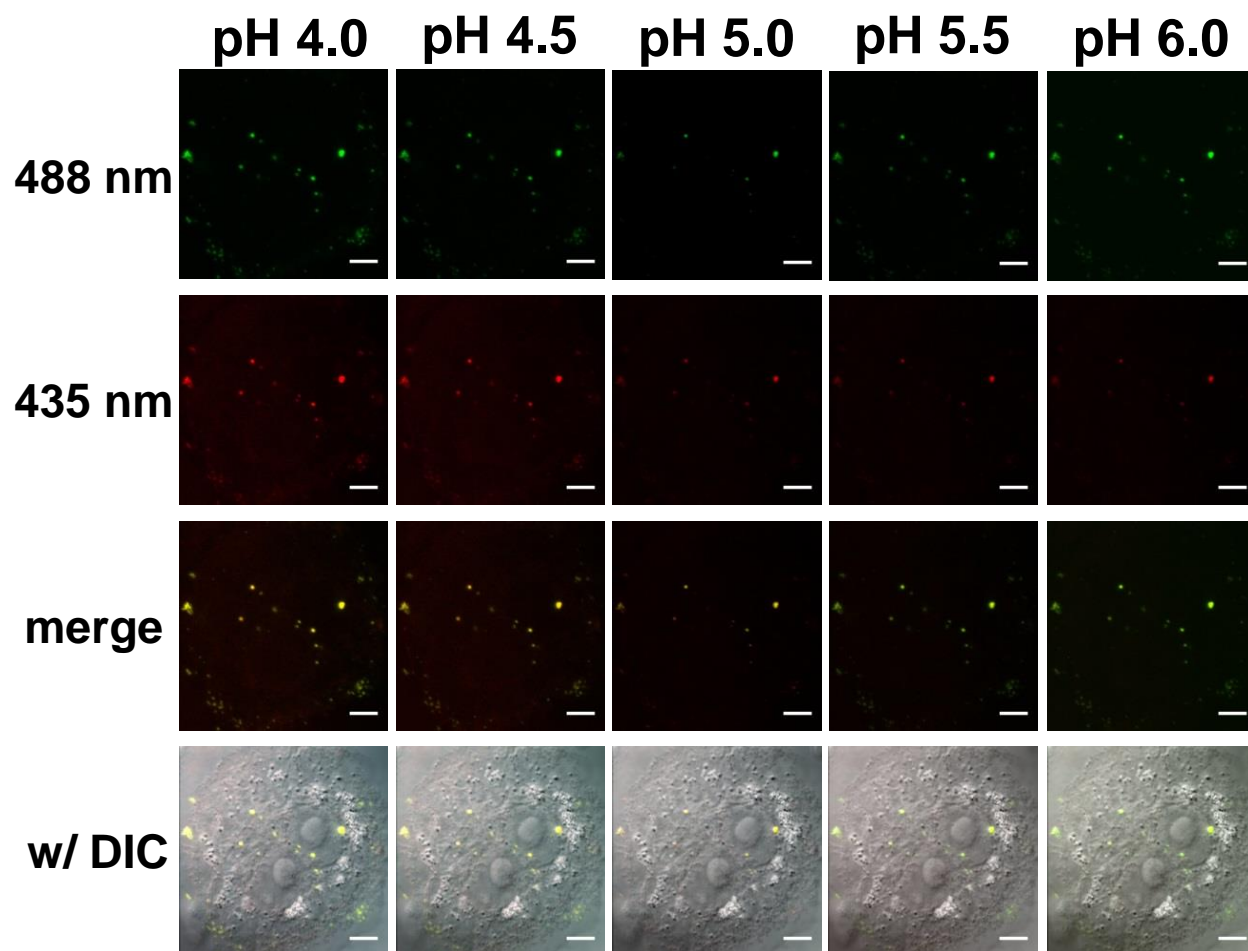


Figure 6-14 CLSM images of live cells clamped at various pH. Bar represented 5 μm .

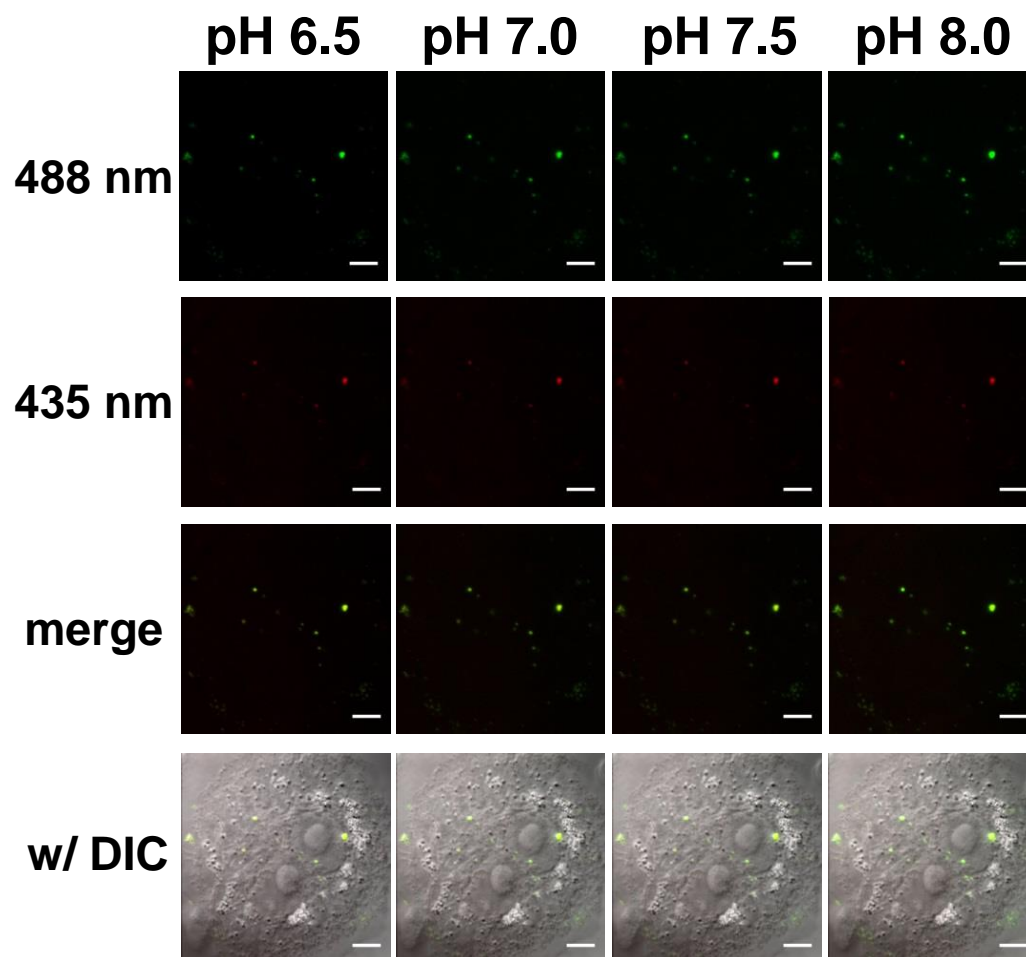


Figure 6-14(Continued) CLSM images of live cells clamped at various pH. Bar represented 5 μm . Reprinted with permission from *J. Am. Chem. Soc.*, **2014**, *136*, 12253–12256. Copyright 2014 American Chemical Society.

The endocytosis of **F-nMOF** in H460 cells was investigated. Time-dependent cellular uptake of **F-nMOF** was quantified by inductively coupled plasma-mass spectrometry (ICP-MS). Efficient cellular uptake was observed for **F-nMOF** in the first 30 min of incubation (Figure 6-16a). No significant difference was noticed between the uptake amounts after incubating for 30 min and 120 min, indicating rapid internalization of **F-nMOF**.

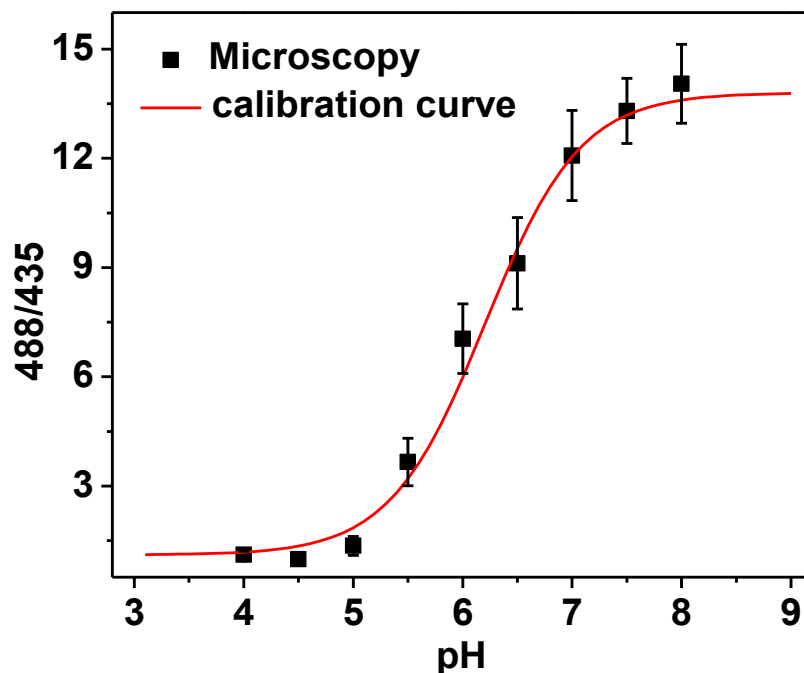


Figure 6-15 pH calibration in live cells by clamping the cells at various pH values. 488/435 in the Y-axis represents $r = I_{488/520} : I_{435/520}$. Reprinted with permission from *J. Am. Chem. Soc.*, **2014**, *136*, 12253–12256. Copyright 2014 American Chemical Society.

Intracellular distribution and stability of **nMOF-1** were directly observed by TEM (Figure 6-16 b-d). Upon entering the cells, **nMOF-1** located at the endosomes and maintained the structural integrity (hexagonal plate-like structure) inside the endosomes. The lattice fringes are clearly visible for endosome-trapped particles. The distance between lattice fringes was measured to be 2.25 nm (Figure 6-16d), in agreement with the d_{100} value of 2.26 nm for the **nMOF-1** structure. Fast Fourier Transform (FFT) analysis of the endosome-trapped **nMOF-1** also gave an electron diffraction pattern that is consistent with that of pristine **nMOF-1**, confirming that **nMOF-1** remain crystalline inside endosomes. These results collectively demonstrate that **F-nMOF** is a reliable pH_i sensor owing to its efficient endocytosis and adequate stability inside cells.

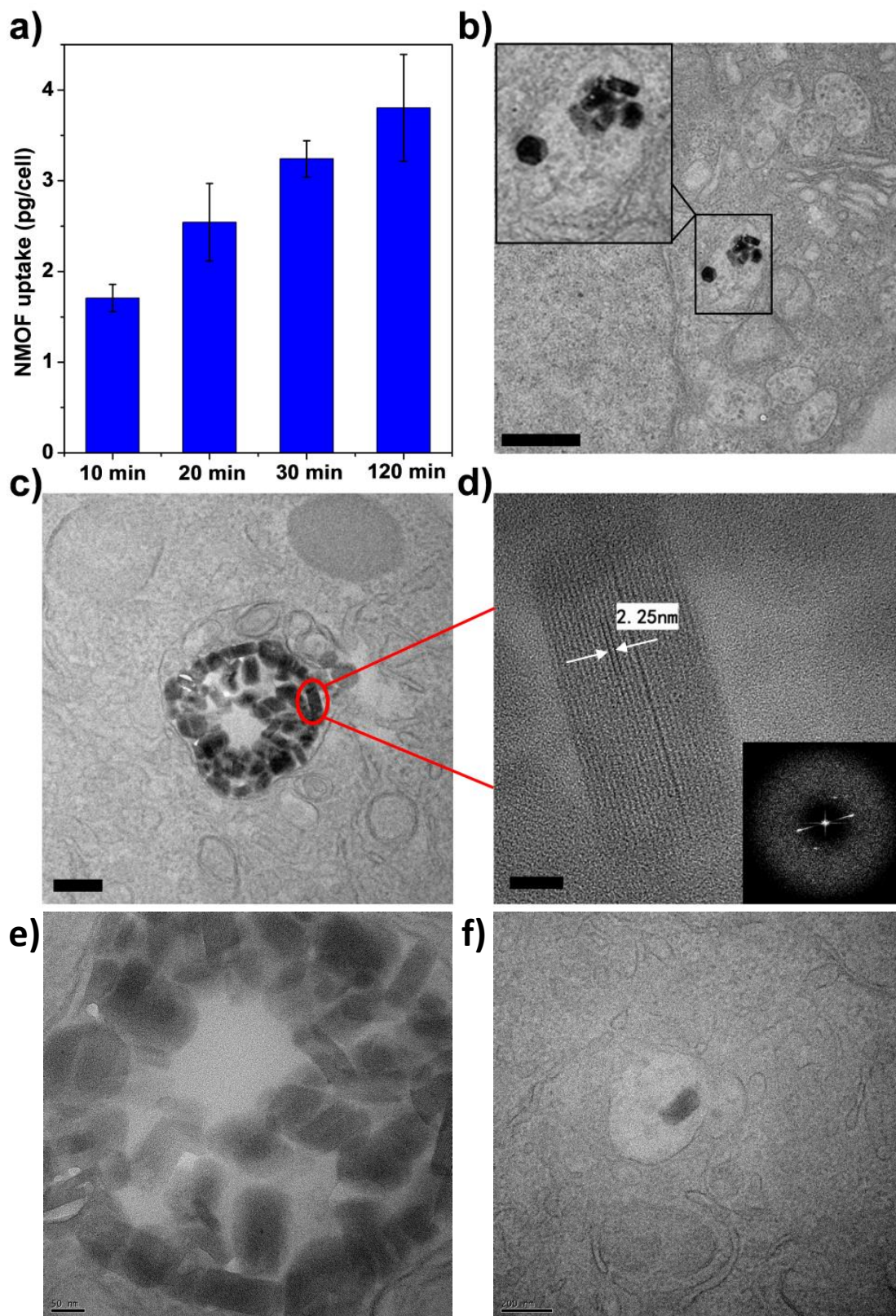


Figure 6-16 Cellular uptake and intracellular distribution of **F-nMOF** in H460 cells. (a) Time-dependent cellular uptake of **F-nMOF** in H460 cells determined by ICP-MS.

Figure 6-16 (Continued) (b)-(f) High-resolution TEM image showing the distribution and structural integrity of **nMOF-1** in the endosomes. Inset in (b) is a zoomed-in view showing the **nMOF-1** inside one endosome. (d) Zoomed-in view showing the **nMOF-1** marked by red circle in (c). Inset in (d) is the FFT image showing the electron diffraction pattern of (d). Bar represents 600 nm, 200 nm, 20 nm, 50 nm and 200 nm in (b)-(f), respectively. Adapted with permission from *J. Am. Chem. Soc.*, **2014**, *136*, 12253–12256. Copyright 2014 American Chemical Society.

The luminal pH of endocytic organelles is acidic, and acidification constitutes an important part of endosome maturation.²⁶ Endosome maturation can be completed within 30 minutes, with the pH dropping from ~6.8 (early endosome) to ~5.0 (late endosome).^{1,26} Because of the high sensitivity of **F-nMOF** in sensing pH ranging from 5.0 to 7.0 and its rapid and efficient endocytosis, we surmised that **F-nMOF** would be able to reveal the endosome acidification process and its own intracellular fate. Live cell imaging was thus performed to monitor the endocytosis of **F-nMOF** (Figure 6-17). Images were acquired every 20 s using dual excitation wavelengths (488 and 435 nm). The internalized **F-nMOF** particles were tracked and the 488/435 fluorescence intensity ratios were quantified by Image J. The pH of each individual endosome with **F-nMOF** entrapment was calculated using the pH calibration curve of **F-nMOF** obtained by CLSM (Figure 6-12c) and plot against time.

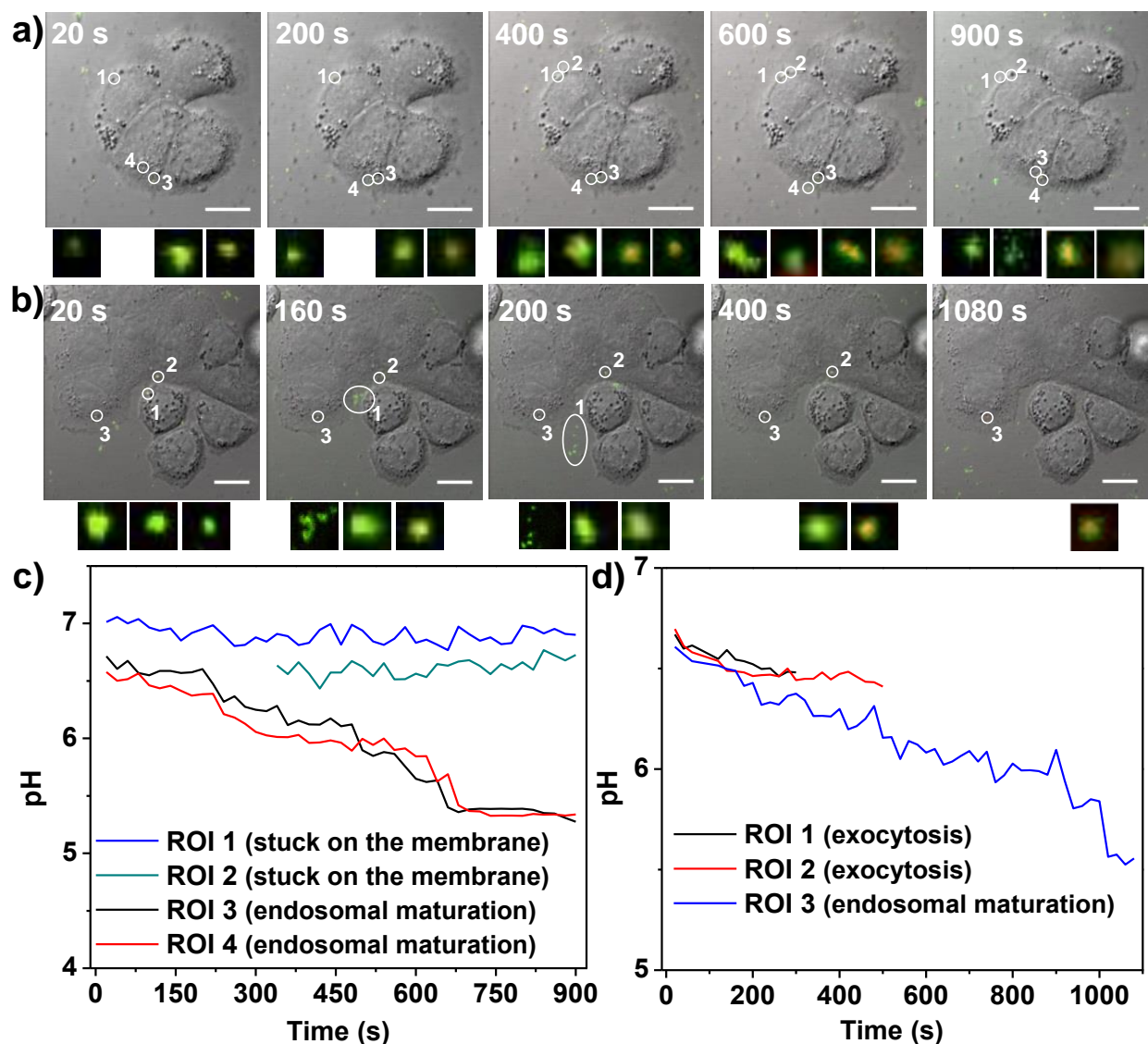


Figure 6-17 Time relapse pH changes in individual endosomes. (a)-(b) CLSM images showing overlays of DIC, 488 nm excitation (green), and 435 nm excitation (red). Each region of interest (ROI) was labeled with white circle and number. Small images showing under each CLSM image are zoomed-in views of overlays of green (488 nm excitation) and red (435 nm excitation) for each ROI. The small images represent ROI 1 to ROI 4 (a, video 1) or ROI 1 to ROI 3 (b, video 2) from left to right. Bar: 10 μm . (c)-(d) The pH evolution curve of each ROI was obtained by fitting the $I_{488/520}:I_{435/520}$ with the calibration curve. (c) and (d) were generated from (a) and (b), respectively. Adapted with permission from *J. Am. Chem. Soc.*, **2014**, *136*, 12253–12256. Copyright 2014 American Chemical Society.

F-nMOF particles shown in region of interest (ROI) 1 and ROI 2 in Figure 6-17a and video 1 (referring to Supplemental File video 1 and Supporting Information, SI of *J. Am. Chem. Soc.*,

2014, *136*, 12253–12256) were stuck on the cell membrane and were not internalized into the cells as evidenced by the orthogonal view obtained from the Z-stack series (Figure 6-18); the pH of these **F-nMOF** particles remained constant at ~6.8-7.0 over time (Figure 6-17c). The pH values of ROI 3 and ROI 4 in video 1 and ROI 3 in video 2 (referring to Supplemental File video 2 and SI of *J. Am. Chem. Soc.*, **2014**, *136*, 12253–12256) dropped from ~6.6-6.8 to ~5.3-5.5 (Figure 6-17 c,d), suggesting that these **F-nMOF** particles were entrapped in endosomes and experienced endosome maturation. Interestingly, we also observed exocytosis of **F-nMOF**: ROI 1 in Figure 6-17b and video 2 did not show significant acidification in the first 300 s and the **F-nMOF** particles were recycled back to the cell membrane and underwent exocytosis in 300 s. Five individual **F-nMOF** particles were observed after exocytosis, likely from one single endosome. Additionally, the pH of ROI 1 in Figure 6-17b and video 2 was about 6.5 before exocytosis (Figure 6-17d), which was consistent with the pH for typical recycling endosomes (pH 6.5). ROI 2 in Figure 6-17b and video 2 also experienced exocytosis after about 500 s and its pH remained at ~6.5 (Figure 6-17d). These results suggest that sufficient endosome acidification is necessary for intracellular trafficking of nMOFs. In the absence of acidification process, nMOFs undergo exocytosis mediated by recycling endosomes.¹

We also performed pH_i measurements on fixed cells that had been incubated with **F-nMOF**. The cells were incubated with **F-nMOF** for 5-20 min, fixed, and subjected to CLSM observation. The pH values of individual endosome in cells incubated with **F-nMOF** for different time periods were analyzed to provide histograms showing the numbers of endosomes of different pH values (Figure 6-19). The endosome maturation evolved over time with peak pH decreasing from 6.4 at 5 min to 5.6 at 20 min, which is consistent with previously reported endosome maturation processes.²⁶

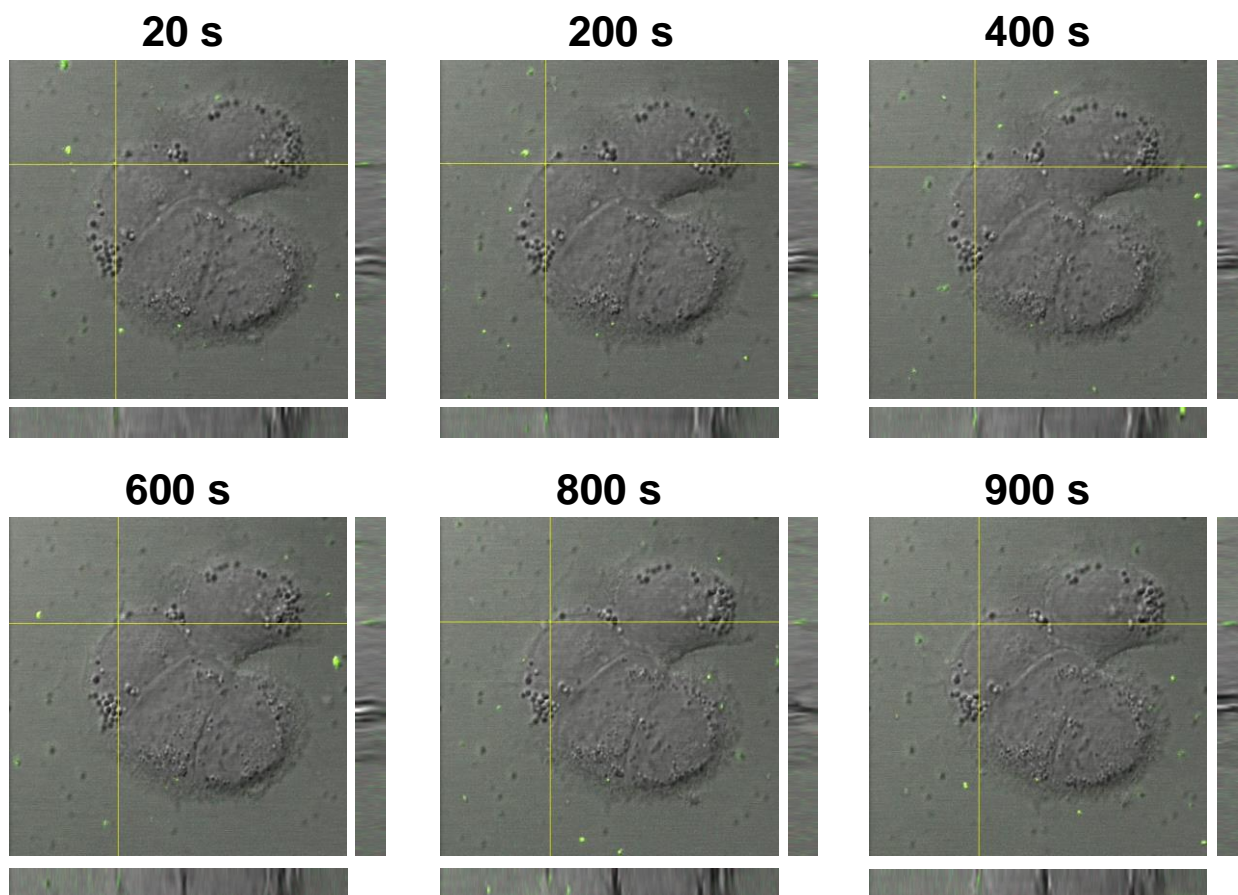


Figure 6-18 Orthogonal views of cells incubated with **F-nMOF** showing that the particle of interest was stuck on the cell membrane over time. Images were obtained from video 1 and showed the overlay of green fluorescence (488 nm channel), red fluorescence (435 nm channel), and DIC. Reprinted with permission from *J. Am. Chem. Soc.*, **2014**, *136*, 12253–12256. Copyright 2014 American Chemical Society.

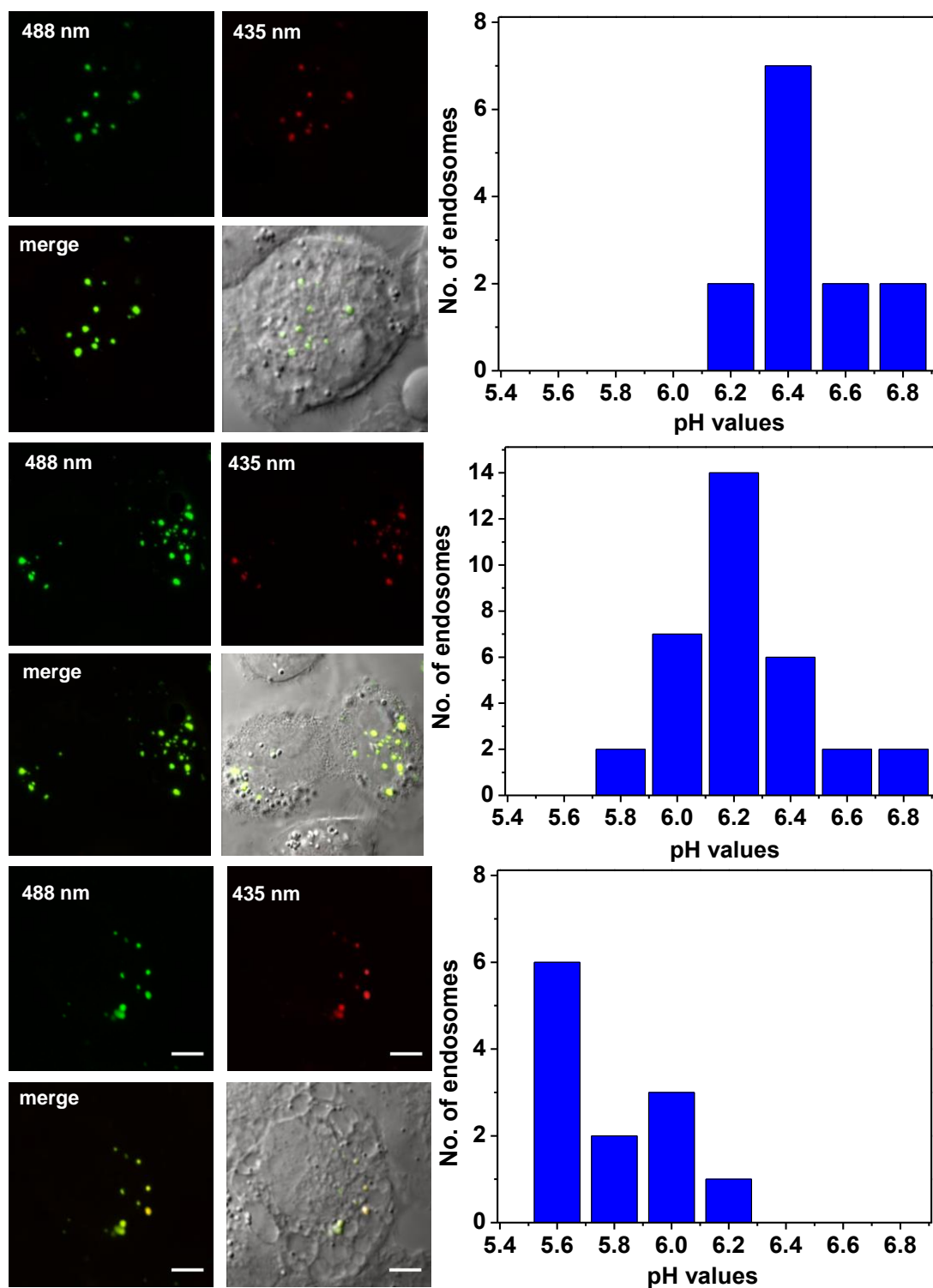


Figure 6-19 CLSM images and histograms showing the numbers of endosomes of different pH values. H460 cells were incubated with **F-nMOF** for 5 min (top), 10 min (middle) and 20 min (bottom) and imaged with CLSM after fixation. The histogram shows the number of endosomes at different pH's. Adapted with permission from *J. Am. Chem. Soc.*, **2014**, *136*, 12253–12256. Copyright 2014 American Chemical Society.

6.3 Conclusion

In this chapter, we report the first example of nMOFs for real-time intracellular pH sensing in live cells. FITC conjugated **nMOF-1** exhibited desired structural stability, fluorescence efficiency, pH response sensitivity, and efficient cellular uptake. Combining all these advantages of **F-nMOF**, this novel fluorescence nanosensor provides a reliable and accurate method for real-time intracellular pH sensing. Additionally, the present study also offers the first insight into the endocytosis and intracellular trafficking process of nMOFs.

6.4 Methods

nMOF-1 synthesis: A dimethylformamide (DMF) solution of 2'-amino-p-terphenyl-4,4''-dicarboxylic acid (**H₂L**, 2 mg/mL) was mixed with a DMF solution of ZrCl₄ (1.4 mg/mL), and the mixture was kept in an 80 °C oven for 5 days. The product was collected by centrifugation and washed with DMF, triethylamine/ethanol (1:20, v/v), and ethanol.

FITC conjugation: For a typical loading, an anhydrous DMF solution of FITC (50 µg/mL) was added to an **nMOF-1** suspension (0.5 mg in 0.5 mL of anhydrous DMF). Different FITC feed amounts (from 1 wt.% to 30 wt.%) were used to evaluate the correlation between FITC loading and fluorescence efficiency. The mixture was stirred at room temperature in the dark for 24 hours and the orange **F-nMOF** product was collected by centrifugation and washed with DMF and ethanol.

Authentic FITC-conjugated ligand (**FITC-L**) was also synthesized for comparison. A mixture of **H₂L** (10.2 mg, 0.031 mmol) and FITC (11.8 mg, 0.030 mmol) was dissolved in 3 mL of

anhydrous dimethylsulfoxide (DMSO) in a 20-mL glass vial. The solution was stirred at room temperature in the dark for 6 hours. The solution was lyophilized to remove most of the solvent. The remaining solution (about 0.5 mL) was added to 100 mL of dichloromethane. Yellow precipitate was collected by centrifugation and was washed with dichloromethane. Yield: 62%. $^1\text{H-NMR}$ (DMSO- d_6): δ =13.01 (br, 2H), 10.13 (s, 2H), 10.02 (s, 1H), 9.86 (s, 1H), 8.06 (d, 2H), 8.05-8.00 (m, 3H), 7.89 (d, 2H), 7.81 (dd, 2H), 7.63 (m, 3H), 7.57 (d, 1H), 7.12 (d, 1H), 6.66 (d, 2H), 6.57 (m, 4H).

^1H NMR sample digestion: For ^1H NMR spectroscopy (Bruker AVANCE II+ 500; 11.7 Tesla NMR), **F-nMOF** or **nMOF-1** was digested in a saturate solution of potassium phosphate in deuterium oxide. The organic species were extracted by DMSO- d_6 . The ^1H NMR spectra of FITC and FITC-L were also obtained in DMSO- d_6 for comparison.

Mass spectroscopy: **F-nMOF** was digested in a saturated potassium phosphate aqueous solution and the ligand was extracted with DMSO. The sample was delivered with 100% methanol on an LC-MS instrument (Agilent 1100 LC/MSD with ESI and APCI ion sources).

Dye leaching test: **F-nMOF** was incubated in HBSS at a concentration of 0.22 g/L. After 15 min, 30 min, 1 h, 2 h or 24 h of incubation the suspension was centrifuged at 13,000 rpm for 15 min to remove nMOFs and 500 μL of supernatant was collected for UV-vis measurement (and 500 μL HBSS was compensated each time). The supernatants were diluted by 5 fold with HBSS and subjected to UV-vis analysis. Accumulative FITC release was calculated by comparing the FITC amount in the supernatant with the total FITC loading.

FITC loading quantification: FITC was dissolved in a triethylamine/DMF (1:9, v/v) solution to obtain a series of FITC solutions with concentrations ranging from 1 to 5 mg/L. Absorption

spectra were recorded with a UV-vis spectrophotometer (UV-2401PC, Shimadzu, Japan). A standard curve was plotted from linear fitting of the absorbance at 523 nm as a function of FITC concentrations. The extinction coefficient was determined to be $0.0840 \text{ L mg}^{-1} \text{ cm}^{-1}$.

The supernatant collected from each washing step after FITC loading was prepared into 3.3 mL of triethylamine/DMF (1:9, v/v) solution, and the FITC amount was quantified by UV-vis spectrophotometer. The FITC loading amount was calculated by subtracting the amount in the supernatant (unloaded) from the feed amount.

Fluorescence efficiency in nMOFs with different FITC loading: nMOF-1 and F-nMOF with different dye loadings were dispersed in phosphate buffered solution (PBS) at an nMOF concentration of 50 mg/L. The absorption spectra of F-nMOF were acquired and corrected by eliminating the scattering background from blank nMOF-1. Meanwhile, the fluorescence intensity of F-nMOF was determined at excitation wavelength of 490 nm and emission wavelength of 516 nm. The absorbance at 490 nm and fluorescence intensity of F-nMOF (excitation at 490 nm and emission at 516 nm) were plotted against FITC loading amount.

Ratiometric pH calibration and measurements in buffers: The pH response of F-nMOF was evaluated in buffered solution with pH ranging from 4.0 to 8.0 with a spectrofluorophotometer (RF-5301PC, Shimadzu, Japan) and by confocal laser scanning microscopy (CLSM, Leica SP5 II, Integrated Microscopy Core Facility at the University of Chicago).

For the calibration by fluorimetry, 20 μL of 1 mg/mL F-nMOF or 0.1 mg/mL FITC free solution was added to 2 mL of buffered solution (acetic buffered solution for pH 4.0-6.0 and phosphate buffered solution for pH 6.5-8.0), respectively. Fluorescence spectra were recorded using two excitation wavelengths, 435 nm and 488 nm. The fluorescence emission intensity ratio was

calculated at emission wavelength of 520 nm. A pH calibration curve was obtained by plotting the ratio of fluorescence intensity at 488 nm and 435 nm ($I_{488/520}:I_{435/520}$) as a function of pH.

For the calibration by CLSM, 1 μ L of 1 mg/mL **F-nMOF** was mixed with 9 μ L of HBSS Hank's Balanced Salt Solution of which the pH was adjusted by 1 M NaOH or 1 M HCl to 4.0-8.0, and added to a glass-bottom petri dish (No. 1.5, uncoated glass, MatTek Corporation). The images were acquired using two different lasers (435 nm and 488 nm) and the same filter for 488 nm laser by CLSM. The fluorescence intensity of nMOF particles at dual excitation wavelengths was quantified directly from the images using Image J, and the fluorescence emission intensity ratio (488 nm versus 435 nm) was calculated accordingly. An *in vitro* pH calibration curve was obtained by plotting the ratio of fluorescence intensity at 488 nm and 435 nm ($I_{488/520}:I_{435/520}$) as a function of pH.

pH clamping and measurement experiments: H460 cells were seeded on a glass-bottom petri dish (No. 1.5, coated with poly-lysine, MatTek Corporation) at cell density of 5×10^5 cells and further cultured for 24 h. The cell culture medium was removed and replaced with fresh HBSS. The cells were further cultured with **F-nMOF** for 2 h. After the incubation, the HBSS was removed and replaced by clamping buffers (120 mM KCl, 5 mM NaCl, 1 mM MgCl₂, 1 mM CaCl₂, 20 mM HEPES) of pH ranging from 4.0 to 8.0, containing 100 μ M nigericin.

Images were collected using Leica SP5 II microscope equipped with 100X, 1.4 oil objective, PMT fluorescence detector, transmitted light detector with DIC polarizer, and full wrap incubator box with warm air heating for live samples controlled by LAS_AF Leica confocal software. For pH measurements, cells were imaged in three channels to yield three images, (i) exciting at 488 nm and collecting at 520 nm (ii) exciting at 435 nm and collecting at 520 nm (iii)

DIC. Mean intensity of **F-nMOF** inside the cells was measured in 488 nm and 435 nm channels and a ratio of 488 nm to 435 nm intensities of **F-nMOF** was obtained. The pH was plot against $I_{488/520} : I_{435/520}$.

Time-dependent cellular uptake: H460 cells were seeded on a 6-well plate at 1×10^6 cells per well and cultured for 24 h. Thirty microliter of 2 mg/mL **F-nMOF** were added to each well. After a 10-min, 20-min, 30-min, and 120-min incubation, cells were collected by cell scraper, washed with PBS three times, and counted with hemocytometer. The cells were centrifuged at 3,000 rpm for 5 min and the cell pellet was digested with 500 μ L of concentrated nitric acid. After 24 h, the digestion was diluted with water and subjected to inductively coupled plasma mass spectrometry (ICP-MS, Agilent 7700X) to determine the Zr concentration. Results were expressed as the amount of **F-nMOF** (pg) calculated from the Zr concentration associated with one cell.

TEM observation of nMOF-1 cellular uptake: The uptake and intracellular trafficking of **nMOF-1** in H460 cells were directly observed by TEM. H460 cells were seeded on 10-cm petri dish at 2×10^6 cells and cultured for 24 h. Two hundred microliters of 1 mg/mL **nMOF-1** were added to the cells. Following incubating for 2 h, the cells were fixed, sectioned at 40-70 nm thickness, and observed under TEM.

Live cell image acquisition and analysis: H460 cells were seeded on a glass-bottom petri dish (No. 1.5, coated with poly-lysine, MatTek Corporation) at cell density of 5×10^5 cells and further cultured for 24 h. The cell culture medium was removed and replaced with fresh HBSS before live cell imaging to avoid auto-fluorescence coming from the culture medium. The live cell imaging started right after adding 25 μ L of 1 mg/mL **F-nMOF** to the cells. Images were

collected using Leica SP5 II microscope equipped with 100X, 1.4 oil objective, PMT fluorescence detector, transmitted light detector with DIC polarizer, and full wrap incubator box with warm air heating for live samples controlled by LAS_AF Leica confocal software. For pH measurements, cells were imaged in three channels to yield three images, (i) exciting at 488 nm and collecting at 520 nm (ii) exciting at 435 nm and collecting at 520 nm (iii) DIC. Cross talk and bleed-through were measured and found to be negligible for the present experimental setup. No auto-fluorescence was observed on blank cells. A time relapse experiment was carried out to monitor the endocytosis and exocytosis of **F-nMOF** in H460 cells at a time interval of 20 s and a total time ranging from 15 to 18 minutes. Z-stack scanning was applied to each frame. Mean intensity of **F-nMOF** was measured in 488 nm and 435 nm channels and a ratio of 488 nm to 435 nm intensities of **F-nMOF** was obtained. The pH evolution of **F-nMOF** experienced was calculated from the pH calibration curve obtained before.

Intracellular pH sensing in fixed cells: H460 cells were seeded on a glass-bottom petri dish (No. 1.5, coated with poly-lysine, MatTek Corporation) at cell density of 5×10^5 cells and further cultured for 24 h. The cell culture medium was removed and replaced with fresh HBSS. The cells were incubated with **F-nMOF** for 5 min, 10 min, and 20 min, and fixed with 4% paraformaldehyde. The cells were imaged using Leica SP5 II microscope equipped with 100X, 1.4 oil objective, PMT fluorescence detector, and transmitted light detector with DIC polarizer. For pH measurements, cells were imaged in three channels to yield three images, (i) exciting at 488 nm and collecting at 520 nm (ii) exciting at 435 nm and collecting at 520 nm (iii) DIC. Mean intensity of **F-nMOF** was measured in 488 nm and 435 nm channels and a ratio of 488 nm to 435 nm intensities of **F-nMOF** were obtained. pH was calculated from the pH calibration curve obtained before.

6.5 References

1. Casey, J.R., Grinstein, S. & Orlowski, J. Sensors and regulators of intracellular pH. *Nat Rev Mol Cell Bio* **11**, 50-61 (2010).
2. Webb, B.A., Chimenti, M., Jacobson, M.P. & Barber, D.L. Dysregulated pH: a perfect storm for cancer progression. *Nature Reviews Cancer* **11**, 671-677 (2011).
3. Paroutis, P., Touret, N. & Grinstein, S. The pH of the secretory pathway: Measurement, determinants, and regulation. *Physiology* **19**, 207-215 (2004).
4. Loiselle, F.B. & Casey, J.R. Measurement of Intracellular pH. *Membrane Transporters in Drug Discovery and Development: Methods and Protocols* **637**, 311-331 (2010).
5. Wray, S. Smooth-Muscle Intracellular Ph - Measurement, Regulation, and Function. *Am. J. Physiol.* **254**, C213-C225 (1988).
6. Modi, S., *et al.* A DNA nanomachine that maps spatial and temporal pH changes inside living cells. *Nat Nanotechnol* **4**, 325-330 (2009).
7. Han, J.Y. & Burgess, K. Fluorescent Indicators for Intracellular pH. *Chem. Rev.* **110**, 2709-2728 (2010).
8. Charier, S., *et al.* An efficient fluorescent probe for ratiometric pH measurements in aqueous solutions. *Angew Chem Int Edit* **43**, 4785-4788 (2004).
9. Clark, H.A., Kopelman, R., Tjalkens, R. & Philbert, M.A. Optical nanosensors for chemical analysis inside single living cells. 2. Sensors for pH and calcium and the intracellular application of PEBBLE sensors. *Anal. Chem.* **71**, 4837-4843 (1999).
10. Benjaminsen, R.V., *et al.* Evaluating Nanoparticle Sensor Design for Intracellular pH Measurements. *ACS nano* **5**, 5864-5873 (2011).
11. Chen, S.J., *et al.* Full-Range Intracellular pH Sensing by an Aggregation-Induced Emission-Active Two-Channel Ratiometric Fluorogen. *J. Am. Chem. Soc.* **135**, 4926-4929 (2013).
12. Patrick, M.J., *et al.* Intracellular pH Measurements Using Perfluorocarbon Nanoemulsions. *J. Am. Chem. Soc.* **135**, 18445-18457 (2013).
13. Doussineau, T., Smaïhi, M. & Mohr, G.J. Two-Dye Core/Shell Zeolite Nanoparticles: A New Tool for Ratiometric pH Measurements. *Adv Funct Mater* **19**, 117-122 (2009).
14. Medintz, I.L., *et al.* Quantum-dot/dopamine bioconjugates function as redox coupled assemblies for in vitro and intracellular pH sensing. *Nature Materials* **9**, 676-684 (2010).

15. Wang, X.D., *et al.* Ultra-Small, Highly Stable, and Sensitive Dual Nanosensors for Imaging Intracellular Oxygen and pH in Cytosol. *J. Am. Chem. Soc.* **134**, 17011-17014 (2012).
16. Lanz Edvard, G.M., Slavik Jan, Kotyk Arnost. Use of FITC as a FLuorescent Probe for Intracellular pH measurement. *Journal of Fluorescence* **7**, 3 (1997).
17. Bradley, M., *et al.* pH sensing in living cells using fluorescent microspheres. *Bioorg. Med. Chem. Lett.* **18**, 313-317 (2008).
18. Rowsell, J.L.C. & Yaghi, O.M. Strategies for hydrogen storage in metal-organic frameworks. *Angew Chem Int Edit* **44**, 4670-4679 (2005).
19. Yang, Q.Y. & Zhong, C.L. Molecular simulation of adsorption and diffusion of hydrogen in metal-organic frameworks. *Journal of Physical Chemistry B* **109**, 11862-11864 (2005).
20. Shigematsu, A., Yamada, T. & Kitagawa, H. Wide control of proton conductivity in porous coordination polymers. *J. Am. Chem. Soc.* **133**, 2034-2036 (2011).
21. Peng, H.S., Stolwijk, J.A., Sun, L.N., Wegener, J. & Wolfbeis, O.S. A Nanogel for Ratiometric Fluorescent Sensing of Intracellular pH Values. *Angew Chem Int Edit* **49**, 4246-4249 (2010).
22. Akers, W.J., *et al.* Noninvasive Photoacoustic and Fluorescence Sentinel Lymph Node Identification using Dye-Loaded Perfluorocarbon Nanoparticles. *ACS nano* **5**, 173-182 (2011).
23. Alvarez-Pez, J.M., Ballesteros, L., Talavera, E. & Yguerabide, J. Fluorescein excited-state proton exchange reactions: Nanosecond emission kinetics and correlation with steady-state fluorescence intensity. *Journal of Physical Chemistry A* **105**, 6320-6332 (2001).
24. Martin, M.M. & Lindqvist, L. Ph-Dependence of Fluorescein Fluorescence. *J Lumin* **10**, 381-390 (1975).
25. Bright, G.R., Fisher, G.W., Rogowska, J. & Taylor, D.L. Fluorescence Ratio Imaging Microscopy - Temporal and Spatial Measurements of Cytoplasmic Ph. *J. Cell Biol.* **104**, 1019-1033 (1987).
26. Huotari, J. & Helenius, A. Endosome maturation. *EMBO J.* **30**, 3481-3500 (2011).

Supplemental Files

The following videos are available online. Both files can be found in Supporting Information of *J. Am. Chem. Soc.*, **2014**, *136*, 12253–12256.

Video 1 The pH evolution of endosomes monitored by **F-nMOF**.

Video 2 Direct observation of **F-nMOF** going through exocytosis.